Viscothermal wave propagation including acousto-elastic interaction

W.M. Beltman

CIP-DATA KONINKLIJKE BIBLIOTHEEK, DEN HAAG

Beltman, Willem Marinus

Viscothermal wave propagation including acousto-elastic interaction /
Beltman, Willem Marinus. [S.1 : s.n.]. -Ill.
Thesis Enschede.- With ref. - With summary in Dutch.
ISBN 90-3651217-4

Subject headings: acoustics, acousto-elasticity, viscothermal wave propagation, finite elements
Cover: Laserium ® "Pink Floyd - The Wall" (*We don't need no education...*) at the Griffith Observatory, Hollywood, California on February 8, 1998. Artist: Tim Barrett. Picture: Marco Beltman. With permission of Laser Images Inc. and the Griffith Observatory.

VISCOTHERMAL WAVE PROPAGATION INCLUDING ACOUSTO-ELASTIC INTERACTION

PROEFSCHRIFT

ter verkrijging van
de graad van doctor aan de Universiteit Twente,
op gezag van de rector magnificus,
prof.dr. F.A. van Vught,
volgens besluit van het College voor Promoties
in het openbaar te verdedigen
op donderdag 22 oktober 1998 te 15:00 uur

door

Willem Marinus Beltman

geboren op 19 juli 1971

te Gorssel

DIT PROEFSCHRIFT IS GOEDGEKEURD DOOR:

PROMOTOR: PROF.DR.IR. H. TIJDEMAN

Preface

Completing this work would not have been possible without the support and co-operation of a large number of people. First of all I thank my supervisor, Henk Tijdeman, for giving me the opportunity to carry out this research. He is always ready to offer support to his students and has created a very pleasant working environment with good facilities. I enjoyed working in the dynamics group with my colleagues Ruud Spiering, Peter van der Hoogt, Bert Wolbert, Frits van der Eerden and Tom Basten. I am indebted to Debbie Vrieze and Piet Laan for their administrative and computer support respectively.

A number of MSc students performed their graduation research within the framework of my thesis project. Their work made very important contributions to the present study. I thank all students for their work and the pleasant time.

This project was carried out in close co-operation with, and supported by, a number of firms and institutions. The co-operation was very enjoyable and the industrial application of the newly developed techniques added an extra dimension to my work. I thank Frank Grooteman, André de Boer (National Aerospace Laboratory), Berend Winter, Marcel Ellenbroek, Jaap Wijker (Fokker Space), Rob Dokter, Freek van Beek, Pieter van Groos (Océ Technologies), Bert Roozen (Philips Research Laboratories), Charles van de Ven, Gerard Westendorp (Nefit Fasto). The financial support from Shell and the Technology Foundation is gratefully acknowledged.

Kees Venner, and Ysbrand Wijnant contributed with valuable suggestions, help and comments. I thank Bart Paarhuis and Katrina Emmett for their help in improving the manuscript.

Finally, I thank my family and friends for all their support. My parents have always stimulated and encouraged my brother, my sister and myself in our efforts, often making sacrifices for our sake. They deserve a big compliment.

Thank you,

Enschede, 22 October 1998

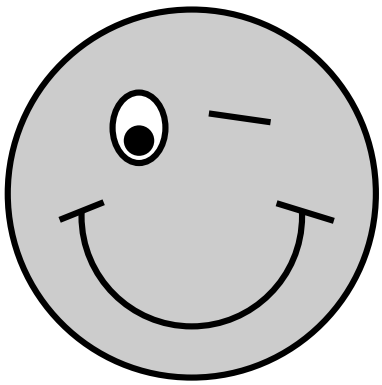

Marco Beltman

Summary

This research deals with pressure waves in a gas trapped in thin layers or narrow tubes. In these cases viscous and thermal effects can have a significant effect on the propagation of waves. This so-called viscothermal wave propagation is governed by a number of dimensionless parameters. The two most important parameters are the shear wave number and the reduced frequency. These parameters were used to put into perspective the models that were presented in the literature. The analysis shows that the complete parameter range is covered by three classes of models: the standard wave equation model, the low reduced frequency model and the full linearized Navier Stokes model. For the majority of practical situations the low reduced frequency model is sufficient and the most efficient to describe viscothermal wave propagation. The full linearized Navier Stokes model should only be used under extreme conditions. The low reduced frequency model was experimentally validated with a specially designed large-scale setup. A light and stiff solar panel, located parallel to a fixed surface and performing a small amplitude normal oscillation, was used. By assuming the panel to be rigid, attention could be focused on the viscothermal model. The large scale of the setup enabled accurate measurements and detailed information to be obtained about the pressure distribution in the layer. Analytical and experimental results show good agreement: the low reduced frequency model is very well suited to describe viscothermal wave propagation. In practical applications the surfaces or walls are often flexible and there can be a strong interaction between the wave propagation and surface or wall motion. As a next step, a new viscothermal finite element was developed, based on the low reduced frequency model. The new element can be coupled to structural elements, enabling fully coupled acousto-elastic calculations for complex geometries. The acousto-elastic model was experimentally validated for a flexible plate backed by a thin air layer. The results show that the viscothermal effects lead to a significant energy dissipation in the layer. Furthermore, the acousto-elastic coupling was essential and had to be included in the analysis. Numerical and experimental results show good agreement: a new reliable viscothermal

acousto-elastic simulation tool has been developed. An additional series of preliminary measurements indicate that obstructions in a layer may further increase the energy dissipation. However, non-linear behaviour was observed that could not be described with the linear viscothermal models. A simple model was developed that explained the non-linear behaviour. Finally, the developed techniques were successfully applied to a number of problems: the behaviour of stacked solar panels attached to a satellite during launch, the design of a new inkjet print head and the acoustic behaviour of double wall panels.

Samenvatting

Dit onderzoek richt zich op het beschrijven van drukgolven die zich voortplanten in een dunne laag gas of in een gas dat zich bevindt in een nauwe buis. In deze gevallen kunnen viskeuze en thermische effecten een belangrijke invloed hebben op de voortplanting van deze golven. Het gedrag wordt bepaald door een aantal dimensieloze kentallen. De twee belangrijkste kentallen zijn het "shear wave" getal en de gereduceerde frequentie. Met deze parameters zijn de modellen die in de literatuur gepresenteerd zijn in perspectief geplaatst. De analyse toont aan dat het volledige parametergebied bestreken wordt door drie klassen modellen: het standaard golfvergelijkingsmodel, het lage gereduceerde frequentie model en het volledige gelineariseerde Navier Stokes model. Voor nagenoeg alle praktische situaties is het lage gereduceerde frequentie model voldoende en het meest efficiënt om golfvoortplanting inclusief viskeuze en thermische effecten te beschrijven. Het volledige gelineariseerde Navier Stokes model hoeft alleen onder zeer extreme omstandigheden gebruikt te worden. Het lage gereduceerde frequentie model is experimenteel gevalideerd aan de hand van een speciaal ontworpen testopstelling. Hiervoor is een licht en stijf zonnepaneel gebruikt dat zich parallel aan een vaste wand bevindt. Het paneel voert een trilling met een kleine amplitude uit loodrecht op de wand. Doordat het paneel zich star gedraagt kan alle aandacht gericht worden op het golfvoortplantingsmodel. De grote afmetingen van de opstelling maken metingen met een hoge mate van nauwkeurigheid mogelijk en bovendien is gedetailleerde informatie verkregen over de drukverdeling in de luchtspleet tussen paneel en vast oppervlak. Analytische en experimentele resultaten komen goed overeen: het lage gereduceerde frequentie model is erg geschikt om golfvoortplanting inclusief viskeuze en thermische effecten te beschrijven. In de praktijk heeft men vaak te maken met flexibele oppervlakken of wanden. Er kan een sterke interactie zijn tussen de golfvoortplanting en de elastische wandbeweging. Als vervolg is daarom een nieuw akoestisch eindig element ontwikkeld, gebaseerd op het lage gereduceerde frequentie model. Dit element is in staat om golfvoortplanting inclusief thermische en viskeuze effecten te beschrijven. Het

kan gekoppeld worden aan constructie elementen, waardoor volledig gekoppelde berekeningen voor complexe geometrieën mogelijk zijn. Het akoestoelastische eindige elementen model is gevalideerd aan de hand van experimenten met een ingeklemde plaat met daaronder een dunne luchtlaag. De resultaten laten zien dat een aanzienlijke hoeveelheid energie gedissipeerd kan worden door viskeuze effecten. Daarnaast is de koppeling erg belangrijk. De numerieke en experimentele resultaten vertonen goede overeenkomst: er is een nieuwe en betrouwbare berekeningsmethode ontwikkeld voor akoestoelastische problemen, inclusief viskeuze en thermische effecten. Oriënterende metingen tonen aan dat obstructies in een dunne laag de energiedissipatie verder kunnen doen toenemen. Dit gedrag is echter sterk niet-lineair van karakter en kan derhalve niet voorspeld worden met de lineaire modellen. Er is een eenvoudig model ontwikkeld dat het niet-lineaire gedrag verklaart. De ontwikkelde technieken zijn tenslotte succesvol ingezet bij een aantal praktische toepassingen: het gedrag van opgevouwen zonnepanelen aan een satelliet tijdens de lancering, het ontwerp van een inkjet printkop en het akoestisch gedrag van dubbelwandige panelen.

Contents

Chapter 1

Introduction

1.1 General introduction

1.1.1 Acoustics

According to Webster's revised unabridged dictionary, acoustics is:
"the science of sounds, teaching their nature, phenomena and laws".
Sound is generated by the motion of particles. It is a compression and rarefaction of the medium (see Figure 1.1).

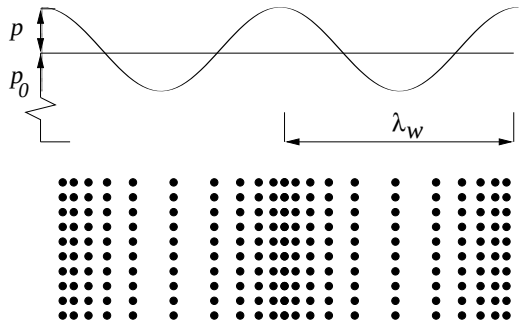

Figure 1.1: Longitudinal sound waves

The particles transmit the vibration and in this way a wave propagates through the medium. This type of behaviour can be illustrated with the following simple example. Consider a row of people. A person at the end of the row steps sideways and bumps into the person next to her or him and then steps back. The second person then transmits this "disturbance" to the third person. In this way a wave propagates down the line of people. This example shows that it is important to distinguish between the particle (person) velocity and the actual wave speed. The particles (persons) perform

a small oscillation around their equilibrium position, while the wave propagates through the medium [1]. In air at atmospheric conditions the speed of sound is approximately 340 m/s. Standard acoustic waves in air are longitudinal waves: the direction of motion of the particles and the propagation direction of the wave coincide. In other media or situations other types of waves may exist.

Due to the compression and rarefaction the motion of the particles is accompanied by pressure disturbances with amplitude p (see Figure 1.1). The pressure disturbances associated with sound waves are usually small disturbances upon a steady state, *e.g.* atmospheric, condition (in Figure 1.1 indicated by p_0). Because sound is a mechanical phenomenon, it cannot propagate in vacuum. In the latter case there simply is no medium to transmit the mechanical vibrations.

The most important quantities that characterize a harmonic sound wave are its speed of propagation, its wavelength and its amplitude. The speed of propagation depends on the medium of interest and the ambient conditions. The wavelength is the distance after which the pressure pattern is repeated (see figure 1.1). The frequency of the wave is the number of cycles per second. For standard acoustic wave propagation the frequency f and the wavelength λ_w are related as:

$$\lambda_w = \frac{c_0}{f} \tag{1.1}$$

where c_0 is the undisturbed (adiabatic) speed of sound. The wavelength thus decreases with increasing frequency. The human ear is able to detect sound in the frequency range between 20 Hz and 20 kHz. For air under atmospheric conditions, this corresponds to wavelengths between roughly 1.7 cm and 17 m.

1.1.2 Standard acoustic wave propagation

The mathematical concept to describe the propagation of sound waves, based on the so-called wave equation, has long been known. It is widely used to describe for instance sound fields in large enclosures and radiation and scattering phenomena. The basis of this acoustic equation is the more general set of fluid dynamics equations: the Navier Stokes equations. This very complicated set of non-linear equations can be drastically simplified for the acoustic case. Small perturbations are introduced and mean flow is assumed to be zero. There is no heat exchange between the medium and the surrounding boundary: the process is assumed adiabatic. The medium is homogeneous:

[1] In the present study the mean flow is zero

the properties of the medium are the same throughout the domain. This condition is satisfied if the wavelength is large compared to the intermolecular spacing, the so-called mean free path. Finally, the viscosity of the medium, a measure for the "stickyness", is neglected. Viscosity effects are typically important in the vicinity of a wall, where the medium sticks to the surface. Viscosity is thus usually neglected when describing sound propagation in large enclosures and unconfined spaces. If these assumptions are used, the Navier Stokes equations can be further simplified to a linearized set of equations. In combination with the equation of continuity and the equation of state, a partial differential equation in terms of the pressure perturbation is obtained: the wave equation. This equation forms the basis for the description of standard acoustic wave propagation.

1.1.3 Solution techniques for standard acoustic wave propagation

The wave equation has been extensively studied and consequently a large variety of solution methods is available. Several analytical techniques were developed. During the last decades the computer has enabled the numerical simulation of sound fields for complex geometries and boundary conditions (see *e.g.* [1]). A popular numerical technique, the Finite Element Method (FEM), is based on a volume modelling of the medium. This method is generally accepted and a large amount of knowledge and experience is available. Finite element models have also been developed to describe the propagation of sound in porous media and to describe the behaviour of absorbing walls. The method is usually applied to confined spaces, although for instance "infinite finite" elements were developed for radiation problems.

Another popular numerical technique is the Boundary Element Method (BEM). This method is based on a surface modelling of the boundaries of the medium. In physical terms, the surface of for instance a vibrating panel is covered with a distribution of acoustic monopoles ("acoustic sources") or dipoles. The strength distribution of these monopoles and dipoles then has to be calculated. This method is especially suited for unconfined spaces because the radiation conditions are automatically satisfied.

Both in FEM and BEM a sufficient number of elements has to be used per wavelength to accurately describe a signal of interest. Since the wavelength dramatically decreases with increasing frequency, the required number of elements shows a strong increase. Furthermore the detailed information, provided by the deterministic FEM and BEM approaches, is not very meaningful in the high frequency range. For the high frequency range, Statistical

Energy Analysis was developed. Essentially, this technique is based on averaging and energy flows.

Finally, multigrid techniques and multilevel integration techniques are used in acoustical problems. For FEM and BEM, the computational efforts show a strong increase with problem size. Multilevel algorithms are more efficient by using the economy of scales. The multigrid techniques are based on a volume modelling, the equivalent of FEM, while the multilevel integration techniques are based on a boundary integral approach, the equivalent of BEM.

It can be concluded that a variety of generally accepted models is available to deal with standard acoustic wave propagation. For a more detailed discussion the reader is referred to [2].

1.1.4 Viscothermal wave propagation

This is the first important aspect of the present thesis. The key issue is that the viscous and thermal effects are now included in the analysis.

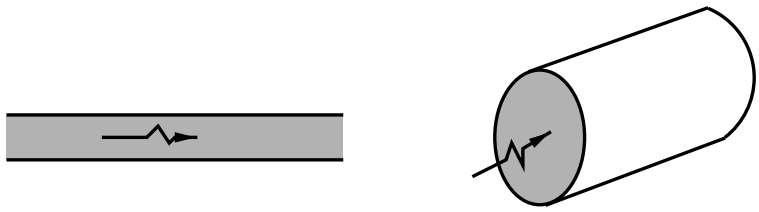

Figure 1.2: Sound waves in thin layers or narrow tubes

Consider the propagation of sound in a thin layer or a narrow tube (see Figure 1.2). At the wall, there is a no-slip condition for the medium: it sticks to the surface. For a thin layer or a narrow tube, this can lead to significant boundary layer effects, where viscosity is important. Furthermore, thermal effects can play an important role. For a mathematical description of viscothermal wave propagation, the Navier Stokes equations and the energy equation are used as a starting point. This time the viscous and thermal effects are retained in the analysis. The following basic assumptions are used: no mean flow, small perturbations and a homogeneous medium. The Navier Stokes equations can be simplified using these basic assumptions.

In the literature a seemingly wide variety of models is presented, each with their own additional assumptions. An overview of viscothermal models for the propagation of sound in tubes was presented by Tijdeman [3]. By using dimensionless parameters, the models were put into perspective. For

layer geometries, however, the viscothermal modelling is less well developed, as will be demonstrated in chapter 2.

1.1.5 Solution techniques for viscothermal wave propagation

For the propagation of sound in tubes, several analytical and numerical techniques are available (see also chapter 2). For layer geometries a number of analytical techniques were developed. These methods however are restricted to very simple geometries and boundary conditions. Recently, a boundary element formulation for viscothermal wave propagation in thin layers was presented by Karra, Ben Tahar, Marquette and Chau [4] and Karra and Ben Tahar [5]. This model is based on a full linearized Navier Stokes model and is not very efficient for viscothermal wave propagation in layers, as will be shown in chapter 2. To the author's knowledge no general, efficient solution technique is available for viscothermal wave propagation in thin layers.

1.1.6 Acousto-elasticity

This is the second important aspect of the present thesis. Consider a layer of gas in a narrow tube with flexible walls or a thin layer of gas trapped between flexible surfaces (see Figure 1.3).

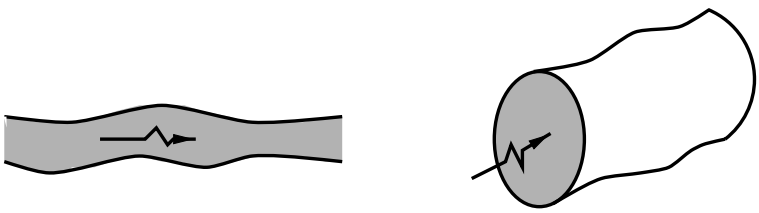

Figure 1.3: Sound waves in thin layers with flexible surfaces or narrow tubes with flexible walls

On the one hand, the pressure field inside the layer or tube puts the flexible surfaces or walls into motion. On the other hand, the motion of the surfaces or walls has to be followed by the medium in the layer or tube. Hence the wall motion affects the pressure distribution in the layer or the tube and vice versa. This indicates that there is a mutual interaction between the pressure field and the elastic deformation: acousto-elasticity. Especially for thin layers or narrow tubes, this interaction can be very important. The behaviour of the coupled system can be completely different from the behaviour of the two uncoupled subsystems. This illustrates the need for a

fully coupled analysis where the motion of the structure and the medium are to be coupled on the interface.

1.1.7 Solution techniques for acousto-elastic problems

The modelling of the dynamical behaviour of flexible structures (in vacuum) is very well developed. Several models are available to deal with a large variety of problems. The description of the interaction for the standard acoustic case is also well established. Finite element and boundary element techniques are widely used to deal with fully coupled acousto-elastic calculations. Reduction techniques, like component mode synthesis, were developed to reduce the computing time.

For the viscothermal case, however, no general, efficient acousto-elastic model is available. The boundary element model, presented by Karra and Ben Tahar [5] is able to deal with coupled calculations for rotatory symmetric problems. Their viscothermal model however is not very efficient (see chapter 2) and in addition a finite element technique is usually more beneficial for small enclosed spaces.

1.1.8 Applications

There is a wide range of applications for the present research. Traditionally, viscothermal models have been used to describe the behaviour of spherical resonators, the propagation of sound waves in tubes, the behaviour of miniaturized transducers and the squeeze film damping between plates (see chapter 3). In the present study the viscothermal models will also be used to describe some other applications: the behaviour of a folded stack of solar panels during launch, the design of an inkjet print head and the acoustic behaviour of double wall panels (see chapter 6).

1.2 Formulation of the problem

Development, implementation, validation and application of a model for the description of viscothermal wave propagation, including acousto-elastic interaction.

1.3 Outline

As far as the development of new models is concerned, attention will be focused on the viscothermal models, since the structural models are already

very well developed. In chapter 2 an overview is presented for viscothermal wave propagation. Based on a parameter approach, as presented by Tijdeman [3] for tubes, the various models are put into perspective. The models are all written in a general form and therefore apply to different co-ordinate systems (*e.g.* spherical, cylindrical or cartesian). The low reduced frequency model of Tijdeman is extended to thin layers for the present study. It is stressed that the models that are described in chapter 2 are not new. However, for the present investigation all models were rewritten into the aforementioned dimenionless form. Based on a parameter analysis, the most efficient model is identified: the low reduced frequency model. Therefore chapter 2 also serves as a justification for the emphasis that is placed on the low reduced frequency model. In order to demonstrate the wide range of applicability of the low reduced frequency model, a number of examples from the literature is discussed in chapter 3. In this chapter an overview of fundamental solutions and general applications is given. Because the models are written in terms of dimensionless parameters and solutions for various co-ordinate systems are given, this chapter also serves as a solution overview. Chapter 4 concerns an experimental validation of the low reduced frequency model. A special large-scale setup with an oscillating solar panel was designed for this purpose. As a next step, in chapter 5 a new finite element model is developed for fully coupled acousto-elastic calculations including viscothermal effects. A number of convergence tests were carried out and the model was experimentally validated with a special test setup. In chapter 6 the newly developed techniques are used in a number of applications: the behaviour of stacked solar panels during launch, the design of an inkjet print head and the acoustic behaviour of double wall panels. A preliminary study was carried out to investigate the influence of obstructions in a thin layer. Finally, the conclusions are presented in chapter 7.

Chapter 2

Linear viscothermal wave propagation

2.1 Introduction

The propagation of sound waves with viscothermal effects has been investigated in several scientific disciplines. The propagation of sound waves in tubes was investigated already by Kirchhoff and Rayleigh [6]. In *tribology*, the Reynolds equation is used to calculate the pressure distribution in fluid films trapped between moving surfaces. Reynolds' theory assumes that the inertial effects are negligible: it is based on a so-called creeping flow assumption. Increasing machine speeds and the use of gas bearings initiated research on the role of inertia [7, 8, 9, 10, 11, 12, 13, 14, 15]. In *fluid mechanics* the progagation of sound waves in tubes and in particular the steady streaming phenomenon have been extensively discussed [16, 17, 18, 19]. Two early papers on thin film theory in *acoustics* were presented by Maidanik [20] and Ungar and Carbonell [21]. A large number of investigations have been carried out since then. Consequently, a seemingly endless variety of models is available now to deal with viscothermal effects in acoustic wave propagation.

The variety of models is deceiving. The models that were presented in acoustics can be grouped into three basic categories. Key words in the characterization of these models are: pressure gradient across layer thickness or tube cross section, and the incorporation of effects such as compressibility and thermal conductivity.

The most extensive type of model clearly must be based on a solution of the full set of basic equations. This means that, for instance, all the terms in the linearized Navier Stokes equations are taken into account. The second type of model incorporates a pressure gradient. However, not all the terms

in the basic equations are retained. In some models, for instance, thermal effects are neglected. The simplest model, the low reduced frequency model, assumes a constant pressure across the layer thickness or tube cross section. The effects of inertia, viscosity, compressibility and thermal conductivity are accounted for. This leads to a very straightforward and useful model.

The main aim of this chapter is to provide a framework for putting models for viscothermal wave propagation into perspective. It is not the intention of the author to present a list of all papers related to viscothermal wave propagation. Wave propagation is considered from a standard acoustical point of view. Non-linear effects are therefore neglected. For an extensive overview of non-linear effects and viscothermal wave propagation the reader is referred to Makarov and Ochmann [22, 23, 24] and Too and Lee [25]. Makarov and Ochmann present an overview of the literature, based on more than 300 references.

The present analysis is based on the use of dimensionless parameters. It is an extension of the work on the propagation of sound waves in cylindrical tubes, as presented by Tijdeman [3]. The three groups of models are all rewritten in a dimensionless form. As a consequence, a number of dimensionless parameters appear in the equations. With the help of these parameters the range of validity for each group is indicated. Furthermore, for each type of model a short list of related literature is given. The list offers information about parameter ranges and applications. Based on this information, one can easily determine which model should be used for a given application. Finally, the problem of acousto-elastic coupling, *i.e.* the mutual interaction between vibrating flexible surfaces and thin layers of gas or fluid, is addressed for each type of model.

2.2 Basic equations

2.2.1 Derivation of equations

The basic equations governing the propagation of sound waves are the linearized Navier Stokes equations, the equation of continuity, the equation of state for an ideal gas and the energy equation. In the absence of mean flow the equations can be written as:

$$\rho_0 \frac{\partial \overline{\boldsymbol{v}}}{\partial t} = -\overline{\boldsymbol{\nabla}}\overline{p} + \left(\frac{4}{3}\mu + \eta\right)\overline{\boldsymbol{\nabla}}\left(\overline{\boldsymbol{\nabla}} \cdot \overline{\boldsymbol{v}}\right) - \mu\overline{\boldsymbol{\nabla}} \times \left(\overline{\boldsymbol{\nabla}} \times \overline{\boldsymbol{v}}\right)$$

$$\rho_0 \left(\overline{\boldsymbol{\nabla}} \cdot \overline{\boldsymbol{v}}\right) + \frac{\partial \overline{\rho}}{\partial t} = 0$$

$$\overline{p} = \overline{\rho} R_0 \overline{T} \tag{2.1}$$

$$\rho_0 C_p \frac{\partial \overline{T}}{\partial t} = \lambda \overline{\Delta}\, \overline{T} + \frac{\partial \overline{p}}{\partial t}$$

where $\overline{\boldsymbol{v}}$, $\overline{p}$, $\overline{\rho}$, $\overline{T}$, μ, η, R_0, ρ_0, λ, C_p and t denote respectively the velocity vector, pressure, density, temperature, viscosity, bulk viscosity [1], gas constant, mean density, thermal conductivity, specific heat at constant pressure and time. The operators $\overline{\boldsymbol{\nabla}}$ and $\overline{\Delta}$ are the gradient and the Laplace operator respectively. The following assumptions are used:

- no internal heat generation,
- homogeneous medium: the dimensions and the wavelength have to be large compared to the mean free path. For air under standard atmospheric conditions this assumption breaks down for lengths smaller than 10^{-7} m or frequencies higher than 10^9 Hz,
- no mean flow,
- small, sinusoidal perturbations,
- laminar flow [2].

[1] For monatomic gases $\eta = 0$, for air $\eta = 0.6\mu$

[2] For the transition to turbulence for oscillating pipe flows, see *e.g.* [19] and [26].

Dimensionless small harmonic perturbations are introduced according to:

$$\begin{aligned} \overline{\boldsymbol{v}} &= c_0 \boldsymbol{v} e^{i\omega t} & \overline{p} &= p_0 \left[1 + p e^{i\omega t}\right] \\ \overline{T} &= T_0 \left[1 + T e^{i\omega t}\right] & \overline{\rho} &= \rho_0 \left[1 + \rho e^{i\omega t}\right] \end{aligned} \tag{2.2}$$

where c_0, T_0, p_0, ω and i are the undisturbed speed of sound, the mean temperature, mean pressure, angular frequency and the imaginary unit. The gradient and the Laplace operators are non-dimensionalized with a length scale l. This length scale can for example represent the layer thickness or the tube radius. An overview of length scales and operators for various geometries is given in Appendix B. At this stage one can write:

$$\begin{aligned} \boldsymbol{\nabla} &= l\overline{\boldsymbol{\nabla}} \\ \Delta &= l^2\overline{\Delta} \end{aligned} \tag{2.3}$$

After further linearization the basic equations can be written in the following dimensionless form [3]:

$$i\boldsymbol{v} = -\frac{1}{k\gamma}\boldsymbol{\nabla} p + \frac{1}{s^2}\left(\frac{4}{3} + \xi\right)\boldsymbol{\nabla}\left(\boldsymbol{\nabla}\cdot\boldsymbol{v}\right) - \frac{1}{s^2}\boldsymbol{\nabla}\times\left(\boldsymbol{\nabla}\times\boldsymbol{v}\right)$$

$$\boldsymbol{\nabla}\cdot\boldsymbol{v} + ik\rho = 0$$

$$p = \rho + T \tag{2.4}$$

$$iT = \frac{1}{s^2\sigma^2}\Delta T + i\left[\frac{\gamma - 1}{\gamma}\right] p$$

The following dimensionless parameters were introduced [4]:

$$\begin{aligned} &\text{shear wave number} && s = l\sqrt{\frac{\rho_0\omega}{\mu}} \\ &\text{reduced frequency} && k = \frac{\omega l}{c_0} \end{aligned}$$

[3] $R_0 = C_p - C_v$

[4] The shear wave number is an unsteady Reynolds number

$$\begin{aligned} \text{ratio of specific heats} \qquad & \gamma = \frac{C_p}{C_v} \\ \text{square root of the Prandtl number} \qquad & \sigma = \sqrt{\frac{\mu C_p}{\lambda}} \\ \text{viscosity ratio} \qquad & \xi = \frac{\eta}{\mu} \end{aligned} \tag{2.5}$$

where C_v is the specific heat at constant volume. The dimensionless equations indicate that the viscothermal wave propagation is governed by a number of dimensionless parameters. These parameters can be used to characterize different flow regimes. Furthermore, they enable solutions given in the literature to be put into perspective: assumptions or restrictions of models can be quantified in terms of these parameters.

The parameters γ and σ depend solely on the material properties of the gas. The most important parameters are the shear wave number and the reduced frequency. The shear wave number is a measure for the ratio between the inertial effects and the viscous effects in the gas: it is an unsteady Reynolds number. For large shear wave numbers the inertial effects dominate, whereas for low shear wave numbers the viscous effects are dominant. In physical terms the shear wave number represents the ratio between the length scale, *e.g.* the layer thickness or tube radius, and the boundary layer thickness. The reduced frequency represents the ratio between the length scale and the acoustic wave length. For very low values of the reduced frequency, the acoustic wave length is very large compared to the length scale l. The parameters presented in this section are essential for the choice of an appropriate model for a specific situation.

2.2.2 Boundary conditions

In order to solve the set of equations boundary conditions must be imposed. The quantities of interest here are the (dimensionless amplitudes of the) velocity, temperature, pressure and density. Boundary conditions for the density are usually not imposed, and will therefore not be considered here.

Velocity

At a gas-wall interface a continuity of velocity is assumed in most cases. Continuity of velocity usually implies that the tangential velocity is zero: a no-slip condition is imposed. The normal velocity is equal to the velocity of the wall. In this way the acousto-elastic coupling between vibrating structures and viscothermal gases is established. For rarefied gases investigations

indicate that it is more appropriate to use a jump in velocity with corresponding momentum accommodation coefficients [5] [27, 28]. For gases under atmospheric conditions a simple continuity of velocity condition suffices.

Temperature

The most common boundary conditions are isothermal walls or adiabatic walls. For an isothermal wall the temperature perturbation is zero, whereas for an adiabatic wall the gradient of the temperature normal to the wall vanishes. When the product of the specific heat per unit volume and the thermal conductivity of the wall material substantially exceeds the corresponding product for the gas, the assumption of isothermal walls is usually accurate (see *e.g.* [29]).

Again, for rarefied gases it is more appropriate to use a jump condition [27, 28]. This condition allows for a jump in temperature across the gas-wall interface with a thermal accommodation coefficient. In the literature some models were presented to model walls with finite heat conduction properties, see *e.g.* [30].

A very interesting consequence of thermal effects is the phenomenon of thermally driven vibrations. As a boundary condition, one could for instance impose a varying temperature across the length of a tube. This temperature gradient drives pressure pulsations in the gas. This effect will not be addressed here: for a detailed discussion the reader is referred to the literature [31, 32, 33, 34, 35, 36, 37, 38].

Pressure

At the ends of a tube or layer boundary conditions can be imposed for the pressure, for instance a pressure release. In the present investigation end effects are neglected. For a more detailed discussion on this subject the reader is referred to the literature [39, 40, 41, 42, 43, 44].

2.2.3 Geometries and co-ordinate systems

The basic equations were given in terms of gradient and Laplace operators. In Appendix B an overview of length scales, dimensionless co-ordinates, gradient operators and Laplace operators is given for a number of geometries.

[5] In this case one assumes a jump condition at the interface, *e.g.* a velocity slip or temperature jump. For the temperature the boundary equation then becomes: $T - T_w = -L\boldsymbol{\nabla} T \cdot \boldsymbol{n}$, where T_w is the wall temperature, L is related to the thermal accomodation coefficients and $\boldsymbol{n}$ is the outward normal.

2.3 Full linearized Navier Stokes model

2.3.1 Derivation of equations

The most extensive type of model is that obtained by solving the complete set of basic equations. The derivation in this section is based on the paper by Bruneau, Herzog, Kergomard and Polack [45]. Their formulation however was rewritten in terms of dimensionless quantities for the present study. In order to solve this problem, the velocity is written as the sum of a rotational velocity $\boldsymbol{v}_v$, due to viscous effects, and a solenoidal velocity $\boldsymbol{v}_l$:

$$\boldsymbol{v} = \boldsymbol{v}_v + \boldsymbol{v}_l \tag{2.6}$$

where these satisfy:

$$\boldsymbol{\nabla} \cdot \boldsymbol{v}_v = 0 \quad ; \quad \boldsymbol{\nabla} \times \boldsymbol{v}_l = 0 \tag{2.7}$$

The following relationship was used in this derivation:

$$\boldsymbol{\nabla} \times (\boldsymbol{\nabla} \times \boldsymbol{v}_v) \equiv \boldsymbol{\nabla} (\boldsymbol{\nabla} \cdot \boldsymbol{v}_v) - (\boldsymbol{\nabla} \cdot \boldsymbol{\nabla}) \boldsymbol{v}_v = -\Delta \boldsymbol{v}_v \tag{2.8}$$

Inserting these expressions into the basic equations and taking the rotation and divergence gives the following set of dimensionless equations:

$$i\boldsymbol{v}_l - \frac{1}{s^2}\left(\frac{4}{3} + \xi\right)\Delta \boldsymbol{v}_l = -\frac{1}{k\gamma}\boldsymbol{\nabla} p$$

$$\boldsymbol{\nabla} \cdot \boldsymbol{v}_l + ik\rho = 0$$

$$i\boldsymbol{v}_v - \frac{1}{s^2}\Delta \boldsymbol{v}_v = 0 \tag{2.9}$$

$$p = \rho + T$$

$$iT = \frac{1}{s^2\sigma^2}\Delta T + i\left[\frac{\gamma - 1}{\gamma}\right] p$$

After some algebraic manipulations the following equation can be derived in terms of the temperature perturbation:

$$\frac{i}{s^2\sigma^2}\left[1 + \frac{i\gamma k^2}{s^2}\left(\frac{4}{3} + \xi\right)\right]\Delta\Delta T + \left[1 + \frac{ik^2}{s^2}\left[\left(\frac{4}{3} + \xi\right) + \frac{\gamma}{\sigma^2}\right]\right]\Delta T + k^2 T = 0 \tag{2.10}$$

It can easily be verified that both $\boldsymbol{v}_l$ and p also satisfy this equation. Note that if $\xi = 0$ in this equation, *i.e.* the bulk viscosity is neglected, a dimensionless equation is obtained that was already derived by Kirchhoff and Rayleigh [6].

2.3.2 Solution strategy

The equation for the temperature perturbation can be written in a factorized form:

$$\left[\Delta + {k_a}^2\right]\left[\Delta + {k_h}^2\right] T = 0 \tag{2.11}$$

where k_a and k_h are the acoustic and entropic wave numbers respectively:

$${k_a}^2 = \frac{2k^2}{C_1 + \sqrt{{C_1}^2 - 4C_2}} \quad ; \quad {k_h}^2 = \frac{2k^2}{C_1 - \sqrt{{C_1}^2 - 4C_2}} \tag{2.12}$$

where:

$$C_1 = \left[1 + \frac{ik^2}{s^2}\left[\left(\frac{4}{3} + \xi\right) + \frac{\gamma}{\sigma^2}\right]\right] \quad ; \quad C_2 = \frac{ik^2}{s^2\sigma^2}\left[1 + \frac{i\gamma k^2}{s^2}\left(\frac{4}{3} + \xi\right)\right] \tag{2.13}$$

The solution for the temperature perturbation can be written as:

$$T = A_a T_a + A_h T_h \tag{2.14}$$

where T_a and T_h are referred to as the acoustic and the entropic temperature. The constants A_a and A_h remain to be determined from the boundary conditions. The quantities T_a and T_h are the solutions of:

$$\left[\Delta + {k_a}^2\right] T_a = 0 \quad ; \quad \left[\Delta + {k_h}^2\right] T_h = 0 \tag{2.15}$$

Once the solution for the temperature is known, the values for the velocity $\boldsymbol{v}_l$ and the pressure p can be expressed in terms of A_a, A_h, T_a and T_h. One obtains:

$$p = \left[\frac{\gamma}{\gamma - 1}\right]\left[A_a\left[1 - \frac{i{k_a}^2}{s^2}\frac{1}{\sigma^2}\right]T_a + A_h\left[1 - \frac{i{k_h}^2}{s^2}\frac{1}{\sigma^2}\right]T_h\right]$$

$$\boldsymbol{v}_l = \boldsymbol{v}_{la} + \boldsymbol{v}_{lh} = \alpha_a A_a \boldsymbol{\nabla} T_a + \alpha_h A_h \boldsymbol{\nabla} T_h \tag{2.16}$$

$$\alpha_a = \frac{i}{k\gamma}\left[\frac{\gamma}{\gamma - 1}\right]\left[\frac{1 - \frac{i{k_a}^2}{s^2}\frac{1}{\sigma^2}}{1 - \frac{i{k_a}^2}{s^2}\left(\frac{4}{3} + \xi\right)}\right] \; ; \; \alpha_h = \frac{i}{k\gamma}\left[\frac{\gamma}{\gamma - 1}\right]\left[\frac{1 - \frac{i{k_h}^2}{s^2}\frac{1}{\sigma^2}}{1 - \frac{i{k_h}^2}{s^2}\left(\frac{4}{3} + \xi\right)}\right]$$

The rotational velocity $\boldsymbol{v}_v$ has to be solved from a vector wave equation with wave number k_v:

$$\left[\Delta + {k_v}^2\right] \boldsymbol{v}_v = 0 \quad ; \quad {k_v}^2 = -is^2 \tag{2.17}$$

The rotational velocity is related to the effects of viscosity, since the wave number is a function of the shear wave number.

In order to solve the full model, solutions must be found to two *scalar wave equations* for the temperature perturbation and a *vector wave equation* for the rotational velocity. With the appropriate boundary conditions the complete solution can then be obtained. An analytical solution for this type of model can only be found for simple geometries and boundary conditions (see sections 2.3.4 and 2.3.5 and chapter 3). For more complex geometries one has to resort to numerical techniques.

2.3.3 Acoustic and entropic wave numbers

The expressions for k_a and k_h are rather complex. In the literature they are often approximated, see *e.g.* [45]. With the help of the dimensionless parameters this approximation can be quantified. A Taylor expansion of the denominator of the wave numbers in terms of k/s gives:

$${k_a}^2 = \frac{k^2}{\left[1 + i\left(\frac{k}{s}\right)^2\left[\left(\frac{4}{3}+\xi\right) + \frac{\gamma-1}{\sigma^2}\right] - \left(\frac{k}{s}\right)^4\left(\frac{\gamma-1}{\sigma^2}\right)\left[\frac{1}{\sigma^2} - \left(\frac{4}{3}+\xi\right)\right]\right]}$$

$${k_h}^2 = \frac{-is^2\sigma^2}{\left[1 - i\left(\gamma-1\right)\left(\frac{k}{s}\right)^2\left[\frac{1}{\sigma^2} - \left(\frac{4}{3}+\xi\right)\right]\right]} \tag{2.18}$$

These expressions are valid for $k/s \ll 1$: the acoustic wavelength is very large compared to the boundary layer thickness. This assumption seems very reasonable. However, it has important implications that actually eliminate the need for a full model, as will also be illustrated in section 2.6. If we set $k/s = 0$ the expressions reduce to:

$${k_a}^2 = k^2 \quad ; \quad {k_h}^2 = -is^2\sigma^2 \tag{2.19}$$

This result shows that the wave number k_a is related to acoustic effects. The wave number k_h is related to entropy effects, since the product $s\sigma$ does not contain the viscosity μ. However, this separation is only possible for $k/s \ll 1$. When the acoustic wavelength is of the same order of magnitude as

the boundary layer thickness, the complete expressions for the wave numbers k_a and k_h must be used. In this situation a separation is not possible.

Note that for $s \gg 1$ the wave numbers k_h and k_v become very large. The solutions for T_h and $\boldsymbol{v}_v$ approach zero. The value of k_a is not affected, since it is not a function of the shear wave number. As a consequence, the full linearized Navier Stokes model reduces to the standard wave equation.

2.3.4 Acousto-elastic coupling

The motion of the gas can be coupled to the motion of a flexible structure, usually by demanding a continuity of velocity across the interface. In general this leads to a very complicated set of equations. The full linearized Navier Stokes model was used in a number of applications, such as spherical resonators or miniaturized transducers, to calculate the acousto-elastic behaviour of systems.

Spherical resonators are used to determine the acoustical properties of gases with a high degree of accuracy. Mehl investigated the effect of shell motion, hereby neglecting viscothermal effects in the gas [46]. Moldover, Mehl and Greenspan [29] used a full linearized Navier Stokes model for the description of the acoustic field inside the resonator. A boundary impedance condition was imposed for the radial velocity in order to account for the effect of shell motion. The models developed by Mehl were used to calculate this shell impedance.

In some types of *miniaturized transducers* a vibrating membrane is backed by a rigid electrode, thus entrapping a thin layer of gas. Plantier and Bruneau [47], Bruneau, Bruneau and Hamery [48], Hamery, Bruneau and Bruneau [49] developed analytical models to describe the interaction between (circular) membranes and thin gas layers. Because of the complexity of the problem, their calculations are restricted to geometries with rotatory symmetry. In order to overcome this problem, recently Karra, Tahar and Chau [4, 5] presented a boundary element formulation for the propagation of sound waves in viscothermal gases. Although their paper only concerns an uncoupled test case, the algorithm is able to deal with fully coupled problems [50]. Their method therefore now offers the possibility to model more complex geometries.

In chapter 3 the spherical resonator and the miniaturized transducers are discussed in more detail.

2.3.5 Literature

In Table 2.1 a list of related literature is presented. The list contains information concerning applications and acousto-elastic coupling. For layer geometries the parameter ranges in the calculations and experiments are given. These values will also be used in section 2.6. For an overview of parameter values for tubes the reader is referred to Tijdeman [3].

Authors	*Ref*	*Year*	*Application*	*Coupling*	*Remarks*
Moldover, Mehl, Greenspan	[29]	1986	spherical resonator	full	analytical model
Bruneau, Polack, Herzog, Kergomard	[51]	1990	spherical resonator cylindrical tubes	no	analytical model
Plantier, Bruneau	[47]	1990	circular membrane	full	analytical model $2.3 \cdot 10^{-9} \leq k \leq 2.3 \cdot 10^{-3}(\bullet)$ $2.9 \cdot 10^{-6} \leq k/s \leq 2.9 \cdot 10^{-3}(\bullet)$
Bruneau	[52]	1994	membrane	no	analytical model
Hamery, Bruneau, Bruneau	[49]	1994	circular membrane	no	analytical model $4.6 \cdot 10^{-5} \leq k \leq 4.6 \cdot 10^{-5}(\bullet)$ $9.0 \cdot 10^{-4} \leq k/s \leq 2.8 \cdot 10^{-2}(\bullet)$
Bruneau, Herzog, Kergomard, Polack	[45]	1989	spherical resonator cylindrical tube plane wall	no	analytical models
Bruneau, Bruneau, Herzog, Kergomard	[53]	1987	tubes	no	analytical model
Karra, Tahar Marquette, Chau	[4]	1996	circular membrane	no	boundary element model $7.9 \cdot 10^{-3} \leq k \leq 1.4 \cdot 10^{-2}(\bullet)$ $8.5 \cdot 10^{-3} \leq k/s \leq 1.1 \cdot 10^{-2}(\bullet)$
Karra, Tahar	[5]	1997	circular membrane	no	boundary element model Case I ($h_0 = 0.5$ mm): $1.0 \leq k \leq 1.4(\bullet)$ $9.9 \cdot 10^{-3} \leq k/s \leq 1.1 \cdot 10^{-2}(\bullet)$ Case II ($h_0 = 1$ μm): $7.9 \cdot 10^{-3} \leq k \leq 1.4 \cdot 10^{-2}(\bullet)$ $2.7 \cdot 10^{-2} \leq k/s \leq 3.6 \cdot 10^{-2}(\bullet)$
Scarton, Rouleau	[26]	1973	tubes	no	
Tijdeman	[3]	1975	tubes	no	
Liang, Scarton	[54]	1994	tubes	no	

Table 2.1: Literature full linearized Navier Stokes models. $(\bullet)$: calculations

2.4 Simplified Navier Stokes models

In this class of models the effects of compressibility or thermal conductivity are neglected compared with the full model described in section 2.3. In this section two models will be discussed in more detail. The two models were rewritten in a dimensionless form for this purpose. Other models are also available, but all simplified Navier Stokes models are inconsistent. An overview is presented in section 2.4.4.

2.4.1 Trochidis model

Trochidis [55, 56] introduces the following assumption in addition to the basic assumptions described in section 2.2.1:

- the gas is incompressible: $\boldsymbol{\nabla} \cdot \boldsymbol{v} = 0$

The dimensionless basic equations (2.4) now reduce to [6]:

$$i\boldsymbol{v} = -\frac{1}{k\gamma}\boldsymbol{\nabla} p - \frac{1}{s^2}\boldsymbol{\nabla} \times (\boldsymbol{\nabla} \times \boldsymbol{v})$$

$$\boldsymbol{\nabla} \cdot \boldsymbol{v} = 0 \tag{2.20}$$

Combining these equations gives:

$$\Delta p = 0$$

$$\left[\Delta - is^2\right] \boldsymbol{v} = \frac{s^2}{k\gamma}\boldsymbol{\nabla} p \tag{2.21}$$

The equation for the pressure is perhaps strange at first sight. Is does not incorporate any viscothermal terms: it is a regular wave equation for incompressible gas behaviour. It seems that the pressure can be completely determined from this equation. However, the boundary conditions must be satisfied. At a gas-wall interface the velocity must be continuous. Usually this means that the tangential velocity is zero and the normal velocity equals the velocity of the wall. With equation (2.21) the boundary condition for the velocity can be expressed in terms of pressure gradients. In this way, viscous effects are introduced into the model.

Clearly, the full linearized Navier Stokes model reduces to the Trochidis model for incompressible behaviour. The role of the compressibility depends, among other things, on for example the frequency and the global dimensions.

[6] The 2D formulation from Trochidis was extended to 3D for the present analysis.

As an example, consider the squeeze film damping between two plates, as described by Trochidis. The effects of compressibility become important when the acoustic wavelength is of the same order of magnitude as the plate dimensions. This means that the incompressible model of Trochidis can only be used for frequencies for which the acoustic wavelength is very large compared to the plate dimensions. In a squeeze film problem, the layer thickness is very small compared with the plate dimensions. In other words: the acoustic wavelength is also very large compared to the layer thickness. The pressure will thus not vary much across the layer thickness. The Trochidis model however incorporates a pressure gradient across the layer thickness. This is a weakness of the model: the assumption of incompressible behaviour on the one hand and the incorporation of a pressure gradient across the layer on the other hand are rather inconsistent for a squeeze film problem.

2.4.2 Möser model

Möser [57] extended the Trochidis model in order to account for the compressibility of the gas. However, only the compressibility term in the equation of continuity is considered: the compressibility terms in the linearized Navier Stokes equations are neglected. Furthermore, the process is assumed to be adiabatic. Möser in fact introduces the following assumptions in addition to the basic assumptions described in section 2.2.1:

- incompressible linearized Navier Stokes equations
- adiabatic process

The basic equations (2.4) now reduce to [7]:

$$\begin{aligned} i\boldsymbol{v} &= -\frac{1}{k\gamma}\boldsymbol{\nabla} p - \frac{1}{s^2}\boldsymbol{\nabla}\times(\boldsymbol{\nabla}\times\boldsymbol{v}) \\ \boldsymbol{\nabla}\cdot\boldsymbol{v} + ik\rho &= 0 \\ p &= \gamma\rho \end{aligned} \tag{2.22}$$

Combining these equations gives:

$$\Delta p + \left[\frac{k^2}{1+i\left(\frac{k}{s}\right)^2}\right] p = 0$$

[7] The 2D formulation from Möser was extended to 3D for the present analysis.

$$\Delta\left(\boldsymbol{\nabla}\times\boldsymbol{v}\right)-is^2\left(\boldsymbol{\nabla}\times\boldsymbol{v}\right)=0 \tag{2.23}$$

In a further analysis, Möser assumes that the acoustic wavelength is very large compared to the boundary layer thickness: $k/s \ll 1$. The wave number in equation (2.23) then reduces to k^2 and thus the equation reduces to the standard wave equation. In this model the viscous effects are also incorporated through the boundary conditions, if the wave number is approximated by k^2.

This model is not very consistent, since the compressibility terms are not fully accounted for. Furthermore, the thermal effects can play an important role. There are indeed several examples where thermal effects do have a significant influence. For a more sophisticated model that incorporates pressure gradients, the thermal effects should be accounted for as well.

2.4.3 Acousto-elastic coupling

In acoustics the simplified Navier Stokes models were mainly used to calculate the squeeze film damping between flexible plates. In the analysis of Trochidis only one-way coupling is considered: the uncoupled deflections of the plates were imposed as boundary conditions for the gas. However, recent experiments and calculations [58, 59] indicate that thin gas layers can have a significant effect on the coupled vibrational behaviour of a plate-gas layer system. The eigenfrequencies of the plate are substantially affected by the presence of the layer, whereas the viscothermal effects induce considerable damping. The full coupling was accounted for in the analysis of Möser. It has to be noted that the models as presented by Trochidis and Möser concern 2-dimensional problems.

The interaction between viscous fluids and flexible structures was also investigated from a more mathematical point of view. Schulkes [60] presented a finite element method to describe the interaction between a viscous fluid and a flexible structure. He assumed the fluid to be incompressible. For more literature related to this topic the reader is referred to Schulkes [60, 61].

2.4.4 Literature

In Table 2.2 a list of papers concerning simplified Navier Stokes models is presented. Experiments were carried out by several authors. The parameter ranges for the layer geometries are also given in the Table.

Authors	*Ref*	*Year*	*Application*	*Coupling*	*Remarks*
Trochidis	[55]	1982	squeeze film	one-way	incompressible Case I (air): $4.6 \cdot 10^{-4} \leq \ k \ \leq 8.8 \cdot 10^{-2}$(○)(●) $2.8 \cdot 10^{-4} \leq k/s \leq 2.3 \cdot 10^{-3}$(○)(●) Case II (water): $5.3 \cdot 10^{-4} \leq \ k \ \leq 4.0 \cdot 10^{-2}$(○)(●) $1.7 \cdot 10^{-5} \leq k/s \leq 1.3 \cdot 10^{-4}$(○)(●)
Möser	[57]	1980	squeeze film	full	incompressible Navier Stokes $2.3 \cdot 10^{-5} \leq \ k \ \leq 2.9 \cdot 10^{-1}$(●) $9.0 \cdot 10^{-5} \leq k/s \leq 5.1 \cdot 10^{-3}$(●)
Schulkes	[60]	1990	general	full	incompressible
Chow, Pinnington	[62]	1987	squeeze film (gas)	one-way	bulk viscosity terms neglected thermal effects neglected Case I (atmospheric air): $2.3 \cdot 10^{-4} \leq \ k \ \leq 7.3 \cdot 10^{-2}$(○)(●) $2.9 \cdot 10^{-4} \leq k/s \leq 2.9 \cdot 10^{-3}$(○)(●) Case II (air, decompression chamber): $3.5 \cdot 10^{-4} \leq \ k \ \leq 3.5 \cdot 10^{-2}$(○)(●) $2.9 \cdot 10^{-4} \leq k/s \leq 4.9 \cdot 10^{-3}$(○)(●)
Chow, Pinnington	[63]	1989	squeeze film (fluid)	one-way	bulk viscosity terms neglected thermal effects neglected $5.2 \cdot 10^{-5} \leq \ k \ \leq 1.3 \cdot 10^{-1}$(○)(●) $2.4 \cdot 10^{-5} \leq k/s \leq 2.4 \cdot 10^{-4}$(○)(●)

Table 2.2: Literature simplified Navier Stokes models. (○): experiments (●): calculations

2.5 Low reduced frequency model

2.5.1 Derivation of equations

In the low reduced frequency models some simplifications are introduced that lead to a relatively simple but very useful model for tubes and layers. In this theory the propagation directions of the waves and the other directions are separated. The following assumptions are introduced in addition to the basic assumptions described in section 2.2.1:

- the acoustic wavelength is large compared to the length scale l : $k \ll 1$
- the acoustic wavelength is large compared to the boundary layer thickness: $k/s \ll 1$

If one introduces these assumptions into the basic equations (2.4), presented in section 2.2.1, one is left with:

$$i\boldsymbol{v}^{pd} = -\frac{1}{k\gamma}\boldsymbol{\nabla}^{pd}p + \frac{1}{s^2}\Delta^{cd}\boldsymbol{v}^{pd}$$

$$0 = -\frac{1}{k\gamma}\boldsymbol{\nabla}^{cd}p$$

$$\boldsymbol{\nabla}\cdot\boldsymbol{v} + ik\rho = 0 \tag{2.24}$$

$$p = \rho + T$$

$$iT = \frac{1}{s^2\sigma^2}\Delta^{cd}T + i\left[\frac{\gamma-1}{\gamma}\right]p$$

where $\boldsymbol{\nabla}^{pd}$, Δ^{pd} and $\boldsymbol{v}^{pd}$ represent the gradient operator, the Laplace operator and the velocity vector containing components for the propagation directions only. The operators $\boldsymbol{\nabla}^{cd}$, Δ^{cd} and $\boldsymbol{v}^{cd}$ contain terms for the other directions, *i.e.* the cross-sectional or thickness directions. Expressions for these operators for various geometries are given in Appendix B [8]. The cross-sectional co-ordinates are denoted by $\boldsymbol{x}^{cd}$ and the propagation co-ordinates are denoted by $\boldsymbol{x}^{pd}$.

[8] Note that a low reduced frequency model does not make sense for a spherical geometry.

2.5.2 Solution strategy

The second equation of (2.24) indicates that the pressure is a function of the propagation co-ordinates only: the pressure is constant on a cross section or across the layer thickness. Hence, the low reduced frequency models are sometimes referred to as constant pressure models. Using the fact that the pressure does not vary with the *cd*-co-ordinates, the temperature perturbation can be solved from a Poisson type of equation. The general solution for adiabatic or isothermal walls can formally be obtained by Green's function[9]. At this stage one can write:

$$T\left(s\sigma, \boldsymbol{x}^{pd}, \boldsymbol{x}^{cd}\right) = -\left[\frac{\gamma-1}{\gamma}\right] p\left(\boldsymbol{x}^{pd}\right) C\left(s\sigma, \boldsymbol{x}^{cd}\right) \tag{2.25}$$

For simple geometries, solution of the function C is very straightforward[10]. For more complex geometries numerical techniques can be used. In the literature several approximation techniques have been developed to describe the propagation of sound waves in tubes with arbitrary cross sections, *e.g.* [64, 65, 66]. Once the solution for the temperature is obtained, the solutions for the velocity and the density can be expressed in a similar way:

$$\boldsymbol{v}^{pd}\left(s, \boldsymbol{x}^{pd}, \boldsymbol{x}^{cd}\right) = -\frac{i}{k\gamma} A\left(s, \boldsymbol{x}^{cd}\right) \boldsymbol{\nabla}^{pd} p\left(\boldsymbol{x}^{pd}\right)$$

$$\rho\left(s\sigma, \boldsymbol{x}^{pd}, \boldsymbol{x}^{cd}\right) = p\left(\boldsymbol{x}^{pd}\right)\left[1 + \left[\frac{\gamma-1}{\gamma}\right] C\left(s\sigma, \boldsymbol{x}^{cd}\right)\right]^{-1} \tag{2.26}$$

Note that, due to the fact that A and C are functions of the *cd*-co-ordinates, the velocity, temperature and density are not constant in these directions. The functions A and C determine the shape of the velocity, temperature and density profiles. For isothermal walls the functions A and C are directly related, whereas for adiabatic walls the function C reduces to a very simple form. One has:

$$\begin{aligned} \text{isothermal walls} &: C\left(s\sigma, \boldsymbol{x}^{cd}\right) = A\left(s\sigma, \boldsymbol{x}^{cd}\right) \\ \text{adiabatic walls} &: C\left(s\sigma, \boldsymbol{x}^{cd}\right) = -1 \end{aligned} \tag{2.27}$$

[9] It is also possible to include a finite thermal conductivity of the wall, see *e.g.* section 2.2.2 and [45]. The low reduced frequency model has to be coupled to a model that describes the thermal behaviour of the wall.

[10] The function C is a function only of the *cd*-co-ordinates for constant cross-sections. For varying cross sections, the value of C depends also on the *pd*-co-ordinates.

The expressions for ρ, T and $\boldsymbol{v}^{pd}$ are now inserted into the equation of continuity. After integration with respect to the *cd*-co-ordinates and some rearranging one obtains:

$$\Delta^{pd} p\left(\boldsymbol{x}^{pd}\right) - k^2\Gamma^2 p\left(\boldsymbol{x}^{pd}\right) = -ikn(s\sigma)\Gamma^2\Re \tag{2.28}$$

where:

$$\begin{aligned}
\Gamma &= \sqrt{\frac{\gamma}{n\left(s\sigma\right)B\left(s\right)}} \\
n\left(s\sigma\right) &= \left[1+\left[\frac{\gamma-1}{\gamma}\right]D\left(s\sigma\right)\right]^{-1} \\
B\left(s\right) &= \frac{1}{A^{cd}}\int_{A^{cd}} A\left(s,\boldsymbol{x}^{cd}\right)dA^{cd} \\
D\left(s\sigma\right) &= \frac{1}{A^{cd}}\int_{A^{cd}} C\left(s\sigma,\boldsymbol{x}^{cd}\right)dA^{cd} \\
\Re &= \frac{1}{A^{cd}}\int_{\partial A^{cd}} \boldsymbol{v}\cdot\boldsymbol{e_n}\,d\partial A^{cd}
\end{aligned} \tag{2.29}$$

where A^{cd} is the cross-sectional area, ∂A^{cd} is the corresponding boundary and $\boldsymbol{e}_n$ is the outward normal on ∂A^{cd}. For simple boundary conditions, the function D can be obtained from:

$$\begin{aligned}
\text{isothermal walls} &: D\left(s\sigma\right) = B\left(s\sigma\right) \\
\text{adiabatic walls} &: D\left(s\sigma\right) = -1
\end{aligned} \tag{2.30}$$

The function Γ is the *propagation constant*. The propagation of sound waves is affected by thermal effects, accounted for in the function $n\left(s\sigma\right)$, and viscous effects, accounted for in the function $B\left(s\right)$. On the right hand side of equation (2.28) a source term is present due to the squeeze motion of the walls. In Tables B.1, B.2, B.3 and B.4 in Appendix B the expressions are listed for various geometries and isothermal wall conditions for the functions A and B. The Tables also contain the asymptotic values of the functions for low and high values of the corresponding argument. It can easily be shown that for low values of the shear wave number [11] the low reduced frequency model reduces to a linearized form of the Reynolds equation. For high shear wave numbers the low reduced frequency model reduces to a modified form of the wave equation. The modification is due to the fact that the low reduced frequency model is associated with a constant pressure in the *cd*-directions.

[11] Considering σ as a constant.

2.5.3 Physical interpretation

Velocity profile

The shape of the velocity profile is completely determined by the function A. This function is thus well suited to illustrate the transition from inertially dominated flow to viscously dominated flow. As an example, consider the layer geometry. In Figure 2.1 the magnitude of the function A is given as a function of the layer thickness for shear wave numbers 1, 5, 10 and 100. The magnitude of the function A is directly related to the magnitude of the in-plane velocities for a layer geometry. Please note that the expression for the velocity is complex: there are phase differences between the points. Consequently not all points pass their equilibrium position at the same time.

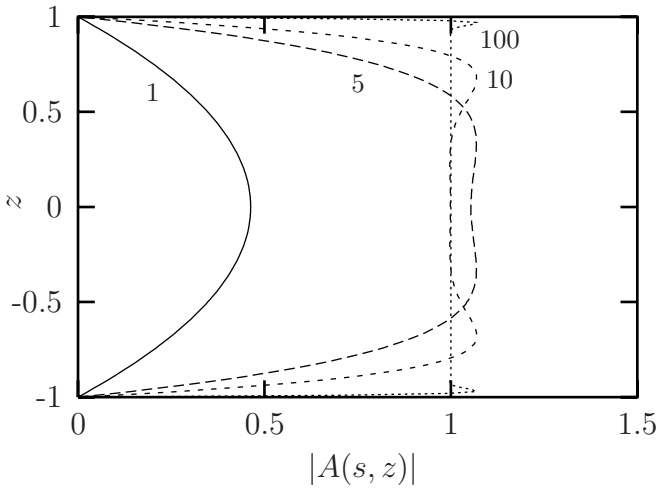

Figure 2.1: Shape of velocity profile (magnitude)

For low shear wave numbers the viscous forces dominate and a parabolic velocity profile is obtained, see also Tables B.3 and B.4. For high shear wave numbers the inertial forces dominate and a flat velocity profile is obtained.

Temperature profile

For isothermal walls the shape of the temperature profile is identical to the shape of the velocity profile. However, the temperature is not a function of the shear wave number s but of the product $s\sigma$: its value does not depend on the viscosity μ. For high values of $s\sigma$, adiabatic conditions are obtained, whereas for low values of $s\sigma$, isothermal conditions are obtained.

Polytropic constant

According to equation (2.26) the density and the pressure are related. If this expression is integrated with respect to the *cd*-co-ordinates one obtains:

$$\rho = p\left[1 + \left[\frac{\gamma - 1}{\gamma}\right] D\left(s\sigma\right)\right]^{-1} \tag{2.31}$$

The same result would have been obtained if, instead of using the energy equation and the equation of state, a polytropic law had been used:

$$\frac{\overline{p}}{\overline{\rho}^{\,n(s\sigma)}} = constant \tag{2.32}$$

where $n(s\sigma)$ is the polytropic constant that relates density and pressure, see equation (2.29). Note however that this only holds in integrated sense: relation (2.31) was obtained by integration with respect to the *cd*-co-ordinates. As an example, the magnitude and the phase angle for the layer geometry are given as a function of $s\sigma$ in Figure 2.2. For low values $n(s\sigma)$ reduces to 1, *i.e.* isothermal conditions. For high values of $s\sigma$ it takes the value of γ corresponding to adiabatic conditions.

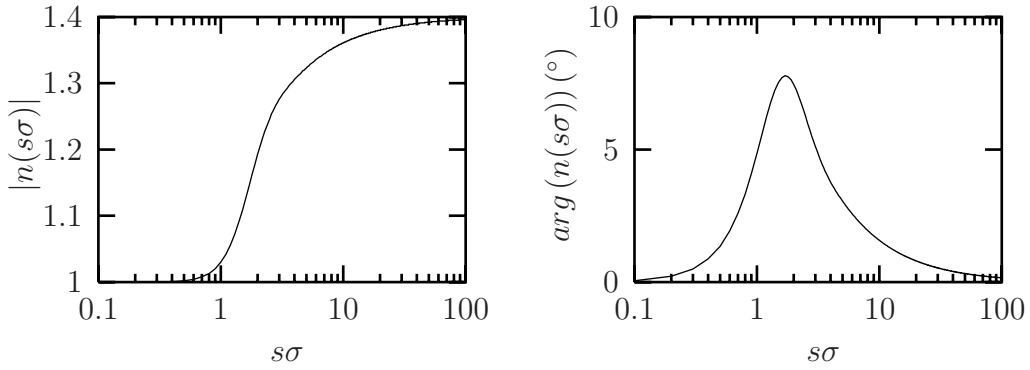

Figure 2.2: Magnitude and phase angle of polytropic constant for air ($\gamma = 1.4$)

2.5.4 Acousto-elastic coupling

The low reduced frequency model results in a relatively simple equation for the pressure. Because of the simplicity of the gas model, it is relatively easy to incorporate the full acousto-elastic coupling. Several investigations are

available which deal with fully coupled calculations, most of them for the squeeze film problem.

Fox and Whitton [67] and Önsay [68, 69] presented models to describe the interaction between a vibrating strip and a gas layer. The model of Önsay was based on a transfer matrix approach: an efficient model for the strip problem. Fox and Whitton, and Önsay, carried out experiments, showing substantial frequency shifts and significant damping.

Recently, Beltman, Van der Hoogt, Spiering and Tijdeman [70, 59, 71, 58, 72] presented a finite element model for fully coupled calculations for the squeeze film problem. A new viscothermal acoustic finite element was developed, based on the low reduced frequency model. This element can be coupled to structural elements, enabling fully coupled calculations for complex geometries. Furthermore, the layer thickness can be chosen for each element. This enables calculations for problems with varying layer thickness. The finite element model was validated with experiments on an airtight box with a flexible coverplate. In this case there was a strong interaction between the vibrating, flexible plate and the closed air layer. Eigenfrequency and damping of the plate were measured as a function of the thickness of the air layer. Substantial frequency shifts and large damping values were observed. In chapter 5 a more detailed discussion is given of these results.

2.5.5 Literature

In Table 2.3 the recent literature on the low reduced frequency models is summarized. For layer geometries the ranges of dimensionless parameters are also given.

Authors	*Ref*	*Year*	*Application*	*Coupling*	*Remarks*
Fox, Whitton	[67]	1980	squeeze film (strip)	full	analytical model Case I (atmospheric air): $1.8 \cdot 10^{-3} \leq k \leq 1.8 \cdot 10^{-1}$(○)(●) $k/s \cong 4.0 \cdot 10^{-4}$(○)(●) Case II (air, decompression chamber): $1.2 \cdot 10^{-4} \leq k \leq 4.6 \cdot 10^{-4}$(○)(●) $9.2 \cdot 10^{-5} \leq k/s \leq 4.1 \cdot 10^{-3}$(○)(●) Case III ($CO_2$, decompression chamber): $2.3 \cdot 10^{-4} \leq k \leq 3.1 \cdot 10^{-4}$(○)(●) $1.0 \cdot 10^{-4} \leq k/s \leq 3.8 \cdot 10^{-3}$(○)(●)
Önsay	[68]	1993	squeeze film (strip)	full	transfer matrix approach $9.2 \cdot 10^{-6} \leq k \leq 4.6 \cdot 10^{-3}$(○)(●) $9.0 \cdot 10^{-5} \leq k/s \leq 9.0 \cdot 10^{-4}$(○)(●)
Önsay	[69]	1994	squeeze film (strip) (strip)	full	step in layer geometry $9.2 \cdot 10^{-5} \leq k \leq 4.6 \cdot 10^{-3}$(○)(●) $9.0 \cdot 10^{-5} \leq k/s \leq 9.0 \cdot 10^{-4}$(○)(●)
Lotton, Husník, Bruneau, Bruneau, Škvor	[52]	1994	circular membrane	full	equivalent network model
Bruneau, Bruneau, Škvor, Lotton	[73]	1994	circular membrane	full	equivalent network model
Tijdeman	[3]	1975	tubes	no	parameter overview
Beltman, Van der Hoogt, Spiering, Tijdeman	[59]	1997	squeeze film (plate)	full	finite element model $4.6 \cdot 10^{-4} \leq k \leq 1.4 \cdot 10^{-1}$(○)(●) $2.0 \cdot 10^{-4} \leq k/s \leq 4.9 \cdot 10^{-4}$(○)(●)
Beltman, Van der Hoogt, Spiering, Tijdeman	[70]	1997	solar panels	no	analytical model $1.8 \cdot 10^{-5} \leq k \leq 6.0 \cdot 10^{-2}$(○)(●) $2.9 \cdot 10^{-5} \leq k/s \leq 9.0 \cdot 10^{-5}$(○)(●)

Table 2.3: Literature low reduced frequency models. (○): experiments (●): calculations

2.6 Dimensionless parameters

2.6.1 Validity of models

In the sections 2.3, 2.4 and 2.5 three types of models were discussed for the modelling of viscothermal wave propagation. The most simple type of model, the low reduced frequency model, is show to be valid for $k \ll 1$ and $k/s \ll 1$. As pointed out in section 2.4, the validity of the simplified Navier Stokes models is difficult to quantify. These models incorporate some additional effects compared to the low reduced frequency models. However, a parameter analysis shows that if a more sophisticated model is desired, in fact all the terms have to be accounted for. The complete parameter range is covered by the low reduced frequency model and the full linearized Navier Stokes model. Summarizing the ranges of validity for the linear viscothermal models and the general wave equation:

- $s \gg 1$
  wave equation (Wave)
- $k \ll 1$ and $k/s \ll 1$
  low reduced frequency (Low)
- $k \ll 1$ and $k/s \ll 1$ and $s \ll 1$
  low reduced frequency, Reynolds equation (Low-Rey)
- $k \ll 1$ and $k/s \ll 1$ and $s \gg 1$
  low reduced frequency, modified wave equation (Low-wave)
- arbitrary k and s
  full linearized Navier Stokes (Full) [12]

A graphical representation of these ranges of validity is given in Figure 2.3. It is stressed that in each area the most efficient model is given. One could for instance use the full model for all situations, but clearly for $k \ll 1$ and $k/s \ll 1$ the low reduced frequency model is far more efficient.

For the case of arbitrary k but $k/s \ll 1$ the simplified wave numbers, as described in section 2.3.3 could be used. However, assuming $k/s \ll 1$ immediately suggests that another model, *i.e.* the low reduced, modified wave or wave, would be more efficient (see Figure 2.3). This assumption, which is often used by authors who use a full linearized Navier Stokes model,

[12] The full linearized Navier Stokes with simplified wave numbers is valid for $k/s \ll 1$. It can easily be seen in the graph that this is not an efficient model. Hence, it is not included.

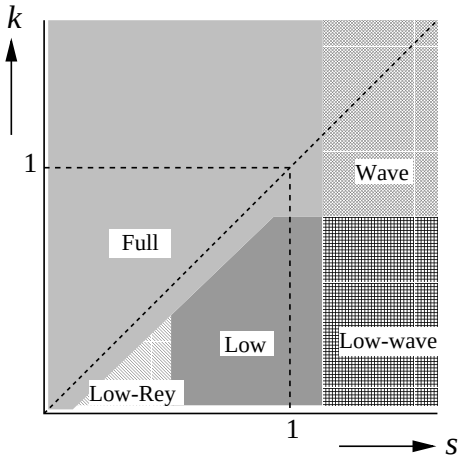

Figure 2.3: Parameter overview of models

at the same time eliminates the actual need for the full model. Only for the most general case of arbitrary k and k/s should the full model be used. Note that for $s \gg 1$ the general wave equation can be used.

2.6.2 Practical implications

The key quantities of interest for a good choice of the appropriate model are obviously k and k/s. In physical terms these quantities represent the ratio between the acoustic wavelength and the length scale l, and the ratio between the boundary layer thickness and the acoustic wavelength respectively. An interesting point is the analysis of these terms. For $s \leq 1$ and $k/s \geq 1$ for instance the full model should be used. The question now arises whether or not these conditions are of any practical interest. With the dimensionless parameters one can write:

$$\begin{aligned} s &= l\sqrt{\frac{\rho_0\omega}{\mu}} \\ \frac{k}{s} &= \sqrt{\frac{\mu\omega}{\rho_0 c_0^2}} \end{aligned} \tag{2.33}$$

For gases under atmospheric conditions, the speed of sound is of the order of magnitude of $5 \cdot 10^2$ m/s, the density is of the order of 1 kg/m^3 and the viscosity is of the order of 10^{-5} Ns/m^2. By varying the frequency or the length scale, the shear wave number can vary from low to very high values. Expression (2.33) shows that the frequency is the only variable quantity in

k/s: it does not depend on the length scale l. For gases under atmospheric conditions, k/s exceeds unity only for frequencies higher than 10^9 Hz. However, for these high frequencies the medium can no longer be regarded as homogeneous and one of the basic assumptions described in section 2.2.1, is violated.

This can be illustrated with the following simple example. Using expression (2.33), the basic conditions $l > 10^{-7}$ m and $f < 10^9$ Hz can be expressed in terms of k/s and s:

$$\begin{aligned} f < 10^9 \text{ Hz} \quad &: \quad \left(\frac{k}{s}\right) < \sqrt{\frac{2\pi\mu}{\rho_0 c_0^2} \cdot 10^9} \\ l > 10^{-7} \text{ m} \quad &: \quad s > \frac{\rho_0 c_0}{\mu} \cdot 10^{-7} \left(\frac{k}{s}\right) \end{aligned} \tag{2.34}$$

For air under atmospheric conditions this gives:

$$\left(\frac{k}{s}\right) < 0.3\pi \quad ; \quad s > 2.24 \left(\frac{k}{s}\right) \tag{2.35}$$

Thus, the full linearized Navier Stokes model is not even valid in the major range where it should be of use for air under atmospheric conditions.

For fluids this reasoning also holds. The quantity k/s contains the ratio between the viscosity and the density. For fluids the viscosity is higher, but compared to gases the ratio between viscosity and density is of the same order of magnitude. Furthermore, the speed of sound in fluids is generally higher. This implies that for fluids the condition $k/s \ll 1$ will also usually be satisfied. If this condition is not satisfied one has to ensure that the basic assumptions are not violated.

This simple analysis shows that the practical importance of the full model is very limited. Only under extreme conditions, *e.g.* at low temperatures or low pressures, one encounters situations were the full model should be used[13]. However, one has to ensure that the basic assumptions are not violated in these cases. This leads to the perhaps surprising conclusion that for gases under atmospheric conditions the full linearized Navier Stokes model is not valid in the parameter range where it should be of use. Most viscothermal problems can be handled with the low reduced frequency models. In fact, a number of papers indicate the necessity of a full model because of the high frequencies involved, whereas a low reduced frequency model would have been sufficient [47, 49, 4]. Some examples will be presented in chapter 3.

[13]For these cases situations are encountered where the jump conditions must be applied at the boundaries, see section 2.2.2

2.6.3 Overview of the literature for layers

The dimensionless parameters are used to analyse the literature for the layer geometry. The overview is based on the references presented in Tables 2.1, 2.2 and 2.3. For this purpose, the values of the dimensionless parameters at which the calculations and experiments were performed were determined from the data given in the references [47, 49, 4, 55, 57, 62, 63, 67, 68, 69, 59, 71]

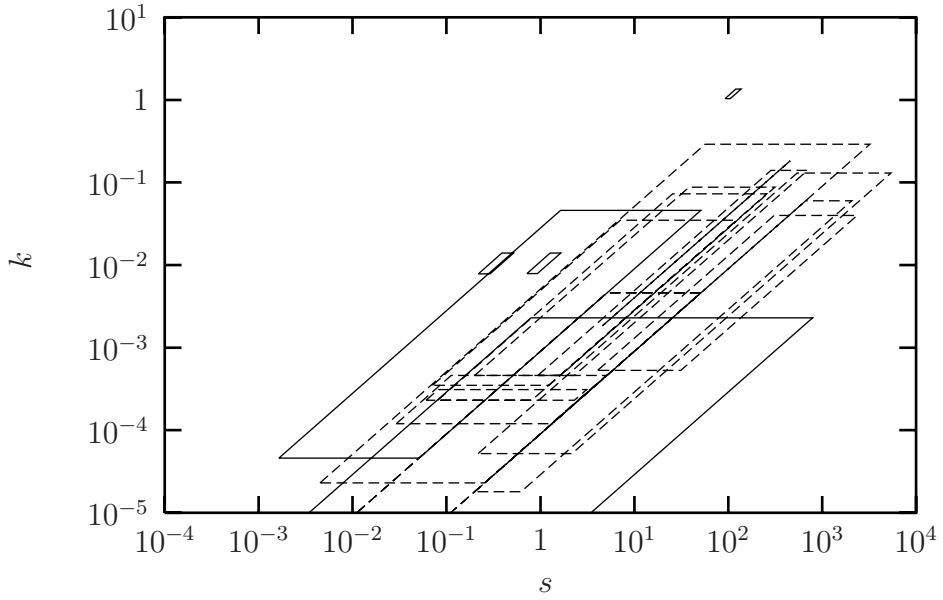

Figure 2.4: Dimensionless parameters in the literature. Calculations (—), experiments (−−)

The graph clearly shows that for all investigations the low reduced frequency models, modified wave equation models or general wave equation models would have been sufficient. None of the present cases required a more sophisticated model, such as the full linearized Navier Stokes model. The conclusion to be drawn from this Figure is that, although a variety of models has been developed, this was not necessary when taking a critical look at the dimensionless parameters. Some investigations mentioned in Tables 2.1 and 2.2 could have been carried out with much simpler models. Analysis of the values of the parameters, listed in the Tables, also immediately reveals that the conditions for the use of simpler models are satisfied.

2.7 Conclusions

The conclusions to be drawn from the present investigation are as follows:

- viscothermal wave propagation is governed by a number of dimensionless parameters. The most important parameters are the shear wave number, s, and the reduced frequency, k;
- the viscothermal models presented in the literature, can be grouped into three categories: full linearized Navier Stokes models, simplified Navier Stokes models and low reduced frequency models. The range of validity of the models is governed by the values of k and k/s;
- the full linearized Navier Stokes model should only be used under extreme conditions. For gases under atmospheric conditions, this model is not even valid in the range of use because the basic assumptions are violated;
- the assumption of small k/s, as often used in the literature concerning full models, actually eliminates the need for a full model;
- the simplified Navier Stokes models are redundant: the complete parameter range is covered by the other models;
- the low reduced frequency model can be used for most problems. Because of the simplicity of this model, models are already available that include the full acousto-elastic coupling for complex geometries. The model is valid for $k \ll 1$ and $k/s \ll 1$;
- in the literature a variety of models was presented for the squeeze film damping problem. Several authors stated that for miniaturized transducers, the full model had to be used because of the high frequencies involved. An analysis of the parameters learns that for all literature concerning squeeze film problems, treated in this chapter, a simple low reduced frequency model is sufficient and the most efficient.

Chapter 3

Fundamental solutions

3.1 Introduction

In chapter 2 an overview of theories for viscothermal wave propagation was presented. As a next step, the theory is applied to present solutions for the behaviour of spherical resonators, the propagation of sound in tubes, the behaviour of miniaturized transducers and squeeze film damping between flexible plates or membranes. Analytical solutions for the full model were obtained for a spherical geometry, a circular tube geometry and a layer geometry. The results of these models are compared with results from simpler models, like the low reduced frequency model. All solutions are written in terms of dimensionless parameters. The use of these parameters leads to some interesting observations.

The author would like to stress that it is not his intention to give an extensive and very detailed description of all the aspects for each application. The present range of applications covers the general application field of linear viscothermal models. Furthermore, solutions are presented for a range of geometries. Thus, the main aim of this chapter is to present an *application overview* and a *solution overview* of linear viscothermal models. The theory and the solutions are quite general and can easily be applied to other situations, because the expressions are all written in terms of dimensionless parameters.

3.2 Spherical resonator

3.2.1 Introduction

Spherical resonators are used to determine the properties of gases, such as the speed of sound, with a high degree of accuracy, see *e.g.* Moldover, Mehl and Greenspan [29]. In Figure 3.1 a schematic drawing is presented of a spherical resonator.

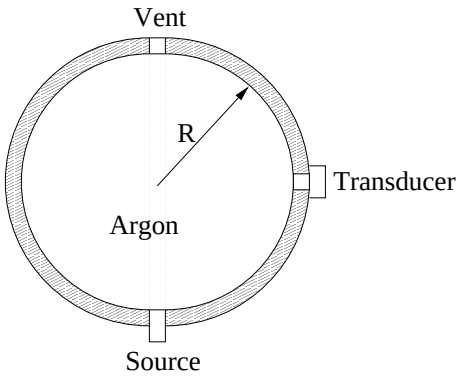

Figure 3.1: Schematic drawing of a spherical resonator

The sphere consists of two parts that are bolted together. The acoustic eigenfrequencies of the enclosed volume are used to determine the properties of the gas under different conditions. Because of the spherical geometry, an analytical solution can be obtained for the full linearized Navier Stokes model as will be described in sections 3.2.2 to 3.2.5. However, the resonator contains a number of small disturbances: vent holes, transducers, transducer holes and a source. Although both parts of the shell are firmly bolted together, a small seam can remain between the two parts. In order to account for the presence of these disturbances, some suggestions to extend the model are introduced in section 3.2.6. Finally, an example with Argon as a gas will be presented in section 3.2.7.

The derivation of the equations is based on the work by Moldover, Mehl and Greenspan [29]. The spherical resonator was also described by Bruneau, Polack, Herzog and Kergomard [51], Bruneau, Herzog, Kergomard and Polack [45] and Mehl [46, 74, 75]. The models were rewritten in terms of dimensionless quantities for the present study.

3.2.2 Basic equations

In order to solve the full linearized Navier Stokes model, two *scalar wave equations* and one *vector wave equation* have to be solved (see chapter 2). In a spherical co-ordinate system (r, θ, ϕ):

$$\left[\Delta + {k_a}^2\right] T_a = 0 \quad ; \quad \left[\Delta + {k_h}^2\right] T_h = 0 \quad ; \quad \left[\Delta + {k_v}^2\right] \boldsymbol{v}_v = \boldsymbol{0} \tag{3.1}$$

3.2.3 Solution of the scalar wave equations

The solution of the scalar wave equations can be obtained by a straightforward separation of variables:

$$T_a = j_n\left(k_a r\right) Y_{mn}\left(\theta, \phi\right) \quad ; \quad T_h = j_n\left(k_h r\right) Y_{mn}\left(\theta, \phi\right) \tag{3.2}$$

where $Y_{mn}\left(\theta, \phi\right)$ is a spherical harmonic function and $j_n\left(k_a r\right)$ is a spherical Bessel function. The spherical Bessel function is related to the fractional Bessel function according to [76]:

$$j_n\left(k_a r\right) = \frac{1}{\sqrt{r}} J_{n+\frac{1}{2}}\left(k_a r\right) \tag{3.3}$$

The solution for the temperature is:

$$T = A_a j_n\left(k_a r\right) Y_{mn}\left(\theta, \phi\right) + A_h j_n\left(k_h r\right) Y_{mn}\left(\theta, \phi\right) \tag{3.4}$$

The solenoidal velocity can be obtained from:

$$\boldsymbol{v}_l = \boldsymbol{v}_{la} + \boldsymbol{v}_{lh} = \alpha_a A_a \boldsymbol{\nabla} T_a + \alpha_h A_h \boldsymbol{\nabla} T_h \tag{3.5}$$

This gives:

$$\begin{aligned} \boldsymbol{v}_l &= \left[\alpha_a A_a \frac{\partial j_n\left(k_a r\right)}{\partial r} + \alpha_h A_h \frac{\partial j_n\left(k_h r\right)}{\partial r}\right] Y_{mn}\left(\theta, \phi\right) \boldsymbol{e}_r \\ &+ \left[\alpha_a A_a j_n\left(k_a r\right) + \alpha_h A_h j_n\left(k_h r\right)\right] \frac{1}{r} \frac{\partial Y_{mn}\left(\theta, \phi\right)}{\partial \theta} \boldsymbol{e}_\theta \\ &+ \left[\alpha_a A_a j_n\left(k_a r\right) + \alpha_h A_h j_n\left(k_h r\right)\right] \frac{1}{r sin(\theta)} \frac{\partial Y_{mn}\left(\theta, \phi\right)}{\partial \phi} \boldsymbol{e}_\phi \end{aligned} \tag{3.6}$$

The pressure is:

$$p = \left[\frac{\gamma}{\gamma - 1}\right] \left[A_a \left[1 - \frac{i{k_a}^2}{s^2 \sigma^2}\right] j_n\left(k_a r\right) + A_h \left[1 - \frac{i{k_h}^2}{s^2 \sigma^2}\right] j_n\left(k_h r\right)\right] Y_{mn}\left(\theta, \phi\right) \tag{3.7}$$

3.2.4 Solution of the vector wave equation

The solution for the vector wave equation can be obtained from the solution of the scalar wave equation. For the present case the solution is, see Morse and Feshbach [77]:

$$\begin{aligned} \boldsymbol{v}_v &= W_1 \boldsymbol{\nabla} \times [\boldsymbol{e}_r r j_n(k_v r) Y_{mn}(\theta,\phi)] \\ &+ W_2 \boldsymbol{\nabla} \times \boldsymbol{\nabla} \times [\boldsymbol{e}_r r j_n(k_v r) Y_{mn}(\theta,\phi)] \end{aligned} \tag{3.8}$$

where W_1 and W_2 are constants that remain to be determined from the boundary conditions. After some algebra one obtains:

$$\begin{aligned} \boldsymbol{v}_v &= W_1 [-r j_n(k_v r)] \frac{1}{r sin(\theta)} \frac{\partial Y_{mn}(\theta,\phi)}{\partial \phi} \boldsymbol{e}_\theta \\ &+ W_1 [r j_n(k_v r)] \frac{1}{r} \frac{\partial Y_{mn}(\theta,\phi)}{\partial \theta} \boldsymbol{e}_\phi \\ &+ W_2 \left[\frac{n(n+1)}{r} j_n(k_v r) \right] Y_{mn}(\theta,\phi) \boldsymbol{e_r} \\ &+ W_2 \left[\frac{\partial}{\partial r} (r j_n(k_v r)) \right] \frac{1}{r} \frac{\partial Y_{mn}(\theta,\phi)}{\partial \theta} \boldsymbol{e}_\theta \\ &+ W_2 \left[\frac{\partial}{\partial r} (r j_n(k_v r)) \right] \frac{1}{r sin(\theta)} \frac{\partial Y_{mn}(\theta,\phi)}{\partial \phi} \boldsymbol{e}_\phi \end{aligned} \tag{3.9}$$

3.2.5 Rigid sphere with isothermal walls

The boundary conditions for the present case for $r = 1$ are:

$$T = 0 \quad ; \quad \boldsymbol{v} = \boldsymbol{v}_l + \boldsymbol{v}_v = \boldsymbol{0} \tag{3.10}$$

The following equation for the spherical resonator is obtained:

$$\begin{aligned} &\left[1 - \frac{\alpha_h}{\alpha_a}\right] \left[\frac{n(n+1)}{1 + \dfrac{1}{j_n(k_v)} \left. \dfrac{\partial j_n(k_v r)}{\partial r} \right|_{r=1}} \right] = \\ &\frac{1}{j_n(k_a)} \left. \frac{\partial j_n(k_a r)}{\partial r} \right|_{r=1} - \left(\frac{\alpha_h}{\alpha_a} \right) \frac{1}{j_n(k_h)} \left. \frac{\partial j_n(k_h r)}{\partial r} \right|_{r=1} \end{aligned} \tag{3.11}$$

The eigenfrequencies of the gas in the resonator can be calculated from this equation. In experiments, a frequency response function is measured. The frequency response of the resonator is calculated by expressing the internal acoustic field in terms of the acoustic eigenmodes. The participation factors can then be calculated, see *e.g.* [29].

3.2.6 Model extensions

Shell motion

As a boundary condition, a zero velocity was imposed for the gas at the shell wall. The shell however can deform under the applied pressure. Mehl [46] developed a model which describes the shell behaviour in terms of an impedance. The effect of shell motion can thus be incorporated in the model by imposing the shell impedance as a boundary condition for the radial velocity and the pressure at the shell wall.

Holes in the shell

The holes will affect the acoustic field inside the resonator. One can distinguish several types of holes, depending on the type of termination. For vent holes, the circular tube is terminated by a radiation or pressure release condition. For the transducer holes, the tube is terminated by the effective impedance of the transducer itself. The propagation of sound waves in a circular tube is governed by the dimensionless parameters. With these parameters, the most efficient model can be identified. The acoustic impedance of the tube with its termination can be calculated and thus the impedance at the entrance of the tube is known. As a consequence, there is a non-uniform boundary impedance condition for the gas in the resonator.

Seam

A small gap at the junction between the two hemispheres can affect the acoustical properties of the resonator. In this case one deals with the propagation of sound waves between parallel surfaces. Again, based on the dimensionless parameters for this layer geometry one can easily identify the model that should be used. The effective impedance of the gap between the hemispheres can then be calculated.

3.2.7 Example: eigenfrequencies of spherical resonator

The properties of the Argon gas and the spherical resonator are (according to the case described by Moldover, Mehl and Greenspan [29]):

$$\begin{aligned} &c_0 = 319 \text{ m/s} && ; \quad \rho_0 = 1.60 \text{ kg/m}^3 \\ &C_p = 528 \text{ J/kgK} && ; \quad \gamma = \frac{5}{3} \\ &\lambda = 16.7 \cdot 10^{-3} \text{ W/mK} && ; \quad \mu = 22.7 \cdot 10^{-6} \text{ Ns/m}^2 \\ &\xi = 0 && ; \quad R = 0.0635 \text{ m} \end{aligned} \tag{3.12}$$

The bulk viscosity is zero and the ratio of specific heats is equal to $\frac{5}{3}$ for a monatomic (ideal) gas like argon. The eigenfrequencies of the resonator were calculated with a simple numerical procedure (see Appendix C). The eigenfrequencies can be divided into groups. For each value of n there are several solutions to the equation. The solutions are denoted here as "ns", where n is the order of the spherical Bessel function and s is the s-th root. The roots are arranged in ascending order. The results for the $n = 0$, $n = 1$ and $n = 2$ modes are given in Table 3.1.

"ns"	Eigenfrequency (Hz)	
	wave equation	full model
01	0	0
02	3593	$3592 + 0.802i$
03	6177	$6175 + 1.073i$
04	8718	$8717 + 1.305i$
11	1664	$1663 + 1.587i$
12	4750	$4748 + 1.054i$
13	7360	$7359 + 1.246i$
14	9918	$9916 + 1.449i$
21	2630	$2628 + 1.988i$
22	5817	$5816 + 1.363i$
23	8482	$8481 + 1.460i$
24	11069	$11067 + 1.623i$

Table 3.1: Eigenfrequencies spherical resonator

The Table shows that the eigenfrequencies for the full model are complex. The imaginary part however is very small compared to the real part. The real part of the frequency is almost equal to the frequency that is obtained with the wave equation. The viscous and thermal effects only seem to have a small effect on the acoustical eigenfrequencies of the resonator. However, the shifts in frequency have to be related to the accuracy of the experiment. In fact, according to the literature a frequency shift of several Hz can be denoted as "significant". The resonance half width, which is equal to the imaginary part of the eigenfrequency, is measured in the experiments. The viscous and thermal effects partly determine the imaginary component of the frequency. For a good model, however, the motion of the shell wall must be included for example by using the impedance approach.

3.3 Circular tubes

3.3.1 Introduction

The propagation of sound waves in tubes was already investigated by Kirchhoff and Rayleigh, see *e.g.* [6]. A large amount of literature is available on this subject, dealing with full linearized Navier Stokes models, simplified models and low reduced frequency models. For an overview of models in terms of dimensionless parameters the reader is referred to Tijdeman [3], whose paper was also one of the first in which numerical results for the fundamental mode (m=0) were presented which took into account the influence of thermal effects. The theory, presented in chapter 2, will now be applied to describe the propagation of sound waves in circular tubes. A solution for the full linearized Navier Stokes model is given. Extending the work of Tijdeman, the present solution includes circumferential harmonic waves of integer order m and the effects of bulk viscosity. The results for the case of $m = 0$ and zero bulk viscosity are compared with the results presented by Tijdeman.

3.3.2 Full linearized Navier Stokes model

Basic equations

In order to solve the full linearized Navier Stokes model, two *scalar wave equations* and one *vector wave equation* have to be solved (see chapter 2). In a cylindrical co-ordinate system (r, θ, x):

$$\left[\Delta + {k_a}^2\right] T_a = 0 \quad ; \quad \left[\Delta + {k_h}^2\right] T_h = 0 \quad ; \quad \left[\Delta + {k_v}^2\right] \boldsymbol{v}_v = \boldsymbol{0} \tag{3.13}$$

Solution of the scalar wave equation

The solution of the scalar wave equations can be obtained by a straightforward separation of variables:

$$T_a = J_m\left(k_{ar} r\right) f_m\left(\theta, x\right) \quad ; \quad T_h = J_m\left(k_{hr} r\right) f_m\left(\theta, x\right) \tag{3.14}$$

where:

$$f_m\left(\theta, x\right) = \left[C_1 e^{-im\theta} + C_2 e^{im\theta}\right] \left[C_3 e^{-\Gamma x} + C_4 e^{\Gamma x}\right]$$

$$k_{ar} = \sqrt{{k_a}^2 + k^2\Gamma^2} \quad ; \quad k_{hr} = \sqrt{{k_h}^2 + k^2\Gamma^2} \tag{3.15}$$

The function $f_m\left(\theta, x\right)$ consists of circumferential harmonics of integer order m that are travelling in the $+x$ and the $-x$-directions. The quantity Γ is the

propagation constant. The solution for the temperature is:

$$T = A_a J_m\left(k_{ar} r\right) f_m\left(\theta, x\right) + A_h J_m\left(k_{hr} r\right) f_m\left(\theta, x\right) \tag{3.16}$$

The solenoidal velocity can be obtained from:

$$\boldsymbol{v}_l = \boldsymbol{v}_{la} + \boldsymbol{v}_{lh} = \alpha_a A_a \boldsymbol{\nabla} T_a + A_h \alpha_h \boldsymbol{\nabla} T_h \tag{3.17}$$

This gives:

$$\begin{aligned} \boldsymbol{v}_l &= \left[\alpha_a A_a \frac{\partial J_m\left(k_{ar} r\right)}{\partial r} + \alpha_h A_h \frac{\partial J_m\left(k_{hr} r\right)}{\partial r}\right] f_m\left(\theta, x\right) \boldsymbol{e}_r \\ &+ \left[\alpha_a A_a J_m\left(k_{ar} r\right) + \alpha_h A_h J_m\left(k_{hr} r\right)\right] \frac{1}{r} \frac{\partial f_m\left(\theta, x\right)}{\partial \theta} \boldsymbol{e}_\theta \\ &+ \left[\alpha_a A_a J_m\left(k_{ar} r\right) + \alpha_h A_h J_m\left(k_{hr} r\right)\right] k \frac{\partial f_m\left(\theta, x\right)}{\partial x} \boldsymbol{e}_x \end{aligned} \tag{3.18}$$

The pressure is:

$$p = \left[\frac{\gamma}{\gamma - 1}\right] \left[A_a \left[1 - \frac{i {k_a}^2}{s^2 \sigma^2}\right] J_m\left(k_{ar} r\right) + A_h \left[1 - \frac{i {k_h}^2}{s^2 \sigma^2}\right] J_m\left(k_{hr} r\right)\right] f_m\left(\theta, x\right) \tag{3.19}$$

Solution of the vector wave equation

The solution of the vector wave equation is, see Morse and Feshbach [77]:

$$\begin{aligned} \boldsymbol{v}_v &= W_1 \boldsymbol{\nabla} \times \left[\boldsymbol{e}_x J_m\left(k_{vr} r\right) f_m\left(\theta, x\right)\right] \\ &+ W_2 \boldsymbol{\nabla} \times \boldsymbol{\nabla} \times \left[\boldsymbol{e}_x J_m\left(k_{vr} r\right) f_m\left(\theta, x\right)\right] \end{aligned} \tag{3.20}$$

where W_1 and W_2 are constants that remain to be determined from the boundary conditions, and:

$$k_{vr} = \sqrt{{k_v}^2 + k^2 \Gamma^2} \tag{3.21}$$

After some algebra one obtains:

$$\begin{aligned} \boldsymbol{v}_v &= W_1 \left[J_m\left(k_{vr} r\right)\right] \frac{1}{r} \frac{\partial f_m\left(\theta, x\right)}{\partial \theta} \boldsymbol{e}_r - W_1 \left[\frac{J_m\left(k_{vr} r\right)}{\partial r}\right] f_m\left(\theta, x\right) \boldsymbol{e}_\theta \\ &+ W_2 \left[\left({k_v}^2 + k^2 \Gamma^2\right) J_m\left(k_{vr} r\right)\right] f_m\left(\theta, x\right) \boldsymbol{e}_x \\ &+ W_2 \left[J_m\left(k_{vr} r\right)\right] k \frac{1}{r} \frac{\partial^2 f_m\left(\theta, x\right)}{\partial \theta \partial x} \boldsymbol{e}_\theta \\ &+ W_2 \left[\frac{\partial J_m\left(k_{vr} r\right)}{\partial r}\right] k \frac{\partial f_m\left(\theta, x\right)}{\partial x} \boldsymbol{e}_x \end{aligned} \tag{3.22}$$

Dispersion equation

For a rigid tube with isothermal walls, the following boundary conditions apply for $r = 1$:

$$T = 0 \quad ; \quad \boldsymbol{v} = \boldsymbol{v}_v + \boldsymbol{v}_l = \boldsymbol{0} \tag{3.23}$$

After some algebraic manipulations one obtains the following dispersion equation:

$$\left[1 - \frac{\alpha_h}{\alpha_a}\right] \frac{{k_v}^2}{{k_v}^2 + k^2\Gamma^2} \left[\frac{m^2}{\left. \dfrac{1}{J_m(k_{vr})} \dfrac{\partial J_m(k_{vr}r)}{\partial r} \right|_1} + \frac{k^2\Gamma^2}{{k_v}^2} \frac{1}{J_m(k_{vr})} \left. \frac{\partial J_m(k_{vr}r)}{\partial r} \right|_1 \right]$$

$$\left. \frac{1}{J_m(k_{ar})} \frac{\partial J_m(k_{ar}r)}{\partial r} \right|_1 - \frac{\alpha_h}{\alpha_a} \frac{\left. \dfrac{\partial J_m(k_{hr}r)}{\partial r} \right|_1}{J_m(k_{hr})} \tag{3.24}$$

For given values of the dimensionless parameters and the order m, the value of the (complex) propagation constant Γ can be solved from this equation.

3.3.3 Low reduced frequency model

For a circular tube with isothermal walls, the low reduced frequency solution for the pressure (see chapter 2 and Appendix B) is:

$$p = C_1 e^{-\Gamma x} + C_2 e^{\Gamma x} \tag{3.25}$$

$$\Gamma = \sqrt{\frac{\gamma}{n(s\sigma)\, B(s)}} \tag{3.26}$$

where:

$$n(s\sigma) = \left[1 + \left[\frac{\gamma - 1}{\gamma}\right] B(s\sigma)\right]^{-1}$$

$$B(s) = \frac{J_2\left(si\sqrt{i}\right)}{J_0\left(si\sqrt{i}\right)} \tag{3.27}$$

The propagation of waves is governed by the value of the propagation constant Γ. There are two waves: one travelling in the negative x-direction and one travelling in the positive x-direction. Note that the pressure is constant across the cross section of the tube in the low reduced frequency model.

3.3.4 Example: propagation constant

$m = 0$

Consider the case $m = 0$, *i.e.* there is no pressure variation in the circumferential direction. The full linearized Navier Stokes model was used to calculate the value of the propagation constant for different values of k and s. When $k \ll 1$ and $k/s \ll 1$ the solution of the full model should converge to the low reduced frequency solution for Γ. Note that the propagation constant does not depend on the value of the reduced frequency k in the low reduced frequency model.

The calculated values for $\xi = 0$ and $\xi = 0.6$ for air under atmospheric conditions ($\gamma = 1.4$ and $\sigma = \sqrt{0.71}$) are given in Figures 3.2, 3.3, 3.4 and 3.5. The basic assumptions are only valid for $k/s < 0.3\pi$ and $s > 2.24\ k/s$. In the Figures the curves are truncated at the point where these basic assumptions are violated. For each value of k and k/s there are several solutions of the dispersion equation, corresponding to different radial wavenumbers. In all Figures the first root is given. The results for the case $\xi = 0$ are identical to the results presented by Tijdeman [3]. The Figures show that the bulk viscosity only has a small influence on the value of the propagation constant for low shear wave numbers. For small values of k/s the solution of the full linearized Navier Stokes model converges to the low reduced frequency solution for Γ. Thus, for air under atmospeheric conditions the low reduced frequency model is accurate. Under more extreme conditions, however, the results could be less accurate and the full linearized Navier Stokes model must be used.

$m = 1$

In this case there is a harmonic variation of the pressure in the circumferential direction. The low reduced frequency model is not able to describe this "spiralizing" type of wave because the pressure is assumed to be constant on a cross-section. In the acoustic non-dissipative case there is a cut-on frequency. For frequencies below the cut-on frequency the solution for Γ is purely real and the wave will die out exponentially in the axial direction. When the frequency exceeds the cut-on frequency, the solution for Γ is purely imaginary and the wave starts to propagate. The cut-on frequency increases with increasing radial wavenumber. The lowest cut-on frequency is calculated from $k = 1.84$. For air under atmospheric conditions the basic assumptions require $k/s < 0.3\pi$. Thus, the shear wave number must be larger than 2, which suggests that viscothermal effects will usually only be of minor importance for these waves. The solution for higher order circumferential

modes including viscothermal effects can be calculated with the full linearized Navier Stokes model. A detailed analysis of this topic, however, is not within the scope of the present study, see *e.g.* [78, 54, 79, 53, 80].

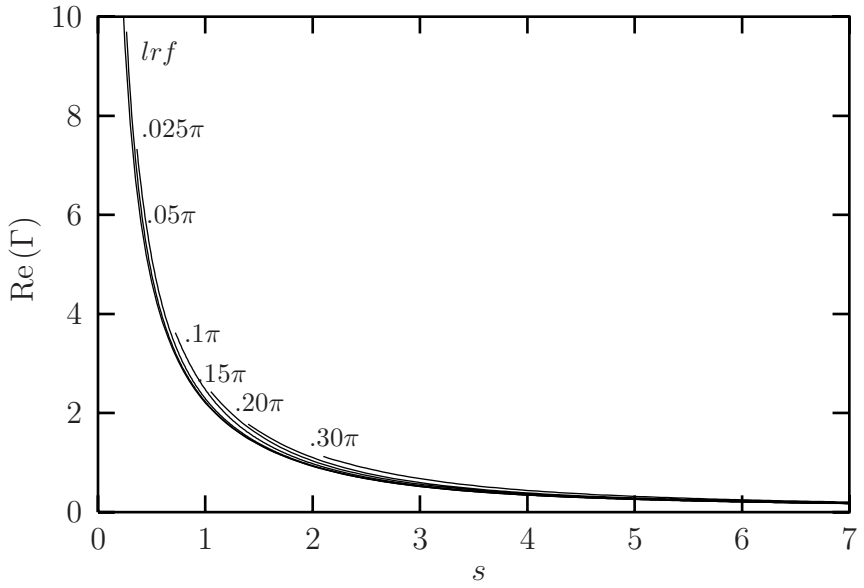

Figure 3.2: Real part of Γ for $\xi = 0$, $m = 0$ (first root), $k/s = 0.025\pi, 0.05\pi, 0.1\pi, 0.15\pi, 0.2\pi, 0.3\pi$ and the low reduced frequency solution

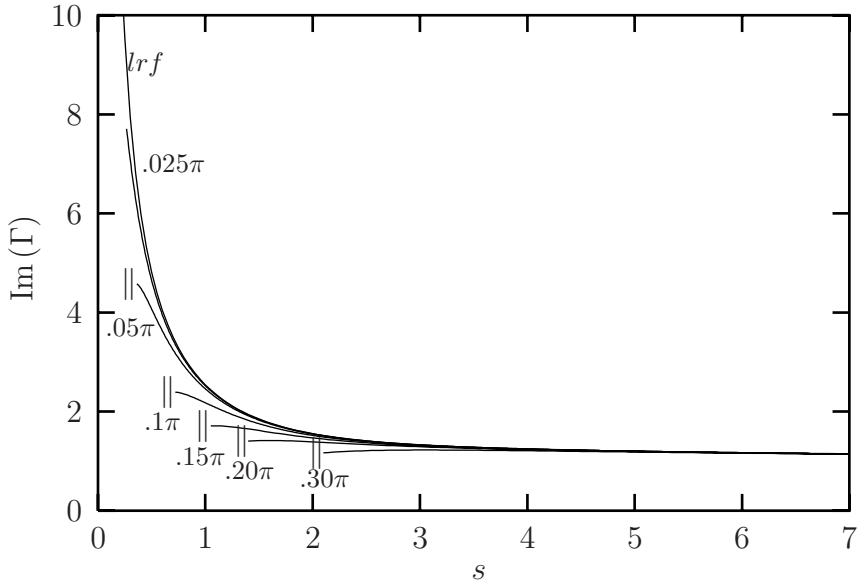

Figure 3.3: Imaginary part of Γ for $\xi = 0$, $m = 0$ (first root), $k/s = 0.025\pi, 0.05\pi, 0.1\pi, 0.15\pi, 0.2\pi, 0.3\pi$ and the low reduced frequency solution

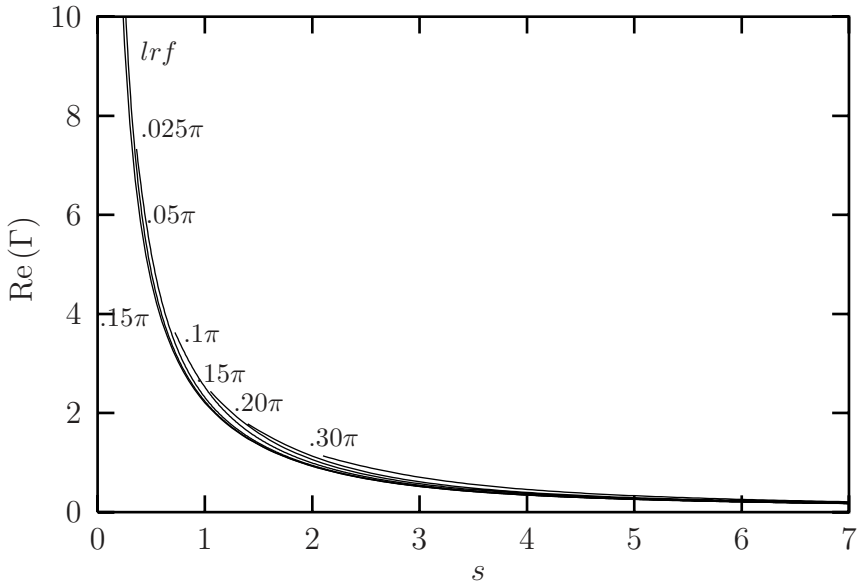

Figure 3.4: Real part of Γ for $\xi = 0.6$, $m = 0$ (first root), $k/s = 0.025\pi, 0.05\pi, 0.1\pi, 0.15\pi, 0.2\pi, 0.3\pi$ and the low reduced frequency solution

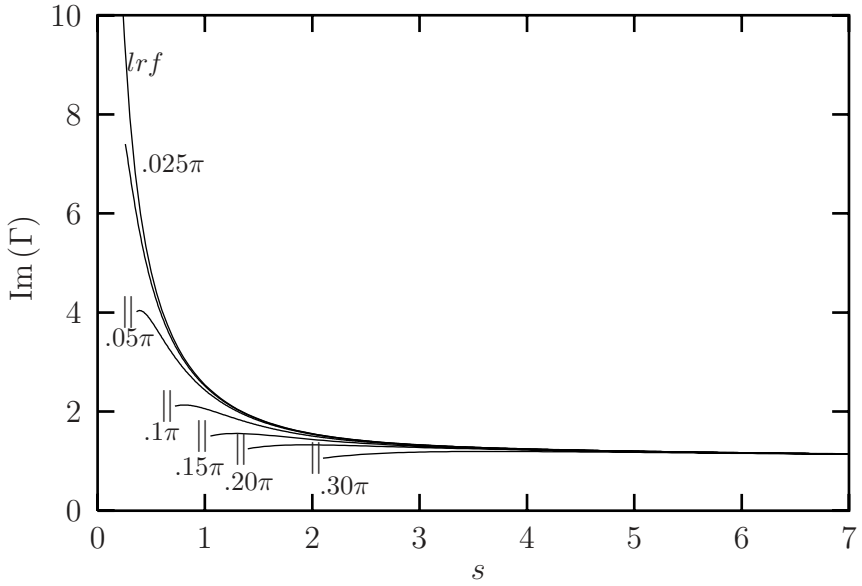

Figure 3.5: Imaginary part of Γ for $\xi = 0.6$, $m = 0$ (first root), $k/s = 0.025\pi, 0.05\pi, 0.1\pi, 0.15\pi, 0.2\pi, 0.3\pi$ and the low reduced frequency solution

3.4 Miniaturized transducer

Consider a vibrating membrane, backed by a rigid electrode (see Figure 3.6). The membrane and the electrode entrap a thin layer of air. The air layer is surrounded by a large reservoir at the periphery.

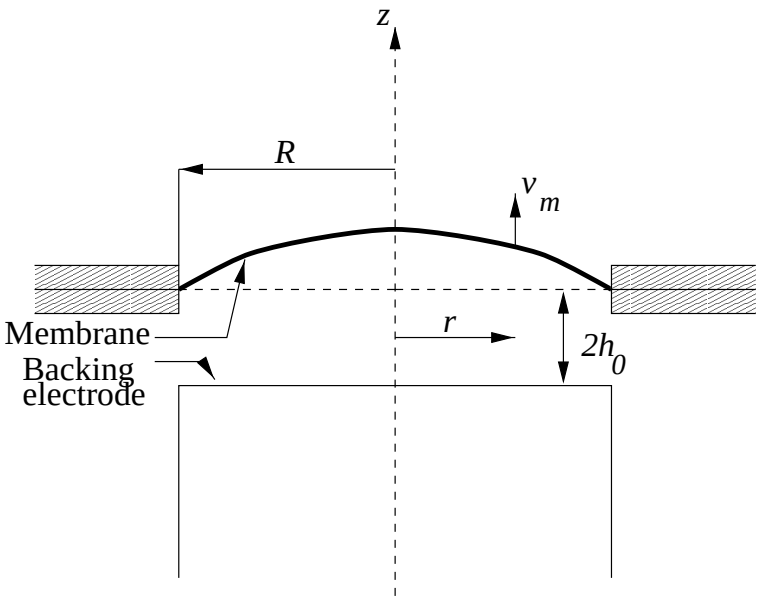

Figure 3.6: Miniaturized transducer

The displacement of the membrane is zero at the edges, *i.e.* at $\overline{r} = R$. The layer thickness is $2h_0$. Because the layer is surrounded by a large reservoir the condition $p = 0$ is imposed at $\overline{r} = R$. The membrane is excited by a plane wave with magnitude $\overline{p}_i$ at $z = h_0$. Only the rotatory symmetric case will be considered in the present analysis. Typical operating ranges for this type of transducer are a layer thickness of the order of 10^{-5} m, a radius $R = 10^{-2}$ m and a frequency range of up to 100 kHz.

3.4.1 Full linearized Navier Stokes solution

The basic equations for the problem are two scalar wave equations, one vector wave equation and the equation of motion for the membrane:

$$\left[\Delta + {k_a}^2\right] T_a = 0 \quad ; \quad \left[\Delta + {k_h}^2\right] T_h = 0$$

$$\left[\Delta + {k_v}^2\right] \boldsymbol{v}_v = \boldsymbol{0} \quad ; \quad \left[\Delta^r + \frac{k^2\Omega^2}{k_r^2}\right] v_m = -i\frac{\Omega^2 \varepsilon k}{\gamma k_r^2}\left[p - p_i\right] \quad (3.28)$$

where k_a, k_h and k_v are the acoustic, entropic and rotational wave numbers, (see expressions (2.12) and (2.17)), v_m is the dimensionless membrane velocity in the z-direction and p_i is the dimensionless external incident pressure. The parameters k_r, Ω (a dimensionless frequency), ε (a coupling parameter) and the operators Δ and Δ^r are defined as:

$$\begin{aligned} \Omega^2 = \frac{\omega^2 R^2 t_m \rho_m}{T_m} \quad ; \quad k_r = \frac{\omega R}{c_0} \quad ; \quad \varepsilon = \frac{\rho_0 h_0}{\rho_m t_m} \\ \Delta = k^2 \frac{\partial^2}{\partial r^2} + k^2 \frac{1}{r} \frac{\partial}{\partial r} + \frac{\partial^2}{\partial z^2} \quad ; \quad \Delta^r = k^2 \frac{\partial^2}{\partial r^2} + k^2 \frac{1}{r} \frac{\partial}{\partial r} \end{aligned} \tag{3.29}$$

where t_m, T_m and ρ_m represent the thickness, the tension and the density of the membrane.

Solution of the scalar wave equation

After extensive algebra the following expressions for the temperatures are found:

$$\begin{aligned} T_a &= \sum_{q=1,2,\cdots} J_0\left(\frac{k_q}{k} r\right) \left[B_{aq} \sin\left(k_{aq} z\right) + A_{aq} \cos\left(k_{aq} z\right)\right] \\ T_h &= \sum_{q=1,2,\cdots} J_0\left(\frac{k_q}{k} r\right) \left[B_{hq} \sin\left(k_{hq} z\right) + A_{hq} \cos\left(k_{hq} z\right)\right] \end{aligned} \tag{3.30}$$

The solenoidal velocity can be obtained from [1]:

$$\boldsymbol{v}_l = \boldsymbol{v}_{la} + \boldsymbol{v}_{lh} = \alpha_a \boldsymbol{\nabla} T_a + \alpha_h \boldsymbol{\nabla} T_h \tag{3.31}$$

This gives:

$$\begin{aligned} \boldsymbol{v}_l &= \sum_{q=1,2,\cdots} -\frac{k_q}{k} J_1\left(\frac{k_q}{k} r\right) \alpha_a \left[B_{aq} \sin\left(k_{aq} z\right) + A_{aq} \cos\left(k_{aq} z\right)\right] \boldsymbol{e}_r \\ &+ \sum_{q=1,2,\cdots} -\frac{k_q}{k} J_1\left(\frac{k_q}{k} r\right) \alpha_h \left[B_{hq} \sin\left(k_{hq} z\right) + A_{hq} \cos\left(k_{hq} z\right)\right] \boldsymbol{e}_r \\ &+ \sum_{q=1,2,\cdots} J_0\left(\frac{k_q}{k} r\right) \alpha_a \left[B_{aq} \cos\left(k_{aq} z\right) - A_{aq} \sin\left(k_{aq} z\right)\right] \boldsymbol{e}_z \qquad (3.32) \\ &+ \sum_{q=1,2,\cdots} J_0\left(\frac{k_q}{k} r\right) \alpha_h \left[B_{hq} \cos\left(k_{hq} z\right) - A_{hq} \sin\left(k_{hq} z\right)\right] \boldsymbol{e}_z \end{aligned}$$

(3.33)

[1] The constants A_a and A_h are contained in A_{aq}, B_{aq}, A_{hq} and B_{hq}

where the different wave numbers are given by:

$$k_{aq}^2 = k_a^2 - k_q^2 \quad ; \quad k_{hq}^2 = k_h^2 - k_q^2 \quad ; \quad k_{vq}^2 = k_v^2 - k_q^2 \tag{3.34}$$

The values of k_q are the roots of the following equation:

$$J_0\left(\frac{k_q}{k}k_r\right) = 0 \tag{3.35}$$

The pressure is:

$$p = \left[\frac{\gamma}{\gamma-1}\right]\left[\left[1 - \frac{ik_a{}^2}{s^2}\frac{1}{\sigma^2}\right]T_a + \left[1 - \frac{ik_h{}^2}{s^2}\frac{1}{\sigma^2}\right]T_h\right]$$

Solution of the vector wave equation

The rotational velocity is given by:

$$\begin{aligned} \boldsymbol{v}_v &= \sum_{q=1,2,\cdots} \frac{k_{vq}}{k_q} J_1\left(\frac{k_q}{k}r\right)\left[A_{vq}\sin\left(k_{vq}z\right) - B_{vq}\cos\left(k_{vq}z\right)\right]\boldsymbol{e}_r \\ &+ \sum_{q=1,2,\cdots} J_0\left(\frac{k_q}{k}r\right)\left[B_{vq}\sin\left(k_{vq}z\right) + A_{vq}\cos\left(k_{vq}z\right)\right]\boldsymbol{e}_z \end{aligned} \tag{3.36}$$

Solution of the problem

There are 6 constants that remain to be determined: $A_{aq}, A_{hq}, A_{vq}, B_{aq}, B_{hq}$ and B_{vq}. The following conditions can be used to determine the values of these constants:

- $T = 0$ for $z = \pm 1$
- $p = 0$ for $r = k_r$
- $[\boldsymbol{v}_l + \boldsymbol{v}_v] \cdot \boldsymbol{e}_r = 0$ for $z = \pm 1$
- $[\boldsymbol{v}_l + \boldsymbol{v}_v] \cdot \boldsymbol{e}_z = v_m$ for $z = 1$

The velocity of the membrane is:

$$\begin{aligned} v_m &= -i\frac{\Omega^2\varepsilon k}{\gamma k_r^2}\frac{p_i k_r^2}{k^2\Omega^2}\left[\frac{J_0\left(\frac{\Omega}{k_r}r\right)}{J_0\left(\Omega\right)} - 1\right] \\ &- i\frac{\Omega^2\varepsilon k}{\gamma k_r^2}\sum_{q=1,2\cdots}\frac{J_0\left(\frac{k_q}{k}r\right)}{\left[\frac{k^2\Omega^2}{k_r^2} - k_q{}^2\right]}\left\{\Lambda_a\left[A_{aq}\cos\left(k_{aq}z\right) + B_{aq}\sin\left(k_{aq}z\right)\right]\right\} \\ &- i\frac{\Omega^2\varepsilon k}{\gamma k_r^2}\sum_{q=1,2\cdots}\frac{J_0\left(\frac{k_q}{k}r\right)}{\left[\frac{k^2\Omega^2}{k_r^2} - k_q{}^2\right]}\left\{\Lambda_h\left[A_{hq}\cos\left(k_{hq}z\right) + B_{hq}\sin\left(k_{hq}z\right)\right]\right\} \end{aligned} \tag{3.37}$$

where the following symbols were used:

$$\Lambda_a = \left[\frac{\gamma}{\gamma-1}\right]\left[1-\frac{ik_a{}^2}{s^2}\frac{1}{\sigma^2}\right] \quad ; \quad \Lambda_h = \left[\frac{\gamma}{\gamma-1}\right]\left[1-\frac{ik_h{}^2}{s^2}\frac{1}{\sigma^2}\right] \tag{3.38}$$

3.4.2 Low reduced frequency solution

The low reduced frequency problem results in two coupled scalar equations:

$$\left[\Delta^r - k^2\Gamma^2\right] p = -\frac{1}{2} ikn(s\sigma)\Gamma^2 v_m \quad ; \quad \left[\Delta^r + \frac{k^2\Omega^2}{k_r^2}\right] v_m = -i\frac{\Omega^2\varepsilon k}{\gamma k_r^2}\left[p - p_i\right] \tag{3.39}$$

The solution is:

$$\begin{aligned} p &= \sum_{q=1,2\cdots} A_q J_0\left(\frac{k_q}{k} r\right) \\ v_m &= \sum_{q=1,2\cdots} B_q J_0\left(\frac{k_q}{k} r\right) \end{aligned} \tag{3.40}$$

where the participation factors A_q and B_q are given by:

$$\begin{aligned} A_q &= \frac{ikn(s\sigma)\Gamma^2}{2\left[k_q^2 + k^2\Gamma^2\right]} B_q \\ B_q &= -i\frac{\Omega^2\varepsilon k}{\gamma k_r^2} \frac{-2p_i}{k_q k_r \left[\frac{k^2\Omega^2}{k_r^2} - k_q^2 + \frac{kn(s\sigma)\Gamma^2}{2\left[k_q^2+k^2\Gamma^2\right]}\frac{\Omega^2\varepsilon k}{\gamma k_r^2}\right] J_1\left(\frac{k_q}{k} k_r\right)} \end{aligned} \tag{3.41}$$

3.4.3 Example: membrane impedance

As a test case, the impedance of the system is calculated. This test case was described by Plantier and Bruneau [47]. They used a full linearized Navier Stokes model with simplified wave numbers. In the present analysis, however, the full expressions for the wave numbers are used, since the simplification of the wave numbers actually eliminates the need for a full model (see chapter 2). The real and the imaginary parts of the impedance are defined in terms of the incident pressure $\overline{p_i}$ and the *average* membrane velocity $\langle\overline{v_m}\rangle$:

$$\overline{Z}_r = 10 \cdot^{10} \log\left[\frac{\left(\mathrm{Re}\left(\overline{Z}\right)\right)^2}{\overline{Z}_0^2}\right] \quad ; \quad \overline{Z}_i = 10 \cdot^{10} \log\left[\frac{\left(\mathrm{Im}\left(\overline{Z}\right)\right)^2}{\overline{Z}_0^2}\right] \tag{3.42}$$

$$\langle\overline{v}_m\rangle = \frac{1}{\pi R^2}\int_0^R \overline{v}_m \, 2\pi\overline{r} \, d\overline{r} \quad ; \quad \overline{Z} = \frac{\overline{p}_i}{\langle\overline{v}_m\rangle} \quad ; \quad \overline{Z}_0 = 1\cdot 10^4 \text{ Ns/m}$$

The following properties were used:

$$\begin{aligned} R = 1.37 \cdot 10^{-2}\ \text{m} \quad &; \quad \rho_m = 4.5 \cdot 10^{3}\ \text{kg/m}^3 \quad ; \quad T_m = 6.2 \cdot 10^{3}\ \text{N/m} \\ t_m = 12.7 \cdot 10^{-6}\ \text{m} \quad &; \quad 2h_0 = 25.4 \cdot 10^{-6}\ \text{m} \quad ; \quad \rho_0 = 1.2\ \text{kg/m}^3 \\ \lambda = 25.6 \cdot 10^{-3}\ \text{W/mK} \quad &; \quad C_v = 716\ \text{J/kgK} \quad ; \quad C_p = 1004\ \text{J/kgK} \\ c_0 = 340\ \text{m/s} \quad &; \quad \mu = 18.2 \cdot 10^{-6}\ \text{Ns/m}^2 \quad ; \quad \xi = 0.6 \end{aligned} \tag{3.43}$$

The results for the full linearized Navier Stokes model and the low reduced frequency model are plotted in Figure 3.7.

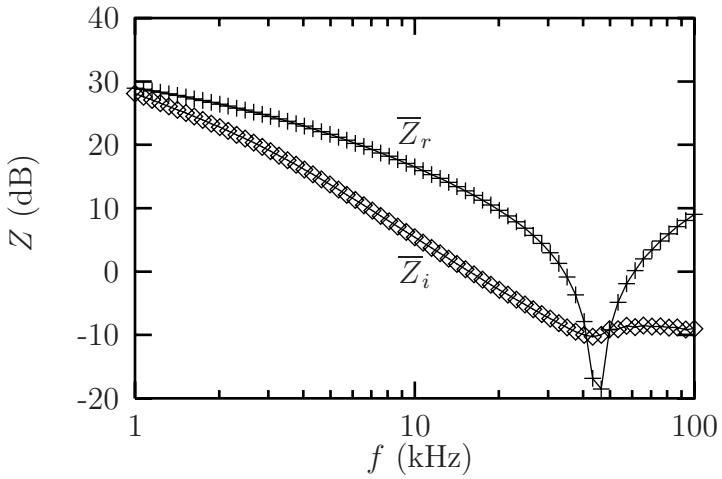

Figure 3.7: Impedance for full model ($\diamond$, $+$) and low reduced frequency model (—)

It is evident from Figure 3.7 that both models give the same results for the impedance of the membrane. The other quantities, like velocity and pressure, are also nearly identical. The pressure, for example, does not vary much across the layer thickness: the maximum deviation in the profile is less than 0.1% for frequencies up to 100 kHz. The assumption of constant pressure is reasonable. This is not too surprising when analysing the values of the dimensionless parameters. The conditions $k \ll 1$ and $k/s \ll 1$ hold for the entire frequency range up to 100 kHz: $k < 10^{-1}$ and $k/s < 10^{-2}$. This indicates that the low reduced frequency model will give reliable results, even in the high frequency range.

In fact, to the author's knowledge, all problems concerning miniaturized transducers that were presented in the literature could have been solved with the simple low reduced frequency model. None of these cases required the use of the full model. For gases under atmospheric conditions the low reduced frequency model is sufficient and clearly the most efficient.

3.5 Squeeze film damping between plates

As a fourth application, a squeeze film damping problem is analysed. Consider a flexible plate, located parallel to a fixed surface (see Figure 3.8). A thin layer of air is trapped between the vibrating plate and the rigid surface. This problem was solved by Trochidis using a simplified Navier Stokes model. An uncoupled approach was used: the vibrational behaviour of the plate was imposed as a boundary condition for the fluid. The results of this model will now be compared with the results from a low reduced frequency model.

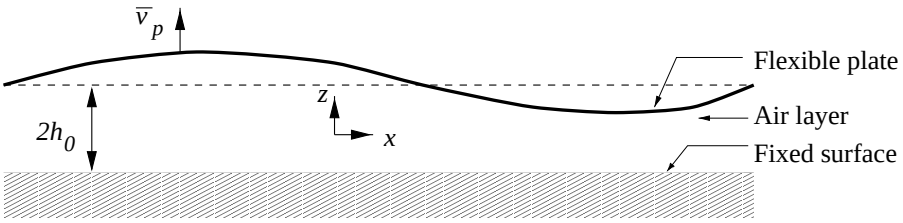

Figure 3.8: Squeeze film damping problem

The plate properties are: thickness t_p, density ρ_p and Young's modulus E_p. The problem to be considered is two-dimensional: there is no variation in the y-direction. The deflection of the plate is imposed as a boundary condition for the fluid. The velocity, imposed by Trochidis, can be written as:

$$\overline{v}_p = c_0 v_p \cos(k_p x)\, e^{i\omega t} \tag{3.44}$$

where v_p is the dimensionless amplitude of the velocity (a constant) and k_p is the wave number. According to Trochidis, the wave number is:

$$k_p = \frac{c_0}{\omega}\left[\frac{\omega^2 \rho_p t_p}{D_p}\right]^{\frac{1}{4}}\left[1+\frac{\rho_0}{\rho_p t_p}\left[\frac{D_p}{\omega^2\rho_p t_p}\right]^{\frac{1}{4}}\right]^{\frac{1}{5}} \quad ; \quad D_p = \frac{E_p {t_p}^3}{12} \tag{3.45}$$

The second term in the expression for k_p accounts for the fact that the free wave number of the plate is affected by the gas or fluid loading on the upper side of the plate. This term can be significant when the plate is loaded with a heavy fluid. For gases, the term can usually be neglected. For the present case the correction in wave number is only 0.1%. Therefore the wave number is simplified to:

$$k_p = \frac{c_0}{\omega}\left[\frac{\omega^2 \rho_p t_p}{D_p}\right]^{\frac{1}{4}} \tag{3.46}$$

3.5.1 Simplified Navier Stokes solution

Basic equations

The equations for incompressible behaviour are:

$$\Delta p = 0$$

$$\left[\Delta - is^2\right] \boldsymbol{v} = \frac{s^2}{k\gamma} \boldsymbol{\nabla} p \tag{3.47}$$

Solution of the equations

Using separation of variables, one obtains:

$$\begin{aligned}
p &= \left[C_1 e^{-k_{p1} z} + C_2 e^{k_{p1} z}\right] \cos\left(k_p x\right) \\
\boldsymbol{v} &= -\frac{s^2}{\gamma} \frac{k_p}{{k_{p1}}^2 - {k_{p2}}^2} \left[C_1 e^{-k_{p1} z} + C_2 e^{k_{p1} z}\right] \sin\left(k_p x\right) \boldsymbol{e}_x \\
&+ \left[C_3 e^{-k_{p2} z} + C_4 e^{k_{p2} z}\right] \sin\left(k_p x\right) \boldsymbol{e}_x \\
&+ \frac{s^2}{\gamma} \frac{k_p}{{k_{p1}}^2 - {k_{p2}}^2} \left[C_1 e^{-k_{p1} z} + C_2 e^{k_{p1} z}\right] \cos\left(k_p x\right) \boldsymbol{e}_z \\
&+ \frac{k_{p1}}{k_{p2}} \left[C_3 e^{-k_{p2} z} + C_4 e^{k_{p2} z}\right] \cos\left(k_p x\right) \boldsymbol{e}_z
\end{aligned} \tag{3.48}$$

where the wave numbers k_{p1} and k_{p2} are given by: [2]

$$k_{p1} = k k_p \quad ; \quad k_{p2} = \sqrt{is^2 + k^2 {k_p}^2} \tag{3.49}$$

The four constants C_1, C_2, C_3 and C_4 are determined from the following boundary conditions:

- $\boldsymbol{v} \cdot \boldsymbol{e}_x = 0$ for $z = \pm 1$
- $\boldsymbol{v} \cdot \boldsymbol{e}_z = 0$ for $z = -1$
- $\boldsymbol{v} \cdot \boldsymbol{e}_z = v_p \cos\left(k_p x\right)$ for $z = 1$

[2] Trochidis approximates the wave number k_{p2} by $s\sqrt{i}$

3.5.2 Low reduced frequency solution

The equation to be solved is:

$$k^2 \frac{\partial^2 p}{\partial x^2} - k^2 \Gamma^2 p = -ikn(s\sigma)\Gamma^2 \frac{1}{2} v_p \cos(k_p x) \tag{3.50}$$

The solution for an infinite plate is simply:

$$p = \frac{in(s\sigma)\Gamma^2}{2k\left[{k_p}^2 + \Gamma^2\right]} v_p \cos(k_p x) \tag{3.51}$$

Note that compressibility effects are accounted for in this expression.

3.5.3 Example: loss factor

Trochidis used the loss factor of the system to compare analytical and experimental results. In order to calculate the loss factor, the different forms of energy in the system have to be identified. In the case of compressible behaviour three terms are of interest: the dissipated energy per cycle, $\overline{E}_{diss}$, the maximum energy stored in the plate, $\overline{E}_p$, and the potential energy stored in the air layer, $\overline{E}_{lay}$. For this problem these quantities can be written as:

$$\begin{aligned} \overline{E}_{diss} &= -\frac{\pi p_0 c_0}{\omega} \int_A \mathrm{Re}\left(p\ v_p^*\right)\ dA \\ \overline{E}_p &= \frac{1}{2} D_p c_0^2 \int_A \left[\frac{\partial^2 v_p}{\partial \overline{x}^2}\right]^2\ dA \\ \overline{E}_{lay} &= \frac{1}{2} \frac{p_0^2}{\rho_0 {c_0}^2} \int_A \int_{\overline{z}=-h_0}^{h_0} \left[\mathrm{Re}(p)\right]^2\ d\overline{z}\ dA \end{aligned} \tag{3.52}$$

where A denotes the surface area of the plate and * denotes a complex conjugate. The loss factor is then obtained from:

$$\zeta = \frac{\overline{E}_{diss}}{2\pi\left[\overline{E}_p + \overline{E}_{lay}\right]} \tag{3.53}$$

The following values were used for the present testcase:

$$\begin{aligned} E_p = 70 \cdot 10^9\ \mathrm{N/m^2} \quad &; \quad t_p = 1 \cdot 10^{-3}\ \mathrm{m} \quad ; \quad \rho_p = 2710\ \mathrm{kg/m^3} \\ \lambda = 25.6 \cdot 10^{-3}\ \mathrm{W/mK} \quad &; \quad \rho_0 = 1.2\ \mathrm{kg/m^3} \quad ; \quad C_v = 716\ \mathrm{J/kgK} \\ \mu = 18.2 \cdot 10^{-6}\ \mathrm{Ns/m^2} \quad &; \quad C_p = 1004\ \mathrm{J/kgK} \quad ; \quad c_0 = 340\ \mathrm{m/s} \\ 2h_0 = 1.5 \cdot 10^{-3}\ \mathrm{m} & \end{aligned} \tag{3.54}$$

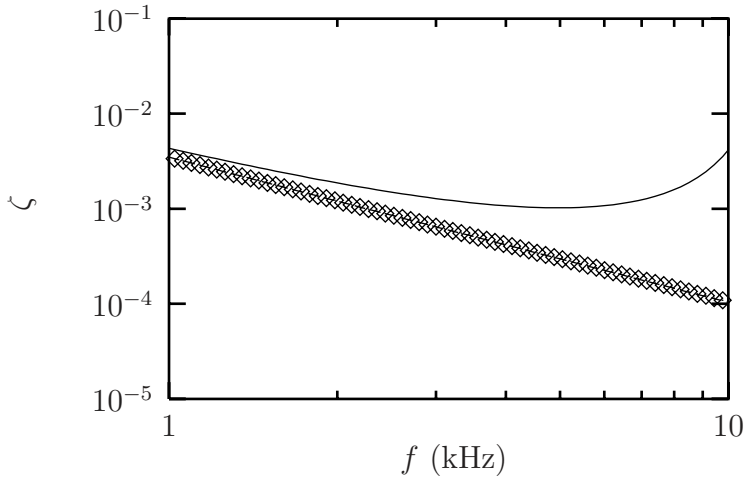

Figure 3.9: Loss factor versus frequency: Trochidis model ($\diamond$), low reduced frequency model (—), incompressible low reduced frequency model ($--$)

The loss factor as a function of frequency is given in Figure 3.9. Results are plotted for the Trochidis model, the low reduced frequency model and the low reduced frequency model for incompressible behaviour.

The Figure clearly shows that the Trochidis model and the low reduced frequency model for incompressible behaviour give the same results. The loss factor shows a decrease with increasing frequency for these incompressible models. The low reduced frequency solution including compressibility effects however shows an increasing loss factor for high frequencies.

The increase can be attributed to a coincidence effect. For the present case the acoustic wavelength and the bending wavelength are equal for a frequency just above 10 kHz. For this frequency, energy is radiated efficiently into the layer. Both $\overline{E}_{diss}$ and $\overline{E}_{lay}$ exhibit a peak at this frequency. The final result is a peak in the loss factor. Note that incompressible models are not able to describe the coincidence phenomenon.

The two incompressible models give the same result for the loss factor. For the entire frequency range, the conditions $k \ll 1$ and $k/s \ll 1$ hold: $k < 1$ and $k/s < 10^{-2}$. Therefore the low reduced frequency assumptions are valid. Again, there is no need to use a more complicated model: the low reduced frequency model is sufficient and the most efficient.

Chapter 4

The low reduced frequency model

4.1 Introduction

This chapter deals with the air loads on a rigid rectangular plate oscillating normal to a fixed surface (see Figure 4.1). We consider a rigid, rectangular plate, suspended by springs attached to the corners of the plate. The plate is mounted parallel to a fixed surface and performs a small harmonic oscillation normal to that surface. The distance between the plate and the fixed surface, $\overline{h}(t)$, is given by the real part of:

$$\overline{h}\,(t) = h_0 \left[2 + he^{i\omega t}\right] \tag{4.1}$$

where $2h_0$ is the mean distance between the plate and the fixed surface, h is the dimensionless amplitude of the oscillation, ω is the angular frequency and t refers to time.

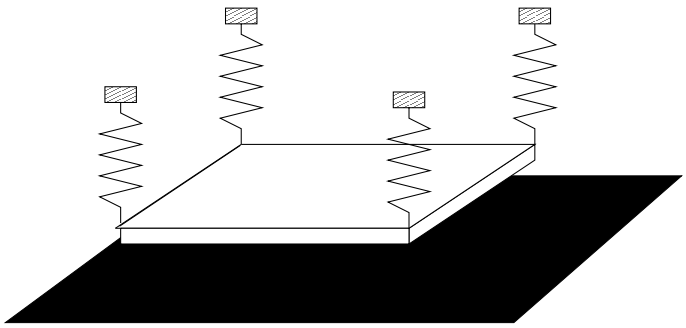

Figure 4.1: Oscillating plate

The plate is assumed to be rigid. Hence, any uncertainty with respect to the dynamical behaviour of the plate is excluded. The forces acting on the plate due to the pressure distribution in the gap will affect the eigenfrequency and the damping of the system. The airloads can thus be determined by measuring the eigenfrequency and the damping of the system.

For the behaviour of the air in the gap between the plate and the fixed surface an analytical solution is presented, based on a low reduced frequency model. As a first check, the results from the analytical solution are compared with the results from a standard finite element technique, based on the wave equation. In these calculations the air is represented as a compressible, inviscid medium. The analytical solution is validated with specially designed experiments.

Most of the experiments described in the literature are carried out at relatively high frequencies. In order to obtain low shear wave numbers, very small gaps widths were used. For these gap widths low damping levels in the frequency range of interest were found. However, such a small gap width is difficult to control and consequently the accuracy of the results is often not very clear. A further drawback is the fact that the amplitude of oscillation has to be kept very small in order to avoid non-linearities. Finally, most experiments were carried out with relatively heavy structural materials. For such materials the air loads have a small influence on the dynamical behaviour of the system. Consequently the frequency shifts and the damping values are not very large.

The experimental setup, presented in this chapter, was specially designed to avoid many of these problems. With the help of the aforementioned dimensionless parameters a large scale setup was constructed. Typical properties of the setup are: plate dimensions 0.98 x 0.98 m^2, plate mass 2.54 kg, gap widths from 3 to 650 mm. The eigenfrequency of the single degree of freedom mass-spring system in vacuum is 9.73 Hz. The frequency range of interest is the range from 1 to 10 Hz. The plate is excited in the centre by an electrodynamic shaker. Because of the fact that the panel is very light, the frequency shift and the amount of damping are very large. The large scale of the setup makes it possible to measure the pressure distribution in the gap. This provides new information regarding the accuracy of the models and the boundary conditions.

4.2 Analytical calculations

4.2.1 Pressure distribution

The low reduced frequency equation for this geometry is (see chapter 2 and Appendix B):

$$\frac{\partial^2 p}{\partial x^2} + \frac{\partial^2 p}{\partial y^2} - \Gamma^2 p = n(s\sigma)\Gamma^2 \frac{1}{2} h \tag{4.2}$$

where the functions $B(s)$ and $n(s\sigma)$ are given by:

$$B(s) = \frac{\tanh\left(s\sqrt{i}\right)}{s\sqrt{i}} - 1 \quad ; \quad n\left(s\sigma\right) = \left[1 + \left[\frac{\gamma - 1}{\gamma}\right] B\left(s\sigma\right)\right]^{-1} \tag{4.3}$$

The boundary conditions are:

$$p = 0 \;\; \text{for} \;\; x = \pm k_x \quad ; \quad p = 0 \;\; \text{for} \;\; y = \pm a k_x \tag{4.4}$$

where k_x is a wave number and a is the aspect ratio of the plate:

$$k_x = \frac{\omega l_x}{c_0} \quad ; \quad a = \frac{l_y}{l_x} \tag{4.5}$$

The applied boundary condition is $p = 0$ (see Figure 4.2). This is a simplification, since the pressure distribution outside the gap will be affected by the pressure distribution in the gap and vice versa. For narrow gaps, however, the magnitude of the pressure perturbation in the gap is very large compared to the magnitude of the pressure perturbation outside the gap. Hence, the boundary condition $p = 0$ is a realistic assumption. This is confirmed by straightforward potential flow calculations, a comparison with finite element results and experimental results. A more extensive discussion on this boundary condition is given in the sections 4.3 and 4.5.3.

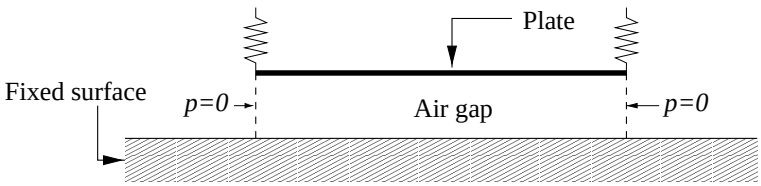

Figure 4.2: Boundary conditions for the analytical model

The solution for the pressure is:

$$p(x,y) = \frac{2n(s\sigma)\Gamma^2 k_x^2 h}{\pi} \sum_{q=1,3,5\cdots} \frac{(-1)^{\frac{q-1}{2}}}{qD^2} \left[\frac{\cosh\left(D\frac{1}{k_x}x\right)}{\cosh\left(D\right)} - 1\right] \cos\left(\frac{q\pi}{2}\frac{1}{ak_x}y\right) \tag{4.6}$$

where:

$$D = \sqrt{\left[\frac{q\pi}{2}\frac{1}{a}\right]^2 - k_x^2\Gamma^2} \tag{4.7}$$

The force on the plate is obtained by integration:

$$\begin{aligned} F_{gap} \equiv & \int_{x=-k_x}^{k_x}\int_{y=-ak_x}^{ak_x} p\left(x,y\right)dxdy \\ = & \frac{16n(s\sigma)\Gamma^2 k_x^4 ah}{\pi^2}\sum_{q=1,3,5\cdots}\frac{1}{q^2}\frac{1}{D^2}\left[\frac{\tanh\left(D\right)}{D}-1\right] \end{aligned} \tag{4.8}$$

4.2.2 Mobility function

The plate is assumed to be rigid, moves only in the z-direction and remains parallel to the fixed surface. The system can therefore be regarded as a single degree of freedom system. When the pressure distribution in the air outside the gap is neglected, the forces acting on the plate are $\overline{F}_{ex}$, the harmonic excitation force generated by an electrodynamic shaker, $\overline{F}_{gap}$, the force acting on the lower side of the plate due to the pressure distribution in the gap between the plate and the fixed surface and $\overline{F}_{springs}$, the spring forces. The plate is suspended by 8 springs, two at each corner. Each spring has a stiffness κ. The forces are written as:

$$\overline{F}_{ex} = l_x l_y p_0 F_{ex} e^{i\omega t} \quad ; \quad \overline{F}_{gap} = l_x l_y p_0 F_{gap} e^{i\omega t} \quad ; \quad \overline{F}_{springs} = 8\kappa h_0 h e^{i\omega t} \tag{4.9}$$

The equation of motion for the plate:

$$-\omega^2 m h_0 h = l_x l_y p_0 \left[F_{ex} + F_{gap}\right] - 8\kappa h_0 h \tag{4.10}$$

where m is the mass of the plate The transfer function $H(\omega)$ relates the force and the displacement for harmonic signals according to:

$$H\left(\omega\right) = \frac{h_0 h}{l_x l_y p_0 F_{ex}} \tag{4.11}$$

For a system with viscous damping it is more convenient to use the mobility function, representing the transfer function between velocity and force. The mobility function is obtained by multiplying $H(\omega)$ with $i\omega$. Inserting the expressions for the air load (see (4.8)) finally gives:

$$Y\left(\omega\right) = \frac{i\omega}{-\omega^2 m - \frac{l_x l_y p_0}{h_0}\left[\frac{16n(s\sigma)k_x^2\Gamma^2}{\pi^2}\sum_{q=1,3,5\cdots}\frac{1}{q^2}\frac{1}{D^2}\left[\frac{\tanh\left(D\right)}{D}-1\right]\right] + 8\kappa} \tag{4.12}$$

The eigenfrequency and the damping coefficient of the system are extracted from a Nyquist plot of the mobility function.

4.2.3 Physical interpretation

When the influence of the surrounding air is neglected and the structural damping is assumed to be negligible (this is confirmed in the tests described in section 4.4.1), the plate-spring system can be regarded as an undamped single degree of freedom system with mass m and stiffness 8κ . The surrounding air however will affect the dynamical behaviour of the plate. Usually the air load is split up into an added mass, an added stiffness and an added damping. An analysis of the load term in the mobility function however reveals that this concept is ambiguous for this situation. The expression for the resulting air load is a general, complex function of the angular frequency. The imaginary part of the force could be used to extract the amount of added damping. Added mass and added stiffness however are, like in the experiments, not directly separable. In the calculations one could define an artificial separation. For instance, the added stiffness could be related to the effects of compressibility. For this choice the amount of added mass is obtained by assuming the air to be incompressible. The added stiffness is then determined from the difference between compressible and incompressible behaviour. However, the added stiffness then strongly depends on the frequency. This indicates that a split-up of the air load is rather arbitrary. Hence, the physical interpretation of the results will be based on a direct analysis of the force expression. Four quantities that influence the force are the gap width, the viscosity, the aspect ratio and the compressibility.

Gap width

One of the most important quantities that governs the air load is the gap width, $2h_0$. The force shows a strong increase with decreasing gap width. In physical terms, this is associated with the amount of pumping in the gap. The motion of the air is mainly perpendicular to the motion of the plate (see Figure 4.3). It can easily be understood that this pumping effect increases with decreasing gap width.

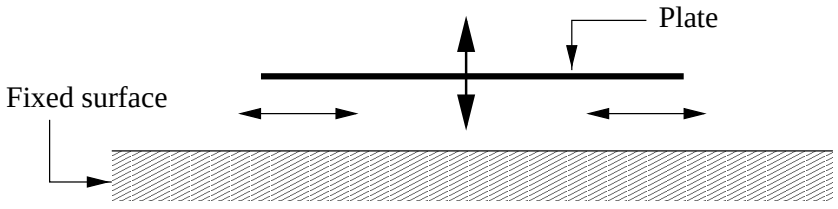

Figure 4.3: Pumping effect

Viscosity

A very interesting point is the role of the viscosity. The viscosity affects both the real and the imaginary part of the propagation constant Γ. The damping depends on the viscosity, as expected. However, the eigenfrequency of the system is also affected by the viscosity. In this investigation the phase resonance frequency is used: the eigenfrequency of the corresponding undamped system. Therefore the eigenfrequency is, by definition, not influenced by the damping. The eigenfrequency shift due to viscosity may thus seem surprising. Simply speaking one would expect the viscosity to affect the damping, but not the eigenfrequency. The change in frequency can be attributed to the change in the velocity profile in the gap. For low shear wave numbers there is a parabolic profile, whereas for high shear wave numbers the velocity profile is flat (see section 2.5.3). It is therefore important that, for a correct estimation of the eigenfrequency, the viscosity is taken into account.

Compressibility

In the calculations one can easily eliminate the effects of the compressibility. For incompressible behaviour, the function D (see expression (4.7)), reduces to:

$$D_{inc} = \frac{q\pi}{2}\frac{1}{a} \tag{4.13}$$

Compressibility effects are important when:

$$|k_x\Gamma| \cong \left(\frac{\pi}{2}\right)\left(\frac{1}{a}\right) \tag{4.14}$$

This can be rewritten to:

$$\left|\frac{\omega l_y}{c_{eff}(\omega)}\right| \cong \frac{\pi}{2} \tag{4.15}$$

where $c_{eff}(\omega)$ is an effective speed of sound:

$$c_{eff}(\omega) = \frac{ic_0}{\Gamma} \tag{4.16}$$

The effective speed of sound is affected by viscous effects and thermal effects. In physical terms, expression (4.15) now simply states that compressibility effects are important when the effective acoustic wavelength is of the same order of magnitude as the plate length.

4.3 Standard acoustic finite element calculations

As a first check, the results from the analytical solution with the results from a standard finite element technique, based on the wave equation. In these calculations the air is represented as a compressible, inviscid medium. The finite element calculations were carried out for the experimental setup (see section 4.4.1) with the program ANSYS [81]. A rectangular solar panel is suspended by 8 springs, two at each corner. The panel has a mass m and (equivalent) Young's modulus E; each spring has a stiffness κ. The thickness of the panel is 0.022 m. The plate is modelled as an elastic body. The deformation of the plate however is shown to be small in the frequency range of interest (see also section 4.4.4). This frequency range is far below the first elastic eigenfrequency of the panel. The gap width between the plate and the fixed surface can be varied between 2 and 650 mm. The following properties are taken according to the measurements [1]:

$$\begin{aligned} &m = 2.540 \text{ kg} \quad ; \quad \kappa = 1186 \text{ N/m} \\ &l_x = 0.49 \text{ m} \quad ; \quad l_y = 0.49 \text{ m} \\ &E = 2.61 \cdot 10^9 \text{ N/m}^2 \end{aligned} \tag{4.17}$$

The properties of the surrounding air at standard atmospheric conditions:

$$\rho_0 = 1.2 \text{ kg/m}^3 \quad ; \quad \mathrm{c}_0 = 343 \text{ m/s} \tag{4.18}$$

The panel is modelled with three-dimensional 8-node solid elements, type SOLID45. The degrees of freedom at each node are the displacements. In ANSYS the air is represented as a compressible, inviscid medium. The behaviour of the air is therefore governed by the wave equation. Three-dimensional 8-node acoustic elements, type FLUID30 , were used. For the acoustic elements, the pressure perturbation is the degree of freedom at each node. With the use of symmetry the mesh is reduced to 1/4 of the system (see Figure 4.4). In the numerical calculations, the two springs at each corner are replaced by a single spring with a double stiffness. The boundary condition for the pressure on the planes of symmetry and the fixed surface is that the pressure gradient normal to the wall should vanish. In physical terms, this condition states that the velocity of the air normal to the surface is equal to zero. This condition is automatically satisfied in the ANSYS program when no other boundary conditions are specified.

[1] The mass of the panel includes the mass of some instrumentation. Young's modulus is an equivalent quantity for the layered honeycomb panel.

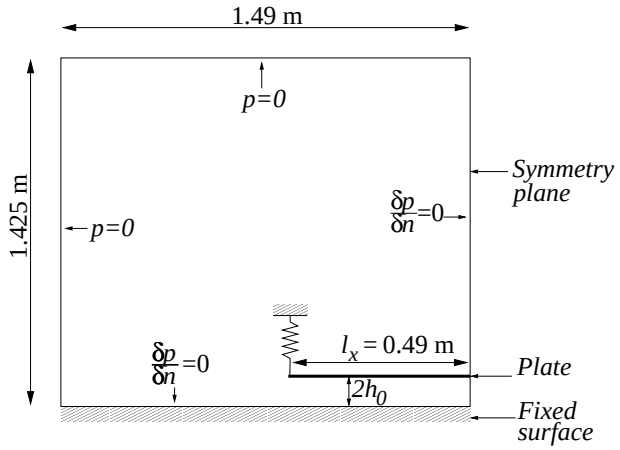

Figure 4.4: Finite element mesh

The boundary condition for the other air boundaries is $p = 0$. This is a simplification of the Sommerfeld radiation condition, which states that all waves are outgoing. The condition $p = 0$ however will give reliable results when the dimensions of the surrounding air domain are sufficiently large (without introducing standing waves). As a test case, the added mass was calculated for an oscillating plate in an infinite air domain for a number of mesh dimensions. The results showed that for an air domain of 1.49 x 1.49 (in-plane) x 1.425 m^3 (perpendicular to the plate), the added mass differs only by 3.8% from the value given in the literature [82]. This justifies the use of the boundary condition $p = 0$ for the finite element calculations. Note that the influence of the air on the upper side of the panel is also accounted for in the finite element model. The accuracy of the $p = 0$ condition, used in the analytical model at the edges of the panel, can be investigated with this model where also (part of) the surrounding air is taken into account. The results for the pressure distribution will be compared with experimental and analytical results.

4.4 Experiments

4.4.1 Experimental setup

In order to measure the effects of the surrounding air, a relatively light and stiff plate must be used. A solar panel is very well suited for this purpose. The measurements were carried out using a square ECS panel (courtesy of Fokker Space & Systems) of 0.98 x 0.98 m^2. The panel consists of 2 carbon

skin plates separated by a honeycomb structure of thin aluminium sheet. The plate is suspended by 8 springs, 2 located at each corner (see figure 4.5). The panel is excited by an electrodynamical shaker, attached to the centre of the plate. The fixed surface is a rectangular rigid plate of 2.20 x 1.80 m^2 supported by three screw jacks. Figure 4.5 shows a schematic drawing of the experimental setup.

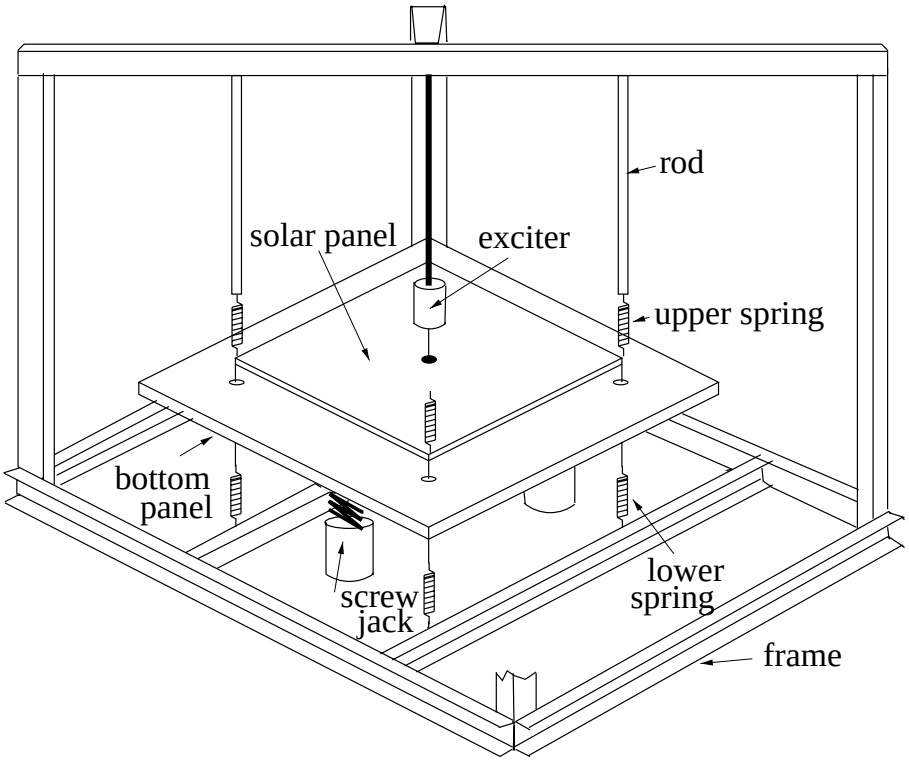

Figure 4.5: Experimental setup

In total there are 4 accelerometers mounted on the panel. The signal from one accelerometer is used as feedback for the shaker to keep the displacement amplitude constant. In this way a measurement can be carried out at a constant displacement amplitude. This enables easy linearity measurements. The other 3 accelerometers are used to verify the assumption of rigid behaviour of the panel. These transducers, $\overline{a}1$, $\overline{a}2$ and $\overline{a}3$, are mounted on the diagonal of the panel (see figure 4.6). A laser distance sensor is mounted in the fixed surface to provide extra information about the gap width and the amplitude of oscillation.

Three pressure transducers are mounted in the fixed surface under the plate. These transducers, $\overline{p}1$, $\overline{p}2$ and $\overline{p}3$, are used to compare analytical

and numerical data with experimental pressure data. The transducer $\overline{p}3$ is mounted at the edge of the gap. In this way the validity of the $p = 0$ boundary condition is investigated (see Figure 4.6).

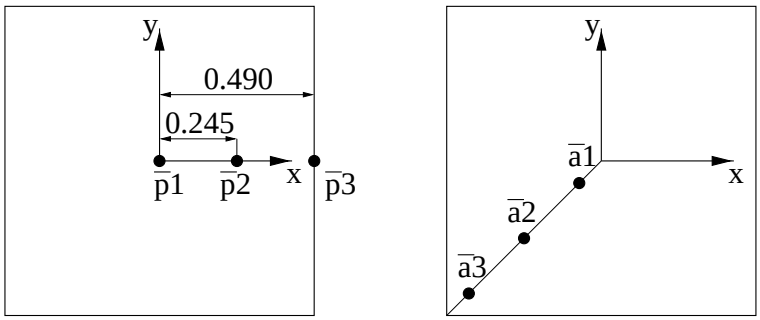

Figure 4.6: Instrumentation, dimensions in m.

The undamped eigenfrequency f_n (phase resonance frequency), the corresponding damping coefficient, the accelerations and the atmospheric conditions are registered. The properties of interest are [2]:

$$\begin{aligned} m = 2.540 \text{ kg} \quad &; \quad R_0 = 287 \text{ J/kgK} \\ l_x = 0.49 \text{ m} \quad &; \quad l_y = 0.49 \text{ m} \\ C_p = 1004 \text{ J/kgK} \quad &; \quad C_v = 716 \text{ J/kgK} \\ \rho_0 = 1.2 \text{ kg/m}^3 \quad &; \quad c_0 = 343 \text{ m/s} \\ \lambda = 25.6 \cdot 10^{-3} \text{ W/mK} \quad &; \quad \mu = 18.2 \cdot 10^{-6} \text{ Ns/m}^2 \\ \kappa = 1186 \text{ N/m} \quad &; \quad T_0 = 290 \text{ K} \end{aligned} \tag{4.19}$$

4.4.2 Dimensionless parameters

The experimental setup is characterized by the value of the dimensionless parameters. The main parameter governing the motion of the air in the gap is the shear wave number. For large gaps the viscosity of the air can be neglected, whereas for small gaps viscous effects become dominant. The distance between the panel and the fixed surface, $2h_0$, can be varied from 2 to 650 mm. For this range of gap widths the shear wave number varies between 0.64 and 667. As σ is a constant for air, the product $s\sigma$ varies between 0.4 and 520. This implies that for narrow gaps the process in the gap is isothermal, while for large gaps it occurs adiabatically. These considerations indicate that even for a relatively large gap, *e.g.* 2 mm, the shear wave number is

[2] For these conditions $\sigma \cong \sqrt{0.71}$

very low. It should be noted that by varying the gap width not only the value of the shear wave number is affected. Another important parameter, the reduced frequency k, varies between 10^{-5} and 0.06; the condition $k \ll 1$ is therefore satisfied.

4.4.3 Validation of the measurement procedure

The experimental setup was used to measure the shift in eigenfrequency and the damping originating from the pressure distribution in the gap. The measurement procedure was validated by adding a known mass to the panel and to demonstrate that this extra mass can be determined accurately with the present measuring technique. The shift in phase resonance frequency was measured and used to determine the added mass. The measurement results for two different gap widths are listed in Table 4.1. The Table shows that the added mass was measured within 3% of the actual, manually added, mass. Hence, it can be concluded that the setup is suited for the measurements in this investigation.

	Measured added mass (kg)	
Added mass (kg)	$2h_0 = 650$ mm	$2h_0 = 35$ mm
0.0604	0.0605	0.0603
0.1208	0.1181	0.1220
0.1816	0.1766	0.1848
0.2420	0.2348	0.2436

Table 4.1: Validation procedure, measurement results

4.4.4 Accuracy of the measurements

The accuracy of the experiments is affected by several mechanisms. In order to determine the accuracy of the results, a number of tests were carried out.

Parasitic oscillations

Parasitic oscillations will affect the dynamical behaviour of the system. In order to determine whether any parasitic motions were present, accelerations of the panel and the frame were measured in several directions. Two parasitic oscillations, an in-plane motion of the plate and a frame vibration, were

identified. Some simple structural modifications were applied such that the parasitic motions were eliminated.

Deformation of the panel

Another oscillation that might affect the accuracy of the results is the deformation of the panel. The first elastic eigenfrequency of the panel in air is 49 Hz. In order to consider the panel as rigid, the frequency range of interest should be far below 49 Hz. The stiffness of the springs is such that the first eigenfrequency of the plate-spring system in vacuum is 9.73 Hz. Due to the influence of the surrounding air, the eigenfrequency will decrease compared to the situation in vacuum. The frequency range of interest therefore was chosen 1 to 10 Hz, and the panel was assumed to be rigid. During the experiments, the deformation of the plate was measured. With three accelerometers mounted on the plate, the accelerations were measured to check that the plate was indeed behaving in a rigid way.

The influence of the deformation of the panel was taken into account in the finite element calculations. In these calculations the panel was modelled as an elastic body. The results indicate that the influence of the elasticity is small. For a gap width of 150 mm the difference in eigenfrequency between a rigid model and a flexible finite element model was less than 0.3 Hz. The difference decreased as the gap width decreased. Thus, the influence of the elasticity was small. This was confirmed by the accelerometer data: accelerations of the points differ mutually by 4% at most, which justifies the assumption of rigidity.

Compliance of the fixed surface

The compliance of the fixed surface was measured using the accelerometers. The measurements show that the amplitude of oscillation for the fixed surface is less than 1% of the amplitude of oscillation of the panel. The fixed surface was therefore regarded as rigid and fixed.

Tilting of the fixed surface

In order to determine the influence of tilting, measurements were carried out for small tilting angles. For gap widths of 35, 10 and 6 mm. tilting angles of 1.2, 0.2 and 0.2 degrees respectively were used. For the panel of interest, with a length of 0.98 m, this corresponds to a variation in gap width of 20, 4 and 4 mm respectively. The results show that the added mass and the added damping differred less than 5% for these tilting angles. Because of the

fact that global quantities (eigenfrequency and damping) were measured, the sensitivity for small tilting angles was limited.

Curvature of the panel and the fixed surface

The most important quantity that governs the accuracy of the experimental results is the gap width. Due to the shape of both the panel and the fixed surface the accuracy is affected.

The deformation of the fixed surface due to its own weight was calculated with a finite element model. A simple static calculation showed that the deformation due to this dead load is smaller than 0.06 mm. The eigenfrequencies of the fixed surface were calculated from a dynamic analysis. All eigenfrequencies were substantially higher than the frequency range of interest.

For a certain gap width the distance between the panel and the fixed surface was measured at 49 points between the panel and the fixed surface. The gap width was not constant but varied with position: $\pm$ 0.8 mm. This could mainly be attributed to the planarity of the fixed surface. With a least squares technique the accuracy was improved. The gap width data was used to find the position of the fixed surface that would lead to the best constant gap width in a least squares sense. The gap width was then correspondingly adjusted in three points for each measurement. Due to this correction, the error introduced by the planarity of the surfaces could be reduced to $\pm$ 0.4 mm in gap width.

The influence of the remaining curvature profile was investigated by means of a special finite element model in the program B2000 [3]. In this model the viscothermal and acousto-elastic effects are accounted for. Viscothermal elements can be coupled to structural elements. The gap width can be specified for each viscothermal element and elements with different gap widths can be coupled. In the calculations the measured curvature profile was used to specify the gap width for each element. The eigenfrequency of the system was calcululated. The results indicate that the remaining curvature of the surfaces has a very small influence: for gap widths between 3 and 35 mm the difference in eigenfrequency between a flat and a curved model is less than 1%. Regarding these considerations, the measurements could be carried out with a satisfying accuracy, especially compared to previous papers in this area.

[3] A detailed description of this model is given in chapter 5

Non-linear effects

The theory used in the present investigation is based on linearized equations. In the experiments the amplitude of oscillation of the panel therefore must be small compared to the gap width. In order to determine whether any non-linear effects are present a number of experiments were carried out with different amplitudes of oscillation. For several gap widths measurements were performed at several amplitude levels. In all situations, the eigenfrequency and the damping were not affected by the amplitude of motion.

Flow around plate edges

The flow around the plate edges was visualized with smoke tests. In the frequency and amplitude ranges of interest, no irregularities or disturbances in the flow pattern were observed.

Reproducibility

The measurement series was repeated a number of times to investigate the reproducibility of the experiments. The results show that the reproducibility was very good. Data of the measurement series are given in Appendix D.

4.4.5 Experimental results

Typical results for the transfer function are presented in Figure 4.7. This Figure shows that the shift in eigenfrequency is relatively large. If one converts this frequency shift to an added mass for a gap of 3 mm, the amount of added mass amounts to about 22 kg, while the mass of the panel is only 2.5 kg! The sharp increase in damping is illustrated by the flattening of the transfer function. The pumping effect induces high viscous losses, which results in damping of the panel. For a gap of 3 mm, the dimensionless damping coefficient ξ is 35%: the panel is almost critically damped. The experimental results are summarized in Table 4.2. For each gap width the eigenfrequency, the damping coefficient and the dimensionless parameters are listed.

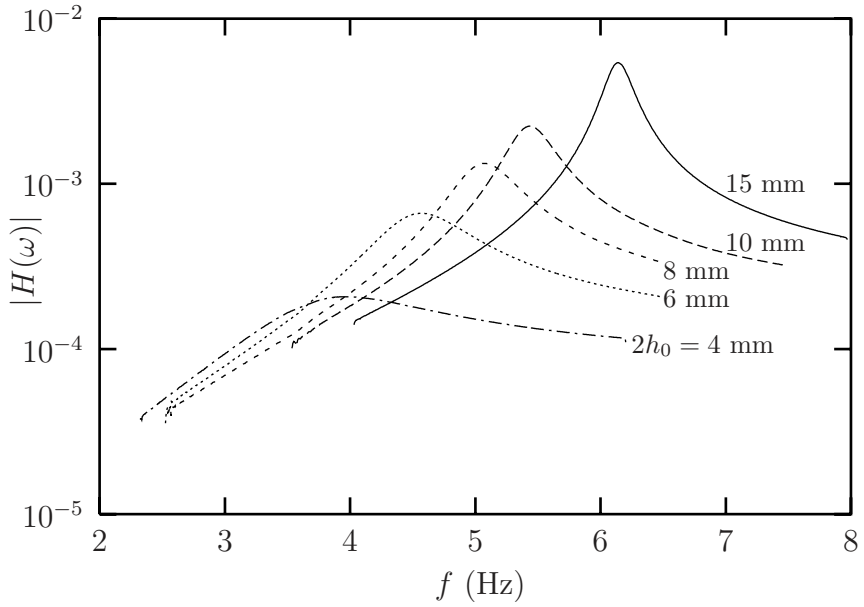

Figure 4.7: Amplitude of transfer function $H(\omega)$

4.5 Comparison between theory and experiments

4.5.1 Eigenfrequency

The measured and the calculated eigenfrequencies are depicted in Figure 4.8. Because of the fact that due to a change in gap width $2h_0$, a number of dimensionless parameters change in value, the Figure is not plotted in a non-dimensional form. Figure 4.8 shows that there is a strong decrease in eigenfrequency with decreasing gap width. The results from both the finite element calculations and the low reduced frequency solution show fair agreement with the experimental results. For very small gaps the finite element calculations overestimate the eigenfrequency because the viscosity of the air is neglected.

4.5.2 Damping coefficient

The corresponding dimensionless damping coefficients are depicted in Figure 4.9. This figure shows that there is a strong increase in damping with decreasing gap width. The results from the low reduced frequency solution show good agreement with the experimental results. It is evident that the

$2h_0$ (mm)	f_n (Hz)	ξ (%)	s	k	$\frac{\overline{p}1}{h_0 h}$ $\left(\frac{\text{Pa}}{\text{mm}}\right)$	$\frac{\overline{p}2}{h_0 h}$ $\left(\frac{\text{Pa}}{\text{mm}}\right)$	$\frac{\overline{p}3}{h_0 h}$ $\left(\frac{\text{Pa}}{\text{mm}}\right)$
650	8.555	0.20	612	$5.15 \cdot 10^{-2}$	—	—	—
150	8.303	0.12	139	$11.5 \cdot 10^{-3}$	—	—	—
80	7.994	0.20	73.0	$5.90 \cdot 10^{-3}$	—	—	—
50	7.635	0.32	44.5	$3.53 \cdot 10^{-3}$	—	—	—
35	7.277	0.52	30.4	$2.36 \cdot 10^{-3}$	6.5	5.8	1.19
25	6.871	0.84	21.1	$1.57 \cdot 10^{-3}$	8.0	7.0	1.23
15	6.139	1.83	12.0	$0.85 \cdot 10^{-3}$	10.1	8.6	1.01
12	5.767	2.60	9.25	$0.64 \cdot 10^{-3}$	12.1	10.3	1.00
10	5.441	3.51	7.50	$0.51 \cdot 10^{-4}$	11.8	9.8	0.82
8	5.050	5.04	5.80	$3.74 \cdot 10^{-4}$	14.8	12.2	0.93
6	4.533	8.24	4.11	$2.52 \cdot 10^{-4}$	14.5	11.8	0.75
5	4.217	11.59	3.31	$1.95 \cdot 10^{-4}$	15.1	12.5	0.58
4	3.839	18.78	2.52	$1.42 \cdot 10^{-4}$	16.3	13.1	0.70
3.5	3.599	24.55	2.14	$1.17 \cdot 10^{-4}$	17.1	13.9	0.60
3	3.337	35.71	1.77	$0.93 \cdot 10^{-4}$	21.7	17.3	0.50

Table 4.2: Experimental results

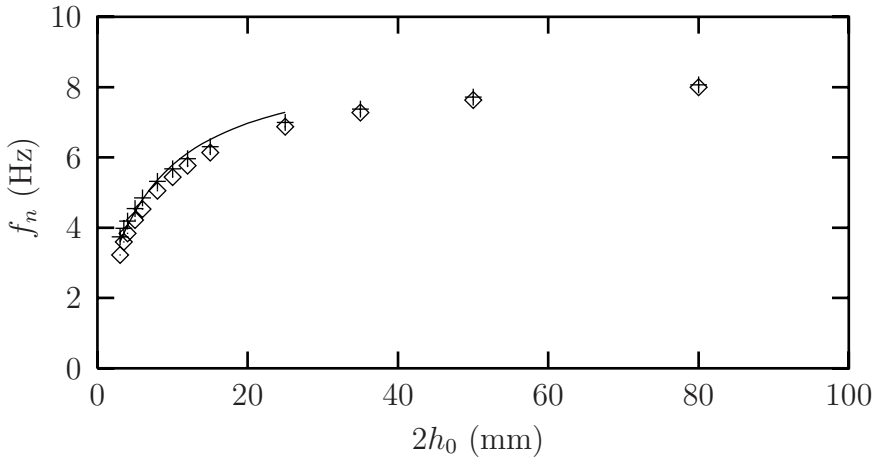

Figure 4.8: Eigenfrequency. Low reduced frequency model (—), experiments ($\diamond$), finite element model (+)

damping coefficients for the finite element calculations are zero, because the dissipative effects are neglected.

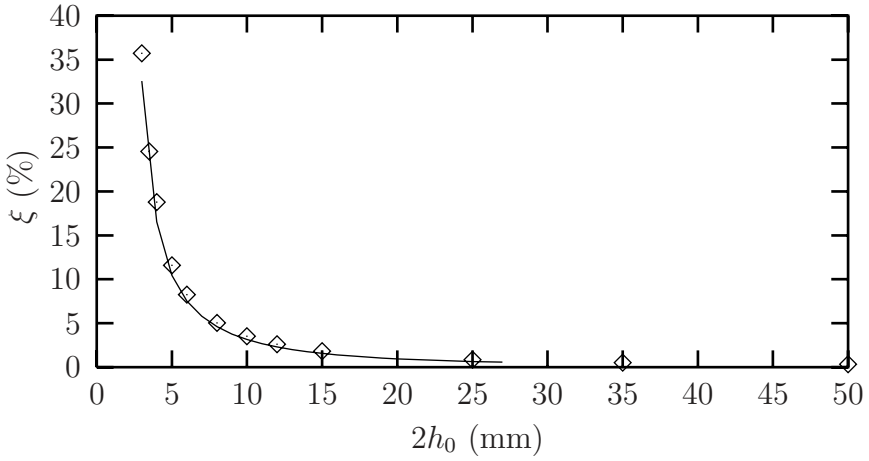

Figure 4.9: Damping coefficient. Low reduced frequency model (—), experiments (◇)

4.5.3 Pressure

The pressure in the layer was measured at three points as a function of the gap width $2h_0$ (see Figure 4.6). Since the pressure in the layer is also frequency dependent, the amplitude of the pressure was measured at the eigenfrequency for each gap width. The maximum pressure was scaled with the displacement amplitude $h_0 h$. The results from the calculations and the measurements are given in Figures 4.10, 4.11 and 4.12. In order to investigate the influence of viscous and thermal effects the analytical low reduced frequency results are also given where viscous and thermal effects were eliminatedby setting $\Gamma = i$ and $n(s\sigma) = \gamma$.

For $\overline{p}1$ and $\overline{p}2$, the pressure shows a strong increase with decreasing gap width. All models predict this increase, but the viscothermal model and the experimental model both show a very strong increase with decreasing gap width. Viscothermal effects thus have a significant influence on the pressure distribution for small gap widths [4].

The results for $\overline{p}3$ indicate that the pressure is not zero at the edges of the panel. For larger gap widths the pressure at the edge is significant compared to the maximum pressure in the layer. For small gaps however the influence

[4]Note that the pressure point for $2h_0 = 3$ mm is significant since it is the result of more measurements with good reproducibility

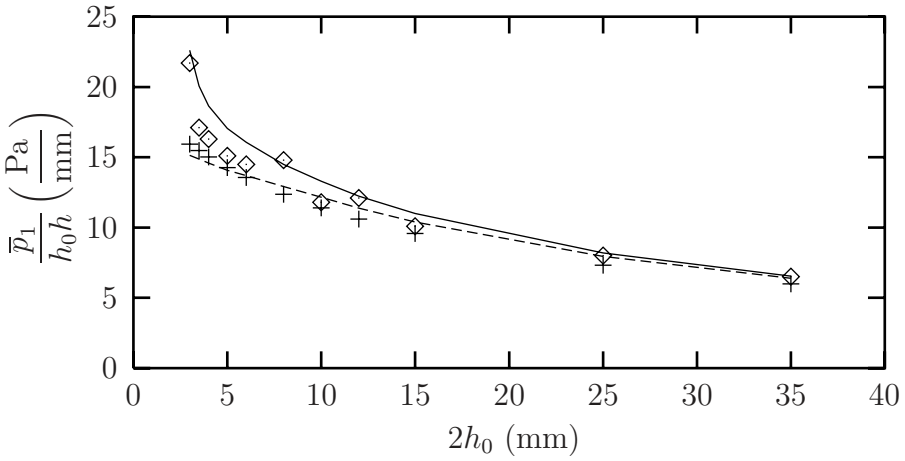

Figure 4.10: Scaled pressure $\overline{p}1$. Low reduced frequency model (—), inviscid and adiabatic low reduced frequency model (−−) , experiments (⋄), ANSYS finite element model (+)

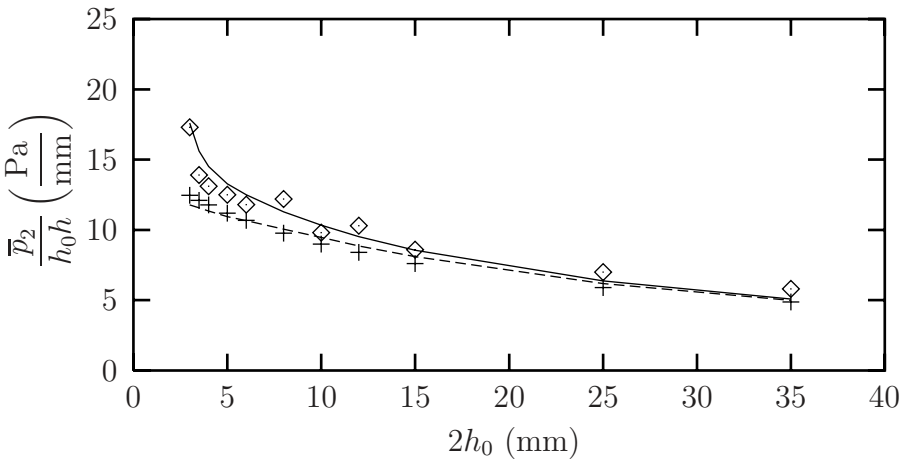

Figure 4.11: Scaled pressure $\overline{p}2$. Low reduced frequency model (—), inviscid and adiabatic low reduced frequency model (−−) , experiments (⋄), ANSYS finite element model (+)

of the non-zero boundary pressure is small. Since the low reduced frequency model is used for small gaps, it can be concluded that the boundary condition $p = 0$ is acceptable regarding the balance between simplicity and accuracy. If a more detailed prediction of the pressure at the edges is required, the low reduced frequency model must be coupled to an acoustic model describing the behaviour of the surrounding air. The standard acoustic finite element

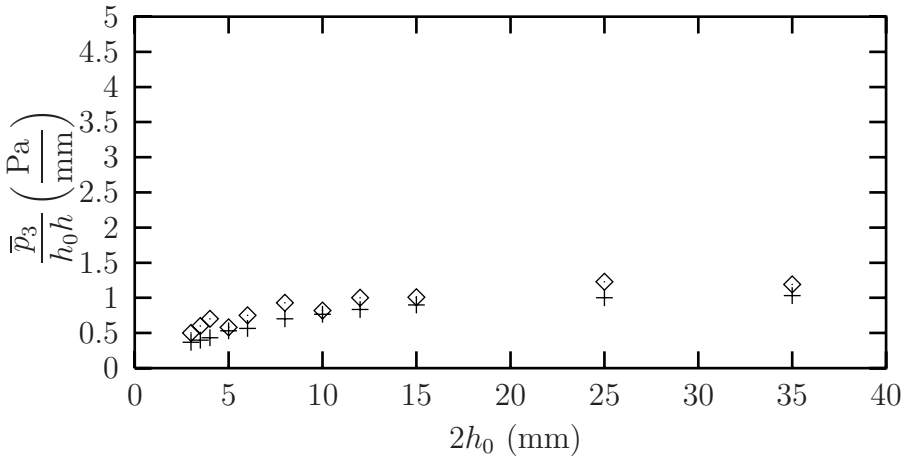

Figure 4.12: Scaled pressure $\overline{p}3$. Experiments ($\diamond$), ANSYS finite element model (+)

model is able to predict the pressure at the edge to a reasonable degree of accuracy. In the next chapter a finite element model is presented for the low reduced frequency model. This model could be coupled to a standard acoustic model describing the behaviour of the surrounding air.

4.6 Panel rotating around central axis

Experiments and calculations were also carried out for a solar panel rotating around a central axis (see Figure 4.13).

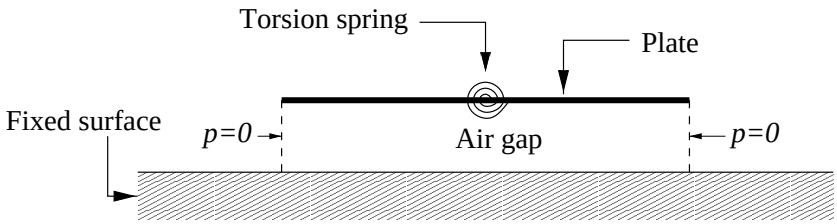

Figure 4.13: Panel rotating around $y = 0$

The panel is located parallel to a fixed surface and performs a small angular oscillation around $y = 0$. It is suspended by a torsion spring [5]. The distance between the plate and the fixed surface is:

$$\overline{h}(x, y, t) = h_0 \left[2 + \alpha \left(\frac{ak_x}{k} \right) y e^{i\omega t} \right] \tag{4.20}$$

where α is the amplitude of the angular oscillation and:

$$k_x = \frac{\omega l_x}{c_0} \quad ; \quad a = \frac{l_y}{l_x} \tag{4.21}$$

For this single degree of freedom system, eigenfrequency and damping were calculated and measured. The same procedure was used as for the translating panel. For the sake of brevity, only the main procedure and the main results will be presented.

4.6.1 Analytical calculations

The low reduced frequency equation for this situation is:

$$\frac{\partial^2 p}{\partial x^2} + \frac{\partial^2 p}{\partial y^2} - \Gamma^2 p = n(s\sigma)\Gamma^2 \frac{1}{2} \alpha \left(\frac{ak_x}{k} \right) y \tag{4.22}$$

where the functions $B(s)$ and $n(s\sigma)$ are given by:

$$B(s) = \frac{\tanh\left(s\sqrt{i}\right)}{s\sqrt{i}} - 1 \quad ; \quad n\left(s\sigma\right) = \left[1 + \left[\frac{\gamma - 1}{\gamma} \right] B\left(s\sigma\right) \right]^{-1} \tag{4.23}$$

[5] In the experiments these are springs at a certain distance from the axis of rotation

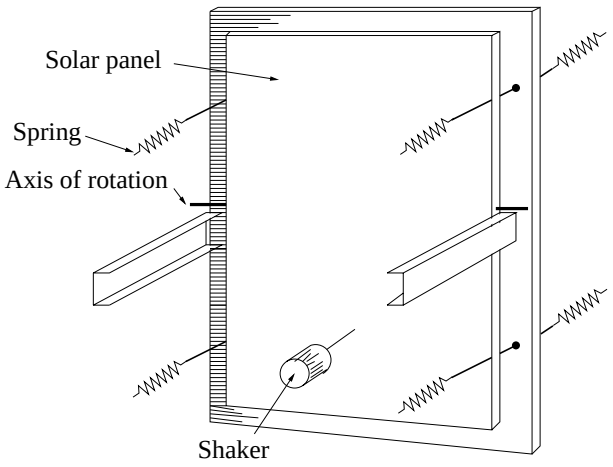

Figure 4.14: Experimental setup rotating panel

The boundary conditions are:

$$p = 0 \quad \text{for} \quad x = \pm k_x \quad ; \quad p = 0 \quad \text{for} \quad y = \pm a k_x \tag{4.24}$$

The solution for the pressure is:

$$p(x,y) = \frac{2n(s\sigma)a\Gamma^2 k_x^3 \alpha}{\pi k} \sum_{q=2,4,6\cdots} \frac{(-1)^{\frac{q-1}{2}}}{qD^2} \left[\frac{\cosh\left(D\frac{1}{k_x}x\right)}{\cosh\left(D\right)} - 1 \right] \sin\left(\frac{q\pi}{2}\frac{1}{ak_x}y\right) \tag{4.25}$$

where:

$$D = \sqrt{\left[\frac{q\pi}{2}\frac{1}{a}\right]^2 - k_x^2\Gamma^2} \tag{4.26}$$

Clearly, the force exerted on the plate is zero for the rotating panel because of the asymmetric pressure distribution. With the pressure distribution, the net moment acting on the plate around $y = 0$ was calculated and inserted into the equation of motion. The mobility function was then constructed and eigenfrequency and damping were extracted.

4.6.2 Experiments

The experiments were carried out with a solar panel of 1.67 x 1.29 m^2. The mass moment of inertia of the panel and the instrumentation was 1.64 kgm^2. The panel was suspended by 8 springs, 2 located in each of the four points at the edges of the panel (see Figure 4.14).

The eigenfrequency of the panel-spring system in vacuum was 2.96 Hz. Due to the influence of the air, the eigenfrequency will be reduced. The frequency range of interest therefore is 1 to 3 Hz. Accelerometers were mounted

on the panel to verify the rigidity of the panel. In the mentioned frequency range the deformation of the panel was negligible. The panel was excited with an electrodynamic shaker. The fixed surface was a rectangular rigid plate of 2.2 x 1.8 m^2, which was mounted on a frame parallel to the panel. The distance between the plate and the fixed surface was varied between 3 and 50 mm. The shear wave number for this configuration varies between 1.9 and 55. This implies that for thin layers the viscous forces are of the same order of magnitude as the inertial forces. The properties of the air were taken according to expression (4.19). The remaining properties of interest are:

$$\begin{aligned} I = 1.64 \text{ kgm}^2 \quad &; \quad \kappa = 245 \text{ N/m} \\ l_x = 0.835 \text{ m} \quad &; \quad l_y = 0.645 \text{ m} \\ l_{spr} = 0.538 \text{ m} \end{aligned} \tag{4.27}$$

where I denotes the mass moment of inertia of the pane, κ is the stiffness of a single spring and l_{spr} denotes the distance between the springs and the axis of rotation. The measured eigenfrequency and damping coefficient are listed in Appendix D.

4.6.3 Comparison between theory and experiments

The experimental results and the analytical results are illustrated in Figures 4.15 and 4.16.

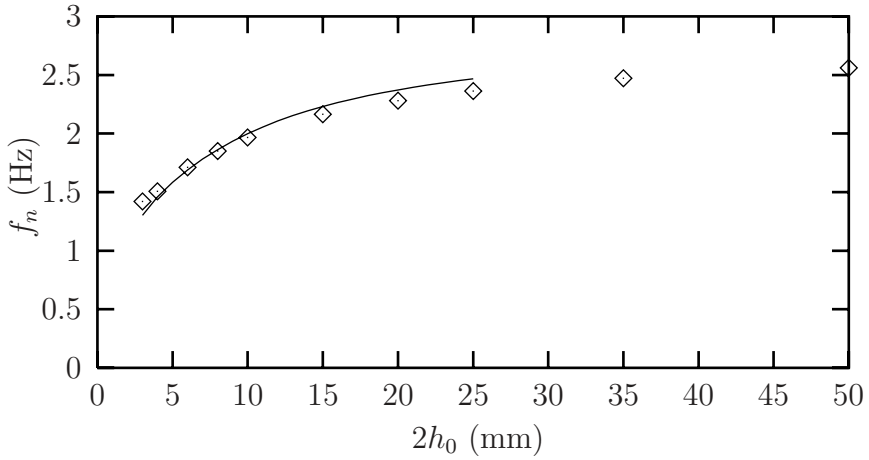

Figure 4.15: Eigenfrequency. Low reduced frequency model (—), experiments (◇)

Figure 4.15 shows that the eigenfrequency of the system decreases with decreasing gap width. For the rotating panel, the shift in eigenfrequency can

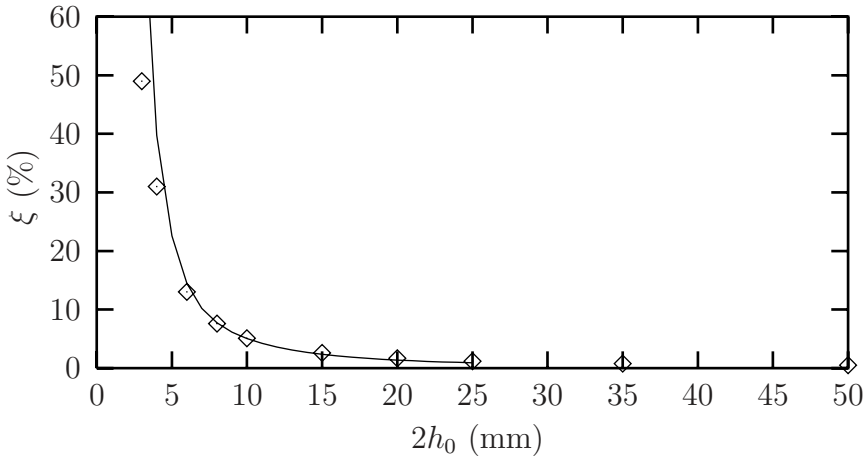

Figure 4.16: Damping coefficient. Low reduced frequency model (—), experiments (◇)

be interpreted as an added mass moment of inertia. For the panel under consideration, the mass moment of ineria is 1.64 kgm^2. For a gap width of 3 mm the added mass moment of inertia due to the pressure in the layer is 5.5 kgm^2. The damping shows a strong increase with decreasing gap width. Calculations and experiments show fair agreement.

4.7 Panel rotating around arbitrary axis

Analytical solutions were obtained for a normal translation of the panel and a central rotation. Because of the linearity of the problem, these solutions can now be used to calculate the behaviour of a rigid panel rotating around an arbitrary axis. Consider for instance a panel rotating around $y = y_a$ (see Figure 4.17). The motion can be decomposed into a translation and a rotation around $y = 0$. In the Figure the resulting forces and moments are also shown. In a similar way, the response for a rotation around an arbitrary axis can be obtained.

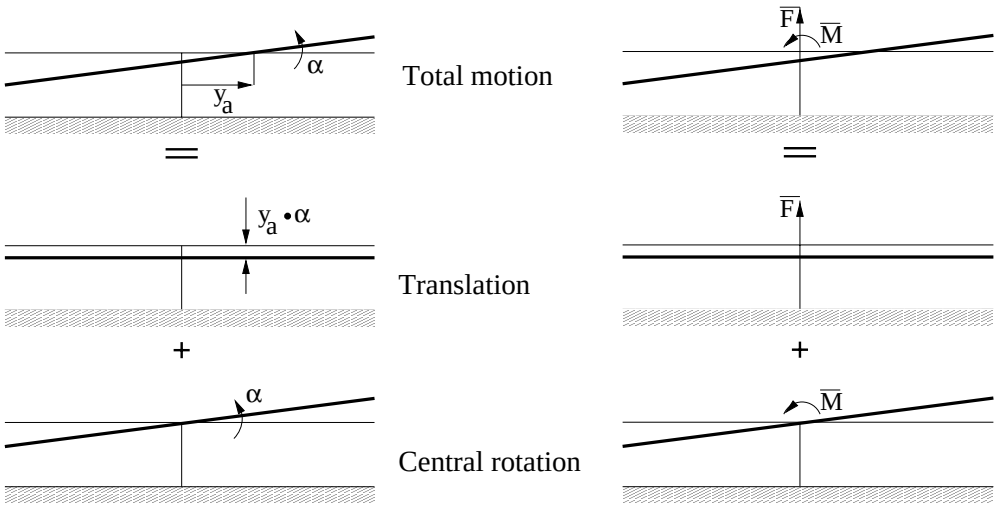

Figure 4.17: Panel rotating around arbitrary axis

4.8 Conclusions

The conclusions to be drawn from this investigation are:

- a special experimental setup was designed to validate the low reduced frequency model. With the use of the dimensionless parameters a new large-scale setup was developed. Substantial frequency shifts, very large damping values and pressures in the layer were measured with satisfactory accuracy;

- calculations and experiments show fair agreement: the low reduced frequency model is a satisfactory means to describe viscothermal wave propagation. The eigenfrequency and damping of the system and the pressure in the layer could be predicted accurately using the low reduced frequency model.

Chapter 5

Acousto-elasticity: viscothermal finite elements

5.1 Introduction

In chapter 2 an overview was presented of models for viscothermal wave propagation. It was demonstrated that the low reduced frequency model is a very simple and useful model. In chapter 4 this model was experimentally validated for a vibrating rigid surface. In view of practical applications, however, it is important to develop models that include the acousto-elastic interaction between flexible surfaces and viscothermal gas layers. Analytical solutions can only be obtained for simple geometries with simple boundary conditions.

This chapter describes the development, implementation and analytical and experimental validation of a new finite element model. The finite element model enables the modelling of more complex geometries and boundary conditions. In chapter 6 this model will be used for a number of practical applications.

5.2 Finite element formulation

The starting point for the new acoustic finite element is the low reduced frequency equation (see equation (2.28)):

$$\Delta^{pd} p\left(\boldsymbol{x}^{pd}\right) - k^2\Gamma^2 p\left(\boldsymbol{x}^{pd}\right) = -ikn(s\sigma)\Gamma^2\Re \tag{5.1}$$

In dimensional form, dropping the $(\boldsymbol{x}^{pd})$ notation:

$$\overline{\Delta}^{pd}\overline{p} - \frac{\omega^2\Gamma^2}{c_0^2}\overline{p} = -\frac{ikn(s\sigma)\Gamma^2\rho_0 c_0^2}{l^2\gamma}\Re \tag{5.2}$$

This equation is multiplied by a weighting function w^w and integrated over the volume. The volume integral can be split up in an integration over $\overline{A}^{cd}$ and $\overline{A}^{pd}$. For layer geometries $\overline{A}^{cd}$ is the thickness of the layer and $\overline{A}^{pd}$ is the total area of the squeezing surfaces. For tube geometries, $\overline{A}^{cd}$ is the cross-sectional area of the tube and $\overline{A}^{pd}$ is the axial direction. This means that, depending on the type of geometry, integration over $\overline{A}^{cd}$ (layers) or $\overline{A}^{pd}$ (tubes) actually is a line integration. In Appendix B a more detailed description is given for each geometry.

$$\int_{\overline{A}^{cd}} \int_{\overline{A}^{pd}} w^w \left[\overline{\Delta}^{pd} \overline{p} - \frac{\omega^2 \Gamma^2}{c_0^2} \overline{p} + \frac{ikn(s\sigma)\Gamma^2 \rho_0 c_0^2}{l^2 \gamma} \Re \right] d\overline{A}^{pd} d\overline{A}^{cd} = 0 \tag{5.3}$$

The integrand is not a function of the *cd*-co-ordinates. The integration over $\overline{A}^{cd}$ is carried out to enable coupling between elements with different cross-sectional areas and to enable coupling with standard acoustic finite elements, see section 5.3. Using Green's theorem and partial integration:

$$\begin{aligned} & \overline{A}^{cd} \int_{\partial \overline{A}^{pd}} w^w \overline{\nabla}^{pd} \overline{p} \cdot \boldsymbol{e}_n \; d\partial \overline{A}^{pd} - \overline{A}^{cd} \int_{\overline{A}^{pd}} \overline{\nabla}^{pd} w^w \cdot \overline{\nabla}^{pd} \overline{p} \; d\overline{A}^{pd} + \\ - \; & \frac{\omega^2 \Gamma^2}{c_0^2} \overline{A}^{cd} \int_{\overline{A}^{pd}} w^w \overline{p} \; d\overline{A}^{pd} + \\ + \; & \frac{ikn(s\sigma)\Gamma^2 \rho_0 c_0^2}{\gamma l^2} \overline{A}^{cd} \int_{\overline{A}^{pd}} w^w \Re \; d\overline{A}^{pd} = 0 \end{aligned} \tag{5.4}$$

where $\partial \overline{A}^{pd}$ is the boundary of $\overline{A}^{pd}$. Inserting the expression for $\Re$, see expression (2.29), and relating the acoustic velocity $\boldsymbol{v}$ on the interface to the structural displacement $\overline{\boldsymbol{u}}_s$, ($\boldsymbol{v} = \frac{i\omega}{c_0} \overline{\boldsymbol{u}}^s$), gives:

$$\begin{aligned} & \overline{A}^{cd} \int_{\partial \overline{A}^{pd}} w^w \overline{\nabla}^{pd} \overline{p} \cdot \boldsymbol{e}_n \; d\partial \overline{A}^{pd} - \overline{A}^{cd} \int_{\overline{A}^{pd}} \overline{\nabla}^{pd} w^w \cdot \overline{\nabla}^{pd} \overline{p} \; d\overline{A}^{pd} + \\ - \; & \frac{\omega^2 \Gamma^2}{c_0^2} \overline{A}^{cd} \int_{\overline{A}^{pd}} w^w \overline{p} \; d\overline{A}^{pd} + \\ - \; & \frac{\rho_0 \omega^2 n(s\sigma)\Gamma^2}{\gamma l} \frac{\overline{A}^{cd}}{A^{cd}} \int_{\overline{A}^{pd}} \int_{\partial A^{cd}} w^w \overline{\boldsymbol{u}}_s \cdot \boldsymbol{e}_n \; d\partial A^{cd} \; d\overline{A}^{pd} = 0 \end{aligned} \tag{5.5}$$

The pressure in each element is expressed in terms of the interpolation functions $[N^a]$ and the nodal pressures $\{P\}$. The structural displacement is also written in terms of interpolation functions:

$$\overline{p} = [N^a] \{P\} \quad ; \quad \overline{\boldsymbol{u}}^s = [N^s] \{U\} \tag{5.6}$$

Following Galerkin's approach, the weighting functions are chosen equal to the interpolation functions. For an acoustic hard wall, the normal derivative

of the pressure is zero. In the case of a prescribed pressure the weighting function is chosen equal to zero. The first term only contributes for an impedance-like boundary condition. However, one has to bear in mind that the pressure is constant across the gap width or cross section, while the in-plane velocities (layer geometry) or the axial velocity (tube geometry) vary. An impedance can therefore only be defined in an integrated sense. The term with the normal derivative of the pressure is set equal to zero in the present study. This finally leads to the following set of equations:

$$-\omega^2 \left[M^a(s)\right] \{P\} + \left[K^a\right] \{P\} = \omega^2 \left[M^c(s)\right] \{U\} \tag{5.7}$$

where $[M^a\,(s)]$ denotes the acoustic mass matrix, $[K^a]$ is the acoustic stiffness matrix, $\{P\}$ is the vector with the nodal pressure degrees of freedom, $\{U\}$ is the vector with the nodal structural degrees of freedom and $[M^c\,(s)]$ is the coupling matrix. Their elements are given by:

$$\left[M^a\,(s)\right] = -\frac{\Gamma^2}{c_0^2} \overline{A}^{cd} \int_{\overline{A}^{pd}} \left[N^a\right]^T \cdot \left[N^a\right] \; d\overline{A}^{pd} \tag{5.8}$$

$$\left[K^a\right] = \overline{A}^{cd} \int_{\overline{A}^{pd}} \left[\overline{\boldsymbol{\nabla}}^{pd} N^a\right]^T \cdot \left[\overline{\boldsymbol{\nabla}}^{pd} N^a\right] \; d\overline{A}^{pd} \tag{5.9}$$

$$\left[M^c\,(s)\right] = -\frac{\rho_0 n(s\sigma)\Gamma^2}{\gamma l} \frac{\overline{A}^{cd}}{A^{cd}} \int_{\overline{A}^{pd}} \int_{\partial A^{cd}} \left[N^a\right]^T \cdot \left[\boldsymbol{e}_n \cdot N^s\right] \; d\partial A^{cd} \; d\overline{A}^{pd} \tag{5.10}$$

Because the propagation constant Γ is complex and depends on the shear wave number, the acoustic mass matrix is also complex and shear wave number, *e.g.* frequency, dependent. In fact, the mass matrix is equal to the corresponding standard acoustic mass matrix, only it is premultiplied by $-\Gamma^2/c_0^2$ instead of $1/c_0^2$. The finite element model for the structure, in the absence of structural damping, can be written in the following standard formulation:

$$-\omega^2 \left[M^s\right] \{U\} + \left[K^s\right] \{U\} = \left[K^c\right] \{P\} + \left\{F^{ext}\right\} \tag{5.11}$$

where $[M^s]$ denotes the structural mass matrix, $[K^s]$ is the stiffness matrix, $[K^c]$ is the coupling matrix resulting from the pressure on the interface and $\{F^{ext}\}$ is the external nodal force vector. The principle of virtual work gives the following expression for the coupling matrix $[K^c]$:

$$\left[K^c\,(s)\right] = \frac{\partial \overline{A}^{cd}}{\partial A^{cd}} \int_{\overline{A}^{pd}} \int_{\partial A^{cd}} \left[\boldsymbol{e}_n \cdot N^s\right]^T \cdot \left[N^a\right] \; d\partial A^{cd} \; d\overline{A}^{pd} \tag{5.12}$$

The acousto-elastic interaction is established by demanding continuity of normal velocity across the interface. This now gives the following coupled

system of equations:

$$-\omega^2 \begin{bmatrix} [M^s] & [0] \\ [M^c(s)] & [M^a(s)] \end{bmatrix} \begin{Bmatrix} \{U\} \\ \{P\} \end{Bmatrix} + \begin{bmatrix} [K^s] & -[K^c] \\ [0] & [K^a] \end{bmatrix} \begin{Bmatrix} \{U\} \\ \{P\} \end{Bmatrix} = \begin{Bmatrix} \{F^{ext}\} \\ \{0\} \end{Bmatrix} \tag{5.13}$$

This system contains the mass matrices and the stiffness matrices of the structural part and the acoustic part. The coupling is established by the two coupling matrices, $[M^c(s)]$ and $[K^c]$, which are related as:

$$[M^c(s)] = -\frac{\rho_0 n(s\sigma)\Gamma^2}{\gamma l} \frac{\partial A^{cd}}{\partial \overline{A}^{cd}} \frac{\overline{A}^{cd}}{A^{cd}} [K^c]^T \tag{5.14}$$

The coupling matrix $[K^c]$ is equal to the standard acoustic coupling matrix for this situation. The matrix $[M^c(s)]$ only differs from the standard coupling matrix due to the premultiplication factor.

5.2.1 Eigenfrequency calculations

The coupled system of equations is complex and asymmetric. Some of the matrices involved are shear wave number, *e.g.* frequency, dependent. Because an eigenvalue solver for complex, asymmetric and frequency dependent matrices was not yet available, an iterative approach was adopted [83]. The iterative process starts with a first estimate of the expected eigenfrequency. The acoustic matrices were calculated and the coupled system was assembled. For this system of equations, the eigenfrequencies were calculated. A solver for complex, asymmetric eigenvalue problems was used in this step. This solver was implemented in B2000 by Grooteman [84]. The eigenfrequency closest to the expected frequency (in an absolute sense since they are complex numbers) was used to construct the matrices for the second iteration step. This process was then repeated. In order for the process to converge, a good first estimate was required. In the present investigation the acousto-elastic coupling was investigated by varying the gap width (see section 5.4.5). The first calculation was carried out for a large gap width. For this gap width the damping was very low and the eigenfrequencies could be estimated by simple wave equation and plate models. Successive calculations were carried out for decreasing gap widths. The value that had already been obtained for a slightly larger gap width was used as a first estimate of the eigenfrequency. In this way a good initial value of the complex eigenfrequency could be provided.

5.2.2 Frequency response calculations

A frequency response calculation can be carried out by solving the coupled set of equations (5.13) for a given excitation and frequency. The frequency dependence of the matrices complicates such a frequency response calculation. However, the special structure of the matrices allows for a very straightforward and elegant way of reducing the computational efforts: component mode synthesis. The coupled viscothermal response can be expressed in terms of the uncoupled inviscid, adiabatic acoustic modes and the uncoupled structural modes. Consider the acousto-elastic model for the *inviscid*, *adiabatic* case:

$$-\omega^2 \begin{bmatrix} [M^s] & [0] \\ \left[\widetilde{M}^c\right] & \left[\widetilde{M}^a\right] \end{bmatrix} \begin{Bmatrix} \{U\} \\ \{P\} \end{Bmatrix} + \begin{bmatrix} [K^s] & -[K^c] \\ [0] & [K^a] \end{bmatrix} \begin{Bmatrix} \{U\} \\ \{P\} \end{Bmatrix} = \begin{Bmatrix} \{F^{ext}\} \\ \{0\} \end{Bmatrix} \tag{5.15}$$

where $\left[\widetilde{M}^c\right]$ and $\left[\widetilde{M}^a\right]$ are the matrices for the inviscid, adiabatic case. These matrices are obtained by simply setting $\Gamma = i$ and $n(s\sigma) = \gamma$ in the expressions for the low reduced frequency model. The uncoupled acoustic modes for this situation are calculated from ($\left[\widetilde{K}^a\right] = [K^a]$):

$$-\omega^2 \left[\widetilde{M}^a(s)\right] \{P\} + [K^a] \{P\} = 0 \tag{5.16}$$

The eigenmodes are stored (columnwise) in the matrix $\left[\widetilde{\Phi}^a\right]$ and the acoustic eigenvalues, *i.e.* the squares of the angular frequencies, are stored in the matrix $\left[\widetilde{\Omega}^a\right]$. The modes are normalized with respect to the acoustic mass matrix:

$$\left[\widetilde{\Phi}^a\right]^T \left[\widetilde{M}^a\right] \left[\widetilde{\Phi}^a\right] = [I] \quad ; \quad \left[\widetilde{\Phi}^a\right]^T [K^a] \left[\widetilde{\Phi}^a\right] = \left[\widetilde{\Omega}^a\right] \tag{5.17}$$

Calculation of the acoustic eigenmodes and eigenfrequencies is very straightforward and efficient. For layer geometries the problem is 2-dimensional, while for tube geometries the problem is only 1-dimensional. All matrices involved are real valued. The uncoupled structural modes are obtained from:

$$-\omega^2 [M^s] \{U\} + [K^s] \{U\} = 0 \tag{5.18}$$

The structural eigenmodes are stored (columnwise) in the matrix $[\Phi^s]$ and the structural eigenvalues, *i.e.* the squares of the angular frequencies, are stored in the matrix $[\Omega^s]$. The modes are normalized with respect to the structural mass matrix:

$$[\Phi^s]^T [M^s] [\Phi^s] = [I] \quad ; \quad [\Phi^s]^T [K^s] [\Phi^s] = [\Omega^s] \tag{5.19}$$

Now consider the viscothermal acousto-elastic problem. The coupled viscothermal response is expressed in terms of uncoupled acoustic modes, $\left[\widetilde{\Phi}^a\right]$, and structural modes, $[\Phi^s]$:

$$\begin{aligned} \{U\} &= [\Phi^s]\,\{\eta^s\} \\ \{P\} &= \left[\widetilde{\Phi}^a\right]\{\eta^a\} \end{aligned} \tag{5.20}$$

Inserting these expressions into the acousto-elastic model, premultiplying the structural part by $[\Phi^s]^T$ and the acoustic part by $\left[\widetilde{\Phi}^a\right]^T$, finally gives:

$$-\omega^2 \begin{bmatrix} [I] & [0] \\ \left[\widehat{M}^c(s)\right] & -\Gamma^2\,[I] \end{bmatrix} \begin{Bmatrix} \{\eta^s\} \\ \{\eta^a\} \end{Bmatrix} + \begin{bmatrix} [\Omega^s] & \left[\widehat{K}^c\right] \\ [0] & \left[\widetilde{\Omega}^a\right] \end{bmatrix} \begin{Bmatrix} \{\eta^s\} \\ \{\eta^a\} \end{Bmatrix} = \begin{Bmatrix} \left\{\widehat{F}^{ext}\right\} \\ \{0\} \end{Bmatrix} \tag{5.21}$$

where:

$$\begin{aligned} \left[\widehat{M}^c(s)\right] &= -\frac{n(s\sigma)\Gamma^2}{\gamma}\left[\widetilde{\Phi}^a\right]^T\left[\widetilde{M}^c\right][\Phi^s] \\ \left[\widehat{K}^c\right] &= -\left[\Phi^s\right]^T[K^c]\left[\widetilde{\Phi}^a\right] \\ \left\{\widehat{F}^{ext}\right\} &= [\Phi^s]^T\left\{F^{ext}\right\} \end{aligned} \tag{5.22}$$

The response of the viscothermal model can thus be expressed in terms of the uncoupled structural modes and the uncoupled inviscid, adiabatic acoustic modes. Once these modes are calculated, the viscothermal response can be determined with this component mode approach. The complex and frequency dependent premultiplication factors will include viscous and thermal effects in the analysis. The number of participation factors in $\{\eta^s\}$ and $\{\eta^s\}$ is usually much smaller than the number of degrees of freedom in $\{U\}$ and $\{P\}$. The component mode technique thus offers an attractive way to calculate the viscothermal acousto-elastic response.

5.3 Implementation in B2000

The finite element models were implemented in the package B2000 [85], a transparent finite element program in which new code and elements can be implemented in an easy way. Several structural elements are available in the standard version of B2000. A large number of extra features were added by the National Aerospace Laboratories NLR. Standard acoustic finite elements and interface elements for instance were implemented in B2000 by Grooteman [84]. These interface elements will be used in the present analysis to establish the coupling between the viscothermal layer elements and the standard structural elements.

5.3.1 Layer elements

Linear 4-noded (Q4.VISC) and quadratic 8-noded layer elements (Q8.VISC) were implemented. The viscothermal elements are equipped with a number of key options which can be used to activate or deactivate for instance viscosity or thermal conductivity. The elements can thus degenerate to modified wave equation elements or elements for the linearized Reynolds equation.

5.3.2 Tube elements

Linear 2-noded (T2.VISC) and quadratic 3-noded tube elements (T3.VISC) were implemented. The viscothermal tube elements are also equipped with a number of key options to control viscous and thermal effects. The elements can have a rectangular or a circular cross section.

If one is interested in the viscothermal acoustic response of a tube system, the finite element approach is not very efficient. Since the tube problem is only a 1-dimensional problem, the transfer function for a given tube geometry can easily be obtained. By assuming continuity of pressure and conservation of mass on the connections between tubes, the behaviour of more complicated systems can be calculated analytically. Even for acousto-elastic problems an analytical, transfer matrix based approach is usually the most efficient.

The finite element model is of use in the general case when the acousto-elastic interaction between a viscothermal gas and a structure of arbitrary shape has to be calculated. The finite element model can for instance be used to describe the behaviour of a flexible material with pores of tubular shape. The present study mainly focusses on thin gas layers. Interface elements for tube geometries were not implemented in B2000 within the framework of the present study.

5.3.3 Convergence tests

The implemented elements were validated by comparing the results to analytical results for a number of test cases. The convergence as a function of the number of elements was investigated. The configurations for the test cases are illustrated in Figure 5.1.

Eigenfrequency calculations and frequency response calculations were carried out for a rectangular layer of Q4.VISC and a layer of Q8.VISC elements. In order to investigate the coupling of elements with different layer thicknesses, eigenfrequency calculations were carried out for a line of elements with a stepwise varying layer thickness (indicated by layer 1 and layer 2 in

the Figure). Finally, the viscothermal elements were coupled to standard acoustic finite elements (HE8.ACOU and HE20.ACOU).

Eigenfrequency calculations were carried out for T2.VISC and T3.VISC elements. Furthermore, elements with different cross sections were coupled (indicated by area 1 and area 2 in the Figure). Finally, the coupling with standard acoustic finite elements was investigated.

A more detailed description of the test cases, the analytical solutions and the finite element results is presented in Appendix E. For all the tests the numerical values converged to the analytical values in the proper way. It can be concluded that the finite elements were functioning correctly.

5.4 Experimental validation

5.4.1 Experimental setup

To validate the viscothermal model including acousto-elastic interaction, experiments were carried out on an airtight box with a flexible coverplate (see Figure 5.2). This experiment was described in a paper by Dowell, Gorman and Smith [86]. Their analysis however concerned large gap widths and did not include viscothermal effects. The setup is very simple and useful to illustrate the different mechanisms at work.

The coverplate is an aluminium plate, 0.49 x 0.245 m^2, with a thickness of 1 mm. The plate is clamped at the edges. The box itself is also made of aluminium to avoid unwanted effects due to differences in thermal expansion of the materials. The gap width, $2h_0$, can be varied between 1 and 50 mm by displacement of the bottom. The material and geometrical properties of the aluminium plate are:

$$\begin{aligned} E_p = 70 \cdot 10^9 \text{ N/m}^2 \quad &; \quad \rho_p = 2710 \text{ kg/m}^3 \\ \nu_p = 0.3 \quad &; \quad t_p = 1 \text{ mm} \end{aligned} \tag{5.23}$$

The properties of the air in the gap under standard atmospheric conditions were given in expression (4.19). The plate is excited by an electrodynamic shaker with a random signal in the frequency range up to 512 Hz. The point of excitation was chosen in such a way that it did not coincide with a node of one of the eigenmodes in this frequency range. The input force was measured with a force transducer. One accelerometer was mounted on the bottom and a number of accelerometers was mounted on the plate to measure the response of the system. All signals were amplified and led to a front end. The data was transferred to a workstation where a modal analysis was

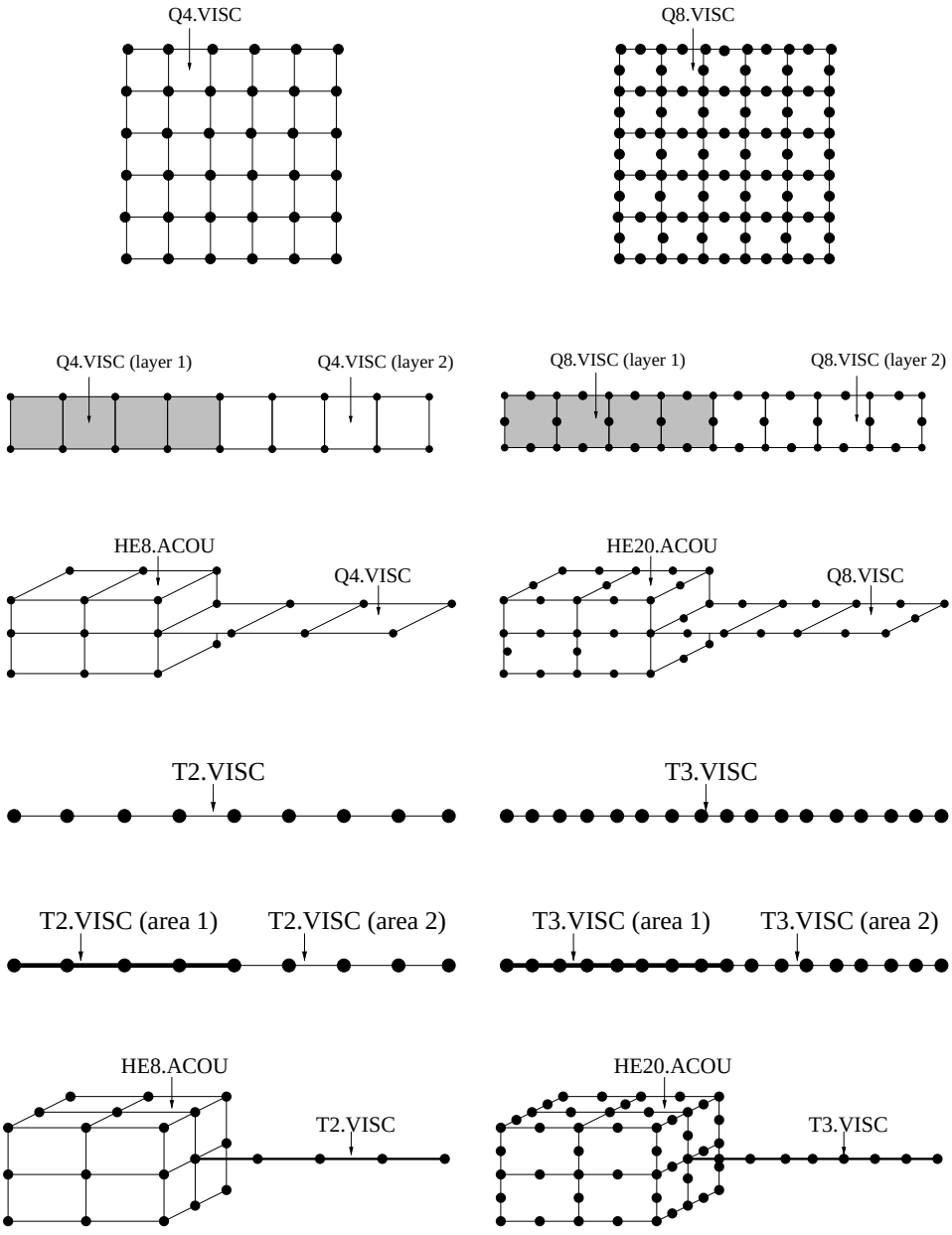

Figure 5.1: Configurations for convergence tests

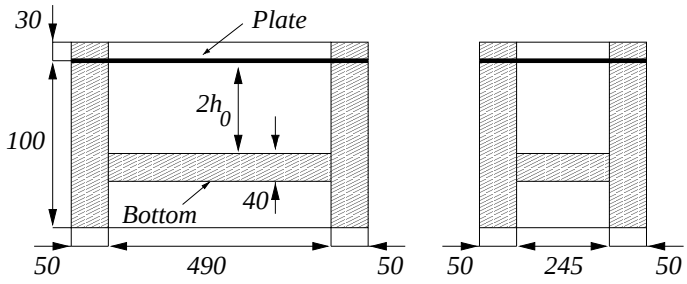

Figure 5.2: Airtight box with flexible coverplate; dimensions in mm

conducted: eigenfrequencies, damping and the mode shapes were determined for a number of gap widths.

5.4.2 Accuracy of the experiments

Eigenfrequencies in absence of the bottom

As a first check of the model, the eigenfrequencies of the plate in the absence of the bottom were measured. In this case one measures the eigenfrequencies of a clamped rectangular plate in an infinite air domain. The structural modes, *i.e.* the modes of the plate in vacuum, can be calculated analytically. In order to account for the influence of the surrounding air, an added mass was calculated according to the formula given by Blevins [87]. This small amount of added mass causes a small decrease in eigenfrequency. The calculated (in air and vacuum) and measured frequencies are listed in Table 5.1. In this Table 'qr' represents the number of half wavelengths in the x- and the y-direction respectively. There is fair agreement between the calculations and the experiments. A further discussion on the structural modes will be presented in section 5.4.4.

Damping in the absence of the bottom plate

The damping of the plate in the absence of the bottom plate was measured and found to be of the order of magnitude of 0.7% for the first seven modes. This damping is relatively high compared to common structural damping levels. However, in the present setup damping was also introduced by means of clamping and acoustic radiation. In order to gain insight in these phenomena, a simple experiment was carried out. The eigenfrequencies and damping values of the free plate in an infinite air domain were measured. Due to the fact that there is no clamping in this case, the modal behaviour of the plate

Mode	Eigenfrequency (Hz)		
qr	Measurements	Analytical (air)	Analytical (vacuum)
11	96.2	95.9	100.6
21	130.1	130.4	130.4
31	181.8	182.6	183.4
12	247.4	261.7	261.7
41	253.8	259.7	259.7
22	280.8	291.2	291.2
32	322.6	341.0	341.0

Table 5.1: Eigenfrequencies of clamped plate in air

will change. However, an impression of the order of magnitude of the radiation damping at least can be obtained. The experimentally determined frequencies showed good agreement with finite element results. The damping for the first seven modes varied between 0.2 and 0.7%. The clamping of the plate does seem to have only a small influence. If one assumes that the radiation damping is relatively low, which was comfirmed by several calculations, the measured damping can be attributed to structural damping. Compared to the viscothermal damping levels that were measured for low gap widths, however, the structural damping and the damping due to acoustic radiation can be neglected.

Boundary conditions

Attention was paid to the clamping conditions of the plate. The experimental results in Table 5.1 showed fair agreement with the calculations. In the experiments the bolts were securely fastened. In order to determine the influence of the torque, measurements were carried out for small variations in the torque. No variations in frequencies were observed due to a change in applied torque.

Linearity

In the experiments the plate was excited with a constant force. In order to check whether the system was behaving in a linear way, experiments were carried out with different excitation levels. The eigenfrequencies and the

damping values were not affected by the amplitude of excitation. This justifies the use of linear theory.

Motion of the bottom plate

In the calculations it was assumed that the box and the bottom plate were rigid and fixed. Since the gap width is a very important parameter in the model, the motion of the bottom plate was measured with accelerometers for a number of gap widths. In all cases the amplitude of the bottom plate was very low, *i.e.* less than 3% of the amplitude of the flexible coverplate. The bottom plate was therefore regarded as rigid and fixed.

Variation of the gap width

In the experiments the gap width was varied from 1 to 50 mm. Due to the fact that the thick bottom plate was not able to tilt inside the box, the in-plane variation in the gap width was small.

5.4.3 Acoustic modes

The acoustic modes are the modes of the air layer when the plate is assumed rigid and fixed (zero velocity). The acoustic modes are calculated from the low reduced frequency model by omitting the squeeze term:

$$\frac{\partial^2 \overline{p}}{\partial \overline{x}^2} + \frac{\partial^2 \overline{p}}{\partial \overline{y}^2} - \frac{\omega^2 \Gamma^2}{c_0^2} \overline{p} = 0 \tag{5.24}$$

The edges of the air layer are closed. The corresponding boundary condition is that the particle velocity is zero. The low reduced frequency model gives the following boundary condition in terms of the pressure:

$$\frac{\partial \overline{p}}{\partial \overline{n}} = 0 \quad \text{for } \overline{x} = \pm l_x \text{ and } \overline{y} = \pm l_y \tag{5.25}$$

where $\overline{n}$ is the outward normal. Straightforward separation of variables gives an equation for the acoustic eigenfrequencies:

$$\omega = \frac{i\pi c_0}{2\Gamma} \sqrt{\left(\frac{q}{l_x}\right)^2 + \left(\frac{r}{l_y}\right)^2} \quad q = 0, 1, 2 \cdots \quad r = 0, 1, 2 \cdots \tag{5.26}$$

Since the propagation constant Γ is a function of the shear wave number the right hand side of (5.26) depends on the frequency and the gap width. The complex eigenfrequencies can now be solved from this equation by a simple

iterative solving procedure. As starting values, the eigenfrequencies for the inviscid, adiabatic case were used: $\Gamma = i$. In Table 5.2 the analytical results and the results from finite element calculations are listed for a gap width of 1 mm. The calculations were carried out with 20 x 20 linear viscous acoustic finite elements. The table shows good agreement between the analytical results and the finite element results. The eigenfrequency of the first acoustic mode without viscous or thermal effects is 347 Hz. For low shear wave numbers the viscous and thermal effects therefore have a significant influence on the propagation of waves in the air layer.

Mode	Eigenfrequency (Hz)	
qr	Analytical	Finite elements
10	317.1+32.3i	317.4+32.4i
01	651.4+44.8i	652.1+44.8i
20	651.4+44.8i	654.1+45.0i
11	730.9+47.2i	731.6+47.3i

Table 5.2: Eigenfrequencies of acoustic modes ($2h_0 = 1$ mm)

5.4.4 Structural modes

The eigenfrequencies of the plate in vacuum were calculated with a mesh of 20 x 20 linear plate elements and compared with analytical results. The results are listed in Table 5.3. The Table shows fair agreement between the numerical and the analytical results. For the higher modes the results show a small deviation due to the number of elements. The first seven mode shapes for the plate in vacuum are given in Figure 5.3. They serve as a reference when the mode shapes change as a function of the gap width.

5.4.5 Acousto-elastic modes

In the case of a thin plate backed by a cavity with air, the acousto-elastic coupling can be very strong. In this section this phenomenon will be demonstrated. For this purpose the first seven eigenfrequencies of the plate will be calculated as a function of the gap width. The eigenfrequencies, damping values and mode shapes are traced in the calculations for gap widths from 300 downto 1 mm. For gaps below 50 mm a comparison is made with the experimental results.

Mode	Eigenfrequency (Hz)	
qr	Analytical	Finite elements
11	100.6	100.9
21	130.4	131.1
31	183.4	186.9
12	261.7	266.1
41	259.7	270.8
22	291.2	295.2
32	341.0	346.8

Table 5.3: Eigenfrequencies of structural modes

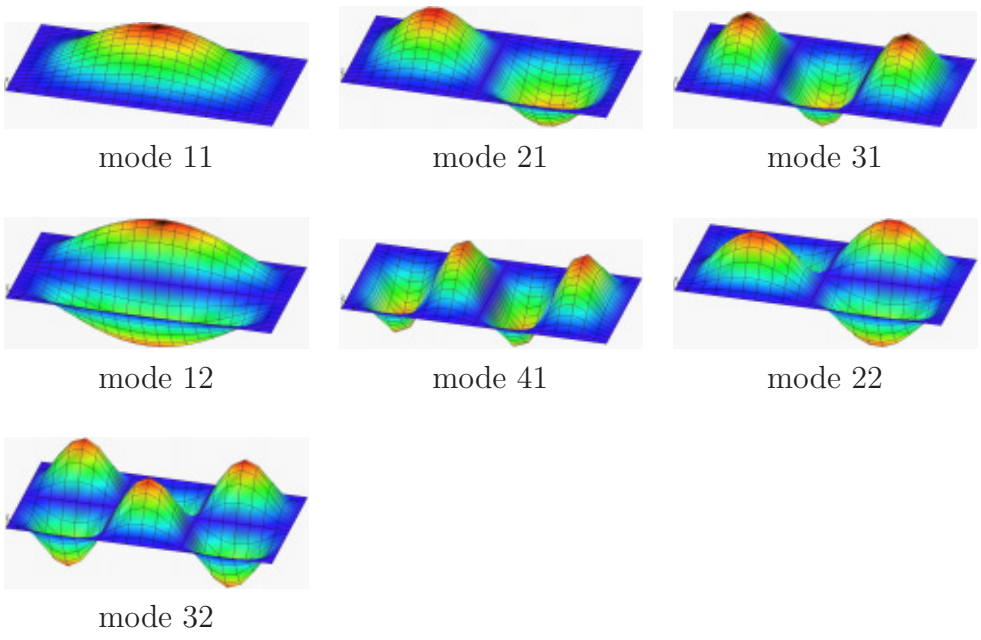

Figure 5.3: Structural modes

The mode shapes and the eigenfrequencies for a gap width of 300 mm are very close to the mode shapes and the eigenfrequencies in vacuum. When the gap width decreases, eigenfrequencies and mode shapes are strongly affected. By tracing the modes from 300 down to 1 mm, the complete evolution of the different modes can be visualized.

The choice for the first seven modes was based on the fact that these modes remain isolated. This means that these modes may show a shift in

frequency or even mutual cross-overs, but they remain isolated from the higher (i.e. 8th and higher) modes. The first acoustic eigenfrequency in the absence of viscous or thermal effects is 347 Hz (see section 5.4.3). Due to the viscous effects this frequency will decrease with decreasing gap width, but the structural frequencies are always lower. Hence, the first seven modes of interest are all structurally dominated modes.

In order to trace the modes from 300 down to 1 mm two types of calculations were carried out. The first type of calculation used standard acoustic finite elements without viscous or thermal effects. These elements were used for the calculations for gap widths between 50 and 300 mm. For these gap widths the shear wave number is very large in the frequency range of interest, so viscous and thermal effects can be neglected. Furthermore the assumption of constant pressure across the gap width breaks down for high reduced frequencies. Note that the damping for these elements is always zero. A mesh consisting of 20 x 20 plate elements, 20 x 20 linear interface elements and 20 x 20 x 6 acoustic finite elements was used.

The second type of calculation was based on the use of viscous acoustic finite elements. These elements were used for gap widths below 50 mm. A mesh consisting of 20 x 20 linear plate elements, 20 x 20 linear interface elements and 20 x 20 linear viscothermal acoustic finite elements was used to perform these calculations. As a check on the accuracy of the finite element model for the experimental setup, the uncoupled modes for the plate and the air layer were calculated and compared to analytical solutions in sections 5.4.3 and 5.4.5 respectively.

The influence of the air on the upper side of the plate is not taken into account in the calculations. In section 5.4.2 it was demonstrated that the air on the upper side of the panel causes a slight decrease in eigenfrequency. For low gap widths however this effect can be neglected compared to the shift in frequency due to the pressure in the layer. The air on the upper side introduces an energy loss due to radiation damping. However, in section 5.4.2 it was shown that the radiation damping and the structural damping are very low compared to the viscothermal damping for small gap widths.

Eigenfrequency

In Figure 5.4 the eigenfrequency is depicted versus the gap width [1]. The labels for the different modes are based on the original modes in vacuum (see Table 5.3). The experimental results and the finite element results show fair agreement. For the lower modes the results are very good. For the higher

[1]The eigenvalue calculation results in complex valued angular frequencies: $\omega = \omega_r + i\omega_i$. For viscous damping the undamped natural frequency is then calculated from: $\omega_n = |\omega|$

modes the finite element results start to be less accurate. This can mainly be attributed to the behaviour of the plate elements, as can be seen in the results for the structural modes. But in general the agreement is satisfying for all modes under consideration. At a gap width of 50 mm the transition from the results with standard acoustic elements to the results with viscous finite elements is good. There seems to be a slight bend in the curve, but the difference in frequency between both calculations is less than 0.7% for this gap width.

The Figure shows a very large shift in eigenfrequency for the different modes. The coupled eigenfrequencies differ considerably from the uncoupled structural eigenfrequencies. This means that in the case of narrow gaps it is essential to take into account the acousto-elastic coupling. Different kinds of behaviour can be observed. The second mode, for instance, shows a steady decrease with decreasing gap width. The first mode however first increases and then decreases with decreasing gap width. At a gap width of about 100 mm the eigenfrequencies cross. In order to analyse this in more detail, several calculations were carried out in this region. The results clearly indicate that there is indeed a cross-over. The 31 mode also exhibits cross-over behaviour with other modes. This was confirmed by the measurements.

Damping

In Figure 5.5 the dimensionless damping coefficient is depicted versus the gap width for the first and second modes [2]. For small gaps the damping increases by up to 25%. This high level of damping can be attributed to the viscous effects in the air layer. The second mode is an asymmetric mode that induces a strong pumping of air in the layer. The corresponding high rate of shear results in significant viscous losses. Thermal effects have a very small influence on the damping, as was already demonstrated by Fox and Whitton [67]. The structural damping and the damping due to acoustic radiation are low compared to the viscothermal damping mechanisms for small gap widths. The Figure shows fair agreement between calculations and experiments. This indicates that the energy dissipation in the layer is correctly described with the new finite element model.

The present investigation allows a detailed comparison between theory and experiments. Because of the systematic approach that was used to develop and validate the models, the different aspects can be addressed in detail. The specially developed experiments offer a good insight in the phenomena

[2] The eigenvalue calculation results in complex valued angular frequencies: $\omega = \omega_r + i\omega_i$. For viscous damping the dimensionless damping coefficient is then calculated from: $\xi = \frac{\omega_i}{|\omega|} \times 100\ \%$

and allow a qualitative and quantitative comparison with calculations. In the present test case with the closed box and a thin flexible plate the frequency shifts were substantial. Furthermore, the damping values were very high. The agreement between theory and experiment is good, even on a linear scale.

Mode shapes

The mode shapes were calculated and measured for a number of gap widths. In Figure 5.6 the calculated mode shapes are depicted for gap widths of 300, 50 and 10 mm. The labels of the modes in this Figure are based on the corresponding mode shapes in vacuum. The modes shapes are almost real; the phase differences between the displacements measured on different locations of the plate are very small. The Figures indicate that the shape of the asymmetric modes is not affected by the gap width. The symmetric modes however show a dramatic change in shape. For small gaps, the 11 mode starts to resemble the 31 mode. A physical interpretation for these phenomena will be given in the next section.

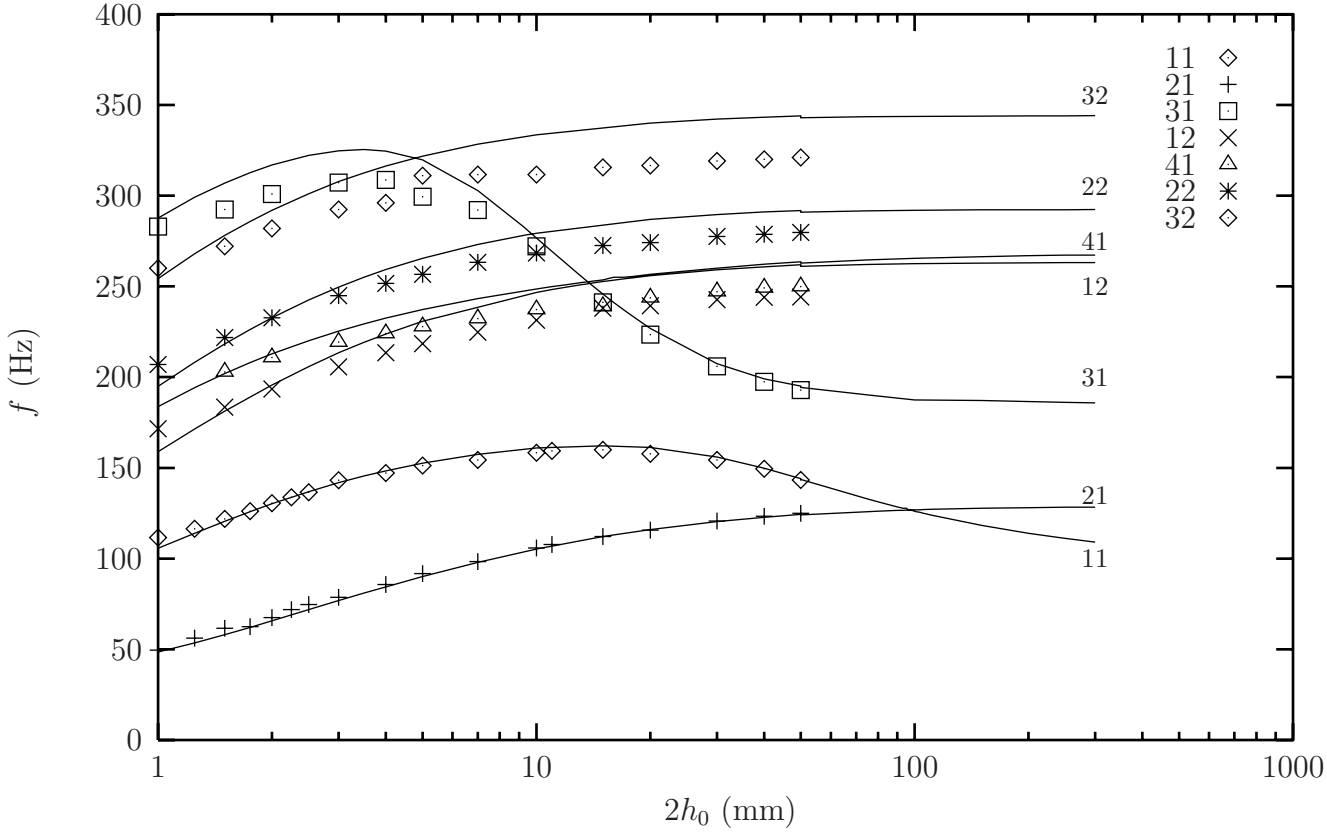

Figure 5.4: Calculated and measured eigenfrequencies. (—): calculations, (◇,+,□,×,△,∗,◇): experiments

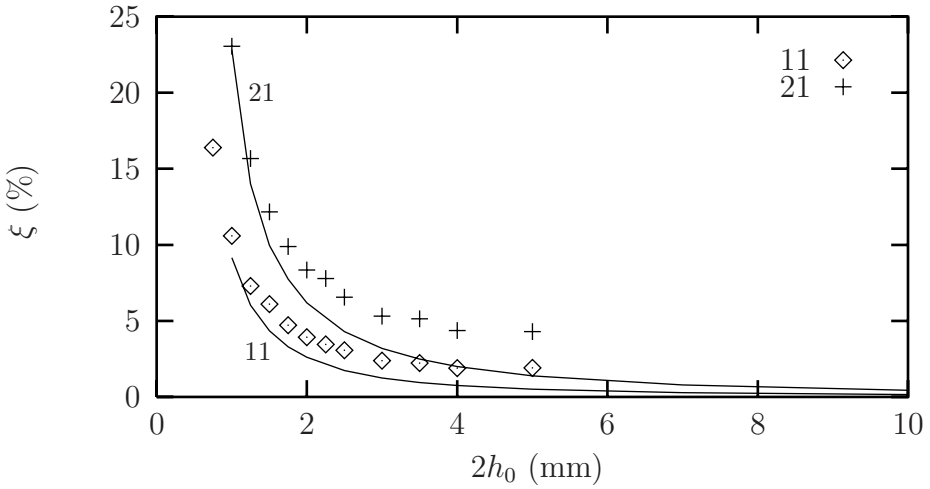

Figure 5.5: Dimensionless damping coefficient versus gap width. (—): calculations, (◇,+): experiments

5.4.6 Physical interpretation

The shifts in eigenfrequency and the changes in mode shape can be explained in terms of (generalized) added mass and (generalized) added stiffness.

Added mass

Due to the squeeze motion of the plate the air is put into motion. This motion of the air is experienced by the plate as an added mass. For the closed cavity, the motion of the air is related to the pumping mechanism. For asymmetric modes, the air is pumped back and forth very efficiently. This pumping effect increases as the gap width decreases. Therefore the added mass increases and the frequency decreases with decreasing gap width.

Added stiffness

The increase in frequency that was observed for some modes can be attributed to an added stiffness effect. For the symmetric modes, the deformation of the coverplate is accompanied by a significant change in cavity volume (see Figure 5.7). This change in volume causes a pressure disturbance in the cavity. In the frequency range of interest, the acoustic wavelength is large compared to the cavity dimensions. Since the pressure disturbance is in phase with the motion of the plate, the plate experiences an added stiffness effect. As the pressure disturbance increases with decreasing gap width, the

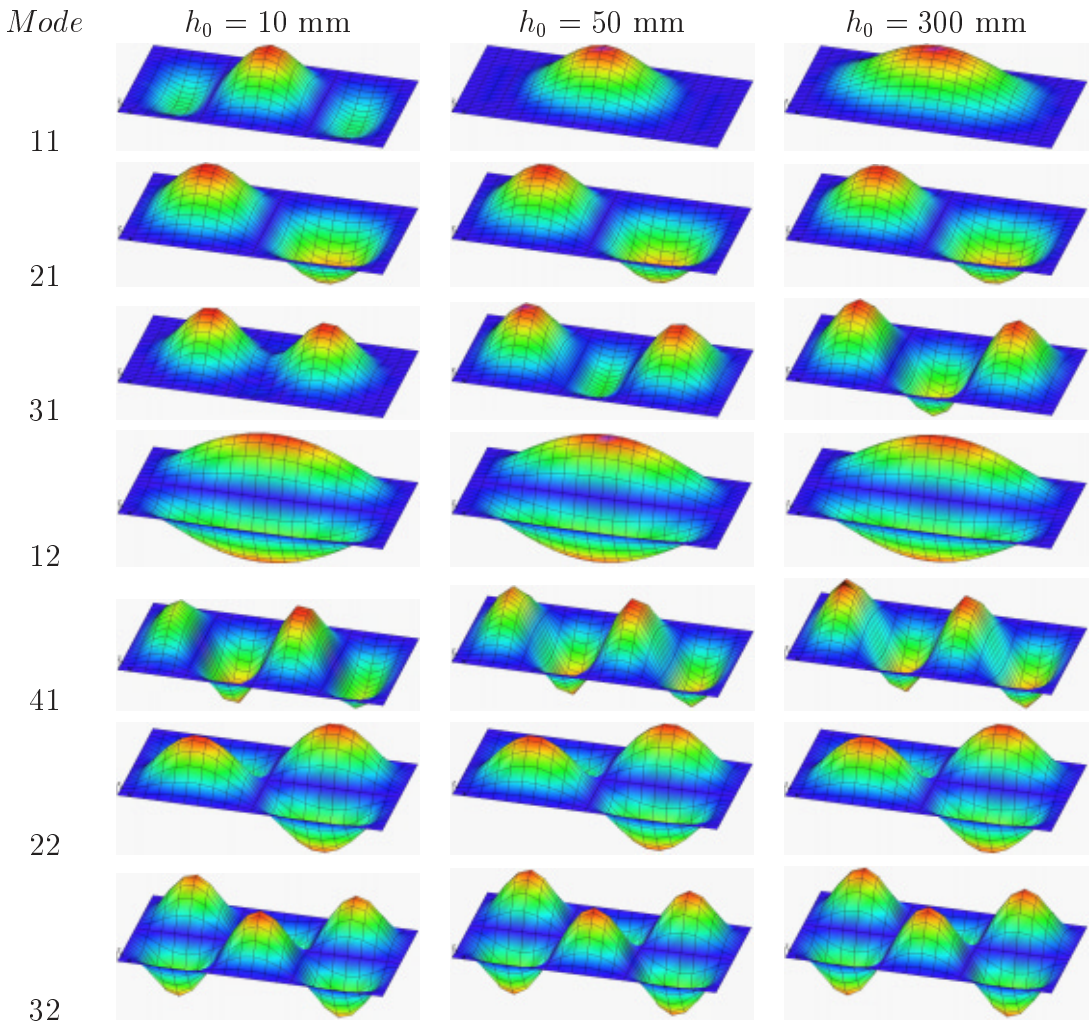

Figure 5.6: Acousto-elastic modes shapes

eigenfrequency will increase. Asymmetric modes do not induce a change in cavity volume: they do not experience an added stiffness effect. Due to the stiffness effect the shape of the symmetric modes also changes. The general trend is that mode shapes tend to a shape for narrow gaps for which the net volume change is zero (see Figure 5.6). This means that the added stiffness effect will vanish, and the added mass effect takes over (see Figure 5.4). This explains the shape of the curves of the eigenfrequencies versus the gap width.

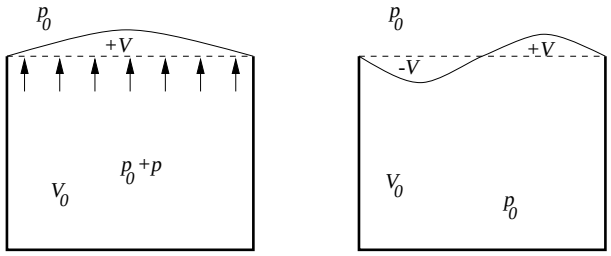

Figure 5.7: Change in cavity volume for the first and the second mode

5.4.7 Dimensionless parameters

The dimensionless parameters are a function of the geometry, the material properties and the frequency. In the experimental setup the gap width is varied from 50 down to 1 mm, while the frequency varies between 50 and 350 Hz.

The ratio between the inertial forces and the viscous forces is given by the shear wave number. For the experimental setup, the shear wave number varies from 4.5 to 600. This means that for small gap widths and low frequencies the effects of viscosity have to be taken into account. In the frequency range of interest, the effects of viscosity are very small for gap widths larger than 50 mm. The use of standard acoustic elements is therefore justified for these larger gap widths.

For low values of the shear wave number, as σ is a constant for air, the thermal conductivity can play an important role. For the experimental setup these thermal effects are relatively small. However, one has to be careful not to generalize this statement. For very small gap widths or other materials for instance the effects can be very significant. Then the process in the layer has to be regarded as isothermal, rather than isentropic.

In the low reduced frequency theory the acoustic wavelength must be large compared to both the gap width and the boundary layer thickness. For the experimental setup and gap widths smaller than 50 mm: $k < 0.3$ and $k/s < 10^{-3}$. This means that the use of the low reduced frequency model is justified for small gap widths.

5.5 Conclusions

Based on the research presented in this chapter, the following conclusions can be drawn:

- new viscothermal finite elements were developed, based on the low reduced frequency model. Layer elements and tube elements were implemented in the finite element package B2000;
- viscothermal elements with different cross sections or layer thicknesses can be coupled. The viscothermal elements can also be coupled to standard acoustic finite elements;
- the viscothermal layer elements can be coupled to structural elements with the standard interface elements. The new acousto-elastic finite element model can be used to calculate the response of complex systems;
- convergence tests confirm that the elements function properly;
- eigenfrequency calculations for the frequency-dependent acousto-elastic system can be performed using an iterative approach;
- frequency response calculations can be performed efficiently with a straightforward component mode technique, using the structural modes and the acoustic modes for the inviscid, adiabatic case;
- experimental verification shows that the acousto-elastic interaction between a viscothermal air layer and a vibrating flexible plate is correctly described by the finite element model. The behaviour of the system is strongly affected by the presence of the air layer. Eigenfrequencies, damping values and mode shapes change as a function of the layer thickness. It is therefore important to include the acousto-elastic coupling;
- a significant amount of energy can be dissipated in the layer by means of viscous shear. This may result in substantial damping values for an adjacent structure. The amount of damping is related to the pumping effect in the layer and thus on the coupled vibration mode of the structure.

Chapter 6

Engineering applications

6.1 Solar panels during launch

During the launch of a spacecraft the solar panels are stowed alongside the structure (see Figure 6.1) [1].

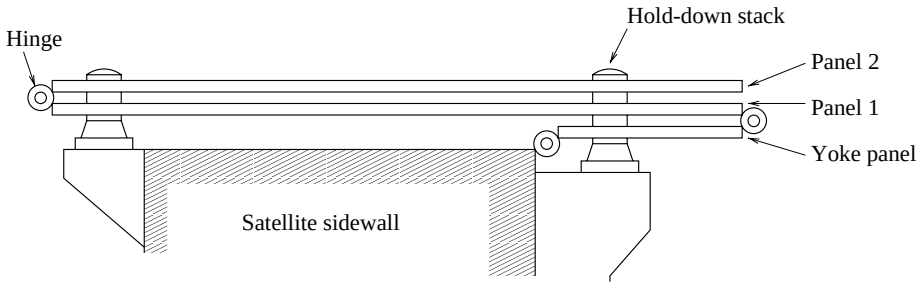

Figure 6.1: SOHO wing in stowed position, side view

The panels are connected by hinges and held together by spacers and hold-down brackets. In space, the array is deployed by cutting kevlar cables with a thermal knife. Springs inside the joints will then open the wing. The solar panels are relatively large, light and stiff. In Figure 6.2 a sketch is presented of a deployed solar array.

During the launch phase the spacecraft and the panels are exposed to severe vibrations. Any damage to the wing or the satellite can lead to critical failures. A structural failure may jeopardize the satellite mission. It is therefore important to have a good understanding of the behaviour and the characteristics of the folded pack of solar panels. Before a spacecraft is launched, several qualification tests are carried out to ensure that the panels

[1] SOHO= **SO**lar and **H**eliospheric **O**bservatory

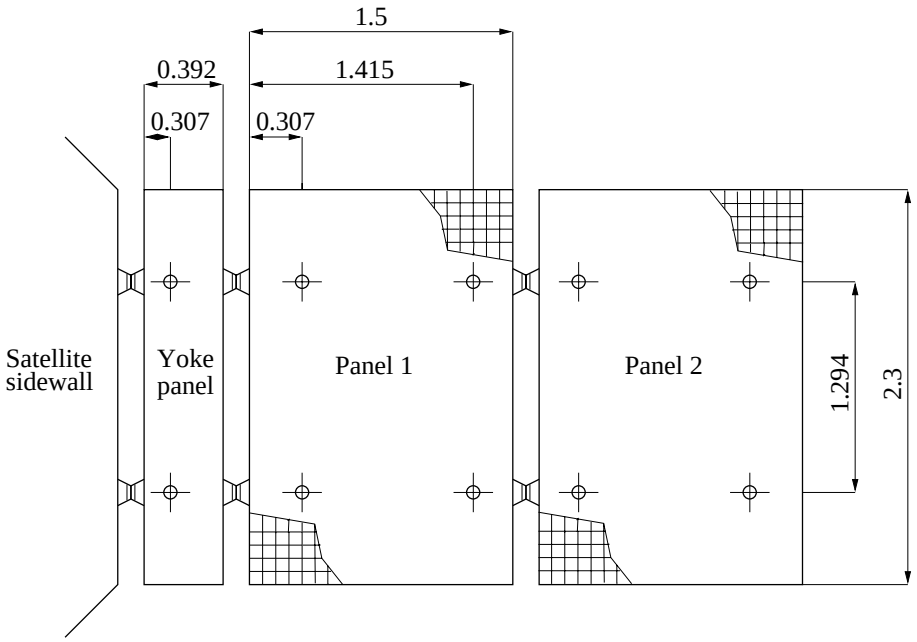

Figure 6.2: Deployed SOHO wing, top view, dimensions in m

can withstand the expected load. For this purpose, the stack of panels is attached to a vibration Table (see Figure 6.3).

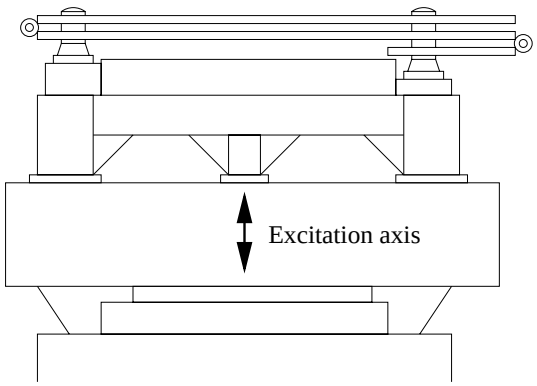

Figure 6.3: Test setup for z-axis excitation

Tests are usually carried out for out-of-plane (z-direction) and in-plane (x and y-directions) excitation. In the frequency range of interest, *e.g.* 5-100 Hz, a sine sweep vibration is performed. Eigenfrequencies, damping coefficients and acceleration, strain and force levels are measured. In addition, random vibration tests are carried out.

The vibration tests indicate that the thin layers of air that are trapped

between the panels have a significant influence on the dynamical behaviour of the system. In general the air layers cause a decrease in eigenfrequency. The influence of the surrounding air is small compared to the influence of the thin layers. Significant damping levels of 3 to 4% were measured in the experiments.

Standard finite element calculations can be carried out to compute the behaviour of such a structure in a vacuum. Several investigations deal with the modelling of the air influence on the behaviour of solar panels, see [88, 89, 90, 91, 92]. At Fokker Space a special finite element model was developed to describe the influence of the thin air layers [93]. However, in none of the aforementioned investigations viscothermal effects were accounted for. Since the problem concerns the behaviour of thin layers at low frequencies, the new numerical techniques were used in a preliminary study to describe the behaviour of a stack of solar panels. The results from the new viscothermal model in B2000 are compared to the results from a standard finite element technique in ANSYS, based on the wave equation.

6.1.1 Simple test problem

As a starting point, the "ARAFOM model 1" wing was used. A full ARAFOM wing consists of 4 panels, and has the following dimensions 2.25 x 2.736 x 0.022 m^3. The panel spacing for this type of solar array is 12 mm. Each panel consists of a honeycomb core with skin layers that are made up of several cross-ply layers. The panels contain local reinforcements around the hold-down points. For the present study the model is simplified by using a two-panel configuration and assuming isotropic and homogeneous material behaviour. Equivalent material properties were calculated for this purpose. The modelling of the hold-down elements and the spacers between the panels is important because they have a significant influence on the vibrational behaviour of the system. By introducing the aforementioned simplifications, one can concentrate on the modelling of the air. The test configuration is given in Figure 6.4. The material and geometrical properties of the panels, the spacers, the hold down elements and the brackets are given in Table 6.1, where E is Young's modulus, I is the area moment of inertia, J is the equivalent torsion constant and m' is the mass per unit length. The thickness of each panel is 0.022 m. In the model only the air layer between the panel is modelled. The influence of the surrounding air is neglected.

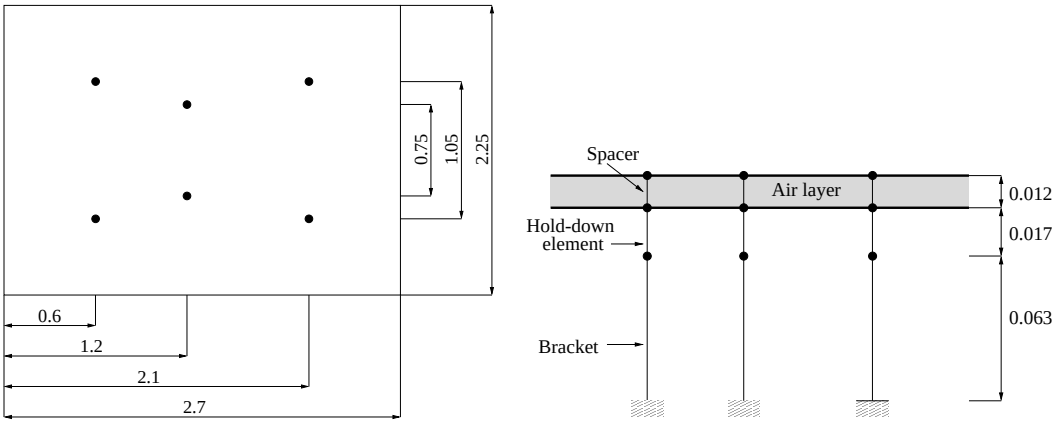

Figure 6.4: ARAFOM model problem, top view (left), front view (right), dimensions in m, panel thickness is 0.022 m

	E (Pa)	I (m^4)	J (m^4)	A (m^2)	m' (kg/m)
solar panel	$52.90 \cdot 10^{12}$	$--$	$--$	$--$	$--$
spacer	$108 \cdot 10^{9}$	$0.87 \cdot 10^{-9}$	$3.50 \cdot 10^{-6}$	$1.0 \cdot 10^{-4}$	7.283
hold-down	$108 \cdot 10^{9}$	$2.50 \cdot 10^{-9}$	$10.0 \cdot 10^{-6}$	$1.0 \cdot 10^{-4}$	2.544
bracket	$70 \cdot 10^{9}$	$39.0 \cdot 10^{-9}$	$0.12 \cdot 10^{-6}$	$1.0 \cdot 10^{-4}$	5.088

Table 6.1: Material and geometrical data test configuration

6.1.2 Finite element calculations

The panels were modelled using 18 x 15 plate elements. In B2000 the rotation around the z-axis was suppressed for these elements. Each spacer was modelled with a line of 6 beam elements, each hold-down structure was modelled with a line of 6 beam elements and each bracket was also modelled with a line of 6 beam elements. The lower ends of the brackets were fully clamped. The beam elements in the finite element models account for bending, extension and torsion. The air was modelled in different ways. In ANSYS, the air was modelled using 3-dimensional acoustic volume elements. These elements are based on the standard wave equation and therefore do not include viscothermal effects. Compressibility however is accounted for. Incompressible behaviour in ANSYS can be artificially simulated by taking the speed of sound to be very large. Three elements were used across the layer thickness. The air model in B2000 was based on the low reduced frequency model. The new viscothermal elements were used to calculate the

pressure distribution in the layer. At the edges of the air layer a pressure release condition ($p = 0$) was imposed. Thus, the influence of the surrounding air is neglected. Calculations indicate that this is justified, both from a frequency and a damping point of view. An overview of element types is given in Table 6.2.

In ANSYS and B2000 the air elements were coupled to the structural elements. In ANSYS a key option has to be activated for acoustic elements not adjacent to the structure. In B2000 interface elements were used to establish the coupling.

	ANSYS	B2000
panels	SHELL63	Q4.ST
spacer	BEAM3	B2
hold-down	BEAM3	B2
bracket	BEAM3	B2
air	FLUID30	Q4.VISC

Table 6.2: Element types for the finite element models

6.1.3 Results for vacuum

The eigenfrequencies for the structure in vacuum are listed in Table 6.3. The modes can be classified as in-phase and out-of-phase modes (see Figure 6.5). Mode 5 is a local mode.

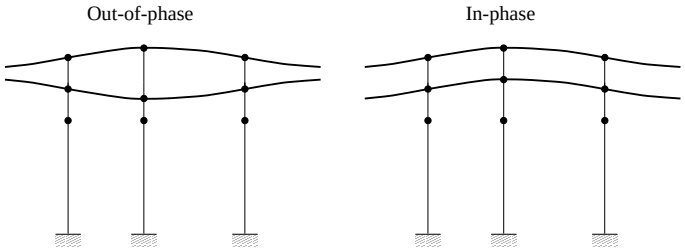

Figure 6.5: Out-of-phase modes and in-phase modes

In the fifth column of Table 6.3 the displacement ratio, calculated using ANSYS, is given. The displacement ratio is defined as the ratio between the maximum deflection of the lower panel and the maximum deflection of the

upper panel. A ratio larger than 1 means that the lower panel is relatively active, while for a ratio smaller than 1 the lower panel is relatively inactive.

Mode	Type	Frequencies (Hz)		Ratio
		ANSYS	B2000	ANSYS
1	Out	44.14	44.65	0.51
2	In	47.89	48.62	1.96
3	In	48.64	49.38	0.47
4	Out	49.53	50.11	0.12
5	Local	51.01	51.67	2.86
6	Out	51.37	52.14	1.89
7	Out	51.88	52.61	0.56
8	In	53.21	54.05	2.70
9	Out	53.95	54.53	0.39
10	In	55.20	55.86	2.63
11	Out	60.67	61.27	0.31
12	Out	60.69	61.31	0.40
13	In	62.08	62.77	2.70
14	In	63.31	64.07	3.03

Table 6.3: Eigenfrequencies ARAFOM test problem in vacuum

The results of the two finite element models show good agreement. This is a requirement for making any judgements about the influence of the air later in the investigation. The small differences are caused by the different type of plate elements.

6.1.4 Results for air

The eigenfrequencies of the system in air are listed in Table 6.4. The results from calculations with ANSYS and B2000 are given. Again, the modes can be classified as in-phase and out-of-phase modes. The results of B2000 calculations with and without viscothermal effect are given in Table 6.5 [2].

Table 6.4 shows that the order of the modes has changed. The lower modes are now all low frequency out-of-phase modes. This is not surprising,

[2]The eigenvalue calculation results in complex valued frequencies: $\omega = \omega_r + i\omega_i$. For viscous damping the natural frequency is then calculated from: $\omega_n = |\omega|$. The dimensionless damping coefficient is: $\xi = \frac{\omega_i}{|\omega|} \times 100\%$

Mode	Type	Frequencies (Hz)			Ratio
		ANSYS		B2000	ANSYS
		Compr	Incompr	Inviscid Adiabatic	Compr
1	Out	21.13	21.27	21.55	0.92
2	Out	23.84	24.13	24.80	0.93
3	Out	23.98	24.25	24.60	0.91
4	Out	25.74	25.95	26.50	0.92
5	Out	29.81	30.10	30.46	0.91
6	Out	30.94	31.10	31.60	0.95
7	Out	33.06	33.29	33.55	0.94
8	Out	34.21	34.37	34.69	0.95
9	In	47.48	47.49	48.26	1.10
10	Out	48.28	48.88	49.17	1.04
11	In	48.87	49.16	49.70	0.97
12	In	50.41	50.44	51.14	0.93
13	In	52.93	52.93	53.85	1.05
14	In	54.92	54.92	55.66	1.02

Table 6.4: Eigenfrequencies ARAFOM test problem in air

since out-of-phase vibrations introduce a significant pumping effect. For the layer with open ends, the added stiffness is very small. Consequently, the large amount of added mass for the out-of-phase modes causes a drastic decrease in frequency. In practical situations, however, the importance of these modes is limited. In the vibration tests for the SOHO configuration for instance, described in section 6.1, these modes were not detected in the sine vibration test because they were not excited by the base excitation.

Secondly, the Table shows that the in-phase modes are affected little by the presence of the air layer. For the in-phase modes there is no strong pumping effect. The pumping for in-phase modes originates from the fact that the panels vibrate with different amplitudes. These effects however are relatively small. Table 6.4 shows that the displacement ratio between the panels is almost equal to 1 for all modes. It is interesting to analyse the values of the displacement ratio in vacuum. Table 6.3 shows that the ratio in vacuum varies between 0.3 and 3. Thus, in vacuum the deflections of both panels can be quite different. This indicates that the air layer provides coupling between the two panels, and forces them to vibrate with the same

Mode	Type	Frequencies (Hz)		Damping (%)
		B2000 inviscid adiabatic	B2000 full	B2000 full
1	Out	21.55	21.22	1.68
2	Out	24.80	24.40	1.74
3	Out	24.60	24.40	1.73
4	Out	26.50	26.13	1.50
5	Out	30.46	30.09	1.32
6	Out	31.60	31.25	1.18
7	Out	33.55	33.18	1.17
8	Out	34.69	34.33	1.10
9	In	48.26	48.31	0.09
10	Out	49.17	48.69	0.99
11	In	49.70	48.73	0.87
12	In	51.14	51.13	0.02
13	In	53.85	53.85	0.00
14	In	55.66	55.66	0.00

Table 6.5: Influence of viscothermal effects

amplitude. Hence, the pumping effects for these modes is small. These considerations are very helpful when analysing the results of the different models. The validity of the various assumptions for the test problem under consideration will now be discussed.

Compressibility

The influence of the compressibility can be analysed by simply comparing the ANSYS results for compressible and incompressible behaviour in Table 6.4. The values indicate that the compressibility effects are very small, especially for the in-phase modes. A parameter that can be used to estimate the influence of compressibility is the ratio between the plate dimensions and the acoustic wavelength. For the present test case, the acoustic wavelength is typically large compared to the plate dimensions while the ends of the layer are open. Compressibility effects are therefore small.

Constant pressure across the gap width

The influence of the assumption of constant pressure across the gap width can be analysed by comparing the ANSYS results for compressible behaviour and the B2000 results for inviscid, adiabatic behaviour in Table 6.4. In ANSYS three linear elements were used across the gap width. Regarding the deviations in the vacuum frequencies, there is no significant difference between the two results. This indicates that the assumption of constant pressure is reasonable.

Viscothermal effects

The influence of viscothermal effects can be deduced from Table 6.5. The shear wave number for the present configuration varies between 15 and 25, which indicates that viscothermal effects could be important. The frequencies of all the modes are affected very little by the viscothermal effects, especially for the in-phase modes. The in-phase modes do not introduce large velocities and pressures in the air and thus the air effects remain small for these modes. There is a significant amount of damping for the out-of-phase modes. These modes introduce a strong pumping of the air, resulting in significant viscous losses. However, these modes are very difficult to excite in the tests.

It can be concluded that viscothermal effects have very little influence in the present test case. The frequencies are not affected and the damping levels for the important in-phase modes remain low.

6.1.5 Practical considerations

In the previous section, it was demonstrated that the introduction of several assumptions is justified for the test problem. Compressibility and viscothermal effects are small, and the pressure can be assumed to be constant across the gap width.

The damping levels that were found in the sine vibration tests cannot be explained by these calculations. There are probably other important effects in the SOHO tests that were not accounted for in the current finite element models. In the tests, for instance, cables are present between the panels. These cables are tied together and obstruct the air flow in the layer. The influence of barriers in the air layer will be investigated in section 6.4. In this section it is demonstrated that barriers can have a very large influence on the energy dissipation in a thin layer.

Finally, the simple test configuration consists of two panels with one air layer. There are several configurations in use with more than two panels. The behaviour of such systems with multiple air layers is more complicated.

6.2 Inkjet print head

The newly developed techniques were used in the design of inkjet print heads. In cooperation with Océ Technologies B.V. projects were defined in order to develop a theoretical model for the description of the dynamical behaviour of a print head. This section briefly discusses the techniques that were used and gives an impression of the results that were obtained. Some literature is available on inkjet print heads, see *e.g.* [94, 95, 96, 97], mostly dealing with the propagation of waves in a single flexible channel using analytical models.

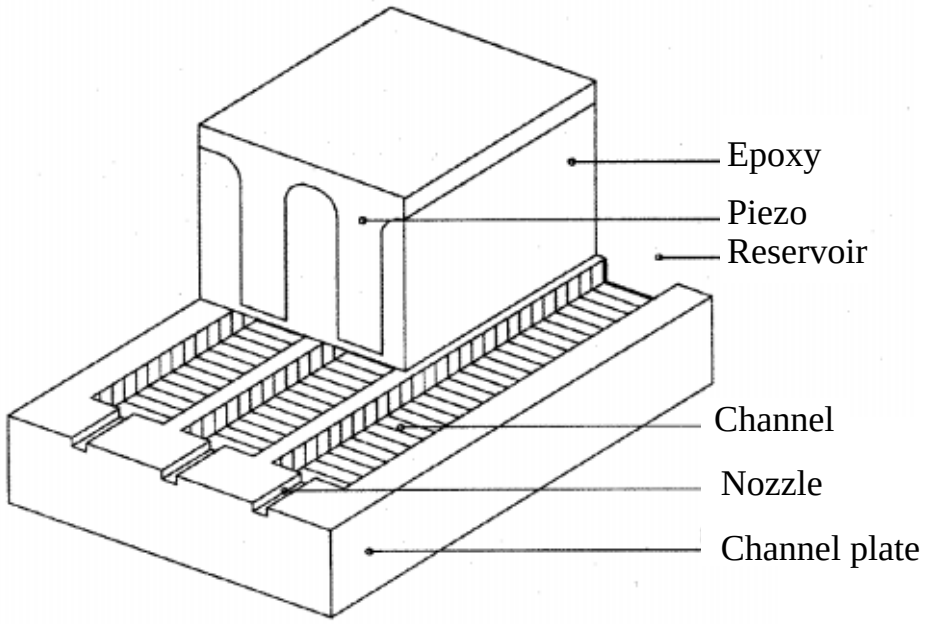

Figure 6.6: Inkjet print head

An inkjet print head consists of a channel plate with a large number of parallel ink channels (see Figure 6.6). A nozzle is attached to one side of the channel. The other side of the channel is connected to the ink reservoir. Piezo-elements on top of the channels are used for activation. A pressure disturbance in the channel is created by means of electric piezo-activation. The piezo expands and consequently a pressure disturbance is introduced. Pressure waves start travelling into the channel and the nozzle. By deactivating the piezo at the right moment, the pressure can increase to a level at which a drop will be released from the nozzle. Clearly, the aim of the print head is to deliver a drop of ink of the *right size* at the *right time* at the *right place*.

In order to achieve this goal, it is essential to have a good understanding of the propagation of waves in the channel and the nozzle, the influence of the elasticity of the walls and the cross-talk between the channels. The present analysis only concerns linear theory and is therefore not able to describe the forming and the release of the drop itself. The linear calculations however provide a good insight into the phenomenon and are very useful in the design process.

The cross-sectional dimensions of the channel and the nozzle are very small, *i.e.* length scales of the order of 100 μm. The frequencies of interest are very high. The properties of some inks are such that in the operational range of the print head, viscous effects can play an important role in the wave propagation. Furthermore, the channels are surrounded by flexible materials. The flexibility of the walls can have a significant influence on the response of the system. The elasticity can also introduce cross-talk between channels, which can disturb the printing process. If cross-talk cannot be eliminated, the activation of the piezos has to be adjusted in such a way that the cross-talk is actively compensated for. It is clear that in the latter case a model is needed that is able to describe the interaction between the channels. These considerations indicate that viscous effects and acousto-elastic effects are important design quantities for the print head.

6.2.1 Simple 2D test problem

Consider a simple 2D geometry with a channel and a nozzle (see Figure 6.7). The channel is supported at the top and bottom by two flexible layers with thicknesses t_t and t_b respectively. The modulus of elasticity of the layers is indicated by E_t and E_b, respectively.

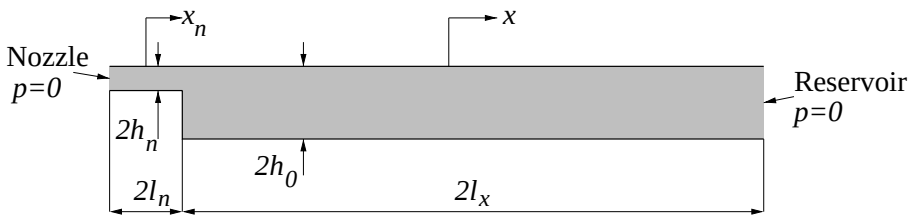

Figure 6.7: Simple 2D test problem

The channel has a length $2l_x$ and a height $2h_0$. The ink is supplied to the channel by a large reservoir on the right side. On the left side, the channel is connected to the nozzle. The nozzle has a length $2l_n$ and a height $2h_n$. In the test problem, the following material and geometrical properties were

used:

$$\begin{aligned}
\rho_0 = 1200\ \mathrm{kg/m^3} \quad &; \quad \mu = 15 \cdot 10^{-3}\ \mathrm{Ns/m^2} \\
c_0 = 1200\ \mathrm{m/s} \quad &; \\
E_t = 70 \cdot 10^9\ \mathrm{N/m^2} \quad &; \quad E_b = 70 \cdot 10^9\ \mathrm{N/m^2} \\
t_t = 1 \cdot 10^{-3}\ \mathrm{m} \quad &; \quad t_b = 0.25 \cdot 10^{-3}\ \mathrm{m} \\
l_x = 3.5 \cdot 10^{-3}\ \mathrm{m} \quad &; \quad l_n = 100 \cdot 10^{-6}\ \mathrm{m} \\
h_0 = 100 \cdot 10^{-6}\ \mathrm{m} \quad &; \quad h_n = 17 \cdot 10^{-6}\ \mathrm{m}
\end{aligned} \tag{6.1}$$

The ratio of specific heats γ is set equal to 1, so that the polytropic constant $n(s\sigma)$ automatically takes the value of 1. At the nozzle exit and the reservoir side of the channel the pressure perturbation is set equal to zero. The excitation is introduced by means of a piezo-electric material on top of the channel. The steady state and the transient response of the system due to this excitation will now be described by a number of simple models. The velocity at the centre of the nozzle exit is calculated, because this is a quantity that can also be determined experimentally (see section 6.2.2). With this simple 2D model the effects of viscosity, wall elasticity, and the use of finite elements are illustrated. These techniques are then used in section 6.2.2 for the design of a new print head.

Model with rigid walls

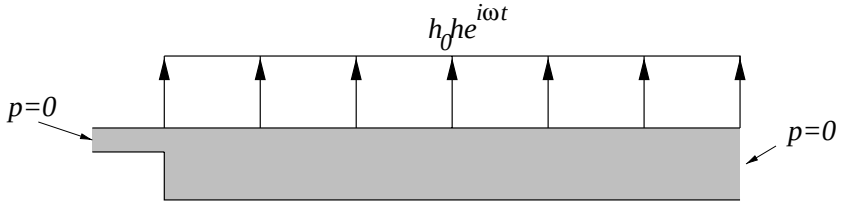

Figure 6.8: Model with rigid walls

In the model with rigid walls the walls of the nozzle and the nozzle are all rigid. The top wall of the channel performs a small normal oscillation with amplitude $h_0 h$. The other walls are fixed. The differential equations for this situation are (see chapter 2 and Appendix B):

$$\begin{aligned}
\text{channel} \quad &: \quad \frac{\partial^2 p}{\partial x^2} - \Gamma^2 p = \frac{1}{2} n\,(s\sigma)\,\Gamma^2 h \\
\text{nozzle} \quad &: \quad \frac{\partial^2 p}{\partial x^2} - \Gamma_n^2 p = 0
\end{aligned} \tag{6.2}$$

where the subscript n refers to the nozzle. The boundary conditions at the exit of the nozzle and the reservoir side of the channel are $p = 0$. By assuming mass conservation and continuity of pressure on the interface between the nozzle and the channel, the problem can be solved. Once the presssure distribution is known, the dimensionless velocity at the centre of the nozzle can be calculated from (see chapter 2 and Appendix B for a layer geometry):

$$v_{xn} = -\frac{i}{\gamma}\left[\frac{1}{\cosh\left(s\sqrt{i}\right)} - 1\right]\frac{\partial p}{\partial x} \tag{6.3}$$

Model with spring walls

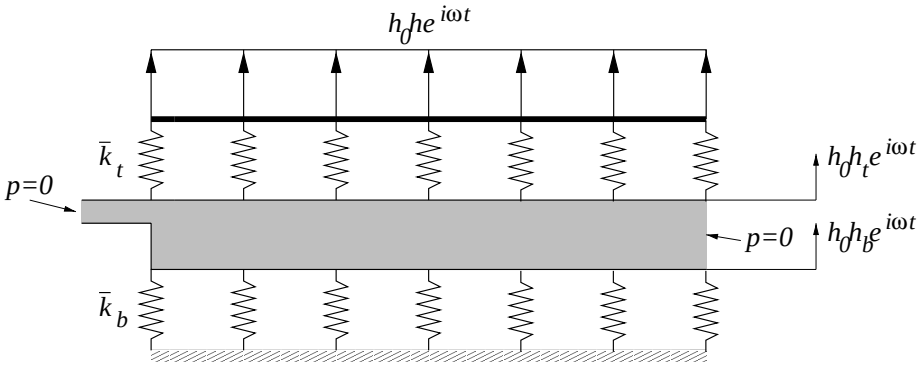

Figure 6.9: Model with spring walls

In this 2-dimensional model the top and bottom walls of the nozzle are rigid and fixed. The walls of the channels are supported at the top and bottom by an elastic foundation of massless springs. The stiffness per unit area of the springs at the top and the bottom of the channel is:

$$\overline{k}_t = \frac{E_t}{t_t} \quad ; \quad \overline{k}_b = \frac{E_b}{t_b} \tag{6.4}$$

where E_t and E_b represent Young's modulus for the top and bottom materials and t_t and t_b represent the thicknesses of the supporting layers. The upper ends of the top springs perform a harmonic displacement oscillation. The lower ends of the bottom springs are fixed. The differential equations governing the behaviour of this model are:

$$\begin{aligned} \text{channel} \quad &: \quad \frac{\partial^2 p}{\partial x^2} - \Gamma^2 p = \frac{1}{2} n\left(s\sigma\right)\Gamma^2\left[h_t - h_b\right] \\ \text{nozzle} \quad &: \quad \frac{\partial^2 p}{\partial x^2} - \Gamma_n^2 p = 0 \end{aligned}$$

$$\begin{aligned} \text{top springs} \quad &: \quad h_t = h + \frac{p}{\gamma k_t} \\ \text{bottom springs} \quad &: \quad h_b = -\frac{p}{\gamma k_b} \end{aligned} \tag{6.5}$$

where the dimensionless stiffnesses are given by:

$$k_t = \frac{h_0}{\rho_0 c_0^2}\overline{k}_t \quad ; \quad k_b = \frac{h_0}{\rho_0 c_0^2}\overline{k}_b \tag{6.6}$$

In physical terms, the dimensionless stiffness represents the ratio between the stiffness of the springs and the stiffness of the ink layer. If the ink acts like a one-dimensional spring, the stiffness is equal to $\rho_0 c_0^2/h_0$. Combining the equations leads to the following two equations to be solved:

$$\begin{aligned} \text{channel} \quad &: \quad \frac{\partial^2 p}{\partial x^2} - \Gamma^2 \left[1 + \frac{1}{2}\frac{n(s\sigma)}{\gamma}\left(\frac{1}{k_t} + \frac{1}{k_b}\right)\right] p = \frac{1}{2} n(s\sigma)\Gamma^2 h \\ \text{nozzle} \quad &: \quad \frac{\partial^2 p}{\partial x^2} - \Gamma_n^2 p = 0 \end{aligned} \tag{6.7}$$

Again, by demanding conservation of mass and continuity of pressure, the coupling between the channel and the nozzle is established. With the boundary conditions at the nozzle exit and the reservoir side of the channel the solution is obtained. The dimensionless velocity can then be calculated.

Expression (6.7) shows that the propagation of waves in the channel is affected by the flexibility of the walls. If the spring stiffnesses are very large compared to the fluid stiffness, *i.e.* $k_t \ll 1$ and $k_b \ll 1$, the model evidently reduces to the rigid wall model. The viscothermal and elastic effects can also be interpreted in terms of an effective speed of sound:

$$c_{eff} = \frac{c_0 i}{\Gamma} \frac{1}{\sqrt{1 + \frac{1}{2}\frac{n(s\sigma)}{\gamma}\left(\frac{1}{k_t} + \frac{1}{k_b}\right)}} \tag{6.8}$$

This expression shows that the flexibility of the walls reduces the effective speed of sound.

Model with finite elements

A schematic drawing of the finite element model is given in Figure 6.10.

The nozzle and the channel are modelled with the new viscothermal Q4.VISC elements. The top and the bottom supporting layers are modelled with 3-dimensional HE8.S elements. These structural elements are coupled to the viscothermal elements with INT.8 interface elements. Frequency response calculations were carried out for a prescribed displacement. In the

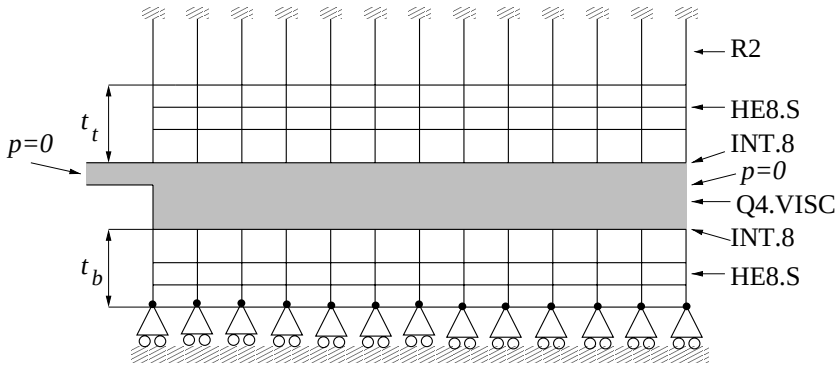

Figure 6.10: Model with finite elements

current version of B2000 a displacement could not be prescribed. This problem was solved by connecting massless rod elements, type R2, to the top nodes of the structural volume elements. The top ends of the rods were fixed. The rods have a very large stiffness that dominates the structural contribution from the HE8.S elements. By imposing the correct force on the lower nodes of the rods, the corresponding displacement could be prescribed.

The velocity at the nozzle exit was extracted from the pressure results, since the pressure is the only degree of freedom for the viscothermal elements. The pressure at the nozzle exit is zero. In the finite element analysis linear elements were used. The velocity at the nozzle exit can therefore be approximated by:

$$v_{xn} \cong -\frac{i}{\gamma}\left[\frac{1}{\cosh\left(s\sqrt{i}\right)}-1\right]\frac{\gamma\omega}{\rho_0 c_0}\frac{nexn}{2l_n}\overline{p}_{e+1} \tag{6.9}$$

where $nexn$ is the number of elements in the nozzle and $\overline{p}_{e+1}$ is the pressure in the nodal point just to the right of the nozzle exit.

Frequency response results

The velocity at the nozzle exit is divided by the amplitude of the displacement for this linear system. The transfer function $H(\omega)$ is:

$$H(\omega) = \frac{\overline{v}_{xn}(\omega)}{h_0 h(\omega)} \tag{6.10}$$

The amplitude of the transfer function is given as a function of the frequency in Figure 6.11.

Figure 6.11 shows that for this type of ink the viscosity has a significant effect on the propagation of waves (compare the results for the rigid inviscid

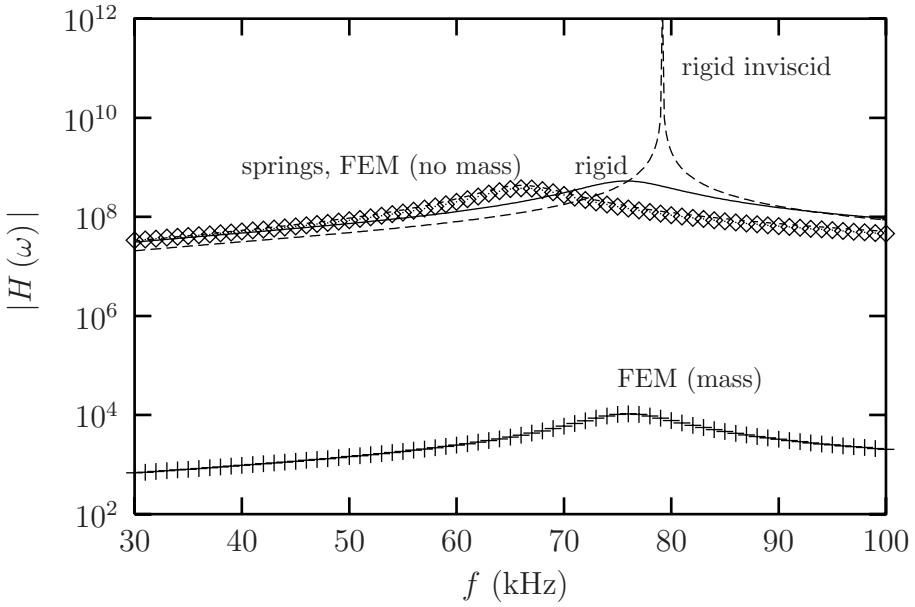

Figure 6.11: Frequency response simple 2D test problem

case and the rigid case). For the present test case the shear wave number varied between 6 and 11. For these low shear wave numbers the viscosity is very important. The eigenfrequency of the system is an important parameter for the print head since it is related to the velocity of the waves and thus determines the most efficient activation strategy of the piezo. Damping causes a decay of pressure waves in time. If a drop has been released from the nozzle, the pressure must decrease to a low level before the piezo can be activated again, otherwise the jetting history can affect the printing process. In the last part of this section this will be illustrated with the transient time response of the system.

The flexibility of the walls can affect wave propagation. When the walls are very flexible, the speed of the waves decreases and the transfer function is affected. In a realistic print head the flexibility is an aspect of serious concern. The finite element calculations with a massless piezo show good agreement with the results of the spring model.

Figure 6.11 shows that for the present problem the mass of the piezo has a large influence on the amplitude of the transfer function. In this test case the excitation forces the whole piezo to move up and down. However, the imposed displacement excitation is not very realistic for the print head under consideration. In reality the piezo is activated electrically and under the applied voltage it will deform and introduce a pressure disturbance in the channel. The piezo is embedded in the print head and will not vibrate as a

whole. This is confirmed by measurements. Thus, in practical situations the mass of the piezo will not have a large effect on the response of the system.

Transient results

The transient response of the channel can be calculated by means of Fourier transforms. Suppose the top of the piezo is subjected to a displacement history $h_0h(t)$. The Fourier transform of the displacement history, $h_0h(\omega)$, is given by:

$$h_0h(\omega) = \int_{-\infty}^{\infty} h_0h(t)\, e^{-i\omega t} dt \tag{6.11}$$

The velocity at the nozzle exit in the frequency domain, $\overline{v}_{xn}(\omega)$, is obtained by simply multiplying the excitation spectrum with the transfer function $H(\omega)$:

$$\overline{v}_{xn}(\omega) = H(\omega)\, h_0h(\omega) \tag{6.12}$$

The transient response is obtained through the inverse Fourier transform:

$$\overline{v}_{xn}(t) = \frac{1}{2\pi} \int_{-\infty}^{\infty} \overline{v}_{xn}(\omega)\, e^{i\omega t} d\omega \tag{6.13}$$

The transient response was calculated with the analytical rigid wall model and the analytical model where the walls were represented by springs. The excitation signal is:

$$h_0h(t) = \begin{cases} 0 & : \ t < 0 \\ 10 \cdot 10^{-9} & : \ 0 < t < 1 \cdot 10^{-5} \\ 0 & : \ t > 1 \cdot 10^{-5} \end{cases} \tag{6.14}$$

A fast Fourier algorithm was used to calculate the Fourier transforms. A time span from -0.2 ms to 0.2 ms was used, with a total of 2^{12} points. The time responses of the rigid wall model and the flexible spring model are given in Figure 6.12.

Due to the activation of the piezo, a pressure disturbance is introduced in the channel. Waves start propagating, reflecting off the open ends at the reservoir side of the channel and the nozzle exit. By deactivating the piezo at the right moment, the pressure in the channel and the velocity in the nozzle can increase to a level at which a drop will be released. A good timing in the activation signal is very important in the printing process. It is evident that the speed of the waves, and thus the viscosity of the fluid, are important factors.

The Figure shows a decay of the ink velocity at the nozzle exit in time. The decay is caused by the dissipation of energy by means of viscous shear.

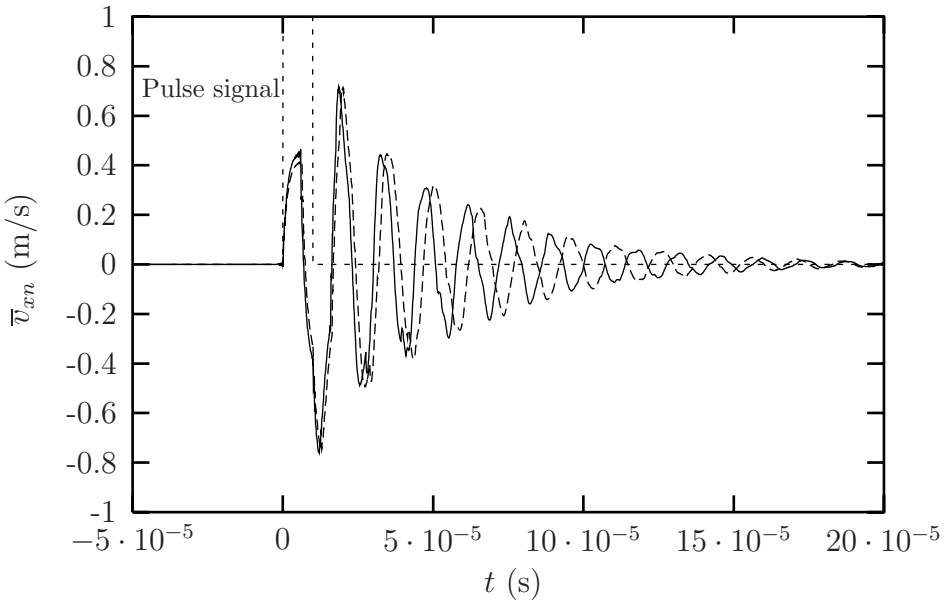

Figure 6.12: Transient response rigid wall and spring wall model 2D test problem rigid walls (—), spring walls (−−)

The decay rate is important for the jetting process, since the ink has to come to rest before another drop can be released. Finally, the flexibility of the walls has a significant influence on the transient response of the system.

6.2.2 Design of a print head

Calculations

The simplest way to include cross-talk is by means of static influence coefficients. In other words: what volume change [3] does a unit pressure in one channel induce in the other channels? For this purpose, finite element calculations were carried out for the cross section of a print head (see Figure 6.13).

With the finite element model, the area change of each channel cross-section due to a unit static pressure in one channel was calculated. In this way a matrix with static influence coefficients was filled. The calculations show that the area change decreases as a function of the distance to the activated channel, as expected.

The total model of the print head consists of a matrix set of equations. The propagation of waves in the nozzle and the channel is described by the

[3]The volume change drives the pressure pulsations, see chapter 2 and Appendix B

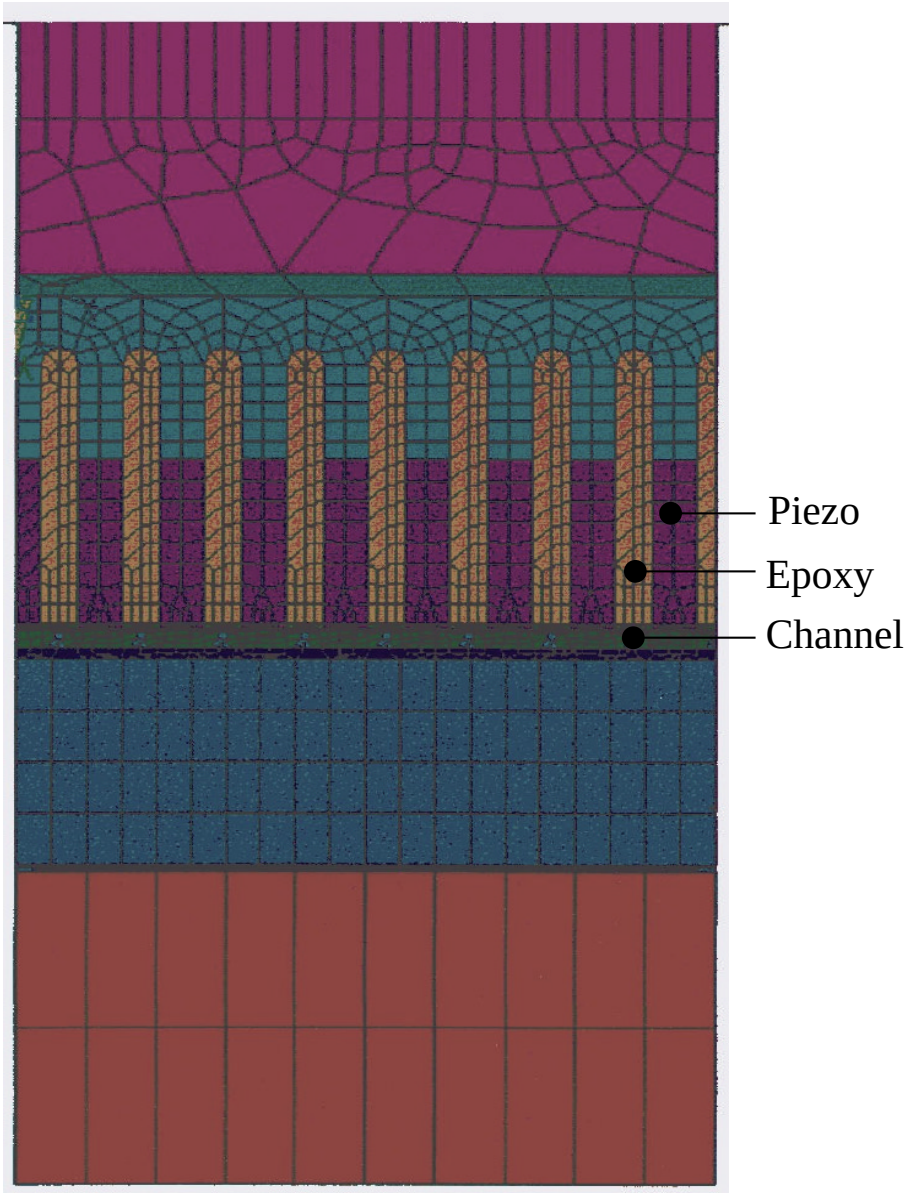

Figure 6.13: Finite element model inkjet

low reduced frequency model for a tube with a rectangular cross section (see chapter 2 and Appendix B.3). The nozzle and the channel are coupled by assuming conservation of mass and continuity of pressure on the interface. The model where the walls of the channel are supported by massless springs, representing the stiffness of the surrounding materials, is used to calculate the propagation of waves. The cross-talk between the channels is introduced

by means of static influence coefficients. The results of this model will now be compared with experimental results.

Experiments

Measurements were carried out at Océ Technologies B.V. Because of the small dimensions of a print head, it is very difficult to obtain experimental data. A quantity that can be determined with a reasonable degree of accuracy is the velocity at the nozzle exit. The velocity was determined using a Laser Doppler interferometer. The setup is shown in Figure 6.14.

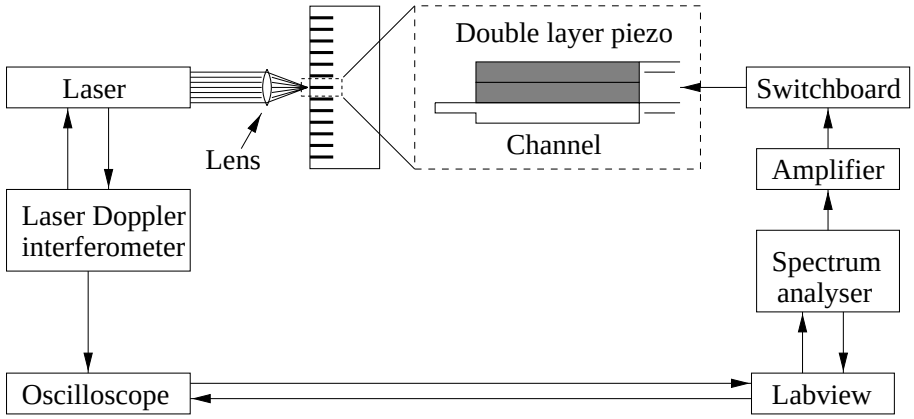

Figure 6.14: Experimental setup inkjet

The laser was pointed at the nozzle meniscus and used to measure the velocity[4] of the meniscus. In the experiments, a low activation level for the piezo was used since no drops were to be released. By varying the electric activation of the piezo, the linearity of the process was ensured. The velocity of the meniscus was determined as a function of the frequency with a frequency sweep. In order to investigate cross-talk, the nozzle velocity of each channel was measured while activating one single channel.

Results

Figures 6.15, 6.16 and 6.17 show the transient time response of the channels, both measured and calculated. The nozzle velocity is non-dimensionalized with a reference velocity $\overline{v}_{ref}$. The time is non-dimensionalized with a reference time t_{ref}. One single channel was activated and the velocity at the nozzle

[4]The Laser Doppler interferometer actually measures a weighted average over a small area. The weighting is related to the intensity distribution and the area is determined by the width of the beam.

exit of the activated channel (Figure 6.15), the first neighbour channel (Figure 6.16) and the second neighbour channel (Figure 6.17) were determined. The first neighbour channel is the channel adjacent to the activated channel. The second neighbour channel is the channel next to the first neighbour channel, *i.e.* there is one channel in between the second neighbour channel and the activated channel.

The Figures show fair agreement between calculated and measured results, both in a qualitative and quantitative sense. The frequency of the signal, the amplitude and the decay rate are predicted well by the model. The cross-talk between the channels is also correctly described by the simple model. One of the main advantages of the current model is its simplicity: only the most important effects are included in the model. Because the model is an analytical model, it is very well suited for parameter studies and design purposes.

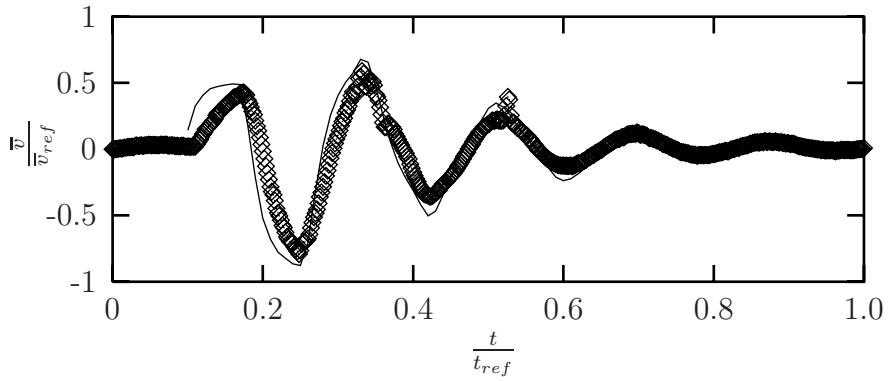

Figure 6.15: Transient response of activated channel: nozzle velocity versus time. Calculations (—), experiments (◇)

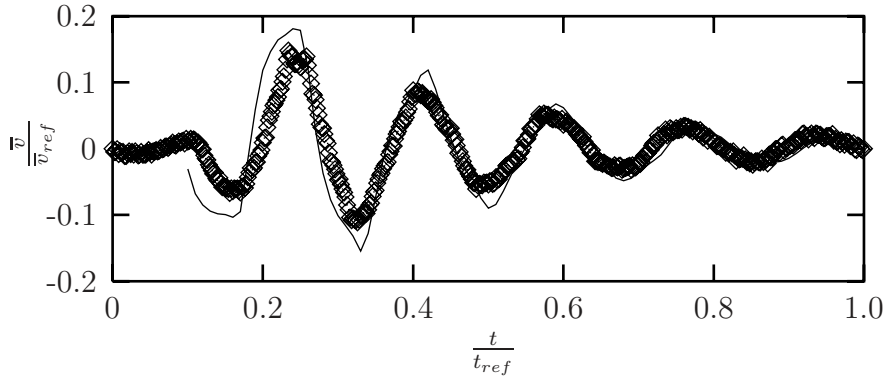

Figure 6.16: Transient response of first neighbour channel: nozzle velocity versus time. Calculations (—), experiments (◇)

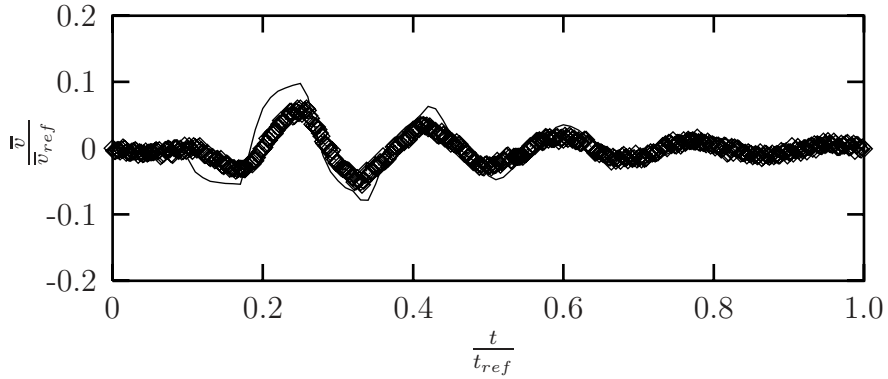

Figure 6.17: Transient response of second neighbour channel: nozzle velocity versus time. Calculations (—), experiments (◇)

6.3 Double wall panels

6.3.1 Configuration

Consider two rooms separated by a double wall panel (see Figure 6.18).

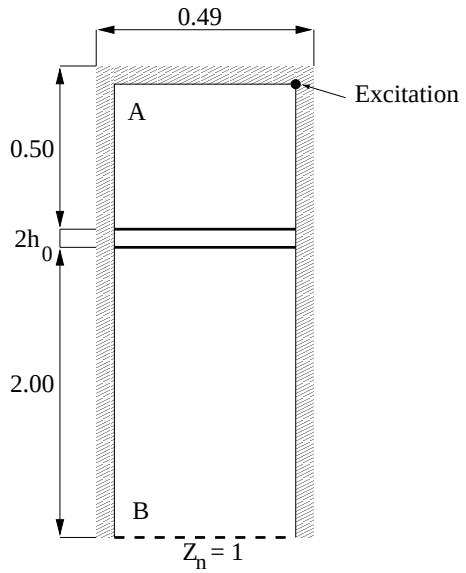

Figure 6.18: Double wall configuration, dimensions in m

In room A an excitation is present due to a prescribed (acoustic) force[5] at a point, causing a pressure field to be generated. The walls of room A are hard, except for the side that is coupled to the double wall panel. The panel will transmit a part of the incident energy into room B. At the far end of room B, a specific acoustic impedance, Z_n, of 1 is prescribed:

$$Z_n \equiv \frac{p_0}{\rho_0 c_0^2} \frac{p}{\boldsymbol{v} \cdot \boldsymbol{e}_n} = 1 \tag{6.15}$$

For normal incident waves, all energy will be absorbed at the boundary. The transmitted sound field will not be a plane wave near the radiating panel. At a certain distance from the panel, however, the wave will have acquired a planar character. Consequently, all transmitted energy will be absorbed at the impedance boundary. There are two ways in which energy can be dissipated in the current model: absorption at the impedance boundary of room B and viscothermal dissipation in the separating layer of the double

[5]This is a prescribed value in the right hand side vector of the viscothermal finite element model.

wall panel. Two different characteristics of the double wall configuration are analysed in the present investigation: the energy dissipation in the layer and the sound transmission through the double wall panel.

The amount of energy that is dissipated per cycle in the layer can be calculated from the net incident energy from room A and the radiated energy into room B:

$$\begin{aligned}\overline{E}_{in} &= \frac{\pi}{\omega} p_0 c_0 \int_{\overline{A}_t} \mathrm{Re}\left\{p\ \boldsymbol{v}^* \cdot \boldsymbol{e}_n\right\} d\overline{A}_t \\ \overline{E}_{rad} &= \frac{\pi}{\omega} p_0 c_0 \int_{\overline{A}_b} \mathrm{Re}\left\{p\ \boldsymbol{v}^* \cdot \boldsymbol{e}_n\right\} d\overline{A}_b \\ \overline{E}_{diss} &= \overline{E}_{in} - \overline{E}_{rad}\end{aligned} \tag{6.16}$$

where $\overline{A}_t$ and $\overline{A}_b$ represent the areas of the top and bottom panels respectively and * denotes a complex conjugate.

The dissipation factor DF, the relative amount of dissipated energy, is:

$$DF = \frac{\overline{E}_{diss}}{\overline{E}_{in}} = 1 - \frac{\overline{E}_{rad}}{\overline{E}_{in}} \tag{6.17}$$

If the viscothermal effects in the layer are neglected, the dissipation factor is evidently equal to zero. In this case there is no mechanism for energy dissipation in the layer and consequently all incident energy is transmitted to room B.

The sound transmission is expressed in terms of the transmission loss, TL. The transmission loss is calculated from:

$$TL = 10 \log \frac{PP_A}{PP_B} \tag{6.18}$$

where PP_A and PP_B are the average quadratic pressures in room A and across the absorbing boundary of room B respectively. The dissipation factor and the transmission loss were calculated in the frequency range from 10 to 300 Hz for various configurations. The layer thickness, $2h_0$, and the thickness ratio between both plates of the double wall panel were varied. The total thickness of both plates was kept equal to 3 mm. The material properties of both aluminium plates were as follows:

$$E_p = 70 \cdot 10^9\ \mathrm{N/m^2} \quad ; \quad \nu_p = 0.3 \quad ; \quad \rho_p = 2710\ \mathrm{kg/m^3} \tag{6.19}$$

6.3.2 Finite element calculations

The finite element mesh for the calculations is shown in Figure 6.19. The following element types were used in the calculations:

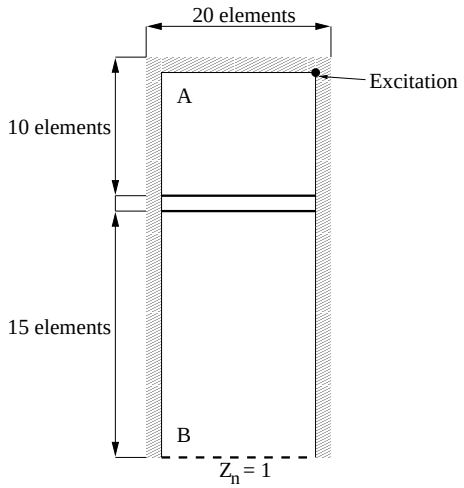

Figure 6.19: Finite element mesh for the double wall configuration

- rooms A and B: standard 8 node acoustic elements HE8.ACOU
- plates: 4 node plate elements Q4.ST
- viscothermal layer: 4 node viscothermal elements Q4.VISC
- interfaces: 8 node interface elements INT.8
- impedance boundary: 4 node impedance elements Q4.IMP

Note that the problem under consideration is 2-dimensional. The finite element calculations were carried out with 3-dimensional elements. By taking a mesh with a small depth and by imposing the appropriate boundary conditions the 2-dimensional situation was simulated. Only 1 element was used in the depth direction.

6.3.3 Dissipation factor

The modes of the coupled system can be divided into in-phase modes and out-of-phase modes. The in-phase modes can easily be recognized in the dissipation factor graphs because of their sharps peaks. The eigenfrequencies of the in-phase modes are not very much affected by the presence of the air layer. Hence, the eigenfrequency does not vary with varying layer thickness for these modes (see Figures 6.23, 6.24 and 6.25). When the plate thickness is varied, the eigenfrequencies of the in-phase modes do vary, as expected (see Figures 6.20, 6.21 and 6.22).

The broad peaks in the graphs are the out-of-phase modes. The eigenfrequencies of these modes are significantly affected by the presence of the thin air layer (see Figures 6.23, 6.24 and 6.25). Since the eigenfrequencies are important for the behaviour of the system, the example illustrates the need for a coupled analysis.

The graphs show that a significant amount of the incident energy is dissipated by viscothermal effects in the layer. This energy dissipation in the layer is related to the pumping of air. In order to create a pumping effect, the layer thickness and the ratio of plate thicknesses have to be chosen carefully. If the layer thickness is chosen to be very large, the viscothermal effects are very small. If the layer thickness is very small, the coupling between the two panels is so strong that no pumping effect is created. If the plate thicknesses are equal, there is no pumping effect for in-phase modes. If the plate thicknesses differ greatly, the behaviour of the coupled system will be dominated by one of the plates and consequently no pumping effect occurs. These considerations show that in order to create a pumping effect, a small gap width must be chosen while the plates are left to vibrate independently. Considering the fact that the air layer provides coupling between the panels, there might be an optimum configuration for a given situation. The present example shows that even the behaviour of this relatively simple configuration is a complex system of interacting factors.

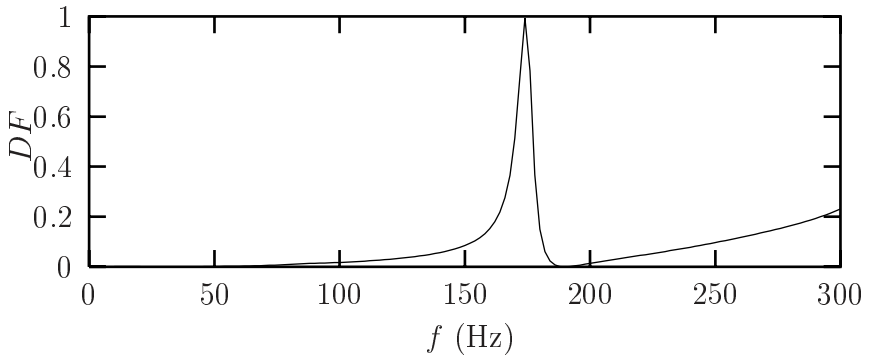

Figure 6.20: DF versus frequency for $t_{p1} = 1.5$ mm, $t_{p2} = 1.5$ mm, $2h_0 = 1$ mm

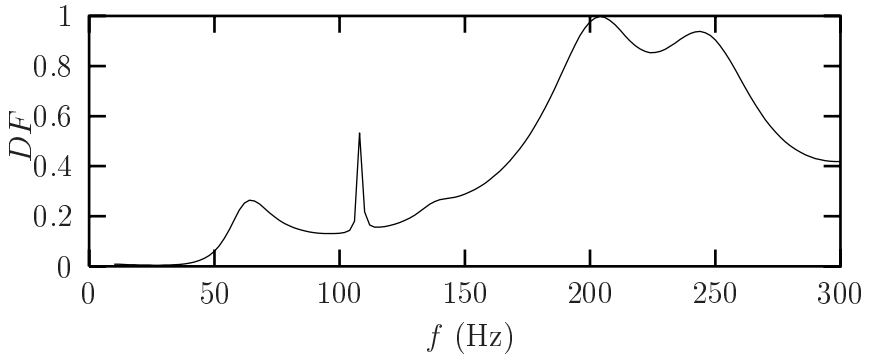

Figure 6.21: DF versus frequency for $t_{p1} = 1$ mm, $t_{p2} = 2$ mm, $2h_0 = 1$ mm

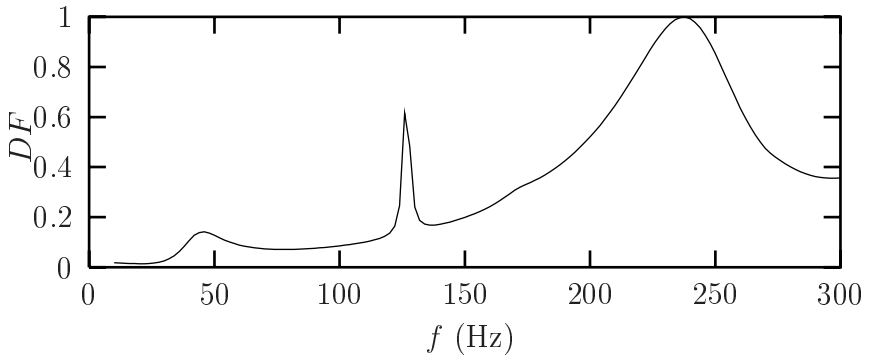

Figure 6.22: DF versus frequency for $t_{p1} = 0.75$ mm, $t_{p2} = 2.25$ mm, $2h_0 = 1$ mm

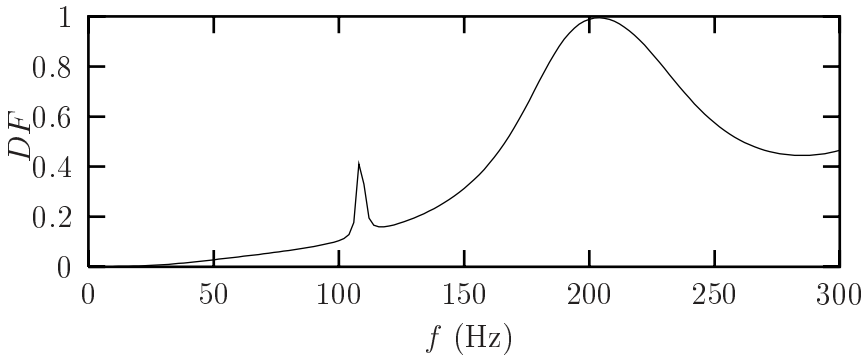

Figure 6.23: DF versus frequency for $t_{p1} = 1$ mm, $t_{p2} = 2$ mm, $2h_0 = 0.5$ mm

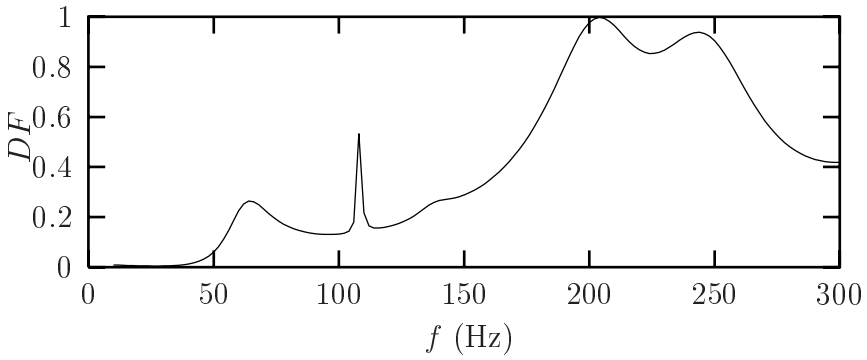

Figure 6.24: DF versus frequency for $t_{p1} = 1$ mm, $t_{p2} = 2$ mm, $2h_0 = 1$ mm

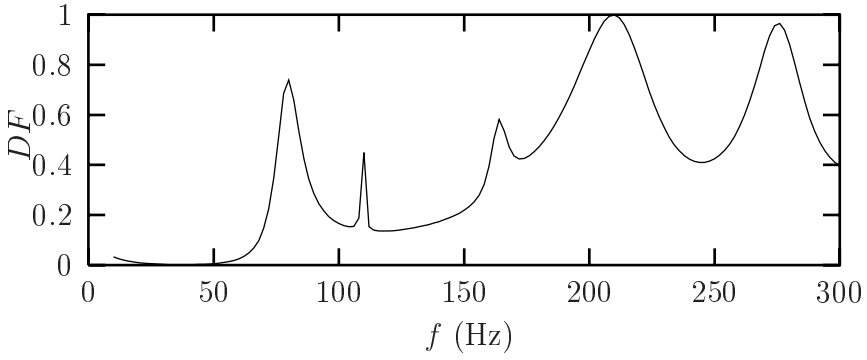

Figure 6.25: DF versus frequency for $t_{p1} = 1$ mm, $t_{p2} = 2$ mm, $2h_0 = 2$ mm

6.3.4 Transmission loss

The transmission loss is shown versus the frequency in Figures 6.26 to 6.31. The graphs contain the results for the viscothermal case and the inviscid, adiabatic case [6]. In this way the influence of the viscothermal effects can easily be seen.

All Figures show that the influence of viscothermal effects is very small. Only around the eigenfrequencies there are minor differences between the results of the calculations. It can be concluded that viscothermal effects only have a very small influence on the transmission loss. This is not very surprising, since in this low frequency range the transmission loss is mainly governed by the mechanical characteristics of the panels. Damping affects or controls the transmission loss around the eigenfrequencies and above the coincidence frequencies of the system, *i.e.* the frequencies at which the structural and the acoustic wavelengths coincide (see *e.g.* [98]).

Although there is no energy dissipation in the layer, there can be a high transmission loss. It is important to distinguish between the transmission loss and the dissipation factor. The dissipation factor relates the net incident energy and the net radiated energy. The transmission loss is based on the energy levels in the two rooms. A high energy level in a room does not imply a high net incident energy: the plate must be excited by the pressure field. Consider for instance the case $t_{p1} = 1$ mm, $t_{p2} = 2$ mm and $2h_0 = 1$ mm (see Figure 6.21 and Figure 6.27). The dissipation factor shows a maximum value around 200 Hz. This means that almost all of the net incident energy is dissipated in the layer. The transmission loss is also high around this frequency, but the viscothermal effects have little influence on the transmission loss. At this frequency the energy level in the first room is high, but only a small portion of this energy is injected into the first plate because the pressure field does not excite the plate very well. In the present example the room dimensions and the frequency range are such that the pressure field in room A is nearly uniform.

[6] Inviscid and adiabatic: $\Gamma = i$ and $n(s\sigma) = \gamma$.

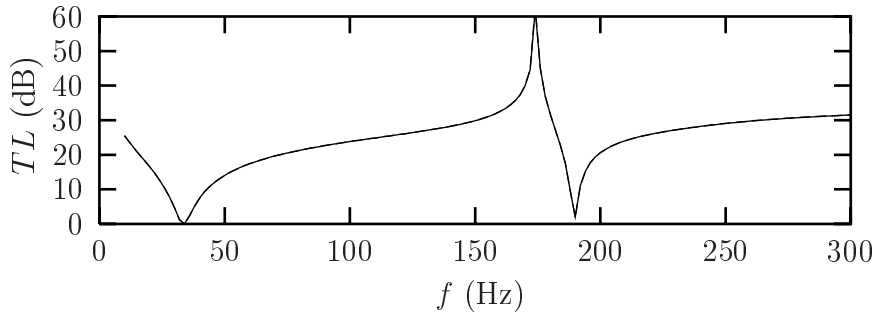

Figure 6.26: TL versus frequency for $t_{p1} = 1.5$ mm, $t_{p2} = 1.5$ mm, $2h_0 = 1$ mm, viscothermal (—), inviscid and adiabatic (−−)

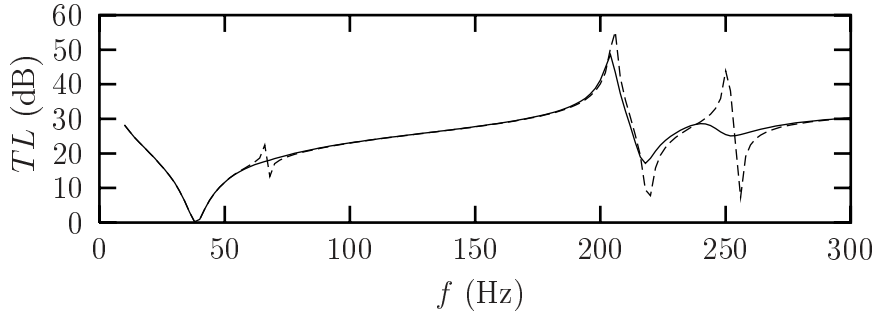

Figure 6.27: TL versus frequency for $t_{p1} = 1$ mm, $t_{p2} = 2$ mm, $2h_0 = 1$ mm, viscothermal (—), inviscid and adiabatic (−−)

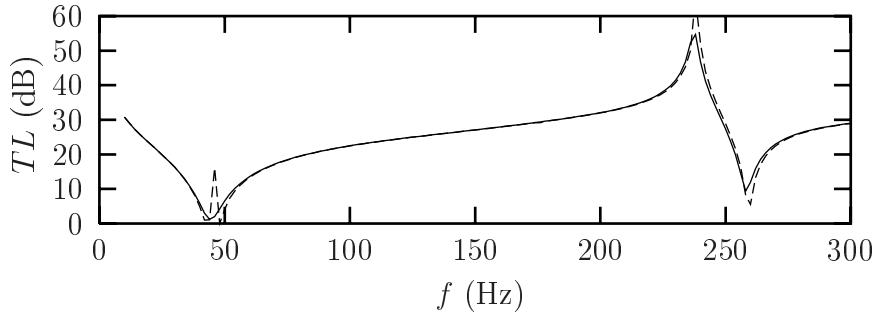

Figure 6.28: TL versus frequency for $t_{p1} = 0.75$ mm, $t_{p2} = 2.25$ mm, $2h_0 = 1$ mm, viscothermal (—), inviscid and adiabatic (−−)

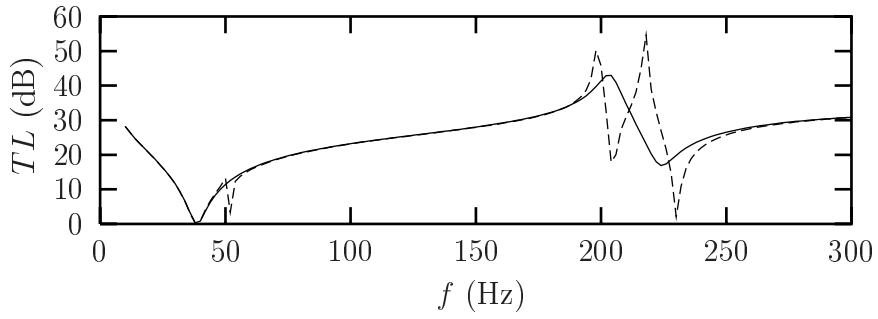

Figure 6.29: TL versus frequency for $t_{p1} = 1$ mm, $t_{p2} = 2$ mm, $2h_0 = 0.5$ mm, viscothermal (—), inviscid and adiabatic (−−)

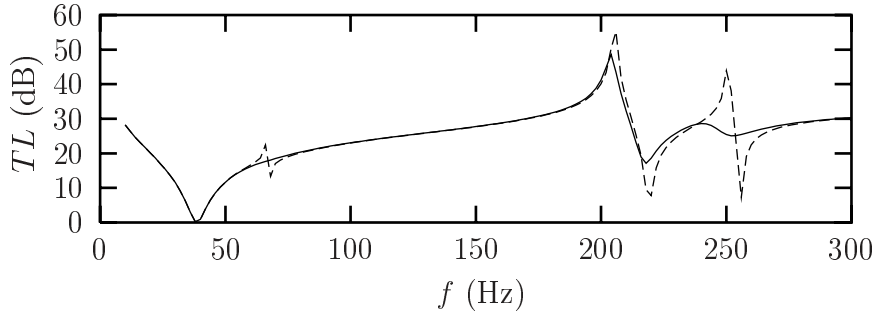

Figure 6.30: TL versus frequency for $t_{p1} = 1$ mm, $t_{p2} = 2$ mm, $2h_0 = 1$ mm, viscothermal (—), inviscid and adiabatic (−−)

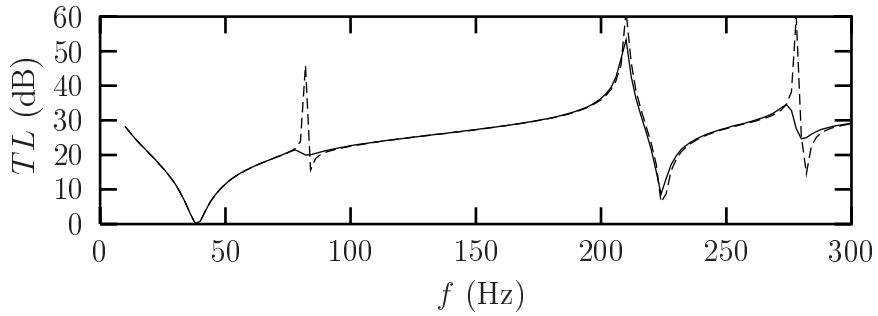

Figure 6.31: TL versus frequency for $t_{p1} = 1$ mm, $t_{p2} = 2$ mm, $2h_0 = 2$ mm, viscothermal (—), inviscid and adiabatic (−−)

6.3.5 Practical implications

The calculations indicate that a significant amount of energy can be dissipated in the layer. If energy is injected into the top plate and the properties are adjusted in the right way, a large part of this energy can be dissipated. This implies that double wall panels with thin gas layers can be used for damping purposes in order to reduce vibrations in which the top panel is excited by for instance a point force or a structural member attached to the plate.

In practical situations the two plates are often connected by structural parts: the connectors. The spacing of the connectors is important and deserves attention. Roughly speaking, the spacing and design of the connectors should be such that a sufficient pumping effect can be created by the plate vibrations. Trochidis [55] performed measurements on the damping characteristics of double wall panels with various connector spacings. He observed a maximum damping when the connector spacing was equal to a whole number of structural wavelengths. The type of connection was also found to be important. Some types of connections allowed a larger relative motion of the plates, and higher damping values were measured in these cases. With the newly developed techniques these phenomena can now be studied in more detail.

Finally, the dissipation capabilities depend on the type of excitation. For a point excitation, significant dissipation can be obtained. For a distributed load with a constant amplitude, however, the performance will be less good, because the important modes are not well excited in this case.

The presented study is a first step in the analysis of the behaviour of double wall panels. As a next step investigations on the optimization of double wall configurations were carried out by Basten [99] at the University of Twente, under contract of the Dutch Technology Foundation. The tools that were developed and validated within the framework of the present study were successfully used in that research.

6.4 Barriers in a thin layer

The calculations and measurements presented so far in this report concerned layers with a constant thickness. In many practical applications, however, a part of the gap is blocked by obstructions. In the case of solar panels for instance, there are two bundles of wiring that block a large part of the gap (see Figure 6.32). Chow and Pinnington [63] suggested to use obstructions or materials in the layer to further increase the damping capabilities. They used porous materials in the layer for this purpose (foam and felt).

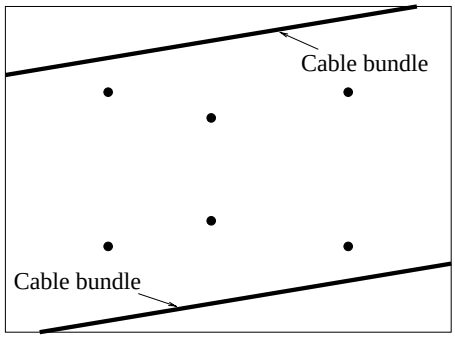

Figure 6.32: Cable bundles in the air layer between solar panels, top view

The main aim of the present investigation is to gain insight into the consequences of obstructions in the layer. Some investigations were presented concerning the viscothermal acousto-elastic behaviour for a non-constant layer thickness, see *e.g.* Önsay [69]. Önsay studied the frequency response of a strip backed by a thin gas layer with a stepwise varying layer thickness. In his investigation however damping and linearity were not specifically addressed. In the present study special attention will be paid to these aspects.

6.4.1 Experimental setup

The setup with the oscillating solar panel described in chapter 4 was also used for the present investigation. Barriers were placed inside the layer to study the influence of obstructions. In Figure 6.33 a setup is shown with 4 rectangular barriers in a box form. In all cases, the gap width $2h_0$, was equal to 12 mm: the panel spacing that is used in most solar panel configurations. The height of the barriers, $2h_b$, was varied. Barriers of 10.66, 10.33, 10.00, 9.00 and 8.00 mm were used. Eigenfrequency and damping of the system were determined for each configuration for a displacement amplitude $h_0 h$ of 0.3 mm. Furthermore, the linearity of the system was investigated by

carrying out measurements at excitation amplitudes $h_0 h$ ranging from 0.15 mm to 0.5 mm for barriers of 10.66, 10.33 and 10.00 mm.

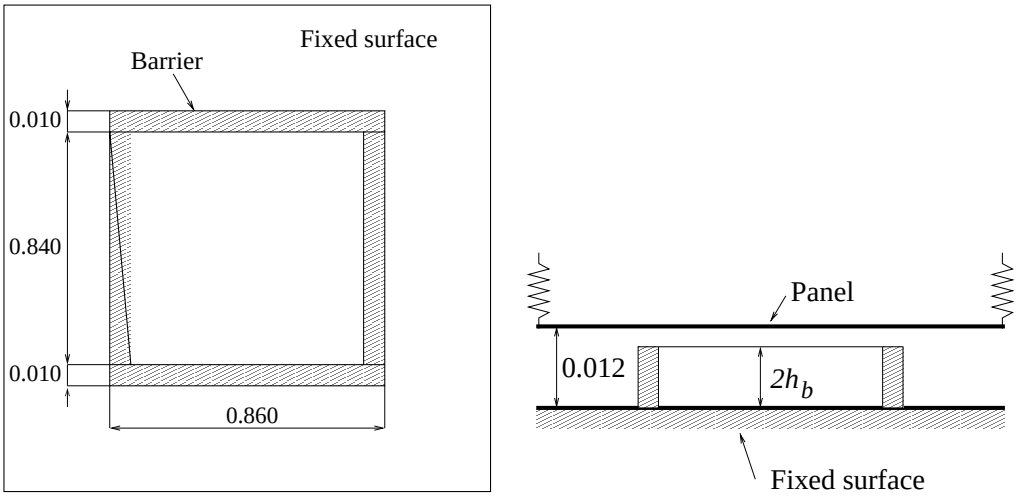

Figure 6.33: Barrier setup, top view (left), side view (right), dimensions in m.

6.4.2 Finite element calculations

The eigenfrequency and the damping coefficient of the system were calculated with the finite element program B2000. The layer was modelled with the new viscothermal Q4.VISC elements. The layer thickness can be specified per element. In this way the barriers could easily be modelled. The viscothermal elements were coupled to the structural Q4.ST elements with interface elements, type INT.8. At the edges of the air layer the pressure disturbance was set to zero: $p = 0$. The springs were modelled with rod elements, type R2.

The mesh density was increased around the barriers, because of the pressure gradients around the barriers. Three elements were used across the width of a barrier. Four elements with a spacing ratio of 1.5 were used to model the air between the barrier and the outer edge of the plate. Two times five elements with a spacing ratio of 1.5 were used in each direction for the area inside the barriers. The mesh is illustrated in Figure 6.34.

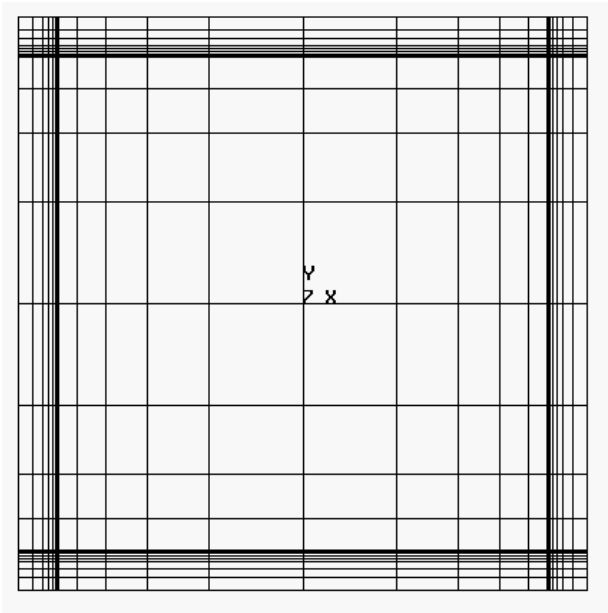

Figure 6.34: Finite element mesh for the calculations with barriers

6.4.3 Results

Linearity

The eigenfrequency of the system was not significantly affected by the amplitude of motion (see Appendix D). The damping however increased dramatically with increasing displacement amplitude. The damping versus amplitude is plotted in Figures 6.35, 6.36 and 6.37 for the three barrier heights. In all cases the damping shows a nearly linear increase with amplitude. The damping predicted by the finite element calculations is very low compared to the damping levels that were measured at high amplitudes. If the measured damping coefficient is extrapolated to a zero displacement amplitude, the same damping coefficient is obtained as was calculated using the finite element model. It can be concluded that non-linearities are present that have a large influence on the damping of the system. This is an important observation. In the literature, several investigations deal with the behaviour of layers with non-constant thickness. The linearity of the problem however was never addressed. A physical interpretation of the phenomenon is given in section 6.4.4.

Eigenfrequency versus barrier height

In Figure 6.38 the eigenfrequency is plotted versus the barrier height.

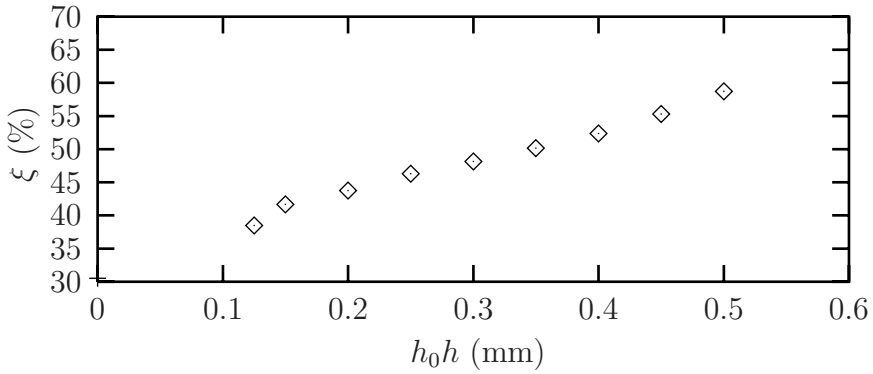

Figure 6.35: Damping versus amplitude, barrier height=10.66 mm. Experiments (⋄), FEM (+)

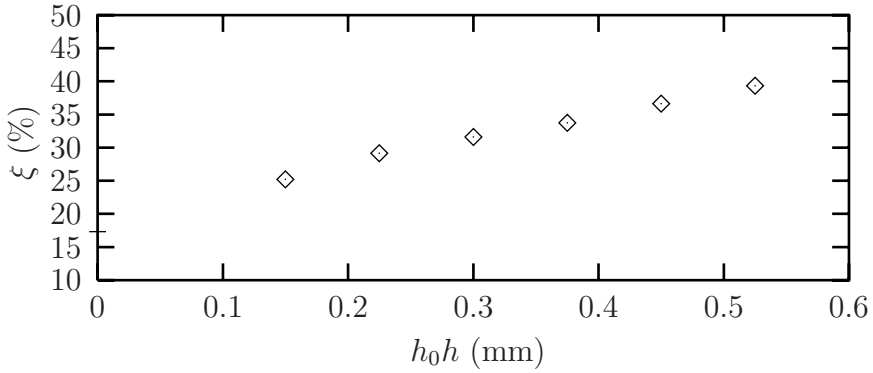

Figure 6.36: Damping versus amplitude, barrier height=10.33 mm. Experiments (⋄), FEM (+)

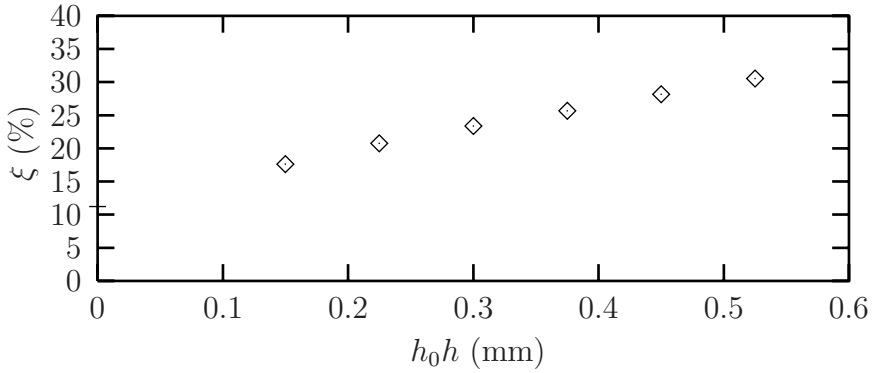

Figure 6.37: Damping versus amplitude, barrier height=10.00 mm. Experiments (⋄), FEM (+)

The eigenfrequency of the system was not affected very much by the amplitude of motion. The finite element results and the experimental results for

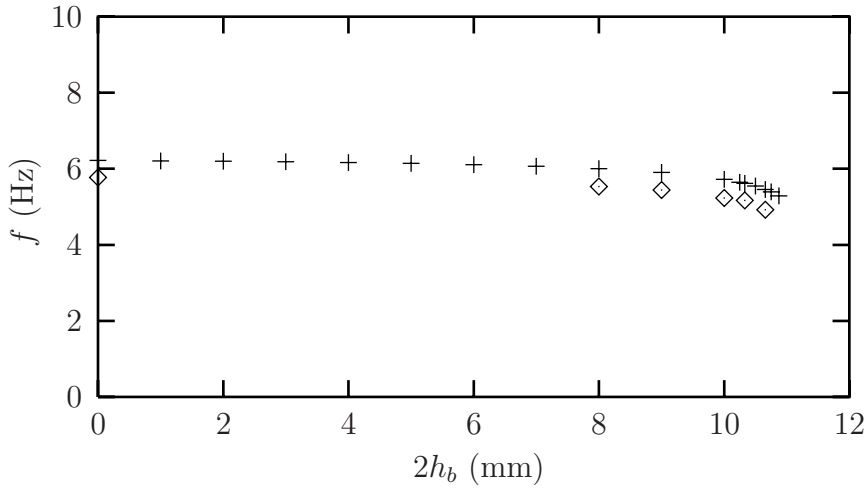

Figure 6.38: Frequency versus barrier height. Experiments ($\diamond$), FEM (+)

the eigenfrequency can therefore be compared. Both calculations and experiments show a decrease in eigenfrequency with increasing barrier height. The experimental frequencies are always lower than the calculated frequencies. This can mainly be attributed to the fact that the influence of the surrounding air is neglected. The shift in eigenfrequency as a function of barrier height is not very large and therefore the added mass remains small. The added mass due to the surrounding air thus has a relatively large influence.

Damping versus barrier height

In Figure 6.39 the damping is plotted versus the the barrier height. The

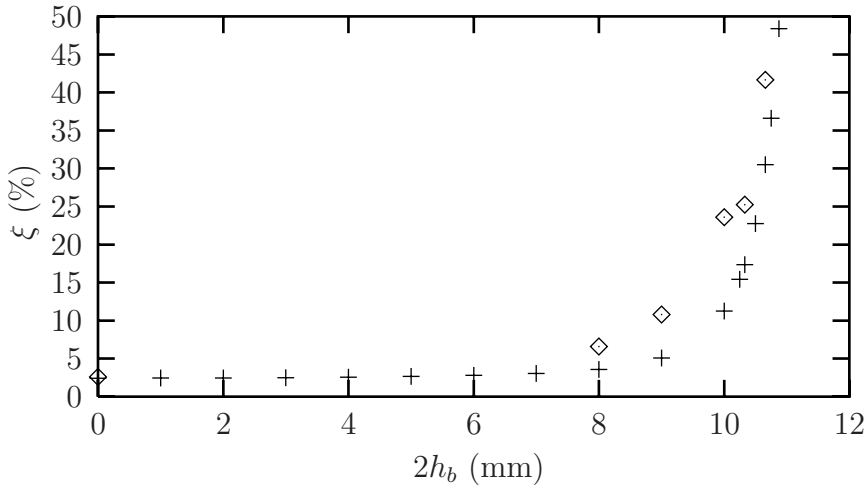

Figure 6.39: Damping versus barrier height. Experiments ($\diamond$), FEM (+)

damping shows a strong increase with increasing barrier height. By using simple obstructions in the layer, the damping values can be increased from 3% to 40%. It was demonstrated that non-linearities are very important in the experiments. The experimental results for an amplitude of 0.3 mm (clearly in the non-linear regime) and the calculated results (obtained with a linear model) should therefore be compared and interpreted with care. Both calculations and experiments predict an increase of damping with increasing barrier height.

6.4.4 Interpretation

The experimental results show that the eigenfrequency of the system hardly varies with the displacement amplitude $h_0 h$. The damping however does show a linear increase with displacement amplitude. Evidently, this behaviour cannot be explained by the linear viscothermal models. There must be another non-linear dissipative mechanism in addition to the linear dissipative viscothermal effects.

Smoke was used to visualize the flow around the barriers. For large barrier heights, a vortex developed behind the barrier during the outflow stage (see Figure 6.40).

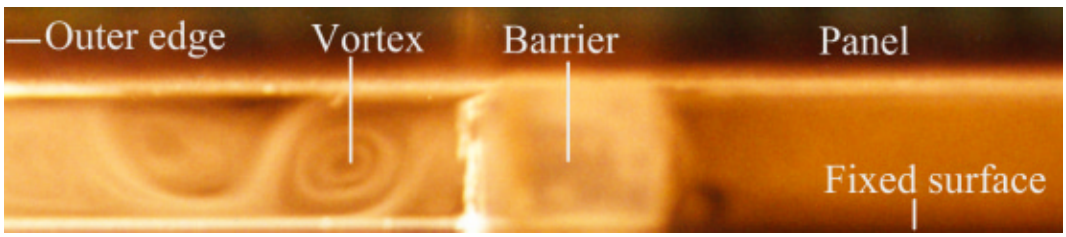

Figure 6.40: Forming of vortex behind the barrier (side view)

The acoustic response of open tubes was studied by Disselhorst and Van Wijngaarden [43], and Peters, Hirschberg, Reijen and Wijnands [44]. In their experiments, non-linear effects were observed related to unsteady flow separation and the forming of vortices at the tube end. This non-linear dissipation mechanism was found to be important for small acoustic Strouhal numbers:

$$Sr = \frac{\omega R}{\overline{v}_x} \tag{6.20}$$

where ω is the angular frequency, R is the radius of the tube and $\overline{v}_x$ is the amplitude of the axial velocity at the tube end. For low acoustic Strouhal

numbers, the dissipated energy per cycle can be calculated from [44]:

$$\overline{E}_{vortex} = \frac{2\rho_0 \overline{v}_x^3 c_d \pi R^2}{3\omega} \tag{6.21}$$

where c_d is a parameter that is determined by the geometry of the pipe end. For a thin-walled unflanged pipe this factor is equal to 2, whereas for a flanged pipe it takes the value $\frac{13}{9}$.

The theory that was developed for tubes will now be used to estimate the additional energy dissipation of this mechanism for the present layer geometry. It must be remembered that this is a qualitative analysis, based on an order of magnitude estimation, aimed at the identification of the dissipation mechanism. A detailed quantitative study of the non-linear separation for the geometry under consideration would require a significant amount of work and is not within the scope of the present study.

The velocity in the thin layer that remains between the barrier and the panel can be estimated by using the equation of continuity for incompressible behaviour. The amplitude of the velocity is:

$$\overline{v} \cong \frac{\omega h_0 h l_{xb} l_{yb}}{[2h_0 - 2h_b]\,[l_{xb} + l_{yb}]} \tag{6.22}$$

where l_{xb} and l_{yb} denote the length of the barriers in the x-direction and the y-direction respectively. For the present investigation $l_{xb} = 0.43$ m and $l_{yb} = 0.43$ m (see Figure 6.33). For the three barriers of interest, the velocities vary between 0.4 and 12 m/s. The Reynolds number, $Re = \rho_0 \overline{v}\,[h_0 - h_b]\,/\mu$, is about 100 for the present situation. The expansion ratio, $h_0/\,[h_0 - h_b]$, varies between 6 and 9. For the present layer geometry the acoustic Strouhal number can be estimated by:

$$Sr = \frac{\omega\,[h_0 - h_b]}{\overline{v}} \tag{6.23}$$

The dimensionless velocity amplitude v was determined by using the equation of continuity for incompressible behaviour. This gives using expression (6.22)[7]:

$$Sr \cong \frac{2\,[h_0 - h_b]^2\,[l_{xb} + l_{yb}]}{h_0 h l_{xb} l_{yb}} \tag{6.24}$$

It can easily be verified that $Sr \ll 1$. Analoguous to expression (6.21), using the appropriate total flow area, the dissipated amount of energy was

[7] A more accurate estimation of the velocity can be provided by using the finite element results, but this degree of accuracy is not relevant in the present qualitative analysis

estimated from:

$$\overline{E}_{vortex} \cong \frac{2\rho_0 \overline{v}^3 c_d \left[2h_0 - 2h_b\right] \left[4l_{xb} + 4l_{yb}\right]}{3\omega} \tag{6.25}$$

Thus:

$$\overline{E}_{vortex} \cong \frac{8}{3}\rho_0 c_d \frac{l_{xb}^3 l_{yb}^3}{\left[l_{xb} + l_{yb}\right]^2} \frac{\left[h_0 h\right]^3 \omega^2}{\left[2h_0 - 2h_b\right]^2} \tag{6.26}$$

The question remains whether the amount of energy that is dissipated by this mechanism is significant compared to the "standard" viscothermal dissipation. In the present study it is assumed that the dissipation mechanisms are not correlated: the dissipated energies are simply superimposed. For the single degree of freedom system with stiffness 8κ and viscous damping coefficient ξ_0, the dissipated energy per cycle is given by:

$$\overline{E}_{diss} = 2\pi 8\kappa \xi_0 \left[h_0 h\right]^2 \tag{6.27}$$

where κ is the stiffness of one spring and ξ_0 denotes the viscous damping coeffient due to "standard" viscothermal effects only. The value of ξ_0 can be calculated with the finite element model. It can also be deduced from the experimental results by extrapolating the measured damping values to a zero displacement amplitude. As stated before, the extrapolated values and the calculated values show good agreement (see Figures 6.35, 6.36 and 6.37). An estimation shows that the energy that is dissipated by the mechanism is of the same order of magnitude as the "standard" viscothermal dissipation. This order of magnitude estimate suggests that it is the vortex mechanism that introduces the strong non-linear damping behaviour.

In the experiments it is not possible to distinguish between the "standard" linear viscothermal dissipation and the dissipation due to the non-linear mechanism. All the dissipated energy is interpreted in terms of a damping coefficient ξ according to the definition given in expression (6.27). The damping level found in the experiments can simply be calculated from:

$$\xi = \frac{\overline{E}_{diss} + \overline{E}_{vortex}}{2\pi 8\kappa \left[h_0 h\right]^2} \cong \xi_0 + \frac{8}{3}\frac{\rho_0 c_d}{16\pi\kappa} \frac{l_{xb}^3 l_{yb}^3}{\left[l_{xb} + l_{yb}\right]^2} \frac{\left[h_0 h\right] \omega^2}{\left[2h_0 - 2h_b\right]^2} \tag{6.28}$$

This expression shows that the damping linearly increases with amplitude $h_0 h$ if all other parameters remain constant. In the experiments the damping coefficient showed a linear increase with amplitude and the frequency hardly varied with amplitude. This type of behaviour is in accordance with the vortex mechanism.

In the literature, several investigations were presented concerning the acoustic behaviour of open pipes and the flow over backward facing steps.

Recently, and investigation was presented by Hofmans [100], dealing with a numerical and experimental study on the flow through a square-edge nozzle at low Mach number. The techniques described in this investigation would allow a more quantitative approach of the present problem, involving a 3D geometry with a driven flow. From a practical point of view, it is interesting to investigate if the non-linear mechanism can be used to increase the damping performance.

The present study only concerns a qualitative analysis, based on an order of magnitude estimation, aimed at the identification of the dissipation mechanism. It can be concluded that the observations and this simple qualitative analysis support the assumption that the flow separation introduces a non-linear damping behaviour.

Chapter 7

Conclusions

The general conclusions are:

- an overview was presented of linear viscothermal wave propagation models. Using dimensionless parameters, the models were compared and the ranges of validity were indicated. The analysis showed that the low reduced frequency model is not only adequate but also the most efficient for describing viscothermal wave propagation;

- the low reduced frequency model was validated with specially designed experiments. The experiments enabled accurate measurements and provided new detailed information. The agreement between theory and experiment was good;

- a new viscothermal acoustic finite element was developed, based on the low reduced frequency model. The new element can be coupled to structural elements, enabling fully coupled calculations for complex geometries. The finite element model was validated with experiments. Calculations and experiments showed fair agreement. Thus, a new and efficient simulation tool has been developed for describing of viscothermal wave propagation, including acousto-elastic interaction;

- the new tools were succesfully used in a number of practical applications: the behaviour of an array of folded solar panels during launch, the design of an inkjet print head and the behaviour of double wall panels.

Bibliography

[1] F. Augusztinovicz. Calculation of noise control by numerical methods - what we can do and what we cannot do - yet. In *InterNoise 97*, pages 27–42, Budapest, Hungary, 1997.

[2] Course on advanced techniques in applied and numerical acoustics. In P.Sas, editor, *ISAAC 7*, Leuven, Belgium, 1996. K.U. Leuven.

[3] H. Tijdeman. On the propagation of sound waves in cylindrical tubes. *Journal of Sound and Vibration*, 39:1–33, 1975.

[4] C. Karra, M.B. Tahar, G. Marquette, and M.T. Chau. Boundary element analysis of problems of acoustic propagation in viscothermal fluid. In F. Allison Hill and R. Lawrence, editors, *InterNoise 96*, pages 3003–3006, Liverpool, United Kingdom, 1996. Institute of Acoustics.

[5] C. Karra and M. Ben Tahar. An integral equation formulation for boundary element analysis of propagation in viscothermal fluids. *Journal of the Acoustical Society of America*, 102(3):1311–1318, 1997.

[6] J.W.S. Rayleigh. *The Theory of Sound*, volume II. Dover publications, second, revised edition, 1945.

[7] W.S. Griffin, H.H. Richardson, and S. Yamanami. A study of fluid squeeze-film damping. *Journal of Basic Engineering*, pages 451–456, 1966.

[8] S.M.R. Hashemi and B.J. Roylance. Analysis of an oscillatory oil squeeze film including effects of fluid inertia. *Tribology Transactions*, 32:461–468, 1989.

[9] E.C. Kuhn and C.C. Yates. Fluid inertia effect on the film pressure between axially oscillating parallel circular plates. *ASLE Transactions*, 7:299–303, 1964.

[10] J. Prakash and H. Christensen. Squeeze film between two rough rectangular plates. *Journal of Mechanical Engineering Science*, 20:183–188, 1978.

[11] P. Sinha and C. Singh. Micropolar squeeze films between rough rectangular plates. *Applied Scientific Research*, 39:169–179, 1982.

[12] R.M. Terrill. The flow between two parallel circular discs, one of which is subject to a normal sinusoidal oscillation. *Journal of Lubrication Technology*, pages 126–131, 1969.

[13] J.A. Tichy and M.F. Modest. Squeeze film flow between arbitrary two-dimensional surfaces subject to normal oscillations. *Journal of Lubrication Technology*, 100:316–322, 1978.

[14] J.A. Tichy. Measurements of squeeze-film bearing forces and pressures, including the effect of fluid inertia. *ASLE Transactions*, 28:520–526, 1984.

[15] J.V. Beck, W.G. Holliday, and C.L. Strodtman. Experiments and analysis of a flat disk squeeze-film bearing including effects of supported mass motion. *Journal of Lubrication Technology*, pages 138–148, 1969.

[16] V. Ramamurthy and U.S. Rao. The steady streaming generated by a vibrating plate parallel to a fixed plate in a dusty fluid. *Fluid Dynamics Research*, 2:47–63, 1987.

[17] C.Y. Wang and B. Drachman. The steady streaming generated by a vibrating plate parallel to a fixed plate. *Applied Scientific Research*, 39:55–68, 1982.

[18] N. Rott. The influence of heat conduction on acoustic streaming. *Journal of Applied Mathematics and Physics*, 25:417, 1974.

[19] P. Merkli and H. Thomann. Transition to turbulence in oscillating pipe flow. *Journal of Fluid Mechanics*, 68:567–575, 1975.

[20] G. Maidanik. Energy dissipation associated with gas-pumping in structural joints. *Journal of the Acoustical Society of America*, 40:1064–1072, 1966.

[21] E.E. Ungar and J.R. Carbonell. On panel vibration damping due to structural joints. *AIAA Journal*, 4:1385–1390, 1966.

[22] S. Makarov and M. Ochmann. Non-linear and thermoviscous phenomena in acoustics, part I. *Acustica*, 82:579–606, 1996.

[23] S. Makarov and M. Ochmann. Non-linear and thermoviscous phenomena in acoustics, part II. *Acustica*, 83:197–222, 1997.

[24] S. Makarov and M. Ochmann. Non-linear and thermoviscous phenomena in acoustics, part III. *Acustica*, 83:827–846, 1997.

[25] G.P.J. Too and S.T. Lee. Thermoviscous effects on transient and steady-state sound beams using non-linear progressive wave equation models. *Journal of the Acoustical Society of America*, 97:867–874, 1995.

[26] H.A. Scarton and W.T. Rouleau. Axisymmetric waves in compressible Newtonian liquids contained in rigid tubes: steady-periodic mode shapes and dispersion by the method of eigenvalleys. *Journal of Fluid Mechanics*, 58:595–621, 1973.

[27] K. Rathnam and M.M. Oberai. Acoustic wave propagation in cylindrical tubes containing slightly rarefied gases. *Journal of Sound and Vibration*, 60:379–388, 1978.

[28] K. Rathnam. Influence of velocity slip and temperature jump in rarefied gas acoustic oscillations in cylindrical tubes. *Journal of Sound and Vibration*, 103:448–452, 1985.

[29] M. Moldover, J. Mehl, and M. Greenspan. Gas-filles spherical resonators: theory and experiment. *Journal of the Acoustical Society of America*, 79:253–270, 1986.

[30] M.J. Anderson and P.G. Vaidya. Sound propagation in a waveguide with finite thermal conduction at the boundary. *Journal of the Acoustical Society of America*, 86:2385–2396, 1989.

[31] H.S. Roh, W.P Arnot, and J.M. Sabatier. Measurements and calculation of acoustic propagation constants in arrays of small air-filled rectangular tubes. *Journal of the Acoustical Society of America*, 89:2617–2624, 1991.

[32] N. Rott. Damped and thermally driven acoustic oscillations. *Journal of Applied Mathematics and Physics*, 20:230, 1969.

[33] N. Rott. Thermally driven acoustic oscillations, part II: stability limit for helium. *Journal of Applied Mathematics and Physics*, 24:24, 1973.

[34] N. Rott. Thermally driven acoustic oscillations, part III: second-order heat flux. *Journal of Applied Mathematics and Physics*, 26:43, 1975.

[35] N. Rott and G. Zouzoulas. Thermally driven acoustic oscillations, part IV: tubes with variable cross-section. *Journal of Applied Mathematics and Physics*, 27:197, 1976.

[36] G. Zouzoulas and N. Rott. Thermally driven acoustic oscillations, part V: gas-liquid oscillations. *Journal of Applied Mathematics and Physics*, 27:325, 1976.

[37] R. Raspet, H.E. Bass, and J. Kordomenos. Thermoacoustics of travelling waves: theoretical analysis for an inviscid ideal gas. *Journal of the Acoustical Society of America*, 94:2232–2239, 1993.

[38] J. Kordomenos, A.A. Atchley, R. Raspet, and H.E. Bass. Experimental study of a thermoacoustic termination of a travelling-wave tube. *Journal of the Acoustical Society of America*, 98:1623–1628, 1995.

[39] E. Stuhlträger and H. Thomann. Oscillations of a gas in an open-ended tube near resonance. *Journal of Applied Mathematics and Physics*, 37:155, 1986.

[40] J.H.M. Disselhorst. *Acoustic resonance in open tubes.* PhD thesis, University of Twente, The Netherlands, 1978.

[41] M.P. Verge. *Aeroacoustics of confined jets.* PhD thesis, Technical University of Eindhoven, The Netherlands, 1995.

[42] U. Ingard. Acoustic non-linearity of an orifice. *Journal of the Acoustical Society of America*, 42, 1967.

[43] J.H.M. Disselhorst and L. van Wijngaarden. Flow in the exit of open pipes during acoustic resonance. *Journal of Fluid Mechanics*, 99:293–319, 1980.

[44] C.A.M. Peters, A. Hirschberg, A.J. Reijen, and A.P.J. Wijnands. Damping and reflection coefficient measurements for an open pipe at low Mach and low Helmholtz numbers. *Journal of Fluid Mechanics*, 256:499–534, 1993.

[45] M. Bruneau, Ph. Herzog, J. Kergomard, and J.D. Polack. General formulation of the dispersion equation in bounded visco-thermal fluid. *Wave Motion*, 11:441–451, 1989.

[46] J.B. Mehl. Spherical acoustic resonator: effects of shell motion. *Journal of the Acoustical Society of America*, 78:782–788, 1985.

[47] G. Plantier and M. Bruneau. Heat conduction effects on the acoustic response of a membrane separated by a very thin air film from a backing electrode. *Journal Acoustique*, 3:243–250, 1990.

[48] M. Bruneau, A.M. Bruneau, and P. Hamery. An improved approach to modelling the behaviour of thin fluid films trapped between a vibrating membrane and a backing wall surrounded by a reservoir at the periphery. *Acustica*, 1:227–234, 1993.

[49] P. Hamery, M. Bruneau, and A.M. Bruneau. Mouvement d'une couche de fluide dissipatif en espace clos sous l'action d'une source étendue. *Journal de Physique IV*, 4:C5–213–C5–216, 1994. (in French).

[50] C. Karra. Private communication, 1996.

[51] M. Bruneau, J.D. Polack, Ph. Herzog, and J. Kergomard. Formulation générale des équations de propagation et de dispersion des ondes sonores dans les fluides viscothermiques. *Colloque de Physique*, 51:C2–17–C2–20, 1990. (In French).

[52] M. Bruneau. Acoustique des cavités: modèles et applications. *Journal de Physique IV*, 4:C5–675–C5–684, 1994. (in French).

[53] A.M. Bruneau, M. Bruneau, Ph. Herzog, and J. Kergomard. Boundary layer attenuation of higher order modes in waveguides. *Journal of Sound and Vibration*, 119:15–27, 1987.

[54] P.N. Liang and H.A. Scarton. Three-dimensional mode shapes for higher order circumferential thermoelastic waves in an annular elastic cylinder. *Journal of Sound and Vibration*, 177:121–135, 1994.

[55] A. Trochidis. Vibration damping due to air or liquid layers. *Acustica*, 51:201–212, 1982.

[56] A. Trochidis. *Körperschalldämpfung durch Viscositätsverluste in Gasschichten bei Doppelplatten*. PhD thesis, ITA Berlin, 1977. (In German).

[57] M. Möser. Damping of structure born sound by the viscosity of a layer between two plates. *Acustica*, 46:210–217, 1980.

[58] W.M. Beltman, P.J.M. van der Hoogt, R.M.E.J. Spiering, and H. Tijdeman. Energy dissipation in thin air layers. In P. Sas, editor, *ISMA 21 Conference on Noise and Vibration Engineering*, pages 1605–1618, Leuven, Belgium, 1996. Katholieke universiteit Leuven.

[59] W.M. Beltman, P.J.M. van der Hoogt, R.M.E.J. Spiering, and H. Tijdeman. Implementation and experimental validation of a new viscothermal acoustic finite element for acousto-elastic problems. *Journal of Sound and Vibration*, 1998. (accepted for publication).

[60] R.M.S.M. Schulkes. Interactions of an elastic solid with a viscous fluid: eigenmode analysis. Technical Report 90-46, Delft University of Technology, Faculty of Technical Mathematics and Informatics, Delft, The Netherlands, 1990.

[61] R.M.S.M. Schulkes. Fluid oscillations in an open, flexible container. Technical Report 89-69, Delft University of Technology, Faculty of Technical Mathematics and Informatics, Delft, The Netherlands, 1989.

[62] L.C. Chow and R.J. Pinnington. Practical industrial method of increasing structural damping in machinery, I: squeeze film damping with air. *Journal of Sound and Vibration*, 118:123–139, 1987.

[63] L.C. Chow and R.J. Pinnington. Practical industrial method of increasing structural damping in machinery, II: squeeze film damping with liquids. *Journal of Sound and Vibration*, 128:333–347, 1989.

[64] M.R. Stinson. The propagation of plane sound waves in narrow and wide circular tubes, and generalization to uniform tubes of arbitrary cross-section. *Journal of the Acoustical Society of America*, 89:550–558, 1991.

[65] A. Cummings. Sound propagation in narrow tubes of arbitrary cross-section. *Journal of Sound and Vibration*, 162:27–42, 1993.

[66] A.D. Lapin. Integral relations for acoustic modes in a channel with arbitrary cross-section. *Acoustical Physics*, 42:509–511, 1996.

[67] M.J.H. Fox and P.N. Whitton. The damping of structural vibrations by thin gas films. *Journal of Sound and Vibration*, 73:279–295, 1980.

[68] T. Önsay. Effects of layer thickness on the vibration response of a plate-fluid layer system. *Journal of Sound and Vibration*, 163:231–259, 1993.

[69] T. Önsay. Dynamic interaction between the bending vibrations of a plate and a fluid layer attenuator. *Journal of Sound and Vibration*, 178:289–313, 1994.

[70] W.M. Beltman, P.J.M. van der Hoogt, R.M.E.J. Spiering, and H. Tijdeman. Air loads on a rigid plate oscillating normal to a fixed surface. *Journal of Sound and Vibration*, 206(3):217–241, 1997.

[71] W.M. Beltman, P.J.M. van der Hoogt, R.M.E.J. Spiering, and H. Tijdeman. Air loads on solar panels during launch. In W.R. Burke, editor, *Conference on Spacecraft Structures, Materials and Mechanical Testing*, pages 219–226, Noordwijk, The Netherlands, 1996. European Space Agency. ESA SP-386.

[72] W.M. Beltman. Damping of double wall panels. *Journal of the Dutch Acoustical Society (NAG)*, 131:27–38, 1996. (in Dutch).

[73] M. Bruneau, A.M. Bruneau, Z. Škvor, and P. Lotton. An equivalent network modelling the strong coupling between a vibrating membrane and a fluid film. *Acustica*, 2:223–232, 1994.

[74] J.B. Mehl. Acoustic resonance frequencies of deformed spherical resonators. *Journal of the Acoustical Society of America*, 71:1109–1113, 1982.

[75] J.B. Mehl. Acoustic resonance frequencies of deformed spherical resonators, II. *Journal of the Acoustical Society of America*, 79:278–285, 1986.

[76] M. Abramowitz and I.A. Stengun. *Handbook of mathematical functions*. Dover publications, seventh Dover printing edition.

[77] P.M. Morse and H. Feshbach. *Methods of theoretical physics*. McGraw-Hill, 1953.

[78] P.N. Liang and H.A. Scarton. Attenuation of higher order circumferential thermoacoustic waves in viscous fluid lines. *Journal of Sound and Vibration*, 193:1099–1113, 1996.

[79] H. Hudde. The propagation constant in lossy circular tubes near the cutoff frequencies of higher order modes. *Journal of the Acoustical Society of America*, 83:1311–1318, 1988.

[80] J. Kergomard, M. Bruneau, A.M. Bruneau, and Ph. Herzog. On the propagation constant of higher order modes in a cylindrical waveguide. *Journal of Sound and Vibration*, 126:178–181, 1988.

[81] Computational Applications and System Integration Inc, 2004 S. Wright Street, Urbana, IL 61821, USA. *Ansys User Manual*, 5.3 edition, 1996.

[82] W. Kay Meyerhoff. Added masses of thin rectangular plates calculated from potential theory. *Journal of Ship Research*, pages 100–111, 1970.

[83] M.D. McCollum and C.M. Siders. Modal analysis of a structure in a compressible fluid using a finite element/boundary element approach. *Journal of the Acoustical Society of America*, 99(4):1949–1957, 1996.

[84] F.P. Grooteman. Coupled acousto-elastic analysis; theory and implementation in the finite element program B2000. Technical Report NLR CR 94218 L, National Aerospace Laboratory, The Netherlands, 1994. (restricted).

[85] S. Merazzi. *Modular finite element analysis tools applied to problems in engineering*. PhD thesis, EPFL Lausanne Nr. 1251, Switserland, 1994.

[86] E.H. Dowell, G.F. Gorman, and D.A. Smith. Acousto-elasticity: general theory, acoustic natural modes and forced response to sinusoidal excitation, including comparisons with experiment. *Journal of Sound and Vibration*, 52:519–542, 1977.

[87] R.D. Blevins. *Formulas for natural frequencies and mode shapes*. Van Nostrand Reinhold, first edition, 1979.

[88] H.T. Koelink, H. Schippers, J.J. Heijstek, and J.J Derksen. Modal analysis of solar panels using boundary integral equations. Technical Report NLR TP 92281 L, National Aerospace Laboratory, The Netherlands, 1992.

[89] P.E. Harrewijne. The influence of air on the eigenfrequencies of a solar array. Technical Report WFW 93.107, Technical University of Eindhoven, Eindhoven, The Netherlands, 1993.

[90] F.P. Grooteman and H. Schippers. Coupled analysis in acoustics on the dynamical behaviour of solar arrays. In P. Sas, editor, *ISMA 19 Conference on Noise and Vibration Engineering*, pages 101–124, Leuven, Belgium, 1994. Katholieke universiteit Leuven.

[91] J.J. Wijker. Acoustic effects on the dynamics of lightweight structures. Technical report, Fokker Space, Leiden, The Netherlands.

[92] P. Santini, F. Morganti, and R. Giovannucci. Acoustics of space structures. In North Atlantic Treaty Organization, editor, *Symposium on Impact of Acoustic Loads on Aircraft Structures*, pages 9A–1–9A–13, Lillehammer, Norway, 1994. AGARD-CP-549.

[93] B.W. Kooi. Air effects on the dynamic behaviour of stowed solar array wings. Technical Report FSS-R-87-134 (restricted), Fokker Space, Leiden, The Netherlands, 1987.

[94] J.F. Dijksman. Hydrodynamics of small tubular pumps. *Journal of Fluid Mechanics*, 139:173–191, 1984.

[95] J.D. Beasly. Model for fluid ejection and refill in an impulsive drive jet. *Photographic Science and Engineering*, 21:78–82, 1977.

[96] D.F. Elger. *An experimental and analytical study of the internal fluid dynamics of an inkjet print head*. PhD thesis, Oregon State University, United States of America, 1986.

[97] D.F. Elger and R.L. Adams. Some notes on inkjet print head design. *Industrial Applications of Fluid Mechanics*, pages 51–54, 1987.

[98] D.A. Bies and C.H. Hansen. *Engineering Noise Control*. E&FN Spon, second edition, 1996.

[99] T.G.H. Basten, W.M. Beltman, and H. Tijdeman. Optimization of viscothermal damping of double wall panels. In *InterNoise 98*, Christchurch, New Zealand, 1998.

[100] G.C.J. Hofmans. *Vortex sound in confined flows*. PhD thesis, Technical University of Eindhoven, The Netherlands, 1998.

Appendix A

Nomenclature

A	function describing velocity and temperature profiles
A_q, B_q	participation factors
$A_{aq}, B_{aq}, A_{hq}, B_{hq}$	constants
$\overline{A}^{cd}$	cross-sectional area
A^{cd}	dimensionless cross-sectional area
∂A^{cd}	dimensionless area of cross-section boundary
$\overline{A}^{pd}$	propagation direction area
$\partial \overline{A}^{pd}$	area of propagation direction boundary
$B(s)$	function accounting for viscous or thermal effects
$a = \frac{l_y}{l_x}$	aspect ratio
C	function describing the temperature profile
C_1, C_2, C_3, C_4	constants
C_p	specific heat at constant pressure
C_v	specific heat at constant volume
c_0	undisturbed speed of sound
c_d	non-linear dissipation factor
c_{eff}	effective speed of sound
D	function describing the temperature profile
DF	dissipation factor
$D_p = \frac{E_p t_p^3}{12}$	bending stiffness
E_p	Young's modulus of plate material
E_t	Young's modulus of top layer
E_b	Young's modulus of bottom layer

$\overline{E}_{diss}$	dissipated energy per cycle
$\overline{E}_{in}$	incident energy per cycle
$\overline{E}_{lay}$	energy stored in the air layer
$\overline{E}_{p}$	energy stored in plate
$\overline{E}_{rad}$	radiated energy per cycle
$\overline{E}_{vortex}$	dissipated energy per cycle by vortex mechanism
$\boldsymbol{e}_n$	unit normal vector
$\boldsymbol{e}_r$	unit vector in the r-direction
$\boldsymbol{e}_x$	unit vector in the x-direction
$\boldsymbol{e}_y$	unit vector in the y-direction
$\boldsymbol{e}_z$	unit vector in the z-direction
$\boldsymbol{e}_\theta$	unit vector in the θ-direction
$\boldsymbol{e}_\phi$	unit vector in the ϕ-direction
$\overline{F}_{ex}$	excitation force
$\overline{F}_{gap}$	force due to the pressure distribution in the gap
$\overline{F}_{gap}$	spring force
f_m	function describing wave propagation in tubes
H	transfer function
h_0	half-layer thickness
h_b	dimensionless displacement of top springs, half-barrier height
h_n	half-nozzle height
h_t	dimensionless displacement of bottom springs
I	area moment of inertia
$i = \sqrt{-1}$	imaginary unit
J	torsion constant
j_n	spherical Bessel function of order n
J_m	Bessel function of the first kind, order m
$k = \frac{\omega l}{c_0}$	reduced frequency
k_a	acoustic wave number
$k_{aq} = k_a^2 - k_q^2$	wave number
$k_{ar} = \sqrt{k_a^2 + k^2\Gamma^2}$	wave number
$\overline{k}_b$	stiffness of bottom spring
k_b	dimensionless stiffness of bottom spring
k_h	entropic wave number
$k_{hq} = k_h^2 - k_q^2$	wave number
$k_{hr} = \sqrt{k_h^2 + k^2\Gamma^2}$	wave number
k_p	plate elastic wave number
$k_{p1} = kk_p$	wave number
$k_{p2} = \sqrt{is^2 + k^2k_p^2}$	wave number

k_q	wave number
$k_r = \frac{\omega R}{c_0}$	wave number in the r-direction
$\overline{k}_t$	stiffness of top spring
k_t	dimensionless stiffness of top spring
$k_x = \frac{\omega l_x}{c_0}$	wave number in the x-direction
k_v	rotational wave number
$k_{vq} = k_v^2 - k_q^2$	wave number
l	characteristic length scale
l_n	half length of nozzle
l_x	half length in the x-direction
l_{xb}	half barrier length in the x-direction
l_y	half length in the y-direction
l_{yb}	half barrier length in the y-direction
l_z	half length in the z-direction
m	mass, order of circumferential harmonic waves
m'	mass per unit length
$n(s\sigma)$	polytropic constant
$\overline{p} = p_0 \left[1 + pe^{i\omega t}\right]$	pressure
p_0	mean pressure
p	dimensionless pressure amplitude
$\overline{p}_i = p_0 \left[1 + p_i e^{i\omega t}\right]$	incident pressure on membrane
p_i	dimensionless incident pressure amplitude
$\overline{p}_1$	pressure in point 1
$\overline{p}_2$	pressure in point 2
$\overline{p}_3$	pressure in point 3
PP_A	average quadratic pressure in room A
PP_B	average quadratic pressure across absorbing boundary of room B
R	radius
$\Re$	squeeze term
R_0	gas constant
$\overline{r}$	radial co-ordinate
r	dimensionless radial co-ordinate
Sr	acoustic Strouhal number
$s = l\sqrt{\frac{\rho_0 \omega}{\mu}}$	shear wave number
$\overline{T} = T_0 \left[1 + Te^{i\omega t}\right]$	temperature
T_0	mean temperature
T	dimensionless temperature amplitude
T_a	acoustic temperature
T_h	entropic temperature
T_m	membrane tension
TL	transmission loss

t	time
t_b	thickness of bottom layer
t_m	membrane thickness
t_p	plate thickness
t_{p1}	thickness plate 1
t_{p2}	thickness plate 2
t_{ref}	reference time
t_t	thickness of top layer
$\overline{\boldsymbol{v}} = c_0 \boldsymbol{v} e^{i\omega t}$	velocity vector
$\boldsymbol{v}$	dimensionless amplitude of the velocity vector
v	dimensionless amplitude of the velocity
$\boldsymbol{v}_l$	solenoidal velocity vector
$\boldsymbol{v}_{la}$	acoustic part of solenoidal velocity vector
$\boldsymbol{v}_{lh}$	entropic part of solenoidal velocity vector
$\boldsymbol{v}_v$	rotational velocity vector
$\overline{v}_m = c_0 v_m e^{i\omega t}$	membrane velocity
$< \overline{v}_m >$	average membrane velocity
v_m	dimensionless membrane velocity
$\overline{v}_p$	plate velocity
v_p	dimensionless plate velocity
v_r	dimensionless velocity component in the r-direction
$\overline{v}_{ref}$	reference velocity
v_x	dimensionless velocity component in the x-direction
$\overline{v}_{xn}$	nozzle velocity in the x-direction
v_{xn}	dimensionless nozzle velocity in the x-direction
v_y	dimensionless velocity component in the y-direction
v_z	dimensionless velocity component in the z-direction
v_θ	dimensionless velocity component in the θ-direction
v_ϕ	dimensionless velocity component in the ϕ-direction
$\boldsymbol{v}^{cd}$	velocity vector in the cd-directions
$\boldsymbol{v}^{pd}$	velocity vector in the pd-directions
W_1, W_2	constants
$\overline{x} = l_x x$	x-co-ordinate
x	dimensionless x-co-ordinate
$\boldsymbol{x}$	spatial co-ordinates
$\boldsymbol{x}^{cd}$	cross-sectional co-ordinates
$\boldsymbol{x}^{pd}$	propagation co-ordinates
$\overline{y} = l_y y$	y-co-ordinate
Y	mobility function
Y_{mn}	spherical harmonic function
y	dimensionless y-co-ordinate

$\overline{z} = h_0 z$	z-co-ordinate
$\overline{Z}$	membrane impedance
$\overline{Z}_0$	reference level for the impedance
$\overline{Z}_i$	imaginary part of membrane impedance
Z_n	specific normal acoustic impedance
$\overline{Z}_r$	real part of membrane impedance
z	dimensionless z-co-ordinate

α	rotation angle
Γ	propagation constant
$\gamma = \frac{C_p}{C_v}$	ratio of specific heats
$\varepsilon = \frac{\rho_0 h_0}{\rho_p t_p}$	ratio of mass per unit area
η	bulk viscosity
$\overline{\theta}$	co-ordinate in the θ-direction
θ	dimensionless co-ordinate in the θ-direction
Λ_a	constant
Λ_h	constant
λ	thermal conductivity
μ	dynamic viscosity
ξ	viscosity ratio, dimensionless damping coefficient
ξ_0	dimensionless damping coefficient for linear viscothermal damping
ν_p	Poisson's ratio of plate material
$\overline{\rho} = \rho_0 \left[1 + \rho e^{i\omega t}\right]$	density
ρ_0	mean density of air
ρ	dimensionless density amplitude
ρ_m	density of membrane material
ρ_p	density of plate material
$\sigma = \sqrt{\frac{\mu C_p}{\lambda}}$	square root of the Prandtl number
Φ	viscous dissipation function
$\overline{\phi}$	co-ordinate in the ϕ-direction
ϕ	dimensionless co-ordinate in the ϕ-direction
Ω	dimensionless frequency
ω	angular frequency

$\overline{\boldsymbol{\nabla}}$	gradient operator
$\boldsymbol{\nabla}$	dimensionless gradient operator
$\boldsymbol{\nabla}^{cd}$	dimensionless gradient operator in the *cd*-directions
$\boldsymbol{\nabla}^{pd}$	dimensionless gradient operator in the *pd*-directions
$\overline{\Delta}$	Laplace operator
Δ	dimensionless Laplace operator
Δ^{cd}	dimensionless Laplace operator in the *cd*-directions
Δ^{r}	dimensionless Laplace operator in the r-direction
ζ	loss factor
*	complex conjugate

$[K^a]$	acoustic stiffness matrix
$\left[\widehat{K}^a\right]$	acoustic stiffness matrix for the inviscid, adiabatic case
$[K^c]$	coupling matrix
$[K^s]$	structural stiffness matrix
$[M^a(s)]$	acoustic mass matrix
$\left[\widehat{M}^a\right]$	acoustic mass matrix for the inviscid, adiabatic case
$[M^c(s)]$	coupling matrix
$\left[\widehat{M}^c\right]$	coupling matrix for the inviscid, adiabatic case
$[M^s]$	structural mass matrix
$[N^a]$	acoustic interpolation functions
$[N^s]$	structural interpolation functions
$\left[\widehat{\Phi}^a\right]$	matrix with uncoupled acoustic modes for the inviscid, adiabatic case
$[\Phi^s]$	matrix with uncoupled structural modes
$\left[\widehat{\Omega}^a\right]$	diagonal acoustic eigenvalue matrix for the inviscid, adiabatic case
$[\Omega^s]$	diagonal structural eigenvalue matrix

$\{F^{ext}\}$	external force vector
$\left\{\widehat{F}^{ext}\right\}$	external force vector for the inviscid, adiabatic case
$\{P\}$	vector with pressure degrees of freedom
$\{U\}$	vector with structural degrees of freedom
$\{\eta_a\}$	vector with generalized acoustic co-ordinates
$\{\eta_s\}$	vector with generalized structural co-ordinates

Appendix B

Geometries, co-ordinate systems and functions

B.1 Sphere

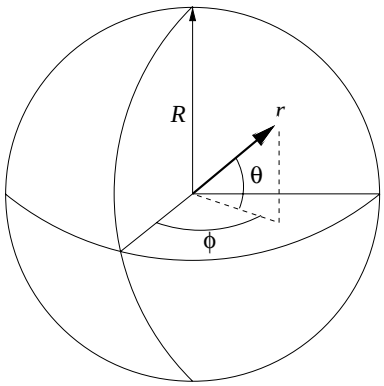

Figure B.1: Geometry of sphere

The basic geometrical dimensions and operators are:

$$\begin{aligned} l &= R \quad ; \quad \boldsymbol{x} = (r, \theta, \phi) \\ r &= \frac{\overline{r}}{R} \quad ; \quad \theta = \overline{\theta} \quad ; \quad \phi = \overline{\phi} \\ \boldsymbol{\nabla} &= \boldsymbol{e}_r \frac{\partial}{\partial r} + \boldsymbol{e}_\theta \frac{1}{r} \frac{\partial}{\partial \theta} + \boldsymbol{e}_\phi \frac{1}{r \sin(\theta)} \frac{\partial}{\partial \phi} \\ \Delta &= \frac{1}{r^2} \frac{\partial}{\partial r} \left[r^2 \frac{\partial}{\partial r} \right] + \frac{1}{r^2 \sin(\theta)} \frac{\partial}{\partial \theta} \left[\sin(\theta) \frac{\partial}{\partial \theta} \right] + \frac{1}{r^2 \sin(\theta)} \frac{\partial^2}{\partial \phi^2} \end{aligned} \tag{B.1}$$

B.2 Circular tube

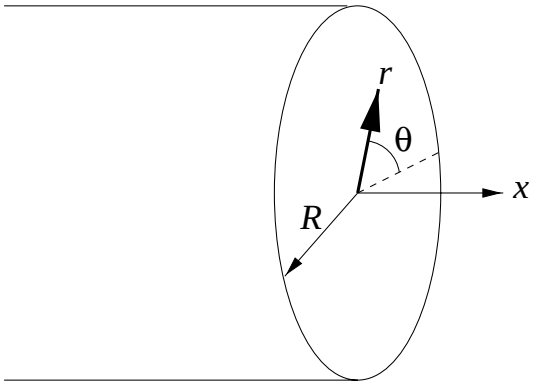

Figure B.2: Geometry of circular tube

The basic geometrical dimensions and operators are:

$$\begin{aligned} l &= R \quad ; \quad \boldsymbol{x} = (r, \theta, x) \\ r &= \frac{\overline{r}}{R} \quad ; \quad \theta = \overline{\theta} \quad ; \quad x = \frac{\omega \overline{x}}{c_0} \\ \boldsymbol{\nabla} &= \boldsymbol{e}_r \frac{\partial}{\partial r} + \boldsymbol{e}_\theta \frac{1}{r} \frac{\partial}{\partial \theta} + \boldsymbol{e}_x k \frac{\partial}{\partial x} \\ \Delta &= \frac{\partial^2}{\partial r^2} + \frac{1}{r} \frac{\partial}{\partial r} + \frac{1}{r^2} \frac{\partial^2}{\partial \theta^2} + k^2 \frac{\partial^2}{\partial x^2} \end{aligned} \tag{B.2}$$

The operators for the low reduced frequency model are:

$$\begin{aligned} \boldsymbol{x}^{cd} = (r, \theta) \quad ; \quad \boldsymbol{x}^{pd} = (x) \\ \boldsymbol{\nabla}^{cd} = \boldsymbol{e}_r \frac{\partial}{\partial r} + \boldsymbol{e}_\theta \frac{1}{r} \frac{\partial}{\partial \theta} \quad ; \quad \boldsymbol{\nabla}^{pd} = \boldsymbol{e}_x k \frac{\partial}{\partial x} \\ \Delta^{cd} = \frac{\partial^2}{\partial r^2} + \frac{1}{r} \frac{\partial}{\partial r} + \frac{1}{r^2} \frac{\partial^2}{\partial \theta^2} \quad ; \quad \Delta^{pd} = k^2 \frac{\partial^2}{\partial x^2} \end{aligned} \tag{B.3}$$

The functions that are used in the low reduced frequency model are given in Table B.1.

	Total	*Low s*	*High s*
A	$\dfrac{J_0\left(sri\sqrt{i}\right)}{J_0\left(si\sqrt{i}\right)} - 1$	$-\dfrac{1}{4}is^2\left[1-r^2\right]$	-1
B	$\dfrac{J_2\left(si\sqrt{i}\right)}{J_0\left(si\sqrt{i}\right)}$	$-\dfrac{1}{8}is^2$	-1
$\Re$	$\dfrac{1}{\pi}\displaystyle\int_{\theta=0}^{2\pi} v_r(x,1,\theta)d\theta$		

Table B.1: Expressions for circular tube

B.3 Rectangular tube

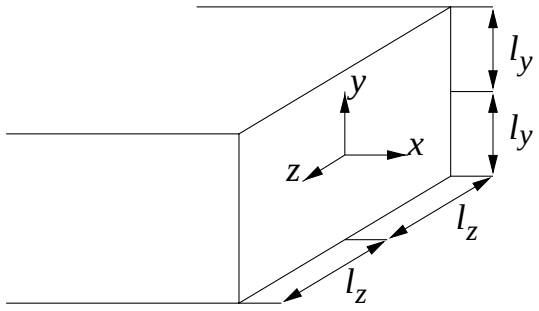

Figure B.3: Geometry of rectangular tube

The basic geometrical dimensions and operators are:

$$\begin{aligned} l &= l_y \quad ; \quad \boldsymbol{x} = (x, y, z) \quad ; \quad a = \frac{l_z}{l_y} \\ x &= \frac{\omega \overline{x}}{c_0} \quad ; \quad y = \frac{\overline{y}}{l_y} \quad ; \quad z = \frac{\overline{z}}{l_y} \\ \boldsymbol{\nabla} &= \boldsymbol{e}_x k \frac{\partial}{\partial x} + \boldsymbol{e}_y \frac{\partial}{\partial y} + \boldsymbol{e}_z \frac{\partial}{\partial z} \\ \Delta &= k^2 \frac{\partial^2}{\partial x^2} + \frac{\partial^2}{\partial y^2} + \frac{\partial^2}{\partial z^2} \end{aligned} \tag{B.4}$$

The operators for the low reduced frequency model are:

$$\begin{aligned} \boldsymbol{x}^{cd} = (y, z) \quad ; \quad \boldsymbol{x}^{pd} = (x) \\ \boldsymbol{\nabla}^{cd} = \boldsymbol{e}_x k \frac{\partial}{\partial x} \quad ; \quad \boldsymbol{\nabla}^{pd} = \boldsymbol{e}_y \frac{\partial}{\partial y} + \boldsymbol{e}_z \frac{\partial}{\partial z} \\ \Delta^{cd} = \frac{\partial^2}{\partial y^2} + \frac{\partial^2}{\partial z^2} \quad ; \quad \Delta^{pd} = k^2 \frac{\partial^2}{\partial x^2} \end{aligned} \tag{B.5}$$

The functions that are used in the low reduced frequency model are given in table B.2.

	Total	*Low s*	*High s*
A	$Q_1 \sum_{q=1,3\ldots}^{\infty} \frac{-1^{\frac{q-1}{2}}}{qQ_2^2} \left[\frac{\cosh(Q_2 z)}{\cosh(Q_2)} - 1\right] \cos\left(\frac{q\pi y}{2}\right)$ $Q_1 = \frac{ia^2 s^2 4}{\pi} \quad ; \quad Q_2 = a\sqrt{\left(\frac{q\pi}{2}\right)^2 + is^2}$	$Q_1 \sum_{q=1,3\ldots}^{\infty} \frac{-1^{\frac{q-1}{2}}}{q\hat{Q}_2{}^2} \left[\frac{\cosh\left(\hat{Q}_2 z\right)}{\cosh\left(\hat{Q}_2\right)} - 1\right] \cos\left(\frac{q\pi y}{2}\right)$ $Q_1 = \frac{ia^2 s^2 4}{\pi} \quad ; \quad \hat{Q}_2 = a\frac{q\pi}{2}$	-1
B	$Q_1 \sum_{q=1,3\ldots}^{\infty} \frac{-1^{\frac{q-1}{2}}}{q^2 Q_2^2} \left[\frac{\tanh(aQ_2)}{aQ_2} - 1\right]$ $Q_1 = \frac{ia^2 s^2 8}{\pi^2} \quad ; \quad Q_2 = a\sqrt{\left(\frac{q\pi}{2}\right)^2 + is^2}$	$Q_1 \sum_{q=1,3\ldots}^{\infty} \frac{-1^{\frac{q-1}{2}}}{q^2\hat{Q}_2{}^2} \left[\frac{\tanh\left(a\hat{Q}_2\right)}{a\hat{Q}_2} - 1\right]$ $Q_1 = \frac{ia^2 s^2 8}{\pi^2} \quad ; \quad \hat{Q}_2 = a\frac{q\pi}{2}$	-1
$\Re$	$\frac{1}{4}\int_{z=-1}^{1} [v_y(x,1,z) - v_y(x,-1,z)]\, dz \; + \; \frac{1}{4}\frac{1}{a}\int_{y=-1}^{1} [v_z(x,y,1) - v_z(x,y,-1)]\, dy$		

Table B.2: Expressions for rectangular tube

B.4 Circular layer

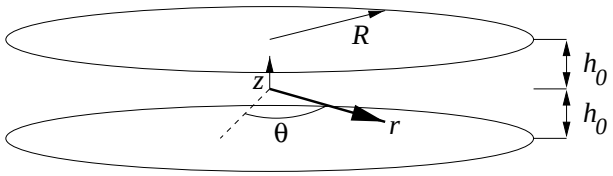

Figure B.4: Geometry of the circular layer

The basic geometrical dimensions and operators are:

$$\begin{aligned} l &= h_0 \quad ; \quad \boldsymbol{x} = (r, \theta, z) \\ r &= \frac{\omega \overline{r}}{c_0} \quad ; \quad \theta = \overline{\theta} \quad ; \quad z = \frac{\overline{z}}{h_0} \\ \boldsymbol{\nabla} &= \boldsymbol{e}_r k \frac{\partial}{\partial r} + \boldsymbol{e}_\theta k \frac{1}{r} \frac{\partial}{\partial \theta} + \boldsymbol{e}_z \frac{\partial}{\partial z} \\ \Delta &= k^2 \frac{\partial^2}{\partial r^2} + k^2 \frac{1}{r} \frac{\partial}{\partial r} + k^2 \frac{1}{r^2} \frac{\partial^2}{\partial \theta^2} + \frac{\partial^2}{\partial z^2} \end{aligned} \tag{B.6}$$

The operators for the low reduced frequency model are:

$$\begin{aligned} \boldsymbol{x}^{cd} = (z) \quad &; \quad \boldsymbol{x}^{pd} = (r, \theta) \\ \boldsymbol{\nabla}^{cd} = \boldsymbol{e}_z \frac{\partial}{\partial z} \quad &; \quad \boldsymbol{\nabla}^{pd} = \boldsymbol{e}_r k \frac{\partial}{\partial r} + \boldsymbol{e}_\theta k \frac{1}{r} \frac{\partial}{\partial \theta} \\ \Delta^{cd} = \frac{\partial^2}{\partial z^2} \quad &; \quad \Delta^{pd} = k^2 \frac{\partial^2}{\partial r^2} + k^2 \frac{1}{r} \frac{\partial}{\partial r} + k^2 \frac{1}{r^2} \frac{\partial^2}{\partial \theta^2} \end{aligned} \tag{B.7}$$

The functions that are used in the low reduced frequency model are given in table B.3.

	Total	*Low s*	*High s*
A	$\dfrac{\cosh\left(sz\sqrt{i}\right)}{\cosh\left(s\sqrt{i}\right)} - 1$	$\dfrac{1}{2}is^2\left[\dfrac{1}{3}z^2 - 1\right]$	-1
B	$\dfrac{\tanh\left(s\sqrt{i}\right)}{s\sqrt{i}} - 1$	$-\dfrac{1}{3}is^2$	-1
$\Re$	$\dfrac{1}{2}\left[v_z(x,y,1) - v_z(x,y,-1)\right]$		

Table B.3: Expressions for the circular layer

B.5 Rectangular layer

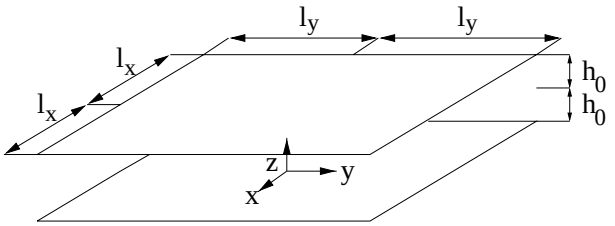

Figure B.5: Geometry of the rectangular layer

The basic geometrical dimensions and operators are:

$$\begin{aligned} l &= h_0 \quad ; \quad \boldsymbol{x} = (x, y, z) \quad ; \quad a = \frac{l_y}{l_x} \\ x &= \frac{\omega \overline{x}}{c_0} \quad ; \quad y = \frac{\omega \overline{y}}{c_0} \quad ; \quad z = \frac{\overline{z}}{h_0} \\ \boldsymbol{\nabla} &= \boldsymbol{e}_x k \frac{\partial}{\partial x} + \boldsymbol{e}_y k \frac{\partial}{\partial y} + \boldsymbol{e}_z \frac{\partial}{\partial z} \qquad \text{(B.8)} \\ \Delta &= k^2 \frac{\partial^2}{\partial x^2} + k^2 \frac{\partial^2}{\partial y^2} + \frac{\partial^2}{\partial z^2} \qquad \text{(B.9)} \end{aligned}$$

The operators for the low reduced frequency model are:

$$\begin{aligned} \boldsymbol{x}^{cd} = (z) \quad ; \quad \boldsymbol{x}^{pd} &= (x, y) \\ \boldsymbol{\nabla}^{cd} = \boldsymbol{e}_z \frac{\partial}{\partial z} \quad ; \quad \boldsymbol{\nabla}^{pd} &= \boldsymbol{e}_x k \frac{\partial}{\partial x} + \boldsymbol{e}_y k \frac{\partial}{\partial y} \qquad \text{(B.10)} \\ \Delta^{cd} = \frac{\partial^2}{\partial z^2} \quad ; \quad \Delta^{pd} &= k^2 \frac{\partial^2}{\partial x^2} + k^2 \frac{\partial^2}{\partial y^2} \end{aligned}$$

The functions that are used in the low reduced frequency model are given in table B.4.

	Total	*Low s*	*High s*
A	$\dfrac{\cosh\left(sz\sqrt{i}\right)}{\cosh\left(s\sqrt{i}\right)} - 1$	$\dfrac{1}{2}is^2\left[\dfrac{1}{3}z^2 - 1\right]$	-1
B	$\dfrac{\tanh\left(s\sqrt{i}\right)}{s\sqrt{i}} - 1$	$-\dfrac{1}{3}is^2$	-1
$\Re$	$\dfrac{1}{2}\left[v_z(x,y,1) - v_z(x,y,-1)\right]$		

Table B.4: Expressions for the rectangular layer

Appendix C

Numerical solution procedures

C.1 The spherical resonator

As an example, the eigenfrequencies of a spherical resonator are calculated. The equation of interest is:

$$\left[1-\frac{\alpha_h}{\alpha_a}\right]\left[\frac{n(n+1)}{1+\dfrac{1}{j_n\left(k_v\right)}\left.\dfrac{\partial j_n\left(k_v r\right)}{\partial r}\right|_1}\right]= \tag{C.1}$$
$$\frac{1}{j_n\left(k_a\right)}\left.\frac{\partial j_n\left(k_a r\right)}{\partial r}\right|_1-\left(\frac{\alpha_h}{\alpha_a}\right)\frac{1}{j_n\left(k_h\right)}\left.\frac{\partial j_n\left(k_h r\right)}{\partial r}\right|_1$$

The partial derivatives of the spherical Bessel functions are:

$$\frac{\partial j_n\left(k_a r\right)}{\partial r}=k_a\left[j_{n-1}\left(k_a r\right)-\left(\frac{n+1}{k_a r}\right)j_n\left(k_a r\right)\right] \tag{C.2}$$

The equation for the eigenfrequencies can now be written as:

$$\left[1-\frac{\alpha_h}{\alpha_a}\right]\left[\frac{n(n+1)}{1+k_v\left\{\dfrac{j_{n-1}\left(k_v\right)}{j_n\left(k_v\right)}-\left(\dfrac{n+1}{k_v}\right)\right\}}\right]= \tag{C.3}$$
$$k_a\left[\frac{j_{n-1}\left(k_a\right)}{j_n\left(k_a\right)}-\left(\frac{n+1}{k_a}\right)\right]-\frac{\alpha_h}{\alpha_a}k_h\left[\frac{j_{n-1}\left(k_h\right)}{j_n\left(k_h\right)}-\left(\frac{n+1}{k_h}\right)\right]$$

For very large values of the imaginary part of the argument, the value of the spherical Bessel functions becomes very large. This causes problems in the

numerical solution of the equation. The spherical Bessel functions can be written as:

$$\begin{aligned} j_0(k_a r) &= \frac{\sin(k_a r)}{k_a r} \\ j_1(k_a r) &= \frac{\sin(k_a r)}{(k_a r)^2} - \frac{\cos(k_a r)}{(k_a r)} \\ j_2(k_a r) &= \left(\frac{3}{(k_a r)^3} - \frac{1}{k_a r}\right)\sin(k_a r) - \frac{3}{(k_a r)^2}\cos(k_a r) \\ j_{n+1}(k_a r) &= \left(\frac{2n+1}{k_a r}\right) j_n(k_a r) - j_{n-1}(k_a r) \end{aligned} \qquad \text{(C.4)}$$

In order to avoid problems for large values of the imaginary part of the argument, the appropriate component was removed from the ratio of Bessel functions by dividing both the numerator and the denonimator by this exponential component. The eigenfrequencies were obtained using a simple function minimization procedure in the program MatLab. However, the solution procedure required some care. For the present test case, the ratio between the real and the imaginary parts of the frequency is of the order of 10^3 to 10^6. The minimization procedure in MatLab is able to minimize a scalar function of multiple variables. The real part of the function to be minimized is mainly related to the real part of the frequency, whereas the imaginary part of the function is mainly determined by the imaginary component of the frequency. As for the frequency, the real and the imaginary parts of the function are of a different order of magnitude. Minimizing the absolute value of the function is therefore not a good approach, since this approach is relatively insensitive to changes in the imaginary part of the frequency. Therefore another strategy was adopted. First, the (square of the) real part of the function was minimized with the real part of the frequency as the minimization variable. In the second step, the (square of the) imaginary part of the function was minimized with the imaginary frequency component as variable. This process was then repeated until convergence was obtained.

Although very simple, this approach proved to be successful. For various starting values the same final result was obtained. A good starting value could be provided by using the eigenfrequencies calculated from the wave equation. The eigenfrequencies from the wave equation are obtained by setting k_a equal to k and taking the limit for $k_h \to \infty$ and $k_v \to \infty$. This gives:

$$\frac{\partial j_n(k)}{\partial r} = 0 \qquad \text{(C.5)}$$

For each value of n there are several solutions to this equation.

C.2 Circular tubes

The dispersion equation to be solved for given values of m, k and s is:

$$\left[1-\frac{\alpha_h}{\alpha_a}\right]\frac{{k_v}^2}{{k_v}^2+k^2\Gamma^2}\left[\frac{m^2}{\left.\frac{1}{J_m\left(k_{vr}\right)}\frac{\partial J_m\left(k_{vr}r\right)}{\partial r}\right|_1}+\frac{k^2\Gamma^2}{{k_v}^2}\frac{1}{J_m\left(k_{vr}\right)}\left.\frac{\partial J_m\left(k_{vr}r\right)}{\partial r}\right|_1\right]$$

$$=\left.\frac{1}{J_m\left(k_{ar}\right)}\frac{\partial J_m\left(k_{ar}r\right)}{\partial r}\right|_1-\frac{\alpha_h}{\alpha_a}\frac{\left.\frac{\partial J_m\left(k_{hr}r\right)}{\partial r}\right|_1}{J_m\left(k_{hr}\right)} \tag{C.6}$$

The partial derivatives of the Bessel functions are:

$$\frac{\partial J_m\left(k_ar\right)}{\partial r}=k_a\left[J_{m-1}\left(k_ar\right)-\left(\frac{m}{k_ar}\right)J_m\left(k_ar\right)\right] \tag{C.7}$$

The dispersion equation can be written as:

$$\left[1-\frac{\alpha_h}{\alpha_a}\right]\frac{{k_v}^2}{{k_v}^2+k^2\Gamma^2}\left[\frac{m^2}{k_{vr}\left[\frac{J_{m-1}\left(k_{vr}r\right)}{J_m\left(k_{vr}r\right)}-\frac{m}{k_{vr}}\right]}+\frac{k^2\Gamma^2}{{k_v}^2}k_{vr}\left[\frac{J_{m-1}\left(k_{vr}r\right)}{J_m\left(k_{vr}r\right)}-\frac{m}{k_{vr}}\right]\right]$$

$$=k_{ar}\left[\frac{J_{m-1}\left(k_{ar}r\right)}{J_m\left(k_{ar}r\right)}-\frac{m}{k_{ar}}\right]-\frac{\alpha_h}{\alpha_a}k_{hr}\left[\frac{J_{m-1}\left(k_{hr}r\right)}{J_m\left(k_{hr}r\right)}-\frac{m}{k_{hr}}\right] \tag{C.8}$$

This equation was solved with a standard function minimization procedure in the program MatLab. The absolute value of the function was minimized with respect to the real and the imaginary parts of the propagation constant. Good starting values were obtained by performing a series of calculations. For a given value of k, the propagation constant was calculated for a high shear wave number s. For this high value of s, the low reduced frequency solution for Γ was used as a starting value. Next, a calculation was varied out for a somewhat smaller value of s. The value for Γ, obtained in the previous calculation for the higher value of s, was now used as the starting value. In this way the values of Γ were determined for decreasing values of s. Given the well chosen starting values, the process converged quickly.

Appendix D

Experimental data

D.1 Oscillating rigid panel

$2h_0$ (mm)	f_n (Hz)	ξ (%)	$p1$ (Pa)	$p2$ (Pa)	$p3$ (Pa)	h_0h (mm)	T_0 (°C)	p_0 (Pa)
3	3.340	35.48	−−	−−	−−	−−	18.0	75.75
3.5	3.590	24.60	−−	−−	−−	−−	19.0	76.15
4	3.816	18.76	−−	−−	−−	−−	18.5	75.53
5	4.215	11.50	−−	−−	−−	−−	20.0	75.60
6	4.535	8.16	−−	−−	−−	−−	21.0	75.72
8	5.055	5.04	−−	−−	−−	−−	21.0	75.56
10	5.426	3.48	−−	−−	−−	−−	18.0	76.28
12	5.766	2.59	−−	−−	−−	−−	20.5	75.48
15	6.137	1.82	−−	−−	−−	−−	22.0	75.63
25	6.859	0.83	−−	−−	−−	−−	20.0	76.10
35	7.270	0.51	−−	−−	−−	−−	21.5	76.11
50	7.633	0.31	−−	−−	−−	−−	18.0	76.70
80	7.988	0.19	−−	−−	−−	−−	18.0	75.51
150	8.301	0.12	−−	−−	−−	−−	19.0	76.48
650	8.554	0.18	−−	−−	−−	−−	21.5	76.13

Table D.1: Oscillating rigid panel: data series 1

D.2 Rotating rigid panel

$2h_0$ (mm)	f_n (Hz)	ξ (%)	$p1$ (Pa)	$p2$ (Pa)	$p3$ (Pa)	h_0h (mm)	T_0 (°C)	p_0 (Pa)
3	3.332	35.48	4.67	3.74	0.09	0.22	18.0	76.43
3.5	3.606	24.39	4.22	3.44	0.25	0.25	19.0	76.28
4	3.848	18.71	4.03	3.24	0.25	0.25	22.0	75.80
5	4.215	11.65	3.61	2.94	0.24	0.24	18.0	76.06
6	4.523	8.24	3.70	3.01	0.26	0.26	21.5	76.66
8	5.043	5.05	3.50	2.88	0.23	0.23	20.5	76.66
10	5.445	3.53	3.24	2.68	0.27	0.27	22.5	76.64
12	5.770	2.61	3.11	2.62	0.25	0.25	21.0	76.23
15	6.137	1.83	2.86	2.42	0.28	0.28	22.0	76.16
25	6.879	0.85	2.23	1.94	0.28	0.28	22.0	75.97
35	7.281	0.52	1.80	1.61	0.28	0.28	21.0	75.80
50	7.637	0.33	−−	−−	−−	−−	22.0	75.80
80	7.996	0.21	−−	−−	−−	−−	21.5	75.87
150	8.305	0.12	−−	−−	−−	−−	19.5	76.44
650	8.559	0.13	−−	−−	−−	−−	24.5	76.18

Table D.2: Oscillating rigid panel: data series 2

$2h_0$ (mm)	f_n (Hz)	ξ (%)	$p1$ (Pa)	$p2$ (Pa)	$p3$ (Pa)	h_0h (mm)	T_0 (°C)	p_0 (Pa)
3	3.340	36.19	4.76	3.79	0.15	0.22	19.5	76.33
3.5	3.602	24.39	4.20	3.40	0.10	0.25	17.0	76.06
4	3.852	18.71	4.00	3.25	0.22	0.25	21.5	75.80
5	4.223	11.65	3.81	3.17	0.14	0.25	20.5	76.10
6	4.539	8.24	3.71	3.05	0.20	0.26	22.5	76.66
8	5.051	5.05	3.46	2.85	0.22	0.24	22.5	76.70
10	5.453	3.46	3.25	2.71	0.22	0.28	24.0	76.64
12	5.766	2.61	3.07	2.62	0.26	0.26	21.5	76.20
15	6.145	1.83	2.81	2.41	0.29	0.28	22.5	76.00
25	6.875	0.85	2.20	1.92	0.34	0.28	20.0	75.76
35	7.281	0.52	1.84	1.63	0.35	0.28	21.5	75.80
50	7.637	0.33	−−	−−	−−	−−	22.0	75.81
80	7.996	0.21	−−	−−	−−	−−	21.5	75.87
150	8.305	0.12	−−	−−	−−	−−	20.5	76.50
650	8.552	0.13	−−	−−	−−	−−	24.5	76.38

Table D.3: Oscillating rigid panel: data series 3

$2h_0$ (mm)	f_n (Hz)	ξ (%)
3	1.421	49.0
4	1.506	31.0
6	1.712	13.0
8	1.851	7.60
10	1.967	5.10
15	2.164	2.60
20	2.280	1.70
25	2.363	1.20
35	2.471	0.77
50	2.560	0.52

Table D.4: Rotating rigid panel: average values of 3 series

D.3 Oscillating rigid panel with barriers

$2h_b$ (mm)	f_n (Hz)	ξ (%)	$p1$ (Pa)	$p2$ (Pa)	$p3$ (Pa)	h_0h (mm)	T_0 (°C)	p_0 (Pa)
10	5.223	23.56	3.47	3.13	0.18	0.31	22.5	76.83
9	5.445	10.77	3.12	2.73	0.20	0.23	24.5	76.78
8	5.527	6.62	3.13	2.72	0.22	0.24	22.0	76.86

Table D.5: Oscillating rigid panel with 4 barriers: data series 1

$2h_b$ (mm)	f_n (Hz)	ξ (%)	$p1$ (Pa)	$p2$ (Pa)	$p3$ (Pa)	h_0h (mm)	T_0 (°C)	p_0 (Pa)
10	5.219	23.67	3.45	3.09	0.20	0.32	22.5	76.84
9	5.438	10.77	3.13	2.78	0.24	0.23	21.5	76.74
8	5.531	6.60	3.12	2.71	0.23	0.24	22.5	76.86

Table D.6: Oscillating rigid panel with 4 barriers: data series 2

$2h_b$ (mm)	f_n (Hz)	ξ (%)	$p1$ (Pa)	$p2$ (Pa)	$p3$ (Pa)	h_0h (mm)	T_0 (°C)	p_0 (Pa)
10	5.215	23.70	3.45	3.09	0.19	0.28	21.0	76.88
9	5.434	10.84	3.14	2.76	0.21	0.24	22.0	76.74
8	5.539	6.56	3.11	2.75	0.25	0.24	22.5	76.81

Table D.7: Oscillating rigid panel with 4 barriers: data series 3

$h_0 h$ (mm)	f_n (Hz)	ξ (%)
0.125	4.92	38.51
0.150	4.92	41.65
0.200	4.94	43.78
0.250	4.93	46.30
0.300	4.96	48.16
0.350	4.99	50.15
0.400	4.96	52.38
0.450	4.96	55.30
0.500	4.94	58.72

$h_0 h$ (mm)	f_n (Hz)	ξ (%)
0.150	5.17	25.23
0.225	5.18	29.16
0.300	5.20	31.59
0.375	5.15	33.74
0.450	5.16	36.65
0.525	5.13	39.34

$h_0 h$ (mm)	f_n (Hz)	ξ (%)
0.150	5.26	17.63
0.225	5.27	20.75
0.300	5.26	23.38
0.375	5.24	25.69
0.450	5.24	28.17
0.525	5.24	30.53

Table D.8: Oscillating rigid panel with 4 barriers: linearity for $2h_b =$ 10.66 mm (left), $2h_b =$ 10.33 mm (middle) and $2h_b =$ 10.00 mm (right)

Appendix E

Convergence tests

E.1 Layer elements

E.1.1 Frequency response calculations

Consider a rigid plate, located parallel to a fixed surface and performing a small normal oscillation (see chapter 4). For this situation the displacement amplitude for all the points on the panel is equal: $h(x, y) = h$. The edges of the layer are open, *i.e.* a $p = 0$ condition is imposed. The analytical solution for this case was given in section 4.2.1. The pressure distribution was also calculated with linear 4-noded and quadratic 8-noded viscothermal finite elements. The number of elements was varied in order to investigate whether the numerical results converged to the analytical values. The properties of the air in the gap under standard atmospheric conditions and the dimensions of the plate are the same as for the setup in chapter 4 (see expression (4.19)). The results are listed in Tables E.1 and E.2. In these Tables nx and ny represent the numbers of grid points in the x- and the y-directions respectively. For each calculation, the L_1 norm [1] of the difference between the numerical and analytical results is given for all calculated nodes and the centre node only. When the grid size is reduced by a factor of two, the corresponding error norm should reduce with a factor of 4 for linear elements and a factor of 16 for quadratic elements. This ratio is also given in the Table. The results indicate that the numerical results converge to the analytical values. It can be concluded that the viscothermal finite element gives good results.

[1] $L_1 = \frac{1}{nmax} \sum_{n=1}^{nmax} |v_n^{num} - v_n^{ana}|$

E.1.2 Eigenfrequency calculations

The acoustic eigenfrequencies of a rectangular layer are calculated with the viscothermal finite elements. The results are compared with analytical results. At the edges a $p = 0$ condition is imposed. The eigenfrequencies are calculated by separation of variables. In the case of a varying layer thickness, continuity of pressure and conservation of mass are imposed on the interface. The analytical and numerical results are listed in Tables E.3 and E.4.

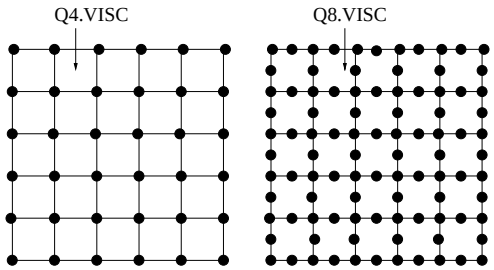

Figure E.1: Configurations for convergence tests of the layer elements

nx	ny	L_1	L_{1c}	$Ratio$	$Ratio_c$
5	5	1.29089	1.70957		
9	9	0.25819	0.39617	4.99	4.31
17	17	0.05763	0.09747	4.48	4.06
33	33	0.01359	0.02429	4.24	4.01
65	65	0.00332	0.00611	4.09	3.98

Table E.1: Convergence for Q4.VISC elements. ($h_0 = 1.5 \cdot 10^{-3}$ m, $l_x = 0.49$ m, $l_y = 0.49$ m, $f = 50$ Hz, $h = 1/(4\pi^2 f^2 h_0)$)

nx	ny	L_1	L_{1c}	$Ratio$	$Ratio_c$
9	9	0.107222	0.065359		
17	17	0.006812	0.003803	15.74	17.19

Table E.2: Convergence for Q8.VISC elements ($h_0 = 1.5{\cdot}10^{-3}$ m, $l_x = 0.49$ m, $l_y = 0.49$ m, $f = 50$ Hz, $h = 1/(4\pi^2 f^2 h_0)$)

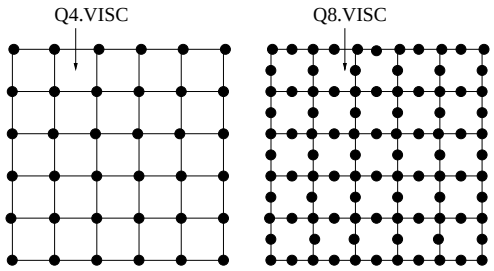

Figure E.2: Configurations for convergence tests of the layer elements

nx	ny	Q4.VISC	Q8.VISC
		Mode 11 analytical: 232.050+8.602i	
9	9	233.571+8.629i	232.115+8.603i
17	17	232.430+8.609i	232.054+8.602i
33	33	232.145+8.604i	232.051+8.602i
65	65	232.074+8.602i	232.051+8.602i
		Mode 21 analytical: 369.604+10.757i	
9	9	377.854+1.087i	370.803+10.774i
17	17	371.656+1.078i	369.683+10.758i
33	33	370.117+1.076i	369.610+10.757i
65	65	369.733+1.075i	369.605+10.757i
		Mode 22 analytical: 468.990+12.070i	
9	9	481.272+12.222i	471.597+12.102i
17	17	472.047+12.108i	469.120+12.071i
33	33	469.753+12.079i	468.998+12.070i
65	65	469.181+12.072i	468.991+12.070i

Table E.3: Convergence for Q4.VISC and Q8.VISC elements. ($h_0 = 1.5 \cdot 10^{-3}$ m, $l_x = 0.5$ m, $l_y = 0.5$ m)

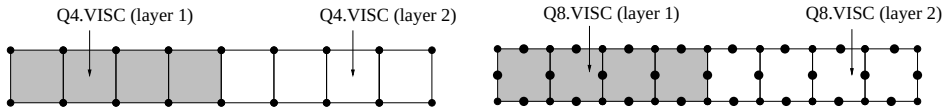

Figure E.3: Configurations for convergence tests of the layer elements

nx	Q4.VISC	Q8.VISC
	Mode 1 analytical: 119.815+4.842i	
17	120.161+4.838i	119.820+4.842i
33	119.901+4.841i	119.815+4.842i
65	119.837+4.842i	119.815+4.842i
129	119.820+4.842i	119.815+4.842i
	Mode 2 analytical: 209.068+6.608i	
17	210.475+6.623i	209.167+6.607i
33	209.421+6.611i	209.074+6.608i
65	209.156+6.608i	209.068+6.608i
129	209.090+6.608i	209.068+6.608i
	Mode 3 analytical: 331.040+9.176i	
17	338.411+9.240i	332.079+9.171i
33	332.882+9.192i	331.111+9.176i
65	331.501+9.180i	331.045+9.176i
129	331.155+9.177i	331.040+9.176i
	Mode 4 analytical: 455.249+9.474i	
17	471.160+9.252i	458.275+9.399i
33	459.318+9.418i	455.492+9.467i
65	456.272+9.460i	455.265+9.474i
129	455.505+9.471i	455.250+9.474i

Table E.4: Convergence for Q4.VISC and Q8.VISC elements (varying layer thickness: $h_{01} = 1.5 \cdot 10^{-3}$ m, $l_{x1} = 0.5$ m, $l_{y1} = 0.005$ m, $h_{02} = 3 \cdot 10^{-3}$ m, $l_{x2} = 0.25$ m, $l_{y2} = 0.005$ m)

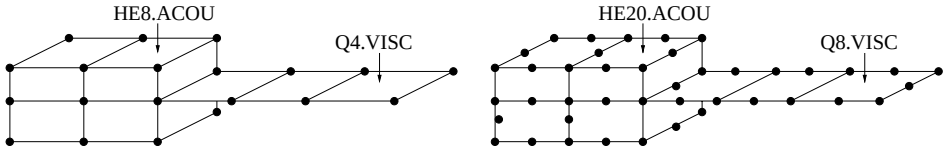

Figure E.4: Configurations for convergence tests of the layer elements

nx	HE8.ACOU/Q4.VISC	HE20.ACOU/Q8.VISC
	Mode 1 analytical **1D**: 104.915+0.911i	
17	105.143+0.916i	104.915+0.911i
33	104.969+0.912i	104.910+0.910i
65	104.923+0.910i	104.906+0.910i
129	104.906+0.910i	104.897+0.909i
	Mode 2 analytical **1D** : 233.158+1.077i	
17	235.248+1.112i	233.318+1.082i
33	233.676+1.087i	233.156+1.079i
65	233.272+1.081i	233.134+1.079i
129	233.156+1.081i	233.110+1.081i
	Mode 3 analytical **1D** : 337.734+2.320i	
17	343.369+2.384i	338.388+2.348i
33	339.091+2.336i	337.694+2.320i
65	337.964+2.322i	337.564+2.317i
129	337.582+2.317i	337.401+2.314i
	Mode 4 analytical **1D** : 444.182+1.611i	
17	460.199+1.706i	447.267+1.616i
33	448.181+1.631i	444.396+1.609i
65	445.158+1.612i	444.160+1.605i
129	444.381+1.604i	444.112+1.599i

Table E.5: Convergence for Q4.VISC/HE8.ACOU and Q8.VISC/HE20.ACOU elements ($l_{x1} = 0.5$ m, $l_{y1} = 0.005$ m, $l_{z1} = 0.005$ m,$h_{02} = 3 \cdot 10^{-3}$ m, $l_{x2} = 0.25$ m, $l_{y2} = 0.005$ m)

E.1.3 Acousto-elasticity

Consider a rectangular simply supported plate backed by a thin gas layer. The behaviour of the plate is decribed using the Kirchhoff equation:

$$\frac{E_p t_p^3}{12\left(1-\nu_p^2\right)}\left[\frac{\partial^4 \overline{v}_p}{\partial \overline{x}^4}+2\frac{\partial^2 \overline{v}_p}{\partial \overline{x}^2}\frac{\partial^2 \overline{v}_p}{\partial \overline{y}^2}+\frac{\partial^4 \overline{v}_p}{\partial \overline{y}^4}\right]+\rho_p t_p \frac{\partial^2 \overline{v}_p}{\partial t^2}=\overline{p}-p_0 \qquad \text{(E.1)}$$

where $\overline{v}_p$ is the velocity of the plate in the z-direction, E_p is Young's modulus, ρ_p is the density and ν_p is Poisson's ratio of the plate material. Introducing dimensionless quantities:

$$\begin{aligned} \overline{v}_p = c_0 v_p e^{i\omega t} \quad &; \quad \overline{p} = p_0\left[1+pe^{i\omega t}\right] \\ x = \frac{\omega \overline{x}}{c_0} \quad &; \quad y = \frac{\omega \overline{y}}{c_0} \end{aligned} \qquad \text{(E.2)}$$

The pressure distribution in the layer is described with the low reduced frequency model. The acousto-elastic behaviour of the system is described by the following set of equations:

$$\begin{aligned} k^4\left[\frac{\partial^4 v_p}{\partial x^4}+2\frac{\partial^2 v_p}{\partial x^2}\frac{\partial^2 v_p}{\partial y^2}+\frac{\partial^4 v_p}{\partial y^4}\right]-\frac{\Omega^2 k^4}{k_x^4}v_p &= i\frac{\Omega^2 \varepsilon k^3}{\gamma k_x^4}p \\ k^2\left[\frac{\partial^2 p}{\partial x^2}+\frac{\partial^2 p}{\partial y^2}\right]-k^2\Gamma^2 p &= -\frac{1}{2}ikn\left(s\sigma\right)v_p \end{aligned} \qquad \text{(E.3)}$$

For a simply supported panel, the mode shapes are:

$$\begin{aligned} v_p &= B_{qr}\sin\left(\frac{q\pi}{2}\left[\frac{x}{l_x}+1\right]\right)\sin\left(\frac{r\pi}{2}\left[\frac{y}{l_y}+1\right]\right) \quad q=1,2,\cdots \quad r=1,2,\cdots \\ p &= C_{qr}\sin\left(\frac{q\pi}{2}\left[\frac{x}{l_x}+1\right]\right)\sin\left(\frac{r\pi}{2}\left[\frac{y}{l_y}+1\right]\right) \end{aligned} \qquad \text{(E.4)}$$

Inserting these expressions finally gives the following set of equations:

$$\begin{bmatrix} A_{11} & A_{12} \\ A_{21} & A_{22} \end{bmatrix}\begin{Bmatrix} B_{qr} \\ C_{qr} \end{Bmatrix} = \begin{Bmatrix} 0 \\ 0 \end{Bmatrix} \qquad \text{(E.5)}$$

where the matrix elements are given by:

$$\begin{aligned} A_{11} &= -i\frac{\Omega^2 \varepsilon k^3}{\gamma k_x^4} \\ A_{12} &= k^4\left[\left(\frac{q\pi}{2k_x}\right)^4+2\left(\frac{q\pi}{2k_x}\right)^2\left(\frac{r\pi}{2ak_x}\right)^2+\left(\frac{r\pi}{2ak_x}\right)^4\right]-\frac{\Omega^2 k^4}{k_x^4} \\ A_{21} &= k^2\left[-\left(\frac{q\pi}{2k_x}\right)^2-\left(\frac{r\pi}{2ak_x}\right)^2\right]-k^2\Gamma^2 \\ A_{22} &= \frac{1}{2}ikn\Gamma^2 \end{aligned} \qquad \text{(E.6)}$$

The structural modes, the acoustic modes and the acousto-elastic modes are obtained from:

$$\begin{aligned} \text{structural modes}: &\quad A_{11} = 0 \\ \text{acoustic modes}: &\quad A_{22} = 0 \\ \text{acousto}-\text{elastic modes}: &\quad A_{11}A_{22} - A_{21}A_{12} = 0 \end{aligned} \tag{E.7}$$

The eigenfrequencies were solved with a simple minimization procedure in Matlab, setting the absolute value equal to zero. This proved to be a fast and stable approach. The results are given in Tables E.6, E.7 and E.8

nx	*ny*	Q4.VISC
Mode 11 analytical: 468.990+12.070i		
9	9	472.047+12.108i
17	17	469.753+12.079i
20	20	469.479+12.076i
33	33	469.181+12.072i
Mode 21 analytical: 745.366+15.119i		
9	9	761.933+15.282i
17	17	749.487+15.160i
20	20	748.002+15.145i
33	33	746.395+15.129i
Mode 22 analytical: 944.909+16.977i		
9	9	969.562+17.192i
17	17	951.046+17.030i
20	20	948.835+17.011i
33	33	946.442+16.990i

Table E.6: Convergence for Q4.VISC elements. ($h_0 = 1.5 \cdot 10^{-3}$ m, $l_x = 0.25$ m, $l_y = 0.25$ m)

nx	*ny*	Q4.VISC
	Mode 11 analytical: 19.326	
9	9	19.640
17	17	19.403
20	20	19.375
33	33	19.344
	Mode 21 analytical: 48.317	
9	9	51.405
17	17	49.054
20	20	48.785
33	33	48.496
	Mode 22 analytical: 77.307	
9	9	82.506
17	17	78.556
20	20	78.100
33	33	77.609

Table E.7: Convergence for Q4.ST elements. ($l_x = 0.25$ m, $l_y = 0.25$ m, $E_p = 70 \cdot 10^9$ N/m^2, $\rho_p = 2710$ kg/m^3, $\nu_p = 0.3$, $t_p = 1 \cdot 10^{-3}$ m)

nx	ny	Q4.VISC
Mode 11 analytical: 10.711+1.094i		
9	9	10.937+1.096i
17	17	10.766+1.094i
20	20	10.746+1.094i
Mode 21 analytical: 35.604+1.150i		
9	9	38.285+1.157i
17	17	36.244+1.152i
20	20	36.011+1.151i
Mode 22 analytical: 62.851+1.096i		
9	9	67.679+1.093i
17	17	64.101+1.095i
20	20	63.588+1.095i

Table E.8: Convergence for Q4.VIS, INT.8 and Q4.ST elements. ($h_0 = 1.5 \cdot 10^{-3}$ m, $l_x = 0.25$ m, $l_y = 0.25$ m, $E_p = 70 \cdot 10^9$ N/m^2, $\rho_p = 2710$ kg/m^3, $\nu_p = 0.3$, $t_p = 1 \cdot 10^{-3}$ m)

E.2 Tube elements

E.2.1 Eigenfrequency calculations

Eigenfrequency calculations were carried out for various configurations. In all cases both ends of the (composed) tube were terminated by a $p = 0$ condition. The results for a line of T2.VISC elements and a line of T3.VISC elements are given in Table E.9 and Table E.10. The results for a line, composed of two different segments of T2.VISC elements or T3.VISC elements with different cross-sectional areas are given in Tables E.11, E.12 and E.13. Finally, the viscothermal tube elements were coupled to standard acoustic volume elements. The results for these calculations are given in Table E.14 and Table E.15

The analytical solution can easily be obtained for these 1-dimensional problems and will not be discussed in detail here. In the case of different segments, continuity of pressure and conservation of mass on the interface is assumed. Please note that in the test cases with the standard acoustic volume elements, the solution does not have to converge fully to the analytical solution, since the finite elements are based on a 3-dimensional volume approach. For a small cross section of the tube, however, the differences are small.

The Tables show good agreement between the analytical and numerical results. It can be concluded that the viscothermal elements give good results. Furthermore, viscothermal elements with different cross sections can easily be coupled. Finally, the viscothermal elements can be coupled to standard acoustic volume elements.

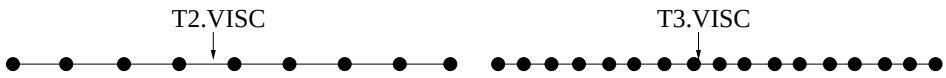

Figure E.5: Configurations for convergence tests of the tube elements

nx	T2.VISC	T3.VISC
	Mode 1 analytical: 155.947+14.126i	
17	156.208+14.138i	155.950+14.127i
33	156.012+14.129i	155.947+14.126i
65	155.963+14.127i	155.947+14.126i
129	155.951+14.127i	155.947+14.126i
	Mode 2 analytical: 320.095+19.953i	
17	322.219+20.017i	320.180+19.956i
33	320.625+19.969i	320.101+19.953i
65	320.227+19.957i	320.096+19.953i
129	320.128+19.954i	320.095+19.953i
	Mode 3 analytical: 485.609+24.428i	
17	492.834+ 24.604i	486.231+24.443i
33	487.410+ 24.472i	485.650+24.429i
65	486.059+ 24.439i	485.612+24.428i
129	485.722+ 24.431i	485.610+24.428i
	Mode 4 analytical: 651.829+28.202i	
17	669.051+28.564i	654.329+28.255i
33	656.115+28.292i	652.000+28.206i
65	652.899+28.225i	651.840+28.202i
129	652.096+28.208i	651.830+28.202i

Table E.9: Convergence for T2.VISC and T3.VISC elements (circular cross section: $R = 1.5 \cdot 10^{-3}$ m, $l_x = 0.5$ m)

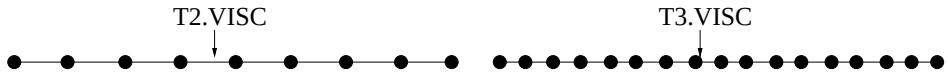

Figure E.6: Configurations for convergence tests of the tube elements

nx	T2.VISC	T3.VISC
	Mode 1 analytical: 157.689+12.190i	
17	157.952+12.200i	157.692+12.190i
33	157.754+12.192i	157.689+12.190i
65	157.705+12.190i	157.689+12.190i
129	157.693+12.190i	157.689+12.190i
	Mode 2 analytical: 322.573+17.292i	
17	324.706+17.348i	322.658+17.294i
33	323.105+17.306i	322.579+17.292i
65	322.706+17.296i	322.574+17.292i
129	322.606+17.293i	322.574+17.292i
	Mode 3 analytical: 488.650+21.209i	
17	495.897+21.364i	489.274+21.223i
33	490.457+21.248i	488.691+21.210i
65	489.101+21.219i	488.653+21.209i
129	488.763+21.212i	488.651+21.209i
	Mode 4 analytical: 655.343+24.512i	
17	672.610+24.829i	657.850+24.559i
33	659.641+24.592i	655.515+24.516i
65	656.416+24.532i	655.355+24.513i
129	655.611+24.517i	655.344+24.512i

Table E.10: Convergence for T2.VISC and T3.VISC elements (rectangular cross section: $l_x = 0.5$ m, $l_y = 1.5 \cdot 10^{-3}$ m, $l_z = 2 \cdot 10^{-3}$ m)

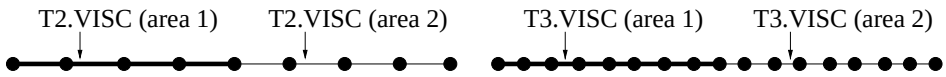

Figure E.7: Configurations for convergence tests of the tube elements

nx	T2.VISC	T3.VISC
	Mode 1 analytical: 125.677+9.722i	
17	126.104+9.703i	125.685+9.721i
33	125.784+9.717i	125.678+9.722i
65	125.704+9.720i	125.678+9.722i
129	125.684+9.721i	125.677+9.722i
	Mode 2 analytical: 192.606+12.081i	
17	193.722+12.132i	192.677+12.082i
33	192.886+12.093i	192.611+12.081i
65	192.676+12.084i	192.606+12.081i
129	192.624+12.081i	192.606+12.081i
	Mode 3 analytical: 321.198+18.892i	
17	329.056+19.076i	322.331+18.902i
33	323.158+18.938i	321.275+18.893i
65	321.688+18.903i	321.203+18.892i
129	321.321+18.895i	321.198+18.892i
	Mode 4 analytical: 457.004+18.900i	
17	473.486+17.859i	460.360+18.527i
33	461.316+18.637i	457.281+18.868i
65	458.094+18.834i	457.023+18.898i
129	457.278+18.883i	457.006+18.900i

Table E.11: Convergence for T2.VISC and T3.VISC elements (circular cross sections: $R_1 = 1.5 \cdot 10^{-3}$ m, $l_{x1} = 0.5$ m, $R_2 = 3 \cdot 10^{-3}$ m, $l_{x2} = 0.25$ m)

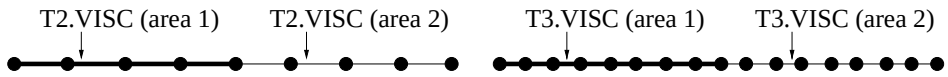

Figure E.8: Configurations for convergence tests of the tube elements

nx	T2.VISC	T3.VISC
	Mode 1 analytical: 126.851+8.375i	
17	127.275+8.360i	126.858+8.375i
33	126.957+8.372i	126.851+8.375i
65	126.877+8.374i	126.851+8.375i
129	126.857+8.375i	126.851+8.375i
	Mode 2 analytical: 194.131+10.476i	
17	195.253+10.522i	194.202+10.478i
33	194.412+10.488i	194.135+10.477i
65	194.201+10.480i	194.131+10.477i
129	194.148+10.477i	194.131+10.477i
	Mode 3 analytical: 323.539+16.371i	
17	331.419+16.533i	324.673+16.381i
33	325.505+16.412i	323.617+16.373i
65	324.030+16.382i	323.544+16.372i
129	323.662+16.374i	323.540+16.372i
	Mode 4 analytical: 459.263+16.341i	
17	475.618+15.456i	462.575+16.028i
33	463.541+16.120i	459.536+16.319i
65	460.344+16.289i	459.281+16.344i
129	459.534+16.331i	459.264+16.345i

Table E.12: Convergence for T2.VISC and T3.VISC elements (rectangular cross sections: $l_{x1} = 0.5$ m, $l_{y1} = 1.5 \cdot 10^{-3}$ m, $l_{z1} = 2 \cdot 10^{-3}$ m, $l_{x2} = 0.25$ m, $l_{y2} = 3 \cdot 10^{-3}$ m, $l_{z2} = 4 \cdot 10^{-3}$ m)

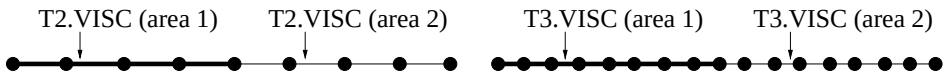

Figure E.9: Configurations for convergence tests of the tube elements

nx	T2.VISC	T3.VISC
	Mode 1 analytical: 133.032+9.686i	
17	133.523+9.650i	133.042+9.684i
33	133.155+9.677i	133.033+9.686i
65	133.063+9.684i	133.032+9.686i
129	133.040+9.685i	133.032+9.686i
	Mode 2 analytical: 186.311+11.015i	
17	187.275+11.088i	186.367+11.018i
33	186.553+11.034i	186.315+11.016i
65	186.372+11.020i	186.311+11.016i
129	186.326+11.017i	186.311+11.016i
	Mode 3 analytical: 320.860+19.218i	
17	328.983+19.426i	322.036+19.237i
33	322.885+19.270i	320.940+19.220i
65	321.366+19.231i	320.865+19.219i
129	320.986+19.222i	320.860+19.218i
	Mode 4 analytical: 464.901+18.728i	
17	481.973+16.825i	468.645+18.051i
33	469.474+18.258i	465.213+18.677i
65	466.062+18.615i	464.921+18.728i
129	465.192+18.702i	464.902+18.731i

Table E.13: Convergence for T2.VISC and T3.VISC elements (circular and rectangular cross sections: $R = 1.5 \cdot 10^{-3}$ m, $l_{x1} = 0.5$ m, $l_{x2} = 0.25$ m, $l_{y2} = 3 \cdot 10^{-3}$ m, $l_{z2} = 4 \cdot 10^{-3}$ m)

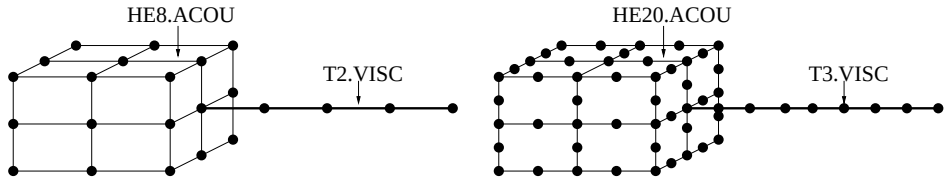

Figure E.10: Configurations for convergence tests of the tube elements

nx	HE8.ACOU/T2.VISC	HE20.ACOU/T3.VISC
	Mode 1 analytical **1D**: 95.877+1.145i	
17	96.060+1.150i	95.876+1.144i
33	95.920+1.146i	95.872+1.144i
65	95.881+1.144i	95.866+1.143i
129	95.866+1.142i	95.855+1.140i
	Mode 2 analytical **1D**: 241.578+1.533i	
17	244.142+1.616i	241.779+1.544i
33	242.210+1.556i	241.570+1.538i
65	241.712+1.544i	241.536+1.542i
129	241.564+1.545i	241.493+1.550i
	Mode 3 analytical **1D**: 333.617+6.465i	
17	337.944+6.552i	333.959+6.504i
33	334.574+6.484i	333.425+6.457i
65	333.608+6.458i	333.177+6.444i
129	333.134+6.440i	332.759+6.424i
	Mode 4 analytical **1D**: 434.907+1.962i	
17	451.333+2.007i	438.203+1.941i
33	438.990+1.965i	435.127+1.954i
65	435.902+1.953i	434.879+1.945i
129	435.109+1.941i	434.824+1.929i

Table E.14: Convergence for HE8.ACOU/T2.VISC and HE20.ACOU/T3.VISC elements (rectangular and circular cross sections: $l_{x1} = 0.5$ m, $l_{y1} = 2.5 \cdot 10^{-3}$ m, $l_{z1} = 2.5 \cdot 10^{-3}$ m, $ny_1 = 3$, $nz_1 = 3$ (HE8.AOU), $ny_1 = 5$, $nz_1 = 5$ (HE20.ACOU), $R_2 = 3 \cdot 10^{-3}$ m, $l_{x2} = 0.25$ m)

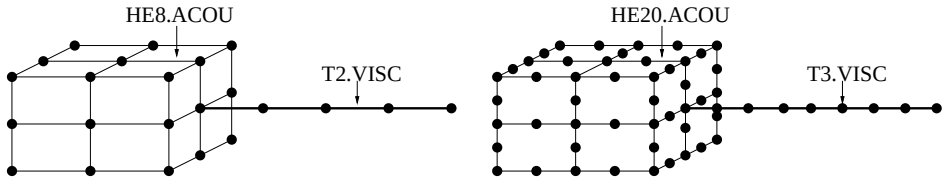

Figure E.11: Configurations for convergence tests of the tube elements

nx	HE8.ACOU/T2.VISC	HE20.ACOU/T3.VISC
	Mode 1 analytical **1D**: 101.489+1.386i	
17	101.697+1.393i	101.485+1.385i
33	101.534+1.386i	101.477+1.384i
65	101.486+1.384i	101.464+1.381i
129	101.461+1.380i	101.439+1.377i
	Mode 2 analytical **1D**: 235.483+1.719i	
17	237.689+1.786i	235.641+1.730i
33	236.015+1.739i	235.454+1.726i
65	235.570+1.731i	235.402+1.731i
129	235.416+1.735i	235.324+1.742i
	Mode 3 analytical **1D**: 335.544+4.516i	
17	340.692+4.618i	335.998+4.560i
33	336.661+4.540i	335.280+4.511i
65	335.483+4.512i	334.941+4.498i
129	334.870+4.495i	334.369+4.479i
	Mode 4 analytical **1D**: 440.339+2.429i	
17	456.434+2.545i	443.471+2.424i
33	444.335+2.449i	440.525+2.418i
65	441.283+2.419i	440.258+2.402i
129	440.470+2.396i	440.153+2.374i

Table E.15: Convergence for HE8.ACOU/T2.VISC and HE20.ACOU/T3.VISC elements (rectangular cross sections: $l_{x1} = 0.5$ m, $l_{y1} = 0.0025$ m, $l_{z1} = 0.0025$ m, $ny_1 = 3$, $ny_1 = 3$ (HE8.ACOU), $nz_1 = 5$, $nz_1 = 5$ (HE20.ACOU), $l_{y2} = 3 \cdot 10^{-3}$ m, $l_{z2} = 4 \cdot 10^{-3}$ m, $l_{x2} = 0.25$ m)